

In situ bulk structural investigation of Mo_5O_{14} -type mixed metal oxide catalysts for partial oxidation reactions

vorgelegt von
Diplom-Chemikerin
Eva Rödel
aus Berlin

Von der Fakultät II - Mathematik und Naturwissenschaften
der Technischen Universität Berlin
zur Erlangung des akademischen Grades
Doktor der Naturwissenschaften
Dr. rer. nat.
genehmigte Dissertation

Promotionsausschuß

Vorsitzender: Prof. Dr. rer. nat. M. Gradzielski

Gutachter: Prof. Dr. rer. nat. R. Schlögl

Gutachter: Prof. Dr. rer. nat. T. Ressler

Tag der wissenschaftlichen Aussprache: 18.12.2006

Berlin, 2006

D 83

Abstract

The calcination and thermal activation of a *MoVW* oxide precursor into Mo_5O_{14} -type structure were investigated by in situ X-ray diffraction (XRD), in situ X-ray absorption spectroscopy (XAS), Thermogravimetry and Difference scanning calorimetry (TG/ DSC) measurements. The observed (redox) stability and (redox) properties of $(Mo_{0.68}V_{0.23}W_{0.09})_5O_{14}$ are compared to $(Mo_{0.91}V_{0.09})_5O_{14}$ material and correlated to a structural characterization of both structures by XRD and EXAFS.

The crystallized *MoVW* mixed oxide consists of different phases of variable crystallinity depending on activation and calcination conditions. In a series of calcination experiments parameters influencing the crystallization and phase purity of $(MoVW)_5O_{14}$ material were investigated. It turned out that the redox potential of the gas atmosphere at the temperature chosen primarily changes the resulting crystallinity and phase purity. All parameters that contribute to the removal of framework molecules from the precursor, namely gas flow and dwell time at any treatment step, are of great importance and have to be coordinated in order to arrive at a crystalline, single phase $(MoVW)_5O_{14}$ catalyst, too. The heating rate affects the crystallinity. From this study it seems possible to decompose the precursor to the desired phase by adequate temperature and gas phase. During heating of *MoVW* oxide precursor in propene and oxygen the crystallization coincides with the onset of catalytic activity. This structure-activity correlation makes $(MoVW)_5O_{14}$ a candidate for the structure that can be assigned to the onset of catalytic activity in the selective oxidation reaction of propene to acrylic acid.

The bulk structural properties of single phase crystalline $(MoVW)_5O_{14}$ and $(MoV)_5O_{14}$ materials were investigated using in situ XRD and in situ XAS at three metal edges. Temperature programmed experiments in reducing (propene) and oxidizing (oxygen) atmosphere and isothermal redox experiments at 773 K revealed differences in the bulk properties of the two phases studied. A structure stabilizing effect of tungsten in $(MoVW)_5O_{14}$ under oxidizing conditions was found. The tungsten centers in a *MoVW* dioxide material exert a structure-directing effect towards re-oxidation to a Mo_5O_{14} -type structure. The structural analysis of $(MoV)_5O_{14}$ indicated a homogeneous distribution of elements on all sites, whereas for $(MoVW)_5O_{14}$ a preferred site occupancy of different elements on different sites was found. Concluding from XRD and XAS investigations vanadium prefers corner linked octahedral sites away from the pentagonal block unit. Tungsten centers are mostly located at pentagonal bipyramids and its neighboring octahedral sites. The promoting and stabilizing effect of tungsten in $(MoVW)_5O_{14}$ may be assigned to its site preference in the Mo_5O_{14} -type structure.

Abstract

Die Methoden in situ X-ray diffraction (XRD), in situ X-ray absorption spectroscopy (XAS), Thermogravimetry und Difference scanning calorimetry (TG/ DSC) wurden zur Untersuchung der Kalzinierung und thermischen Behandlung eines *MoVW* oxid Präkursors zu einem Oxid mit Mo_5O_{14} Struktur angewendet. Die dabei beobachtete (Redox-) Stabilität und (Redox-) Eigenschaften von $(Mo_{0.68}V_{0.23}W_{0.09})_5O_{14}$ wurden mit denen von $(Mo_{0.91}V_{0.09})_5O_{14}$ verglichen und die Ergebnisse auf die mittels XRD und EXAFS untersuchten Strukturen beider Materialien bezogen.

Bei der Kristallisation des *MoVW* oxid Präkursors entsteht abhängig von der Aktivierungs- und Kalzinierungsprozedur eine oder mehrere mehr oder weniger kristalline Phase(n). In einer Meßreihe wurden verschiedene Parameter der Kalzinierung untersucht, die sowohl den Kristallisationsgrad als auch die Phasenreinheit des entstehenden $(MoVW)_5O_{14}$ Materials beeinflussen. Den größten Einfluß auf Kristallisationsgrad und Phasenreinheit hat das Redox-Potential der Gasphase bei der betreffenden Kalzinierungstemperatur. Alle Parameter, die zur Entfernung in die Struktur eingelagerter kleiner Moleküle beitragen, im Wesentlichen der Gasfluß und die Haltezeit jedes Behandlungsschrittes, sind von Bedeutung und müssen aufeinander abgestimmt werden um einen kristallinen, phasenreinen $(MoVW)_5O_{14}$ Katalysator zu erhalten. Eine höhere Heizrate bewirkt einen höheren Kristallisationsgrad. Aufgrund dieser Forschungsergebnisse erscheint es möglich den Präkursor durch passende Temperaturbehandlung in geeigneter Gasphase gezielt zur gewünschten Phase zu zersetzen. Beim Aufheizen des anfangs XRD-amorphen *MoVW* oxid Präkursors in Propen und Sauerstoff beginnt die katalytische Aktivität zusammen mit der Kristallisation. Aufgrund dieser Struktur-Aktivitätskorrelation ist phasenreines $(MoVW)_5O_{14}$ ein vielversprechendes Modell auf der Suche nach einer Struktur, die der einsetzenden katalytischen Aktivität bei der selektiven Oxidation von Propen zu Acrylsäure zugeordnet werden kann.

Die Festkörpereigenschaften von phasenreinem $(MoVW)_5O_{14}$ und $(MoV)_5O_{14}$ wurden mit in situ XRD und in situ XAS an den Absorptionskanten aller enthaltenen Metalle untersucht. Temperaturprogrammierte Experimente in reduzierender (Propen) und oxidierender (Sauerstoff) Atmosphäre bei 773 K zeigten unterschiedliche Festkörpereigenschaften der beiden Materialien. Ein die Mo_5O_{14} Struktur stabilisierender Effekt wurde für $(MoVW)_5O_{14}$ unter oxidierenden Bedingungen gefunden. Bei der Re-oxidation von *MoVW* dioxid dirigieren die Wolframzentren die Struktur zur Mo_5O_{14} Struktur. Die Strukturuntersuchungen an $(MoV)_5O_{14}$ deuten auf eine homogene Verteilung der Elemente auf allen kristallographischen Positionen an, dagegen wurde für $(MoVW)_5O_{14}$ eine bevorzugte Besetzung einiger kristallographischer Positionen mit einem bestimmten Element gefunden. XRD und XAS Untersuchungen lassen darauf schließen, daß Vanadium eckenverknüpfte Positionen entfernt von der pentagonal-bipyramidalen Einheit und ihrer umgebenden Oktaeder bevorzugt. Die Wolframzentren sind hauptsächlich auf den pentagonal-bipyramidalen Positionen und den direkt kantenverknüpften Oktaedern anzutreffen. Der reaktionsfördernde und stabilisierende Einfluß von Wolfram in $(MoVW)_5O_{14}$ kann mit seiner Bevorzugung einzelner kristallographischer Positionen in der Mo_5O_{14} Struktur erklärt werden.

Content

1	Introduction	1
1.1	Catalysis	1
1.2	Heterogeneous catalysis	2
1.3	Selective oxidation reaction	3
1.4	Structural defects	4
1.5	Molybdenum oxide based catalysts	5
1.5.1	Selective oxidation of propene to acrylic acid	6
1.5.2	Selective oxidation of propane to acrylic acid	6
1.6	Mixed metal oxide systems	7
1.6.1	Molybdenum/ vanadium oxide system	7
1.6.2	Molybdenum/ vanadium/ tungsten oxide system	8
1.7	Rational catalyst design	9
1.8	Motivation	11
2	Structures	13
2.1	Structure of ammonium heptamolybdate	13
2.2	Structure of ammonium tungstate	13
2.3	Structure of MoO_3	14
2.4	Structure of V_2O_5	15
2.5	Structure of V_2O_3	16
2.6	Structure of WO_3	16
2.7	Structures of MoO_2 , VO_2 and WO_2	17
2.8	Structure of MoV_2O_8	18
2.9	Structure of $Mo_xV_{2-x}O_5$	19
2.10	Oxides with pentagonal bipyramidal coordination	20
2.11	Mo_5O_{14} -type structure	21
2.12	Structure of M1 and M2 phase	22
3	Methods	23
3.1	X-ray powder diffraction	23
3.2	X-ray absorption spectroscopy	24
4	Experimental	28
4.1	Preparation conditions	28
4.2	Crystallization and calcination experiments	28

4.3	Heating and redox experiments	30
4.4	X-ray powder diffraction	30
4.4.1	Data analysis	31
4.4.2	Structure refinement of $(MoVW)_5O_{14}$ and $(MoV)_5O_{14}$	31
4.5	X-ray absorption spectroscopy	32
4.5.1	Data processing	32
4.5.2	XAS structure model for investigation of Mo_5O_{14}	34
4.5.3	XAS refinement strategy	36
4.5.4	Investigation of XAS refinement strategy on simulated data	36
4.5.5	XAS multiple edge investigation of Mo_5O_{14} -type catalysts	38
4.6	TG/ DSC	38
4.7	Mass spectrometry	39
5	Results	40
5.1	Crystallization of $MoVW$ oxide precursor	40
5.1.1	In situ XRD crystallization	41
5.1.2	Thermal analysis of crystallization in TG/ DSC	65
5.1.3	In situ XAS crystallization	82
5.2	XRD structural investigation	93
5.3	XAS structural investigation	95
5.3.1	Refinement strategy	95
5.3.2	Refinement of $(MoVW)_5O_{14}$ and $(MoV)_5O_{14}$	98
5.4	Catalytic properties of $(MoVW)_5O_{14}$	101
5.4.1	In situ XRD	102
5.4.2	In situ XAS	104
5.5	Catalytic properties of $(MoV)_5O_{14}$	106
5.5.1	In situ XRD	106
5.5.2	In situ XAS	107
5.6	Thermal stability of $(MoVW)_5O_{14}$	108
5.6.1	In situ XRD	108
5.6.2	In situ XAS	110
5.7	Thermal stability of $(MoV)_5O_{14}$	113
5.7.1	In situ XRD	113
5.7.2	In situ XAS	114
5.8	Redox properties	117
5.8.1	In situ XRD	117
5.8.2	In situ XAS	120
6	Discussion	125
6.1	Crystallization and calcination experiments	125
6.1.1	Comparability of data obtained by different methods	125
6.1.2	Structural characterization of the $MoVW$ oxide precursor with XAS	125
6.1.3	Structure-activity correlation of $(MoVW)_5O_{14}$	126

6.1.4	Optimized thermal treatment conditions forming single phase ($Mo_{0.68}V_{0.23}W_{0.09}$) ₅ O_{14} material	126
6.1.5	Influence of redox potential of the gas phase	127
6.1.6	Removal of oxalate, nitrate, and ammonia	128
6.1.7	Structural changes during first calcination step	128
6.1.8	TG/ DSC investigation of calcination	130
6.1.9	Anisotropic crystallization of the Mo_5O_{14} -type structure	131
6.1.10	Structure formation of ($MoVW$) ₅ O_{14}	132
6.1.11	Direct morphology imaging by TEM	133
6.1.12	Perspectives from reduced mixed metal dioxide	133
6.2	Structural characterization	135
6.2.1	XRD investigation of ($MoVW$) ₅ O_{14} and (MoV) ₅ O_{14}	135
6.2.2	Investigation of XAFS refinement strategy on simulated data	135
6.2.3	XAFS refinement of ($MoVW$) ₅ O_{14} and (MoV) ₅ O_{14}	136
6.2.4	Characterization of ($MoVW$) ₅ O_{14} and (MoV) ₅ O_{14}	137
6.3	Bulk structural properties	138
6.3.1	Average valence of molybdenum	138
6.3.2	Average valence of vanadium	138
6.3.3	Change in unit cell volume owing to metal substitution	138
6.3.4	Effect of vanadium on electronic and geometric structure	139
6.3.5	Stabilizing effect of tungsten in Mo_5O_{14} -type structures	139
6.4	Catalysis of Mo_5O_{14} -type material	141
6.4.1	The model catalyst system ($MoVW$) ₅ O_{14}	141
6.4.2	Structure-functionality correlation of ($MoVW$) ₅ O_{14} and (MoV) ₅ O_{14} for different products in catalysis	141
6.4.3	Reaction mechanism for the selective oxidation of propene	142
6.4.4	Consideration of active site models proposed in literature	143
7	Summary	146
8	Acknowledgement	148
9	References	149
10	Curriculum vitae	159

Chapter 1

Introduction

1.1 Catalysis

Catalysis contributes significantly to the net product of the chemical sector in economy. Catalytic processes are one of the key technologies in the chemical and pharmaceutical sector. A large variety of widely used everyday products based on catalytic reactions contribute to our life. Useful things like plastics, medicals, cosmetics, convenience food or cars would either be absent, expensive, or of lower quality. Most industrial processes include one or more catalyzed reaction steps. From this point of view catalysis gives access to a higher standard of living.

But not only in industry catalysis is found, catalytic reactions occur in natural systems. Catalytic reaction steps performed by enzymes occur everywhere in the metabolism of each organism. Plants, mushrooms, animals, or humans, and bacteria utilize catalytic reaction mechanisms. With the help of enzymes produced by microorganisms, biotechnology uses catalysis on purpose.

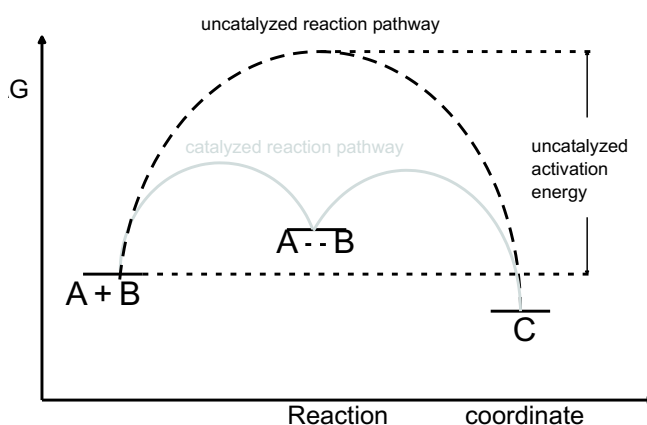


Figure 1.1: Schematic illustration of a catalyst's effect on the reaction pathway.

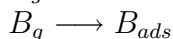
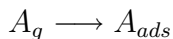
Understanding, developing, and improving catalytic processes is favored for economical and ecological reasons. The economic side is reducing the costs of chemical processes with more efficient catalysts requiring less energetic input and allowing faster processes. The catalyst offers control over the reaction pathway from reactants to products. As represented in Figure 1.1, the new reaction pathway in presence of the catalyst is of lower activation energy and/ or higher selectivity. In presence of the catalyst the thermodynamic barriers of the uncatalyzed reaction are overcome and the equilibrium adapts to the modified conditions. The detailed knowledge of the dependencies between reaction mechanism and catalyst helps to optimize processes and catalysts. A new or improved catalyst reduces waste from unwanted side products and increases the yield. This is how ecological aspects are promoted because energy and raw material resources are used more efficiently as the catalyst opens up a new reaction pathway of lower activation energy or higher selectivity.

1.2 Heterogeneous catalysis

A catalytic reaction between two phases in contact with one another is denoted as heterogeneous catalysis. Usually the catalyst is solid and reactants and products can be either in liquid or gaseous state. In solid-gaseous systems heterogeneous catalysis involves the reaction on the surface of the solid. The steps important for forming the product in a heterogeneously catalyzed reaction are adsorption and diffusion of reactants on the surface. The interaction of the reactant with the surface forms new bonds and weakens bonds in the reactant molecules. Depending on the reaction dissociation of the reactants may occur. The diffusion of adsorbed species can either lead to reformation and desorption of the reactant or formation and desorption of product. In heterogeneous catalysis two basic mechanisms are distinguished:

- Langmuir-Hinshelwood mechanism

both reactants are adsorbed to the surface of the catalyst



reaction on catalyst surface

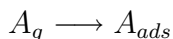


desorption of the product

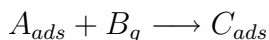


- Eley-Rideal mechanism

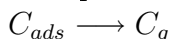
one reactant is adsorbed to the surface of the catalyst



reaction of adsorbed with free reactant on catalyst surface



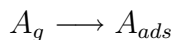
desorption of the product



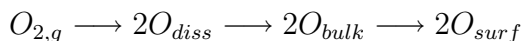
In case of a selective oxidation reaction on a metal oxide based catalyst the following mechanism is considered:

- Mars-van-Krevelen mechanism

one reactant is adsorbed to the surface of the catalyst



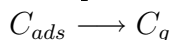
oxygen adsorbs on another surface of the catalyst, dissociates and diffuses through bulk to adsorbed reactant



reaction on the surface of the catalyst



desorption of the product



Oxidation catalysis on metal oxide based catalysts is still a matter of understanding. The Mars-van-Krevelen mechanism is a process of oxygen diffusion through the bulk oxide catalyst to the reactive site. The surface of a metal oxide catalyst under reaction conditions is dynamic, not a simple termination of the bulk structure. Multiple adsorption-desorption, reduction-oxidation steps may take place. Lattice oxygen diffusion, formation of lattice defects and surface reconstruction are important reaction steps that influence the catalytic performance. Possibly catalytic activity and selectivity arise not on a single active site, so that a combination of several phenomena involving multiple active sites and/or their interaction and proximity to each other play an important role for the catalytic reaction mechanism [1].

1.3 Selective oxidation reaction

Recently Grasselli [2, 3] summarized several properties that many selective heterogeneous oxidation catalysts have in common, the so-called '7 pillars':

- lattice oxygen
- metal-oxygen bonds
- host structure
- redox properties
- multifunctional active sites
- site isolation
- cooperation of phases

Selective oxidation reactions usually employ transition metal oxide catalysts. The variability of valence and flexible coordination geometry of transition metals enables lattice oxygen transfer between bulk metal oxide and species adsorbed on the oxide surface

according to the Mars-van-Krevelen mechanism [4]. The concept of this mechanism is that oxygen delivered from the catalyst has less nucleophilic properties than oxygen from the gas phase and is weakly bound to the surface. The more electrophilic oxygen at the surface has less oxidizing power than oxygen delivered from the gas phase and therefore reacts more selectively. The oxidizing power of the surface lattice oxygen can be adjusted with the catalysts metal composition changing the metal-oxygen bond strength [5]. The host structure of a catalyst provides metal-oxygen bonds of desired strength and enables lattice oxygen transfer. Therefore, oxygen from the catalyst selectively oxidizes the adsorbed and activated hydrocarbon molecules. The reactive surface lattice oxygen atoms need to be separated from one another by the host structure in order to achieve selectivity. The concept of site isolation indicates that the number of reactive surface lattice oxygens at a site determines the stoichiometry of the reaction and the products formed. During reaction the oxygen from the metal oxide is incorporated into the hydrocarbon and the remaining lattice vacancy refilled by diffusion of bulk oxygen through the lattice. The oxygen uptake of the metal oxide may occur remote from the reactive site. Dioxygen from the gas phase dissociates at the catalyst surface, oxygen then diffuses on the surface or via vacancies through the lattice. Under reaction conditions the uptake and transfer of oxygen in the catalyst has to be faster than the reduction. Therefore, knowledge about the redox properties of a material help to gain insight to the function as a catalyst. In case the requirements for a suitable host structure are not fulfilled by one phase the next best approach is cooperation of two or more phases in close proximity with each other. Despite their wide and variable application only few selective oxidation reactions are understood on the level of mechanistic details on the catalyst during reaction.

1.4 Structural defects

A single crystal structure represents the ideal structure of a solid. In the real solid structure an equilibrium concentration of point defects remains at $T > 0$:

$$\Delta G = \Delta H - T \cdot \Delta S$$

Figure 1.2 shows how ΔH (that is needed to form the defect, thus increasing ΔG) and the increasing entropy (thus decreasing $-T \cdot \Delta S$) lead to the real structure of the crystalline solid at the minimum of ΔG . At elevated temperatures crystals contain additional defects [6]. Fazit: in a real solid deviations from the ideal lattice structure occur. For catalysis the real structure of a catalyst is relevant [7, 8]. The defects are necessary for ion mobility and reactivity of a solid and open the path for diffusion and transport through the rigid arrangement of atoms in the crystal lattice. Defects are responsible for properties [9] like ion conductivity, mechanical stability, super conductivity, and catalytic activity of solids. The dynamics of defects in a solid depend on the temperature needed for overcoming the activation energies to break bonds or exchange lattice sites. In a solid different defects can occur. For a structural unit different orientations in the structure may be possible. A superstructure can be embedded

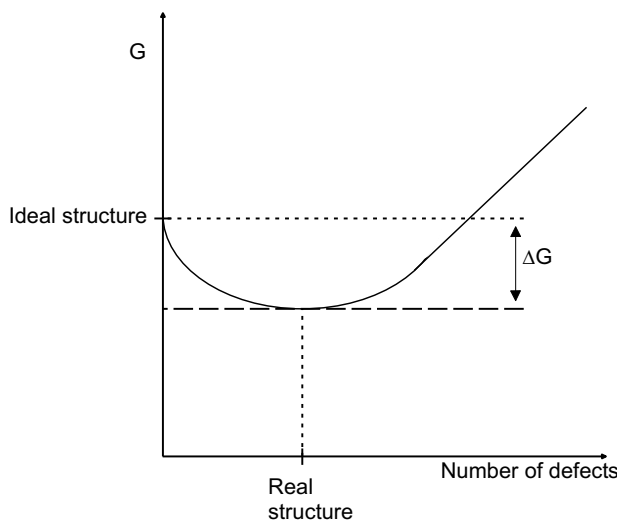


Figure 1.2: The real structure of a crystalline material depends on the concentration of defects in the solid.

in the host structure. Defects in solids are classified referring to their dimension. A two-dimensional defect could be chains that have no periodic arrangement among one another. A shear plane or a stacking fault in layered structures are one-dimensional defects. There the periodicity in the direction perpendicular to the layers is disturbed either by insertion of a wrong layer to the sequence or the translation between layers changes. Point defects are zero-dimensional defects. Impurities of foreign elements are a possible zero-dimensional defect. Site occupancy defects appear where an atom of one element occupies a site usually occupied by another element. Site displacement of an atom from its position can result in splitting to two or more sites. Atoms of impurity elements may occupy interstitial sites more likely than the elements of the host structure and thus leading to more defects. With increasing temperature for all crystals an increasing number of sites becomes statistically unoccupied. Two types of point defects occur. A Schottky defect has vacancies in the anion- and cation lattice and stays electrically neutral. A Frenkel defect is a missing atom (vacancy) on one site that has moved to an interstitial site.

1.5 Molybdenum oxide based catalysts

Selective oxidation reactions usually employ transition metal oxide compounds. These solid catalyst systems contain at least one transition metal of variable oxidation state. Therefore the total oxygen content of the catalyst varies with oxidation state of the metal. The valence state of the metal can be detected with bulk sensitive in situ methods as X-ray absorption spectroscopy or electron spin resonance. Mixed transition metal compounds offer a wide range of possible catalyst combinations. Molybdenum based oxide catalysts containing several other metals can be applied for many reactions:

1. $W \Rightarrow$ selective alkylation of benzene with propene into propylbenzene [10]

2. Sn \Rightarrow selective oxidation of propene into acetone [11]
3. Bi or Te \Rightarrow selective oxidation of propene into acrolein [12, 13]
4. Fe \Rightarrow selective oxidation of propene into acrolein [14]
5. Au \Rightarrow selective oxidation of propene into 1,2-epoxypropane [15]
6. V+W \Rightarrow selective oxidation of acrolein into acrylic acid

Catalysts commonly used for selective oxidation reactions are based on molybdenum and vanadium oxides [16, 17, 18]. The recurrent presence of these two transition metals in catalysts is remarkable and has been starting point of previous studies. For that reason the focus of this work is on a molybdenum based oxide catalyst, too.

1.5.1 Selective oxidation of propene to acrylic acid

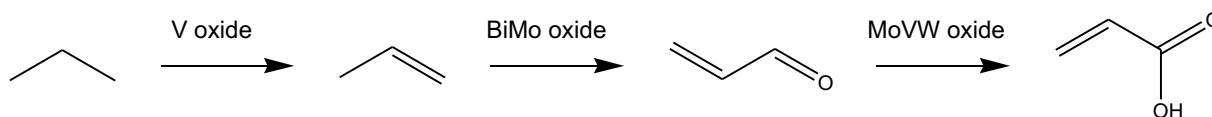


Figure 1.3: Industrially utilized selective oxidation catalysts

The formation of acrylic acid from propane is industrially performed in three steps. The dehydrogenation of propane to propene proceeds in presence of a vanadium based oxide [19] or platinum catalyst [20], the selective oxidation of propene into acrolein in presence of a *BiMo* oxide catalyst [21], and the subsequent oxidation of acrolein into acrylic acid in presence of a *MoVW* oxide catalyst [22].

1.5.2 Selective oxidation of propane to acrylic acid

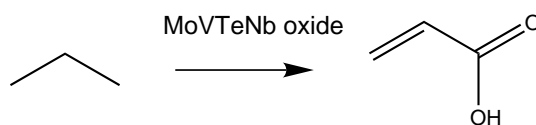


Figure 1.4: Desired process

The direct conversion of propane into acrylic acid is the desired process for future application in industry [16, 23]. The use of propane instead of propene would reduce the costs of the reactant in acrylic acid production. At present the most promising catalyst for this selective oxidation reaction are *MoVTenb* oxides. Depending upon preparation conditions the final catalyst crystallizes in M1 or M2 phase (see Paragraph 2.12) or as a phase mixture [24].

1.6 Mixed metal oxide systems

Phase diagrams of the binary systems Mo_xO_y [25], V_xO_y [26], and W_xO_y [27] exist in literature and single crystal structures of many compounds are found in the Inorganic Crystal Structure Database (ICSD) [28]. In these phase diagrams several stoichiometries exist with the metal component in mixed oxidation states. With the additional structural information from single crystal data the stability of different coordination geometries for the varying oxidation states can be discussed. In the phase diagram covering stoichiometries from MoO_2 [29] to MoO_3 [30] several shear structures occur, i.e. $Mo_{18}O_{52}$ [31] and Mo_8O_{23} [32]. In MoO_3 molybdenum is distorted octahedrally coordinated. In the shear structures with stoichiometry between MoO_2 and MoO_3 besides the distorted octahedral coordination tetrahedral coordination appears. Metastable systems do not occur in the phase diagrams. Depending on the reaction conditions the crystallization process of a solid may be kinetically or thermodynamically controlled. In case of thermodynamic control the structures as presented in the phase diagram are formed. In case of kinetic control the structure of lowest activation energy is formed, which is not necessarily the thermodynamically stable structure (e.g. the Mo_5O_{14} -type structure). Therefore, control of the crystallization process offers a preparation route to metastable structures.

1.6.1 Molybdenum/ vanadium oxide system

First systematic investigation on the ternary molybdenum/ vanadium oxide system were published by Volkov [33] in a phase diagram shown in Figure 1.5. In the phase diagram appear the thermodynamically stable compounds between MoO_3 and V_2O_5 . In most cases the formation of the solid solution is accompanied by the partial reduction of V^{5+} to V^{4+} and release of oxygen.

Detailed single crystal investigation on V_2MoO_8 [34, 35, 36] and on several stoichiometries of $Mo_xV_{2-x}O_5$ in the range of $0.02 < x < 0.97$ [37, 38, 39, 40] confirmed the validity of the phase diagram. Additional information on the stability of the molybdenum/

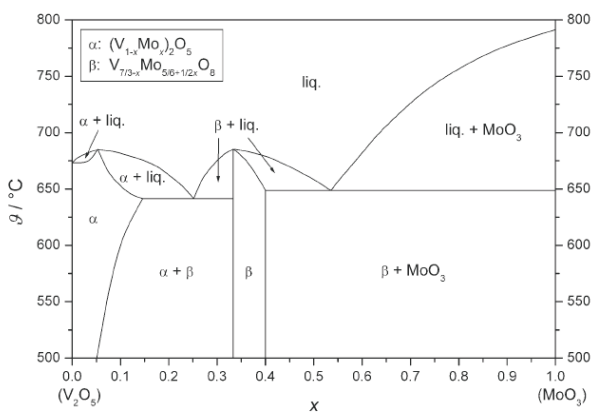


Figure 1.5: Phase diagram of the quasi binary system MoO_3/V_2O_5 .

vanadium oxide system is given by investigation of $Mo_xV_{2-x}O_3$ [41, 42] in the range of $0.02 < x < 0.2$, on vanadium in $Mo_{17}O_{47}$ [43], and on $V_9Mo_6O_{40}$ [44].

The powder diffraction data ICDD-PDF [31-1437] originates from a molybdenum/vanadium oxide of stoichiometry $(Mo_{0.93}V_{0.07})_5O_{14}$ [45]. This structure has not been published as single crystal data and does not occur in the phase diagram (Figure 1.5). Therefore it can be argued to be a metastable structure. Concerning the catalytic properties of (amorphous or crystalline, but not Mo_5O_{14} structured) MoV oxides previous studies concluded that an additional dopant for long time stability, activity and selectivity of MoV oxide as a catalyst is necessary [46].

1.6.2 Molybdenum/ vanadium/ tungsten oxide system

Little information is known about the quaternary molybdenum/ vanadium/ tungsten oxide system. Neither a phase diagram nor single crystal structures exist in literature. Presumably this system is not sufficiently crystalline for X-ray structure investigations or a multiphase system. In the selective oxidation reaction with $MoVW$ oxide catalysts vanadium was found necessary for the high catalytic performance and tungsten as a structure stabilizing agent [47]. Detailed structural analysis was limited by phase purity of the material.

Table 1.1 lists the effective ionic radii of molybdenum, vanadium and tungsten. The similar ionic radii for Mo^{6+} and W^{6+} in sixfold coordination generate similar geometric conditions for coordination. The elements may replace one another quite well for a wide range of stoichiometries and/ or structures, e.g. for the ReO_3 -type structure a homologous series of mixed molybdenum/ tungsten oxides exists [48]. This structure exhibits defects denoted as 'recurrent dislocations'. When looking at the thermodynamically stable structures of the fully oxidized elements, MoO_3 and WO_3 , it appears that additional effects like band structure affect the crystal structure. For MoO_3 orthorhombic (ICSD [35076]) and monoclinic (ICSD [68136]) structures are possible, whereas for WO_3 hexagonal (ICSD [32001]), tetragonal (ICSD [2796]), orthorhombic (ICSD [836]), monoclinic (ICSD [14332]) and triclinic (ICSD [80053]) are known. Even though most of these structures are not thermodynamically stable at RT, they outline coordination geometries possible for the respective cation.

Molybdenum oxides and tungsten oxides with their similar metal ionic radii (Table 1.1) have a similar coordination geometry. In most structures the coordination geometry of the metal centers is distorted octahedrally. Vanadium cations possess smaller ionic radii and reach a maximum oxidation state of only V^{5+} . Their structural chemistry differs strongly from that of molybdenum and tungsten. In V_2O_5 the strongly distorted octahedral coordination geometry could as well be described as squared pyramidal coordination geometry. Vanadium centers in more reduced state like in VO_2 or V_2O_3 with V^{4+} and V^{3+} (respectively) are more suitable to replace Mo^{6+} or Mo^{4+} , respectively. From charge equilibration the replacement of molybdenum by tungsten is more likely than replacement by vanadium in a mixed metal oxide structure. From a geometric point of view the incorporation of vanadium instead of molybdenum favors vanadium that is not in its maximum oxidation state and thus lowers the average valence of metals in the oxide. One possibility of the mixed metal oxide to adapt to

	C.N.	ionic radii (Å)
Mo^{6+}	7	0.87
Mo^{6+}	6	0.73
Mo^{5+}	6	0.75
Mo^{4+}	6	0.79
W^{6+}	6	0.74
W^{5+}	6	0.76
W^{4+}	6	0.80
V^{5+}	6	0.68
V^{4+}	6	0.72
V^{3+}	6	0.78

Table 1.1: Effective ionic Radii according to Shannon and Prewitt [49]

the incorporation of metals in lower oxidation state is the generation of defects in the oxygen sub-lattice. A highly defective oxygen sub-lattice in the mixed metal oxide could enhance the incorporation of vanadium - or, the other way round, the presence of vanadium with its lower maximum oxidation state could increase the number of oxygen defects. Additionally to the different coordination geometry of the three metals incorporated disorder is stabilized by the Peierls-distortion [50]. The binary metal oxides of $MoO_3/V_2O_5/WO_3$ exhibit some structural relation. The system MoO_3/V_2O_5 contains three mixed metal phases. If tungsten could easily replace molybdenum, a similar phase diagram as for MoO_3/V_2O_5 could be expected, but this seems not to be the case. Maybe in the molybdenum/ vanadium/ tungsten oxide system there do exist only few stable structures incorporating all three metal cations with a limited stability range. One of these structures is an Mo_5O_{14} -type phase.

1.7 Rational catalyst design

For a long time catalyst development was based on chemical intuition and on trial and error. Empirical development and optimization of catalysts based on high throughput screening [51] was successful finding many catalysts, e.g. most catalysts that are nowadays industrially used. Alternatively, a catalyst can be improved by rational catalyst design [52, 53, 54, 55, 56, 46]. This approach aims at optimizing the catalyst based on the knowledge of a model system and then elucidating the catalytic mechanism. Therefore, a number of catalysts are prepared under well-defined reaction and calcination conditions [57] and characterized by many analytical methods. The samples are tested for their catalytic performance, and parameters that show a correlation of preparation conditions and catalytic activity or selectivity are determined. Based on these parameters the next generation of catalysts is prepared as model system for the specific correlation. Systematic investigations of elements, their interaction, processes in liquid phase, calcination conditions, dependence on surface and bulk structure allow the determination of the preparation step(s) that significantly contribute to the catalytic activity. During this iterative process the model catalyst is optimized according

to the chemical or structural species that is investigated. In the specified preparation step(s) the active species can be determined and characterized. With this knowledge the structural and chemical species that are correlated to the catalytic activity are selectively increased in the preparation procedure. The characterization and in situ investigation during preparation or of a working catalysts provide knowledge about the structures and electronic states of catalyst sites [58]. From that catalytic systems can be optimized or new systems developed and that is why the investigation of structure-activity correlation of a model catalyst under reaction conditions is an important step on the way to a rational catalyst design [58, 59].

1.8 Motivation

Mixed molybdenum based oxides selectively oxidize propene to acrolein and acrylic acid with high catalytic performance [60]. Recent studies have shown that mixed metal *MoVNb* oxides possessing a Mo_5O_{14} -type structure are active for the selective oxidation of ethane [61, 62] and were determined to be important for the selective oxidation of propane [63]. Also, in the selective oxidation of methanol increased activity was found for thermally treated *MoVW* mixed metal oxides and correlated to the appearance of structural defects and shear structures [64]. There, in the thermally treated sample a major Mo_5O_{14} -type phase and MoO_3 - and MoO_2 -type minority phases with inhomogeneous elemental distribution were found. Similarly, mixed metal *MoVW* oxides possessing a Mo_5O_{14} -type structure are particularly active for the selective formation of acrylic acid [65, 66, 67]. A study on the morphology of *MoVW* oxides concluded the importance of a defective Mo_5O_{14} -type structure with ill-defined surface termination [68].

The stabilization of molybdenum based Mo_5O_{14} -type materials by metal substitution has been described in literature [69], but the stability range of the mixed metal oxides $(Mo_{1-x}M_x)_5O_{14}$ (M : substitute metal) in the Mo_5O_{14} -type structures is narrow and depends on the type of substitute metal M . For low valence substitutes $M^{4+}=Ti$ the stability range is $x \approx 0.04$ [70], which is roughly half the amount of substitute compared to $M^{5+}=V$ with $x \approx 0.09$ [45], $M^{5+}=Nb$ with $x \approx 0.09$ [71] and $M^{5+}=Ta$ with $x \approx 0.07$ [71], whereas for high valence $M^{6+}=W$ $0.05 < x < 0.30$ [72] the structure tolerates more substitute metal. The stabilizing effect of metal substitutes is explained in terms of electron concentration or stabilizing certain sites in the structure [73]. In the single crystal data of Mo_5O_{14} [74] disorder of the metal sites and a superstructure were found. Similarly, in Ta -substituted Mo_5O_{14} -type material a puckering scheme and superstructure were described for the metal sites [75].

The structure of Mo_5O_{14} corresponds to a pentagonal column structure and possesses an open framework with parallel channels [76]. The Mo_5O_{14} -type structure is related to that of the M1 phase of mixed *MoVTeNb* oxides [77] that is correlated to the activity of *MoVTeNb* oxides [78, 79]. If there is a correlation of structure and functionality, the similar structural motifs in both systems facilitate the assignment of structural features necessary for the functionality. The molybdenum based oxides selectively oxidize propane to acrylic acid. However, the chemical and structural complexity of *MoVTeNb* oxides makes studies on the structure of the catalyst under reaction conditions difficult. Hence, suitable model systems are required for elucidating structure activity relationships of selective oxidation catalysts. Single phase crystalline $(MoVW)_5O_{14}$ exhibits catalytic activity in the selective oxidation of propene into acrylic acid. Therefore it constitutes a model system for the industrial *MoVW* oxide catalyst and could be considered as a model system for *MoVTeNb* oxides. $(MoVW)_5O_{14}$ is the next more complicated system after investigation of MoO_3 , which has been studied in-depth [80] and holds as a model system for the selective oxidation of propene to acrolein. These model systems exhibit a less complicated chemical composition than industrial catalysts. Furthermore, they form a crystalline single-phase material that simplifies the structural analysis under reaction conditions.

Previous authors found the necessity of dopands for the long time stability, activity, and selectivity of the *MoV* oxide catalysts, e.g. tungsten was found to be a suitable promoter for stability and activity in the selective oxidation reaction [46]. The structure-activity correlation can be extended for investigation of the effect of tungsten on the single-phase Mo_5O_{14} -type structure when compared to a tungsten-free sample exhibiting the same Mo_5O_{14} -type structure.

In a mixed metal oxide as the $(MoVW)_5O_{14}$ system specific site occupancy by different elements is possible. Eventually the stabilizing effect of tungsten observed for the *MoW* oxide system in Mo_5O_{14} -type structure could originate from this site preference, too. Different stability of different elements located on the crystallographically unequal sites is likely. In case of the *MoTa* oxide system tantalum could be located in the pentagonal bipyramids exclusively [75] and similar behavior could be expected for its lighter analogue vanadium. Hence, vanadium as well as tungsten potentially occupies the pentagonal bipyramidal sites. In the present $(MoVW)_5O_{14}$ - incorporating both substitutes for molybdenum - it was up to now unclear which metal site is occupied by which element.

Chapter 2

Structures

2.1 Structure of ammonium heptamolybdate

The monoclinic structure of ammonium heptamolybdate tetrahydrate (AHM) with the stoichiometry $(NH_4)_6 Mo_7 O_{24} \cdot 4H_2O$ in space group $P2_1/c$ crystal is described [81] (ICSD [4153]). In the heptamer units shown in Figure 2.1 the molybdenum cations are coordinated by oxygen in form of distorted octahedra linked via edges and corners. The heptamer units are arranged in a framework of ammonium ions and water molecules in the structure. AHM is related to the Anderson phases, in which a heteroatom replaces molybdenum in the central position of the heptamer unit.

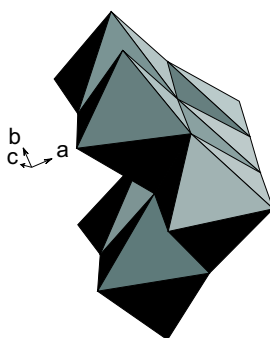


Figure 2.1: The heptamer in AHM is built from octahedrally arranged oxygen enclosing the central molybdenum (ICSD [4153]).

2.2 Structure of ammonium tungstate

In the triclinic structure of ammonium metatungstate (AMT) [82] in space group $P\bar{1}$ (ICSD [8123]) and monoclinic ammonium paratungstate (APT) [83] in space group $P2_1/n$ (ICSD [15237]) have the same polyoxometallate anion $[H_2W_{12}O_{42}]^{10-}$. In the polyoxometallate anion shown in Figure 2.2 tungsten is coordinated octahedrally by six oxygen anions. The distorted octahedra are structured in two triades as the building

blocks of Keggin cluster ions and heteropolyacids. In a triade the octahedra share one edge with each of the two other octahedra. Two triades in layers are corner sharing with two times three octahedra groups separating the two layers of triades. In the two groups octahedra are edge sharing among one another.

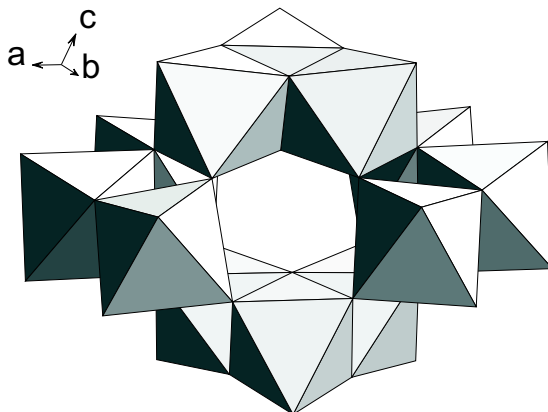


Figure 2.2: The polyoxometallate anion $[H_2W_{12}O_{42}]^{10-}$ as it occurs in APT and AMT. Top and base are formed by triades.

The structures of ammonium metatungstate and ammonium paratungstate differ in the framework of ammonium and water molecules and the relative arrangement of the polyoxometallate anions $[H_2W_{12}O_{42}]^{10-}$ to one another.

Polyoxometallates containing tungsten and different heteroelements are exploited in catalysts. The respective heteroatoms strongly effect the catalytic properties. Therefore a structural investigation of the polyoxometallates at the same time with elemental interrelations gives access to the mechanistic understanding of the catalytic process.

2.3 Structure of MoO_3

α - MoO_3 [30] forms an orthorhombic structure in space group $Pbnm$ (ICSD [35076]). The molybdenum cations are coordinated by six oxygen anions in distorted octahedral geometry. The structure is formed by edge sharing octahedra that are arranged in layers. Between the layers the octahedra are not linked. Besides orthorhombic α - MoO_3 there exist monoclinic modifications of MoO_3 [84, 85, 86], a monoclinic high pressure phase [87], and a so-called 'hexagonal' MoO_3 structure [88] that may incorporate vanadium [89, 89]. Monoclinic and 'hexagonal' MoO_3 are constructed from molybdenum in distorted octahedral coordination. The octahedra are linked corner sharing and edge sharing. 'Hexagonal' MoO_3 is an intermediate in the decomposition of AHM to α - MoO_3 [90] and the structure may incorporate vanadium [46]. The octahedra form parallel channels large enough for small molecules that may have an stabilizing effect. In the open framework of the hexagonal structure molecules of H_2O and NH_3 are embedded, so the 'hexagonal' MoO_3 is not a binary molybdenum oxide.

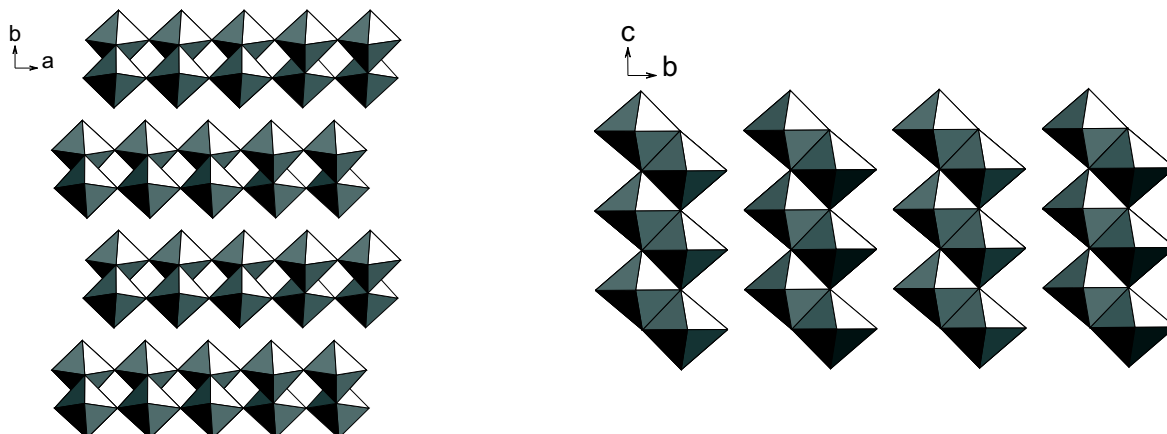


Figure 2.3: View on the ab -plane of αMoO_3 (ICSD [35076], left) and on the bc -plane (right).

2.4 Structure of V_2O_5

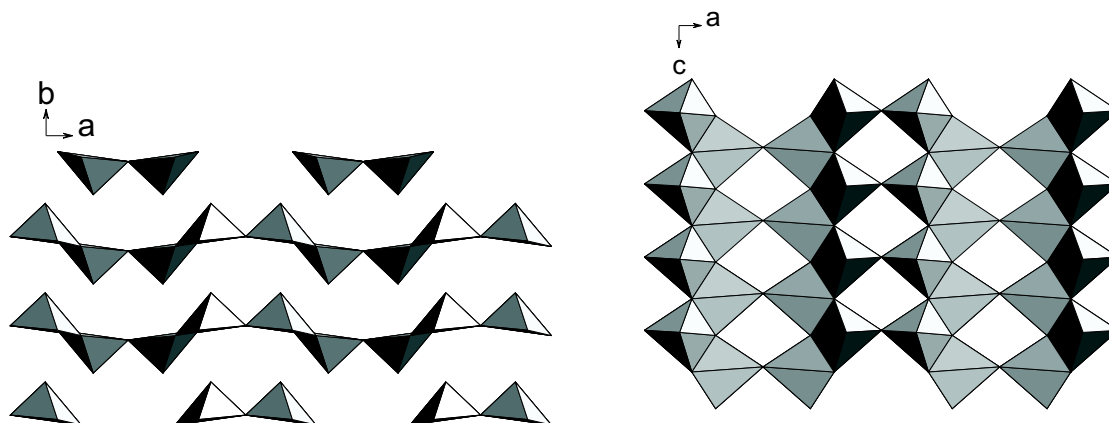


Figure 2.4: View on the ab -plane of orthorhombic V_2O_5 (ICSD [15984], left) and on the ac -plane (right).

The orthorhombic structure of V_2O_5 [91] crystallizes in space group $Pmn2_1$ (ICSD [15984]). The typical coordination geometry of vanadium in oxidation state V^{5+} in oxidic structures is a squared pyramidal coordination by five oxygen anions shown in Figure 2.4. Among one another the squared pyramids are arranged edge and corner sharing. The distance to the oxygen at top position of the pyramid is rather short and is associated with a vanadyl bond. Four oxygen anions at medium distance are arranged in a plane square. A sixth oxygen is located below the squared base and opposite to the short vanadyl oxygen. The long vanadium-oxygen distance can be described either as a long bond or as a short intermolecular contact. This coordination

geometry is the limiting case between strongly distorted octahedral and squared pyramidal. Both descriptions are complementary and helpful for the understanding of the structure of V_2O_5 . For comparison with metals as molybdenum and tungsten which occur in distorted octahedral coordination vanadium can be seen as strongly distorted octahedrally coordinated.

2.5 Structure of V_2O_3

V_2O_3 [92] crystallizes in a monoclinic structure in space group $I2/a$ (ICSD [6286]). In this structure the coordination geometry of oxygen around vanadium is more symmetric than in case of V_2O_5 . The description as a squared pyramidal coordination does not hold here. The vanadium cations are coordinated by six oxygen anions in distorted octahedral geometry. The octahedra are linked face sharing, edge sharing and corner sharing. The structure contains more edge sharing coordination polyhedra than V_2O_5 leading to a denser packing shown in Figure 2.5.

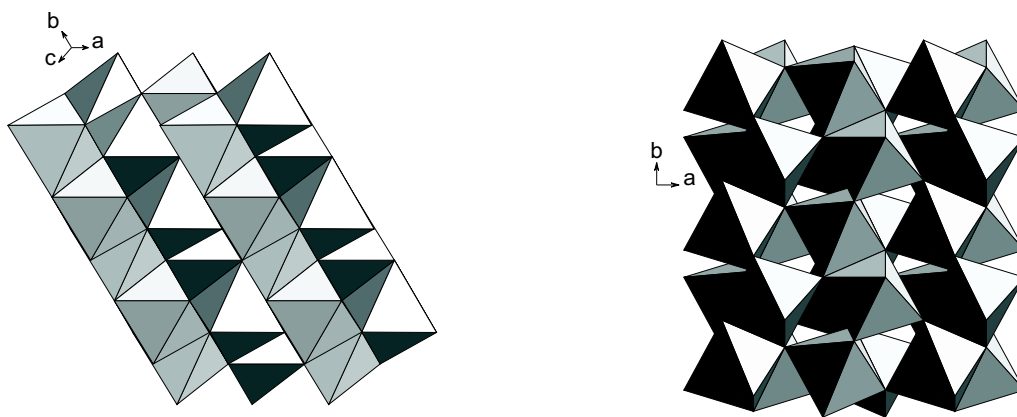


Figure 2.5: View along the $[111]$ direction of monoclinic V_2O_3 (ICSD [6286], left) and on the ab -plane (right).

2.6 Structure of WO_3

The orthorhombic WO_3 structure [93] in space group $Pmnb$ is built up from tungsten in distorted octahedral coordination of oxygen. Each octahedron is corner sharing to six neighbored octahedra similar to the ReO_3 structure. Orthorhombic WO_3 (ICSD [836]) deviates from the cubic ReO_3 structure in the distorted octahedral coordination of tungsten by oxygen that leads to tilted octahedra along the a -axis shown in Figure 2.6. As shown in Figure 2.7 in monoclinic WO_3 (ICSD [14332]) in space group $P12_1/n1$ and triclinic WO_3 (ICSD [1620]) in space group $P\bar{1}$ the distorted octahedra

are additionally tilted along the c -axis in alternating direction. With respect to the coordination polyhedra binary tungsten oxides form structures of higher symmetry than molybdenum and vanadium. Bronzes are formed by intercalation of hydrogen or other small species into the cavities of the WO_3 structure.

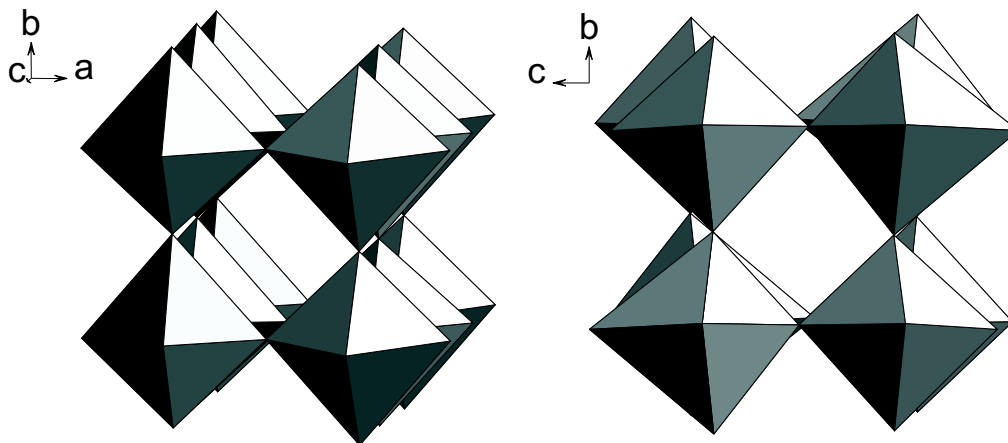


Figure 2.6: Cut out of the orthorhombic WO_3 structure (ICSD [836]). View on the ab -plane (left) and on the bc -plane (right).

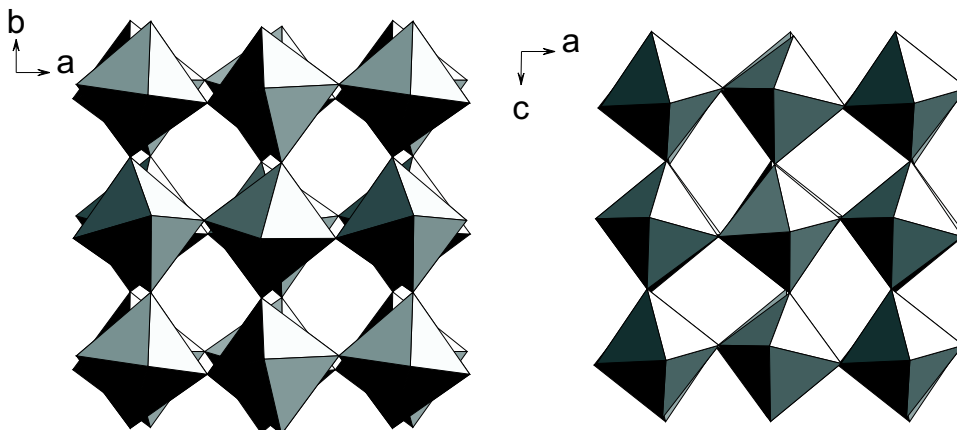


Figure 2.7: Monoclinic WO_3 structure (ICSD [14332]): octahedra tilted in alternating direction along the c -axis (left), view on the ac -plane (right).

2.7 Structures of MoO_2 , VO_2 and WO_2

For the metal dioxides of molybdenum, vanadium and tungsten monoclinic modifications exist besides other polymorphs. These monoclinic structures in space group

$P2_1/c$ are a distorted modification of the rutile structure of TiO_2 [94]. As shown in Figure 2.8 oxygen atoms are slightly distorted octahedrally coordinated around the metal cations in monoclinic MoO_2 [29] ICSD [23722], monoclinic VO_2 [95] ICSD [15889], and monoclinic WO_2 [96] ICSD [8217]. The deviation of the monoclinic angle from 90° increases from WO_2 to MoO_2 to VO_2 .

The occurrence of a monoclinic structure for all three metal dioxides allows the formation of mixed metal dioxides in this structure [79, 97].

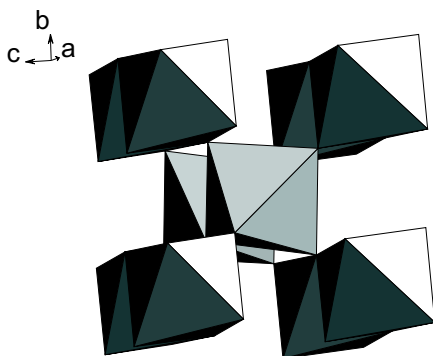


Figure 2.8: Edge sharing and corner sharing octahedra in monoclinic MoO_2 (ICSD [23722]). The structures of VO_2 and WO_2 are similar.

2.8 Structure of MoV_2O_8

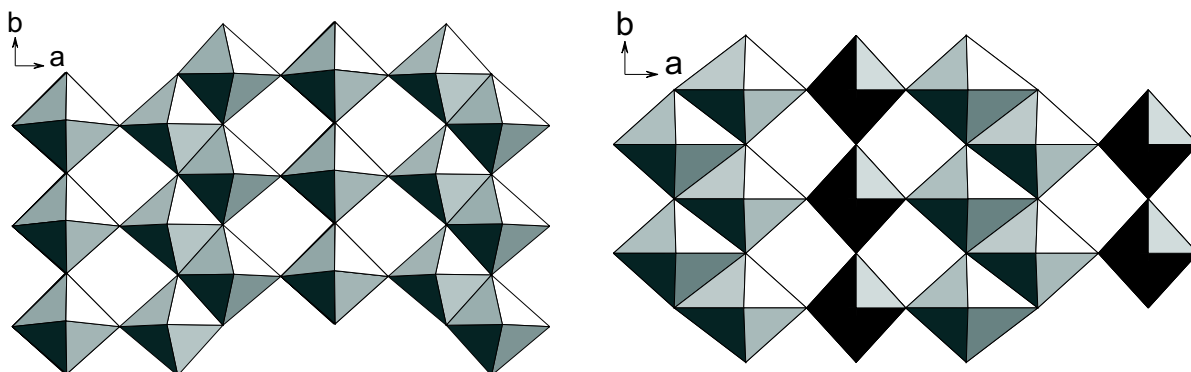


Figure 2.9: Representative domain of the monoclinic structure MoV_2O_8 (ICSD [27317], left). Orthorhombic structure of ICSD [28471], the light grey octahedra are occupied by vanadium and the dark tetrahedra by molybdenum (right).

The structure of mixed molybdenum/vanadium oxide with the stoichiometry MoV_2O_8 is described as an orthorhombic [34] structure in space group $C2/m$ (ICSD [25378]) or as a monoclinic structure [35] in space group $C2$ (ICSD [27317]) represented in Figure 2.9. In the ab -plane MoV_2O_8 forms layers of edge sharing octahedra like the

bc-plane in $\alpha\text{-}MoO_3$ (Figure 2.3) or the ac-plane in V_2O_5 (Figure 2.4). In the ab-plane and the layers of edge sharing octahedra are only corner sharing with their neighbors. In the other directions the octahedra are corner sharing to their neighbors.

In the structure of MoV_2O_8 an exclusive site occupancy exists [34, 36]. The octahedra in the edge sharing layers are occupied by vanadium and the ones only corner sharing to their neighbors are occupied by molybdenum.

2.9 Structure of $Mo_xV_{2-x}O_5$

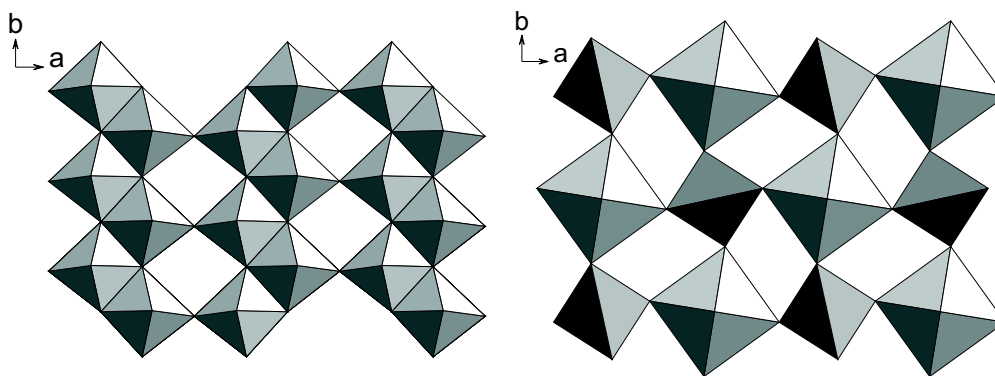


Figure 2.10: Representative domain of the monoclinic $Mo_xV_{2-x}O_5$ structure ICSD [24338] (left) and monoclinic $MoVO_5$ structure ICSD [27315], the light grey octahedra are occupied by vanadium and the dark tetrahedra by molybdenum (right).

The structure of mixed molybdenum/vanadium oxide with the stoichiometry $Mo_xV_{2-x}O_5$ changes depending on the metal ratio. On the vanadium rich side the mixed metal oxide forms an orthorhombic structure [40] related to V_2O_5 (Figure 2.4). At higher molybdenum content the mixed molybdenum/vanadium oxide transforms into a monoclinic structure [38] (ICSD [24338]) in space group $C2$ represented in Figure 2.10. In the mixed metal oxide structures, either orthorhombic or monoclinic, the lattice constants depend on the ratio molybdenum/ vanadium. In the ab-plane $Mo_xV_{2-x}O_5$ forms layers of edge sharing octahedra like the bc-plane in $\alpha\text{-}MoO_3$ (Figure 2.3) or the ac-plane in V_2O_5 (Figure 2.4) and the octahedra are corner sharing in the other directions of the crystal. Thus, in the ab-plane the edge sharing layers in $Mo_xV_{2-x}O_5$ are corner sharing with the next layer, in MoO_3 the layers share no common oxygen atoms with one another and have contact only by electrostatic interaction. Compared to the orthorhombic structure formed in the vanadium rich system that is mostly molybdenum doped V_2O_5 , the monoclinic $Mo_xV_{2-x}O_5$ structure adapts to the higher molybdenum content and expresses structural characteristics of MoO_3 . The structures of $Mo_xV_{2-x}O_5$ is an example how the structure in a solid solution is determined by the metal ratio.

According to the publication another mixed molybdenum/ vanadium oxide the defined stoichiometry $MoVO_5$ [98] (ICSD [27315]) in the tetragonal space group $P4/n$. In this

structure an exclusive site occupancy occurs. Vanadium is exclusively present in octahedral coordination geometry and molybdenum in tetrahedral coordination as shown in Figure 2.10. The coordination polyhedra are corner sharing among one another.

2.10 Oxides with pentagonal bipyramidal coordination

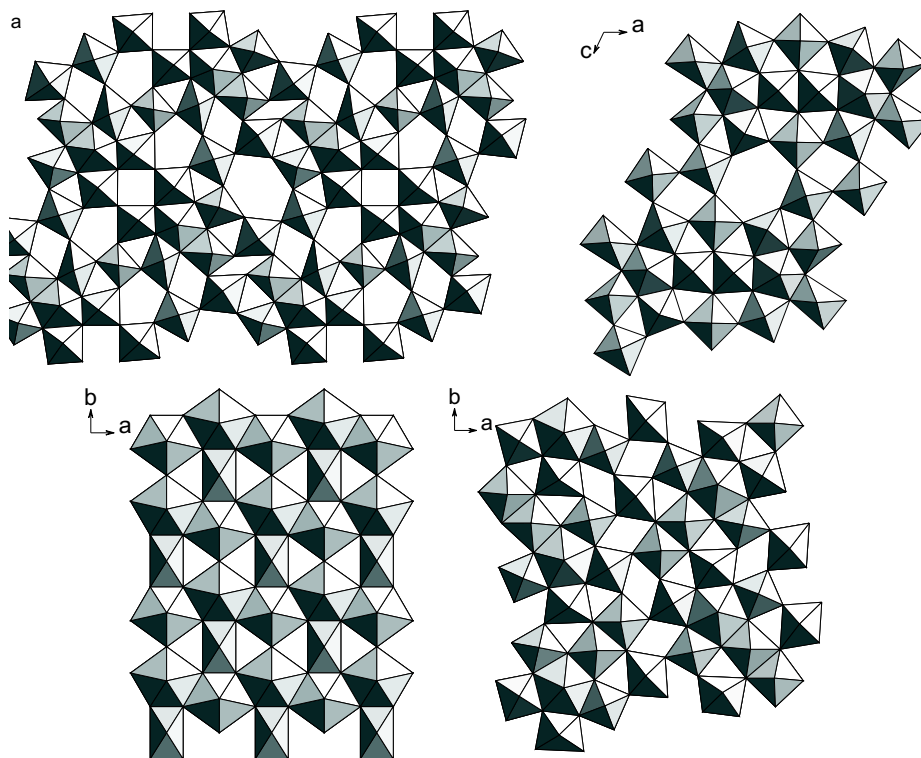


Figure 2.11: View on W_xO_y structures with the pentagonal bipyramidal motif. From upper left to right below: monoclinic $W_{17}O_{47}$ (ICSD [65084]), monoclinic $W_{18}O_{49}$ (ICSD [15254]), orthorhombic W_3O_8 (ICSD [73719]), and orthorhombic $W_{32}O_{84}$ (ICSD [39557]).

Between WO_3 and WO_2 several phases of defined stoichiometry and structure exist. Starting from the structure of WO_3 the oxygen deficit is compensated by a change in linking of coordination polyhedra from corner sharing to edge sharing. For some tungsten sites the coordination geometry rearranges from octahedral to pentagonal bipyramidal. A pentagonal bipyramidal site is edge sharing with five neighboring octahedra, therefore the change in coordination geometry compensates the oxygen deficit. Apparently the pentagonal bipyramidal coordination geometry sufficiently stabilizes tungsten oxides of mixed metal valence. As shown in Figure 2.11 the structures including this motif are monoclinic $W_{17}O_{47}$ [99] (ICSD [65084]) in space group $P2/m$ with an average valence of $W^{5.53+}$, monoclinic $W_{18}O_{49}$ [100] (ICSD [15254]) in space group $P2/m$ with an average valence $W^{5.44+}$, orthorhombic W_3O_8 [101] (ICSD [73719]) in space group

$C222$ with an average valence $W^{5.33+}$, and orthorhombic $W_{32}O_{84}$ [102] (ICSD [39557]) in space group $Pbam$ with an average valence of $W^{5.25+}$. Likewise molybdenum occurs in pentagonal bipyramidal coordination in the suboxide $Mo_{17}O_{47}$ [103] (ICSD [4111], [28333], [36098]). Each of the octahedra is corner sharing with six neighbored polyhedra. The pentagonal bipyramids are linked edge sharing with five neighboring octahedra in the plane perpendicular to the fivefold axis. Along the fivefold axis octahedra and pentagonal bipyramids are linked corner sharing.

In the molybdenum oxide supramolecular chemistry the pentagonal bipyramid is a common structure unit [104, 105]. The significance of d-electrons in such complex transition metal systems is assumed [106, 107, 108].

2.11 Mo_5O_{14} -type structure

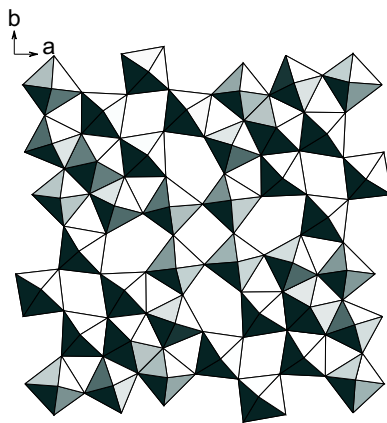


Figure 2.12: View on the ab -plane of the Mo_5O_{14} structure (ICDS [27202]).

The chemistry of molybdenum oxides includes several complex oxides with shear elements [109], which easily transform into one another [110, 111]. The tetragonal Mo_5O_{14} structure in space group $P4/mbm$ (ICSD [27202]) was published from single crystal data [74]. In this structure solution all metal positions are doubled by the mirror plane in the ab -plane and therefore half occupied [74]. The metal cations are coordinated by oxygen either in distorted octahedral coordination geometry or in pentagonal bipyramidal geometry. Each octahedron is corner sharing with six neighbored polyhedra. As shown in Figure 2.12 the pentagonal bipyramids are edge sharing with the neighbored octahedra perpendicular to the fivefold axis. Along the fivefold columns the pentagonal bipyramids are linked corner sharing. Apart from the pentagonal bipyramidal block units it is a relatively open structure with five- and sixfold channels parallel to the c -axis.

The average metal valence in the Mo_5O_{14} structure is $Mo^{5.6+}$. Different metal cations (e.g. vanadium [45], tungsten [72], tantalum [75, 69], niobium [71], titanium [70]) stabilize the molybdenum based structure. Titanium with the highest oxidation state

Ti^{4+} , as well as vanadium, niobium, and tantalum with the highest oxidation state M^{5+} help to adjust the appropriate average valence of the oxide [73].

2.12 Structure of M1 and M2 phase

As shown in Figure 2.13 two different structures denoted as M1 (ICSD [55097]) and M2 (ICSD [55098])[112] are found in *MoVTaNb* oxide catalysts [113]. The major coordination geometry of the incorporated metal cations is distorted octahedral. Besides octahedral coordination geometry in the M phases different types of bipyramidal coordination occur.

The M2 phase is an orthorhombic structure in space group $Pmm2$. Due to its large number of sixfold channels (occupied by metal cations) and for easy differentiation from the M1 phase it is often denoted 'pseudo-hexagonal' structure. In the *ab*-plane of the M2 phase each octahedron is edge sharing with two hexagonal bipyramids. Perpendicular to the *ab*-plane the octahedra and hexagonal bipyramids are linked corner sharing with each other.

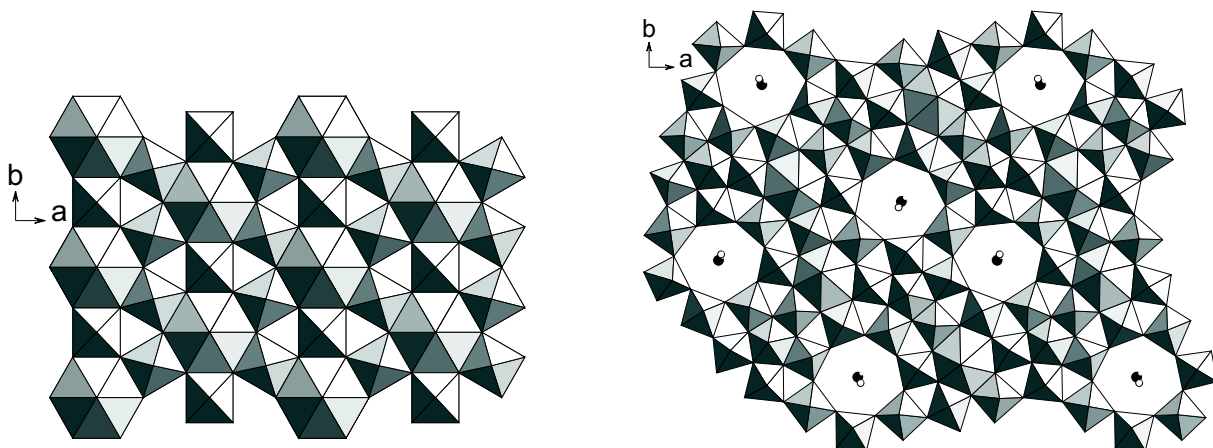


Figure 2.13: View on the *ab*-plane of the 'pseudo-hexagonal' M2 phase (left) and on *ab*-plane of M1 phase (right).

The M1 phase is an orthorhombic structure in space group $Pba2$. In M1 phase each octahedron is edge sharing with two bipyramids in the *ab*-plane, either pentagonal, hexagonal, or heptagonal bipyramids. In direction of the *c*-axis corner sharing occurs for all types of coordination geometry. As the Mo_5O_{14} -type structure the M1 phase is a relatively open structure with channels that may be occupied by metal cations. For the *MoVTaNb* oxides a certain elemental distribution on the different metal sites in the structure [114] was proposed.

Chapter 3

Methods

3.1 X-ray powder diffraction

X-ray diffraction (XRD) is a non-destructive method for analysis of the periodic long range structure of a crystalline solid [115, 116, 117]. Photons are elastically scattered by the electrons of the atoms of a crystal if their wavelength is in the range of the bond distances. The three-dimensional arrangement of the atoms in a crystal structure acts as a suitable matrix for diffraction of the photons. Figure 3.1 illustrates this effect described by the Bragg equation:

$$n\lambda = 2d_{hkl}\sin\theta$$

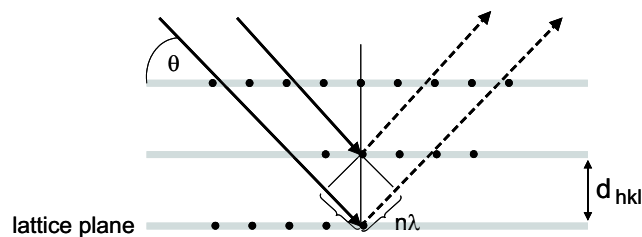


Figure 3.1: Bragg reflection of X-ray photons at lattice planes of the crystal structure.

Numerous diffracted photons result in an interference pattern that is characteristic for a structure. Positions of positive interference are described by the Bragg equation depending on the wavelength λ of the radiation, the diffraction angle θ , the distance between the lattice planes d_{hkl} and the diffraction order n . The position of peaks depends on the lattice constants a , b , c and α , β , γ of the originating crystal system and can be analyzed for its determination. Systematic extinctions of hkl -pairs characterize the space group of the structure. The intensity of peaks results from the type of atoms at the different positions in the structure. The intensity I of a peak is proportional to the square of the structure factor F_{hkl} :

$$I \propto |F_{hkl}|^2$$

The structure factor F_{hkl} is defined as a sum over the atomic structure factors f_j , the position of the atoms in reciprocal space hkl and real space xyz :

$$F_{hkl} = \sum f_j \exp(-2\pi i (hx_j + ky_j + lz_j))$$

Since the X-ray photons are diffracted at the electrons of the atoms, elements with similar number of electrons can not be separated from one another and light elements neighbored to heavy elements are difficult to detect. Depending on the diffraction angle θ the intensity of the diffraction peaks is reduced by atomic displacement described in the Debye-Waller factor B_j :

$$\exp\left(\frac{-B_j \sin^2 \theta}{\lambda^2}\right)$$

The Debye-Waller factor in the expression for the the XRD structure factor describes a spacial probability of the atom on a site. Atomic displacement parameters determined from crystal structure refinement principally embody thermal vibration of the atoms, but they can also include effects of structural disorder.

If single crystal data of a crystalline solid material are either not available or of poor data quality X-ray powder patterns can be used for determination of phase composition, purity and crystallinity. The samples are analyzed as powders with grains in random orientation and the (usually monochromatic) beam detects all crystallographic directions. The line broadening of the diffraction lines in a powder XRD pattern is due to the instrumental function of the diffractometer geometry or dislocations or small crystallite domains in non-ideal crystallites. The Scherrer equation [115] estimates the average domain size D of the particles in the powder from wavelength λ , diffraction angle θ and the integral breadth of the diffraction line β :

$$D = \frac{\lambda}{\beta \cos \theta} \quad (3.1)$$

Experimentally determined pattern can be calculated. The lattice constants determine the peak positions in the pattern. The atom positions and the type of atom determine the peak intensity. Principally a structure can be solved successfully from a high quality X-ray powder pattern in a Rietveld structure refinement [118]. The Rietveld refinement [115] is based on analysis of the complete powder pattern for evaluation of the structure information.

3.2 X-ray absorption spectroscopy

X-ray absorption spectroscopy (XAS) is an element specific characterization technique [119, 120, 121, 122, 123]. When X-ray photons of appropriate energy pass through matter the electrons from the core level in the atoms are excited. The photon energy that exceeds the binding energy of the core electrons of the atoms is characteristic for each element. At this energy the absorption strongly increases. Depending on the initial $1s$, $2s$, $2p_{\frac{1}{2}}$, or $2p_{\frac{3}{2}}$ state of the excited electron the absorption spectra are denoted as K edge, L_I -, L_{II} -, or L_{III} edge, respectively. The electron can either be excited into

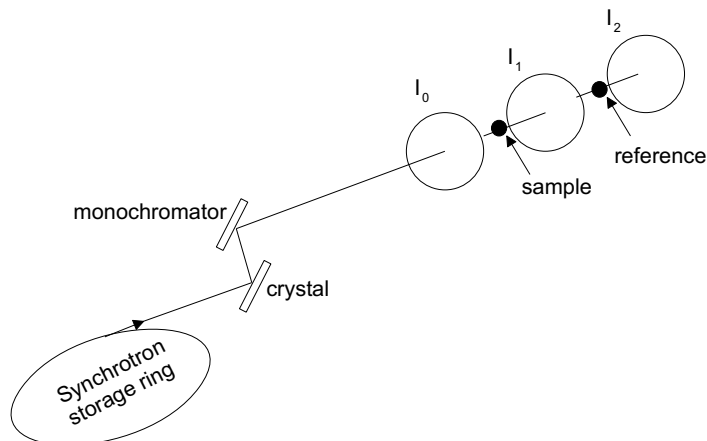


Figure 3.2: Arrangement for a transmission XAS experiment at a synchrotron source.

an unoccupied state or leave the atom which is thereby ionized.

A schematic representation of a XAS experiment at a synchrotron source is shown in Figure 3.2. The incident photon beam intensity $I_0(E)$ through a sample of thickness x and the decreased intensity $I_1(E)$ after the sample depend on the linear absorption coefficient $\mu(E)$ by Lambert's Law:

$$I_1(E) = I_0(E) e^{-\mu(E)x}$$

Generally the position of the edge indicates the electron binding energy of the core electron. It depends mainly on the ordering number Z of the atom. Additional small shifts indicate the average oxidation state of the atom. The height of the edge or edge jump μ depends on the sample mass m , linear absorption coefficient μ_i , the density ρ_i , the weight amount w_i of absorbing element i in the sample divided by the area A of the sample:

$$\mu = \frac{m \sum w_i \left(\frac{\mu_i}{\rho_i} \right)}{A}$$

In this rough estimation the absorption of other elements at the energy of investigation is neglected. In fact this may become a limiting issue if trace elements are investigated or elements with neighbored edges. At the inflection point of the edge the energy of the photon $h\nu$ matches the binding energy $E_{binding}$ of the electron in the core level. At higher energy the remaining kinetic energy E_{kin} of the photoelectron is given by:

$$E_{kin} = h\nu - E_{binding}$$

As shown in Figure 3.3 the regions in a XAS spectrum are classified as X-ray near edge structure (XANES) and extended X-ray absorption fine structure (EXAFS). Small attenuations in $\mu(E)$, the X-ray absorption fine structure (XAFS) of the edge, appear

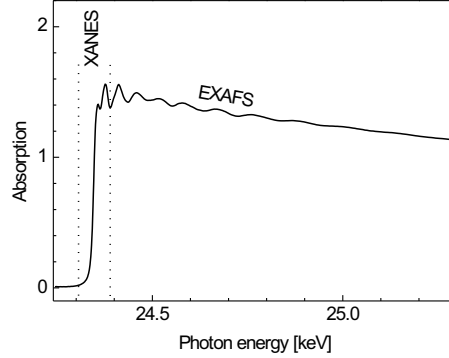


Figure 3.3: XANES and EXAFS region of an experimental spectrum.

when the energy of the incoming photon is large enough to excite an electron from the core level to an unoccupied state or the continuum.

The XANES is sensitive to electronic transitions of the excited core electron into unoccupied electronic states. Each transition is proportional to the transition probability of the underlying excitation from the initial state φ_i to the final state φ_f due to Fermi's Golden Rule:

$$\mu(E) \propto A |\langle \varphi_f | er | \varphi_i \rangle|^2 \delta(E_f - E_i - h\nu)$$

In this quantum mechanical model the outgoing photoelectron is seen as spherical wave with a wavelength corresponding to the energy of the photoelectron. Conveniently the EXAFS is described in k-space. The photoelectron wavevector k is related to the photoelectron energy:

$$k = \sqrt{\left(\frac{8\pi^2 m_{photoel}}{h^2}\right) (h\nu - E_{binding})}$$

The region at the high energy side of the edge after the XANES is denoted as EXAFS. The outgoing spherical wave $\varphi_{outgoing}$ is backscattered at the neighboring atoms. Phase and amplitude of the backscattered wave $\varphi_{backscattered}$ depend on position and type of the backscattering atom. Constructive and destructive interference of outgoing and backscattered wave result in oscillations that are characteristic for distances and elements in the structure. This way the nearby atoms effect the final state wave function φ_f at the excited atom and give access to information on the short range order of the element under investigation:

$$\varphi_f = \varphi_{outgoing} + \varphi_{backscattered}$$

The information on distances, type and symmetry of the neighboring atoms in the absorption variation of the EXAFS can be extracted and interpreted.

Experimentally the absorption variation is revealed from the measured data during the data reduction. The spectra measured in energy over absorption are calibrated to the

tabulated energy value of a metal reference, background corrected for the continuous decrease of absorption with increasing photon energy, and normalized. After transformation from energy range to k -space the XANES is cut off. From the remaining experimental μ the contribution of inneratomic processes μ_0 is subtracted by a spline. The experimental $\chi(k)$ is the average of all atoms of the excited element in the sample:

$$\chi(k) = \frac{\mu(k) - \mu_0}{\mu_0}$$

The EXAFS function $\chi(k)$ that is extracted from the experimental data can be theoretically described as sum over all single and multiple scattering paths from the outgoing photoelectron. Therefore, the EXAFS formula summarizes the number of atoms N of an element with the backscattering amplitude F_j at a distance R_j . F_j and the phase shift δ from the backscattering event are element specific and depend on energy:

$$\chi(k) = \sum S_0 F_j(k) \frac{N_j}{k R_j} \exp\left(-2k^2 \sigma_j^2\right) \exp\left(\frac{-2R_j}{\lambda(k)}\right) \sin(2k R_j + 2\delta)$$

The amplitude reduction factor S_0 accounts for many body effects and shake-up processes at the absorbing atom. Further amplitude loss of $\chi(k)$ appears due to the exponential terms describing disorder σ_j^2 and mean free path length $\lambda(k)$ of the photoelectron. Thermal disorder $\sigma_{thermal}$ and structural (static) disorder σ_{static} of the sample contribute to the total disorder of the system represented by the Debye-Waller factor σ_j^2 :

$$\sigma_j^2 = \sigma_{static} + \sigma_{thermal} \quad (3.2)$$

In order to obtain quantitative agreement between the experimentally extracted $\chi(k)$ and theory all these parameters need to be determined accurately. Since experimental data can only support a limited number of fitting parameters these factors must be known from another source. The potentials describing the wavefunction of the atoms for the calculation of F_j , phase shift δ , and $\lambda(k)$ that can be used for simulation of $\chi(k)$ are provided by databases. For a structure refinement the $\chi(k)$ is multiplied with k , k^2 , or k^3 . The higher k -weighting increases the oscillations at higher k caused by the heavy elements among the backscattering atoms. From comparison of the differently k -weighted $\chi(k)$ the contribution of the light and heavy backscattering neighbors can be identified.

Chapter 4

Experimental

4.1 Preparation conditions

The brown *MoVW* oxide precursor of the $(MoVW)_5O_{14}$ material was prepared as described in literature [124]. Ammonium heptamolybdate (AHM) ($c = 0.963$ mol/L) and ammonium metatungstate (AMT) ($c = 0.27$ mol/L) were dissolved in bidistilled water at 353 K. V_2O_5 was dissolved in an aqueous solution of 1.93 mol/L oxalic acid at 353 K (vanadyl oxalate aqueous solution $c = 0.379$ mol/L). The solutions were mixed in a 2 L batch and heated to 353 K for 1 h. After spray-drying of the mixed solutions the resulting material was calcined for 2 h in synthetic air at 623 K and then heated for 2 h in helium at 713 K. The metal content in the $(MoVW)_5O_{14}$ phase amounted to 68 mol-% Mo, 23 mol-% V, and 9 mol-% W.

The $(MoV)_5O_{14}$ material was prepared as follows: an aqueous solution of vanadyl oxalate was obtained by dissolving 7.7 mg V_2O_5 and 15.9 mg oxalic acid in 132 ml water. The dark yellow suspension changed color from olive-green, dark-green to dark-blue while vesication. The resulting blue solution was mixed with a solution of 200 g AHM in 500 ml water at 353 K. After stirring at this temperature for 1 h, the solution was spray-dried. The spray-dried dark violet *MoV* oxide precursor powder was treated in helium at 773 K for 4 h followed by dissolution of impurities in 1 mol/L ammonia solution at 313 K for 5 min. Subsequently, the resulting material was heated in helium to 773 K for 4 h. The metal content in the $(MoV)_5O_{14}$ phase amounted to 91 mol-% Mo and 9 mol-% V.

4.2 Crystallization and calcination experiments

For in situ XRD crystallization experiments the short 2θ range from 21° to 26° shown in Figure 4.1 was scanned. The observable peaks are indexed. For in situ XRD calcination experiments ca. 160 mg *MoVW* oxide precursor were used. Different thermal treatment conditions listed in Table 4.1 were applied.

Thermal treatment of the precursor was conducted in 10% oxygen and 5% propene [125] in the range from 300 K to 773 K in a one-step procedure. Alternatively, a two-step calcination procedure reported to result in a highly crystalline Mo_5O_{14} -type structured

Exp.	Flow [ml/min]	1 st step			2 nd step				
		Gas	Heat. rate [K/min]	Temp. [K]	Hold@T	Gas	Heat. rate [K/min]	Temp. [K]	Hold@T
A	100	10%O ₂ +5%propene	1.38	773	10min	No 2 nd step	-	-	-
B	100	20%O ₂ /N ₂	3.65	623	10min	100%He	3.46	713	2h
C	10	20%O ₂ /N ₂	3.65	623	2h	100%He	3.46	713	2h
D	100	20%O ₂ /N ₂	3.33	623	2h	100%He	2.16	713	2h
E	100	20%O ₂ /N ₂	3.3	623	3h	100%He	2.93	713	3h
F	100	20%O ₂ /N ₂	3.46	713	4h	No 2 nd step	-	-	-
G	100	100%He	4.04	713	2h	No 2 nd step	-	-	-
H	100	20%O ₂ /He	2.9	623	2h	100%He	2.9	713	2h

Table 4.1: In situ XRD experiments with variation of calcination parameters gas atmosphere, gas flow, dwell time and temperature.

material (i.e. 300 K to 623 K in oxygen/ nitrogen and 300 K to 713 K in helium [124]) was performed. Variations of these conditions were applied to explore the significant parameters of calcination. The influence of the various treatment parameters in this two-step procedure on phase composition, structure, crystallinity, and performance of the resulting catalyst was to be elucidated. Several parameters were changed: heating rate, gas atmosphere, gas flow, treatment temperature, and dwell times at 623 K or 713 K. The effective heating rate changed due to different length of XRD scans. All variants of thermal treatment resulted in a black powder. The catalytic activity of the obtained material was tested in 10% oxygen and 5% propene from 300 K to 773 K.

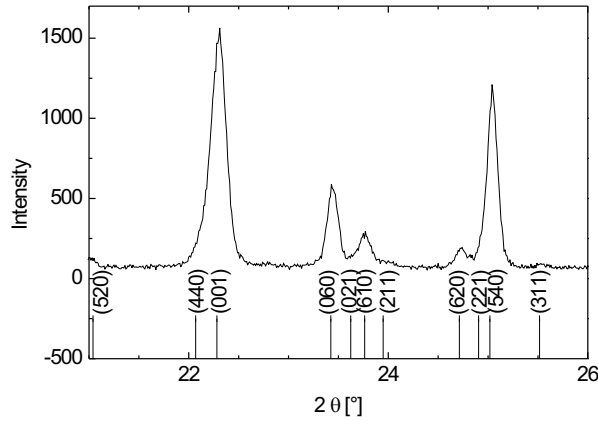


Figure 4.1: Range of in situ XRD crystallization experiments.

4.3 Heating and redox experiments of $(MoVW)_5O_{14}$ and $(MoV)_5O_{14}$

For in situ XRD experiments 30-80 mg of powdered $(MoVW)_5O_{14}$ or $(MoV)_5O_{14}$ were used. The measurements were conducted under atmospheric pressure in flowing atmosphere at 100 ml/min. For in situ XAS experiments 0.2-8 mg sample were mixed with 30 mg BN. The measurements were conducted under atmospheric pressure in flowing atmosphere at 30 ml/min. The thermal stability and structural evolution of $(MoVW)_5O_{14}$ and $(MoV)_5O_{14}$ were investigated during temperature-programmed experiments in different atmospheres. For temperature-programmed measurements reducing (10% propene or hydrogen) and oxidizing (20% oxygen) atmospheres were applied in the temperature range from 300 K to 773 K. The heating rate was 3 K/min (XAS) or 0.4 K/min (XRD).

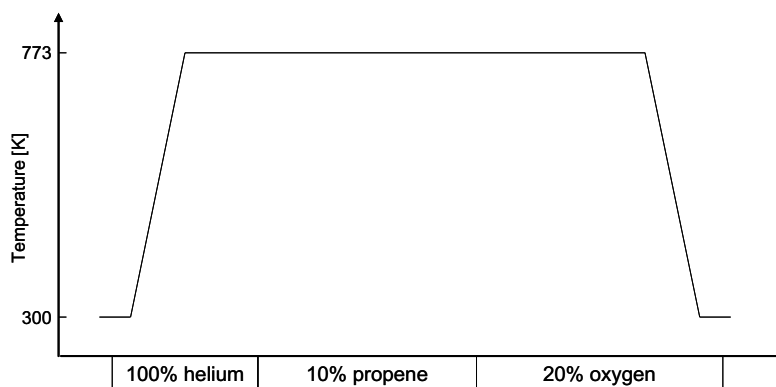


Figure 4.2: Experimental procedure denoted as redox experiment. Heating in helium with 10 K/min to 773 K, then isothermal at 773 K reduction in 10% propene, and re-oxidation in 20% oxygen.

Figure 4.2 illustrates the isothermal redox experiments. $(MoVW)_5O_{14}$ or $(MoV)_5O_{14}$ were heated in helium to 773 K with a heating rate of 10 K/min. In helium at 773 K one XRD or XAS scan was taken, then the atmosphere was isothermally switched to 10% propene or 10 % hydrogen and XRD or XAS scans were taken until complete reduction of the sample. The resulting materials were re-oxidized in 20% oxygen and XRD or XAS scans were collected until no reduced phase was detectable. Scans at 300 K before and after experiment completed the investigations.

4.4 X-ray powder diffraction

Combined in situ powder XRD/ MS experiments were performed on a STOE Theta/theta diffractometer with secondary Si (111) monochromator (Cu K_α radiation). The diffractometer was equipped with a XRK 900 high temperature cell from Anton Paar for in situ measurements. The gas entered the cell over three inlets, one

from the front side, the second from the back and the third from the bottom of the cell flowing around the shell of the sample holder. The bottom of the sample holder was made from a sieve that allows the gas to flow through the sample into the outlet. The bottom of the sample holder with its holes was covered with glass microfiber filter to prevent the sample from blocking the gas flow. This in situ cell enables a good contact between sample and gas atmosphere. Conversely, on a heated steel ribbon sample holder the resulting mixed oxide was X-ray amorphous. All measurements were conducted under atmospheric pressure in flowing atmosphere. The gas phase composition at the cell outlet was analyzed on line with a mass spectrometer (Omnistar, QMS Pfeiffer).

Ex situ powder XRD measurements were taken on a STOE STADI-P diffractometer with a Ge (111) primary monochromator and a position sensitive detector.

4.4.1 Data analysis

Phase analysis was performed with the DIFFRAC PLUS Evaluation software [126] and Rietveld [127, 115] structure refinement with the Topas software package [128] using single crystal data from the Inorganic Structure Database (ICSD [28]). Crystallite sizes were calculated from the integral breadth of the (001) peak of the Mo_5O_{14} -type structure at about 22° in 2θ using the Scherrer equation (Equation 3.1, [115]). Phase purity was evaluated by refining so-called 'hkl phases' to the whole XRD powder pattern [128]. An 'hkl phase' is calculated from theoretical hkl-peak positions according to space group and lattice constants. Lattice constants, peak intensities and breadth are refined in the fitting procedure. This procedure allows a more reliable assignment of the peaks in the experimental pattern to the theoretical hkl-peaks. Especially for less symmetric structures with complex diffraction patterns, this whole pattern fitting procedure makes it easier to detect additional phases or confirm phase purity.

4.4.2 Structure refinement of $(MoVW)_5O_{14}$ and $(MoV)_5O_{14}$

The structure refinement of $(MoVW)_5O_{14}$ and $(MoV)_5O_{14}$ was conducted using the TOPAS software and single crystal structure data ICSD [27202]. The background was modeled with a second order polynomial and a $1/2\theta$ contribution that describes air scattering at low angles. A pseudo-Voigt function modified according to Thompson-Cox-Hastings [129] described the anisotropic profile asymmetry of the peak shape. The lattice constants a and b of the tetragonal unit cell and a scale factor were refined. One isotropic temperature factor for all metal sites and a second isotropic temperature factor for all oxygen sites were refined. This temperature factor should account for slight deviations from the atom positions in the single crystal structure or absorption effects. Atomic coordinates were not refined. Subsequently, the obtained structure parameters were fixed and two alternative strategies for determination of the metal site occupancy were tested. In the first approach the metal site occupancy factors were refined. As second approach the refined lattice parameters of the structure were fixed. For each metal in the sample one structure model with the metal sites exclusively occupied by that element was refined. This means, for $(MoV)_5O_{14}$ two structurally identical phases

were refined, one with molybdenum (' Mo_5O_{14} '), the other with vanadium on the metal sites (' V_5O_{14} '). For $(MoVW)_5O_{14}$ three structurally identical phases were taken, one with molybdenum (' Mo_5O_{14} '), one with vanadium (' V_5O_{14} '), and one with tungsten (' W_5O_{14} ') on the metal sites. Due to the fixed lattice constants and site occupancy factors this approach calculates the same ratio of vanadium/ molybdenum for all metal sites. Scale factor and particle size of each phase were refined.

4.5 X-ray absorption spectroscopy

At a synchrotron source especially the tunable energy of the beam is advantageous in order to reach the absorption edges of all desired elements. Transmission in situ XAS experiments were performed at the Mo K edge (19.999 keV), W L_{III} edge (10.204 keV), and V K edge (5.465 keV) at beamline X1 and E4 at the Hamburger Synchrotronstrahlungslabor, HASYLAB, respectively. For temperature programmed in situ XAS measurements the experiments were conducted in a flow reactor [130] of ca. 4 ml volume at atmospheric pressure in 30 ml/min flowing reactants. The gas phase composition at the cell outlet was analyzed on line with a mass spectrometer (Omnistar, QMS Pfeiffer) in a multiple-ion detection mode. Samples were mixed with ca. 30 mg boron nitride and pressed at a force of 1 t into a pellet of 5 mm in diameter. The resulting edge jump was about $\mu \approx 1$ at the Mo K edge, about $\mu \approx 0.06-0.3$ at the V K edge, and about $\mu \approx 0.8$ at the W L_{III} edge. Average valences of vanadium were determined from the pre-edge peak height [131]. The average valence of molybdenum was obtained from analyzing the Mo K edge position according to a previously reported procedure [132].

4.5.1 Data processing

The XAS data processing and analysis was performed with the software packages WinXAS 3.1 [133] and viper [134]. Figures 4.3 and 4.4 show that both programs gave nearly identical $\chi(k)$ after data reduction. The refinement utilities of both programs slightly differ and were applied according to the aim of structural analysis.

The energy was calibrated with respect to the edge position of a simultaneously measured metal foil. A first order polynomial was used for background subtraction. Third order (Mo K edge) or second order (V K edge, W L_{III} edge) polynomials were used for normalization. The E_0 position was set to the first inflection point of the sample spectrum at the V K edge and the W L_{III} edge, the second inflection point was employed at the Mo K edge. The Mo K edge XAFS spectrum was extracted using cubic splines with 7 nodes in the k range from 3 to 14 \AA^{-1} . The V K edge XAFS spectrum was extracted using cubic splines with 6 nodes in the k range from 3 to 12.76 \AA^{-1} . Because of the highly absorbing matrix, a detailed analysis at the V K edge is restricted to in situ XANES spectra. Ex situ EXAFS spectra at the V K edge can be analyzed. The W L_{III} edge XAFS spectrum was extracted using cubic splines with 6 nodes in the k range from 2 to 13 \AA^{-1} . The k^3 -weighted experimental $\chi(k)$ multiplied by a Bessel window (window parameter 4) was Fourier transformed to the R space. Theoretical

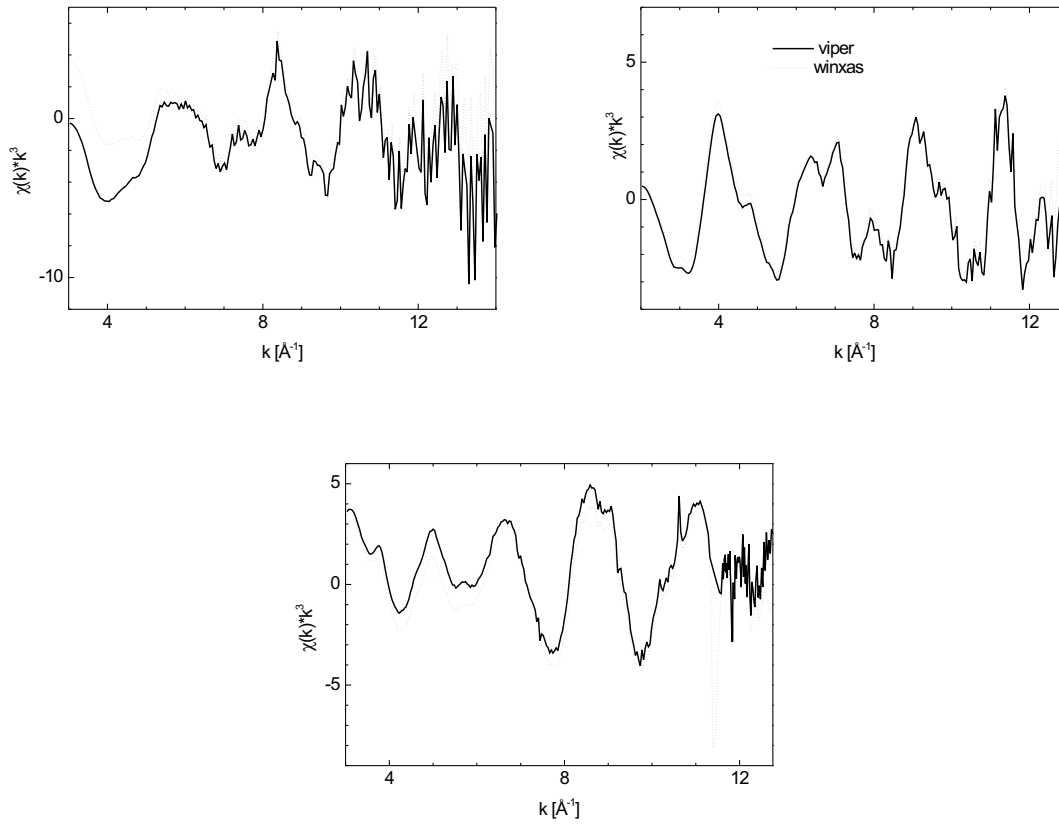


Figure 4.3: Comparison of $\chi(k) * k^3$ of $(MoV)_5O_{14}$ processed by the software WinXAS 3.1 [133] or viper [134]. Mo K edge (left), W L_{III} edge (center), and V K edge (right).

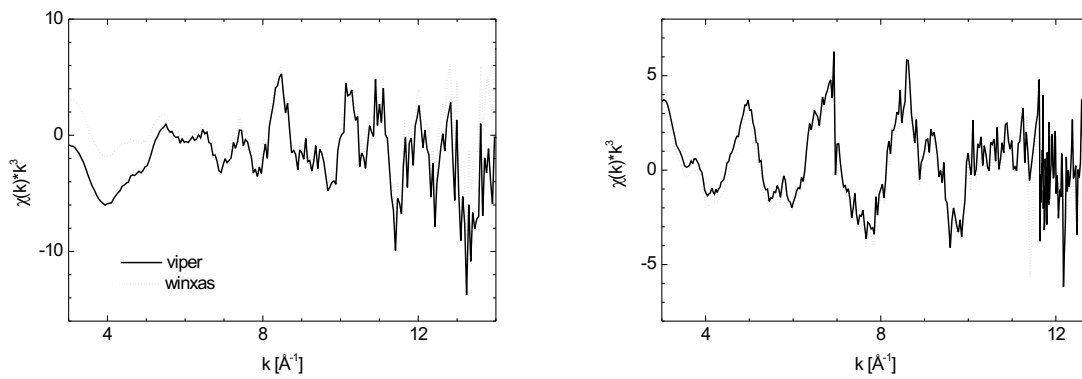


Figure 4.4: Comparison of $\chi(k) * k^3$ of $(MoV)_5O_{14}$ analyzed by the software WinXAS 3.1 [133] or viper [134]. Mo K edge (left) and V K edge (right).

backscattering phases and amplitudes were calculated with FEFF7 [135] up to 4 Å.

4.5.2 XAS structure model for investigation of Mo_5O_{14}

In the Mo_5O_{14} -type structure (Figure 4.5) exist six crystallographically different metal sites and 16 oxygen sites in the asymmetric unit. Additionally, the six metal sites are disordered with respect to the mirror plane perpendicular to the c -axis (see Paragraph 2.11). In a XAS experiment the average over all metal atoms of the excited element in the structure is measured. In case of the Mo_5O_{14} -type structure the spectrum is the average over all metal sites that the element under investigation occupies (possibly all sites).

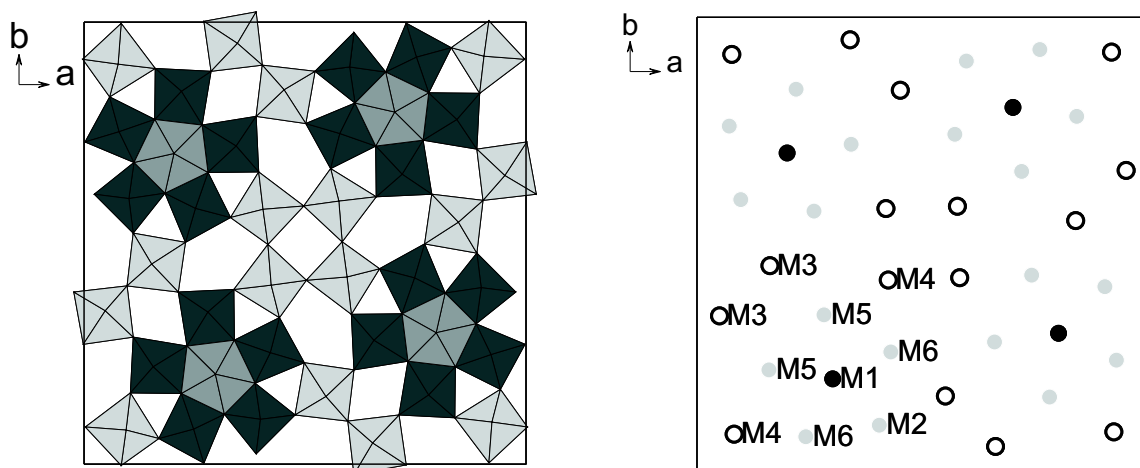


Figure 4.5: Schematic representation of the Mo_5O_{14} -type structure (ICSD [27202]). Left: the pentagonal bipyramidal site (grey), the octahedral sites that share an edge with the pentagonal bipyramid (dark grey), and the octahedral sites that share corners with the neighboring octahedra (light grey) are indicated. Right: the six different metal sites in the unit cell.

In EXAFS data analysis the numerous metal sites raise a problem. In a simulation of $\chi(k)$ it is mandatory to locate the excited metal site. Of course the $\chi(k)$ of all six possible sites can be simulated. But the refinement of all six simulations to one experimental spectrum requires a larger number of free parameters than experimentally obtained. Therefore the refinement strategy was changed from simulation and refinement of the complete structure to simulation of an average of the structure. In literature several cases of averaging of distances in a complex or unknown structure were applied successfully [136, 137, 138]. The investigated structures contained less metal sites than the Mo_5O_{14} -type structure, less interchangeable elements, and were not as disordered as the given model catalyst.

The structure model that was refined to the $\chi(k)$ was based on distances in the Mo_5O_{14} single crystal data (ICSD [27202]) refined to the experimental XRD pattern

of the sample (lattice constants $a=b=22.763 \text{ \AA}$ and $c=3.985 \text{ \AA}$ for $(MoVW)_5 O_{14}$, and $a=b=22.876 \text{ \AA}$ and $c=3.9977 \text{ \AA}$ for $(MoV)_5 O_{14}$, see also Table 5.8). As listed in Table 4.2 six average values of the XRD distances (three metal-oxygen and three metal-metal distances) in the Mo_5O_{14} -type structure were calculated for the XAS structure model (in the following denoted as 'model of average distances'). For the metal-metal distances the different possible backscattering elements had to be con-

$(MoV)_5 O_{14}$ Metal-oxygen	Average distance	$(MoVW)_5 O_{14}$ M-O	Average distance	Average C.N.
1.697	1.720	1.689	1.713	1.67
1.701		1.695		
1.703		1.698		
1.705		1.699		
1.710		1.705		
1.716		1.711		
1.724		1.719		
1.743		1.735		
1.755		1.747		
1.841	1.994	1.828	1.984	3.5
1.837		1.832		
1.845		1.836		
1.855		1.846		
1.928		1.918		
1.964		1.955		
1.978		1.968		
2.010		2.000		
2.014		2.004		
2.031		2.021		
2.037		2.027		
2.040		2.030		
2.049		2.039		
2.057		2.047		
2.073	2.063			
2.106	2.095			
2.204	2.193			
2.301	2.307	2.293	2.300	1
2.303		2.294		
2.307		2.296		
2.300		2.300		
2.311		2.310		
2.318		2.304		
$(MoV)_5 O_{14}$ Metal-metal	Average distance	$(MoVW)_5 O_{14}$ M-M	Average distance	Average C.N.
3.235	3.270	3.219	3.254	1.33
3.268		3.251		
3.326		3.309		
3.567	3.689	3.550	3.671	3.33
3.598		3.580		
3.633		3.615		
3.641		3.623		
3.666		3.648		
3.694		3.676		
3.705		3.687		
3.763		3.744		
3.862		3.843		
3.947	3.994	3.927	3.980	2.3
3.998		3.985		

Table 4.2: How the average distances are calculated from the XRD distances of $(MoV)_5 O_{14}$ (left) and $(MoVW)_5 O_{14}$ (right). The metal-oxygen and metal-metal distances are averaged over all crystallographic sites.

sidered, e.g. for the three molybdenum-metal distances in $(MoV)_5O_{14}$ in total six different single scattering events may happen: either scattering between two molybdenum atoms or between one molybdenum center and one vanadium backscattering atom are possible. In case of $(MoVW)_5O_{14}$ spectra metal-tungsten scattering paths for each average distance were additionally taken into account.

4.5.3 XAS refinement strategy

The following refinement was performed with the software WinXAS [133]. The Debye-Waller factor in the EXAFS equation can be calculated assuming the Debye model [139]. The refinement strategy applied to the XAFS spectra of the Mo_5O_{14} -type structured samples consisted of three successive steps:

- refinement of one overall E_0 shift and Debye temperature for each element in the sample
- refinement of average distances, one overall E_0 shift and Debye temperature for each element
- refinement of coordination numbers, average distances, and one overall E_0 shift; Debye temperature for each element fixed to value of the previous refinement cycle.

The refinement strategy avoids simultaneous refinement of coordination numbers + Debye-Waller or distances + E_0 -shift which would cause correlations [140]. Aim of the EXAFS structure analysis of $(MoVW)_5O_{14}$ and $(MoV)_5O_{14}$ was determination of the type of site occupancy. If the element under investigation is not homogeneously distributed over all metal sites but preferably or exclusively occupies a certain coordination geometry of a specific site, this changes the measured EXAFS spectrum. Auxiliary for the determination of the type of site occupancy in the Mo_5O_{14} -type structure is the unequal coordination of the metal sites with oxygen anions and neighboring next metal cations. There should be a difference on the stability of different elements located on these sites. Since the elements contained in the catalyst under investigation have different characteristic coordination geometry, atomic radii, and redox potentials they are assumed to prefer one or the other coordination environment of oxygen anions and stabilize or destabilize the short metal-metal distances at the pentagonal bipyramidal block units.

4.5.4 Investigation of XAS refinement strategy on simulated data

XAS is a technique that averages over all sites occupied by the element under investigation. Prior to refinement of the experimental data the refinement strategy based on the model of average distances was evaluated. The following questions have to be considered:

- Is averaging a suitable method for description of a complex oxide as the Mo_5O_{14} -type structure?
- How does the averaging of distances effect the other parameters of refinement, i.e. order/ disorder parameters?
- How does the refinement strategy limit the information we can get from the refinement?

As inquired in the second question, the disorder contained in the Mo_5O_{14} -type structure complicates the extraction of site occupancy parameters. Given in Equation 3.2 the total disorder of a system is the sum of thermal disorder and structural disorder. A detailed analysis how thermal vibrations in a solid change the Debye-Waller factor in the $\chi(k)$ is given in literature [141]. For investigation of the problem of (dis)order

Disorder σ	Homogeneous distribution 90% Mo and 10% V structurally disordered	10% V exclusively in pentagonal bipyramids, rest 90% Mo in octahedra structurally ordered
Debye temperature 5000 K for all elements not thermally disordered	S1	S2
Debye temperature oxygen 600 K, metals 300 K thermally disordered	S3	S4

Table 4.3: Approach for investigation of the refinement strategy applied to the model catalyst. Simulated $\chi(k)$ with variable extent of thermal and structural disorder were refined with a model of average distances.

a Mo K edge $\chi(k)$ was simulated for each of the 6 metal sites in the $(MoV)_5O_{14}$ system and then averaged (as a XAS measurement does). The Debye-Waller factor contains thermal and/or structural disorder. Thermal disorder was introduced to the simulated $\chi(k)$ of $(MoV)_5O_{14}$ by different Debye temperatures: (i) the absence of thermal disorder was simulated at a Debye temperature of 5000 K (above 3000 K the amplitudes in the XAFS function do not change significantly) and (ii) the $\chi(k)$ of a thermally disordered system was simulated at a Debye temperature of 600 K for oxygen and 300 K for the metal components (the amplitudes are remarkably damped). For simulating structural (static) disorder the $\chi(k)$ of the $(MoV)_5O_{14}$ system was calculated with 90% molybdenum and 10% vanadium, but different elemental distribution in the Mo_5O_{14} -type structure: (i) with a homogeneous distribution of molybdenum and vanadium on all sites - a structurally disordered system, and (ii) with vanadium exclusively located at the pentagonal bipyramidal coordinated site - a structurally ordered system.

To verify if the refinement strategy and the structure model provide insight to the question of site occupancy in the complex oxide system, it was tested on constructed data of $(MoV)_5O_{14}$. Table 4.3 lists the simulated $\chi(k)$ representing four limiting cases of thermal and structural order/ disorder. The data were simulated from 3 to 14 \AA^{-1}

in k-space (the range of the experimental spectra at the Mo *K* edge). The structural model gained from the average XRD distances was refined to the simulated data according to the refinement procedure described above (see Paragraph 4.5.3). The limits of information accessible from the EXAFS refinement of the complex Mo_5O_{14} -type structure with the model of average distances were revealed.

4.5.5 XAS multiple edge investigation of Mo_5O_{14} -type catalysts

In a multiple edge refinement with the program viper [134] the structure model was refined simultaneously to the experimental $\chi(k)$ of the $(MoV)_5O_{14}$ sample at the Mo *K* edge and the V *K* edge. In an initial refinement cycle one E_0 -shift was fixed to -0.1 eV, the Debye-Waller factors were fixed to 0.004 \AA^{-3} , and distances were refined. Then in a second refinement the distances and the coordination numbers were refined. Determining the presence or absence of molybdenum-vanadium distances becomes more reliable when both edges are analyzed simultaneously. Furthermore, using both XAFS spectra for developing a structure model increases the number of independent parameters in the refinement. The distances of the structure model obtained from the multiple edge refinement procedure were then applied in a single edge refinement with the WinXAS software [133]. In an initial refinement cycle one E_0 -shift and the Debye temperatures of each element were refined. In a second refinement cycle one E_0 -shift and the coordination numbers were refined, while the Debye temperatures were fixed. The same refinement strategy was applied to the $\chi(k)$ of $(MoVW)_5O_{14}$ at the Mo *K* edge, the W *L_{III}* edge, and the V *K* edge. In $(MoVW)_5O_{14}$, at the Mo *K* edge a small number of significant distances that are conform to the results of the V *K* and W *L_{III}* edge spectra were refined in a structure model. In refinement of one structure model to the three XAFS spectra the starting parameters for the single edge refinement were generated. The distances of the structure model derived in multiple edge refinement were then applied in a single edge refinement with the software WinXAS [133]. The same strategy for refining Debye temperatures and coordination numbers as in $(MoV)_5O_{14}$ was applied.

4.6 Thermogravimetry and Differential Scanning Calorimetry

Thermogravimetry (TG) and Differential Scanning Calorimetry (DSC) were performed with a Netzsch STA 499 C TG/ DSC instrument coupled with a mass spectrometer for direct gas phase analysis (Omnistar, QMS Pfeiffer). The calcination procedure as reported in literature [124] was carried out with about 20 mg $MoVW$ oxide precursor placed in an open Al_2O_3 crucible with 2 h dwell time at 623 K and 2 h dwell time at 713 K at heating rates of 1 K/min, 3 K/min, 5 K/min and 10 K/min with a total gas flow of 100 ml/min. The gas atmosphere was changed after the first calcination step without exposure of the sample to air. The thermal treatment in helium was performed in an additional experiment with the same heating rate as in the calcination

step. In an additional experiment with heating rate 5 K/min the carrier gas in the first calcination step (20% oxygen/ nitrogen) was replaced by helium. Data analysis was performed with the NETZSCH Thermokinetics software [142]. Arrhenius plots were generated from the maximum change in the DSC curve and the corresponding temperature. The use of the DSC curve allowed separation of four events, whereas in the TG trace only three decomposition steps appeared. The software NETZSCH Thermokinetics [143] was used for kinetic analysis of data measured at different heating rates during calcination of the *MoVW* oxide precursor. Activation energy values were obtained by means of the Friedman method [144].

4.7 Mass spectrometry

m/e	Catalytic atmosphere	m/e	Thermal treatment
41	propene	12	Carbon
44	CO_2	14	Nitrogen
56	acrolein	15	NH
72	acrylic acid	17	NH_3, OH
		18	H_2O
		28	N_2, CO
		30	NO
		32	O_2
		44	CO_2, N_2O
		46	NO_2

Table 4.4: Assignment of m/e measured in catalytic atmosphere and under thermal treatment conditions.

During in situ measurements the gas phase was simultaneously analyzed for reaction products or gaseous products evolved in the thermal treatment procedure. All fragments were detected with a channeltron detector. Additionally traces of air (m/e = 28, 32, 40) were detected with Faraday-cup.

Chapter 5

Results

5.1 Crystallization of *MoVW* oxide precursor

	Final material	Catalytically active
A	$(V_x Mo_{1-x})_2 O_5$ besides $(MoVW)_5 O_{14}$	yes
B	Poorly crystalline $(MoVW)_5 O_{14}$	Not tested
C	Poorly crystalline $(MoVW)_5 O_{14}$	Not tested
D	Crystalline $(MoVW)_5 O_{14}$	Yes
E	Crystalline $(MoVW)_5 O_{14}$	Yes
F	Crystalline $(MoVW)_5 O_{14}$	Yes
G	Crystalline MoO_2 -type phase	Not tested
H	Poorly crystalline $(MoVW)_5 O_{14}$	Not tested

Table 5.1: In situ XRD: effect of variation of thermal treatment parameters gas atmosphere, gas flow, dwell time and temperature on phase composition and crystallinity.

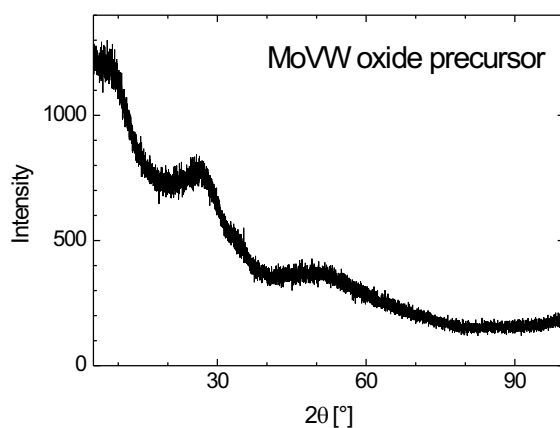


Figure 5.1: Ex situ XRD of X-ray amorphous *MoVW* oxide precursor.

Figure 5.1 shows the initially X-ray amorphous *MoVW* oxide precursor. Around 22° in 2θ a broad peak is present where in Mo_5O_{14} -type structured material besides smaller ones the prominent (001) peak appears. The crystallization of *MoVW* oxide precursor was investigated by in situ XRD and the region of the (001) peak was observed to be most sensitive to beginning crystallization. The various thermal treatment conditions employed are given in Table 4.1. The effect of gas atmosphere, gas flow, dwell time and temperature on phase composition and crystallinity of the resulting material are listed in Table 5.1.

5.1.1 In situ XRD crystallization

Experiment A

Thermal treatment of the *MoVW* oxide precursor in 10% oxygen and 5% propene in a one step procedure in the temperature range from 300 K to 773 K is denoted as experiment A. Figure 5.2 shows crystallization of the precursor in the first heating ramp. From the in situ XRD patterns measured it can be noticed that the crystallization of more than one mixed oxide phase started at 673 K (Figure 5.2). Figure 5.3 shows the corresponding MS traces of acrolein ($m/e = 56$) and acrylic acid ($m/e = 72$). While the formation of acrolein was detected at 630 K, acrylic acid was obtained at temperatures above 670 K. The latter coincides with the onset of crystallization of the solid mixed oxide phases. After cooling to room temperature, the resulting mixed oxide was again heated in propene and oxygen under the same conditions. In the corresponding MS data of this second heating cycle, selective oxidation products acrolein and acrylic acid were already detected at 550 K and 620 K, respectively. After activation in 10% oxygen and 5% propene, an Mo_5O_{14} -type structured phase (70%) and $Mo_xV_{2-x}O_5$ (ICSD [24338], 30%) were detected in the XRD pattern of the resulting mixed oxide (Figure 5.4) by Rietveld refinement. From the neighboring diffraction peaks of both phases at 22° in 2θ it can be deduced that the phases crystallized simultaneously. Little orange spots on top of the catalyst sample after heat treatment may be associated with traces of vanadium oxides but could not be identified by XRD.

TEM investigations of the material obtained after catalytic testing contained only crystalline material (Figure 5.5). As shown in Figure 5.6 $(MoVW)_5O_{14}$ proved to be the major phase. The electron diffraction pattern shows a ring corresponding to $d = 3.9 \text{ \AA}$, but the streaks correspond to $d = 3.7 \text{ \AA}$. The lattice parameter $b = 3.652 \text{ \AA}$ in $Mo_xV_{2-x}O_5$ would fit that number.

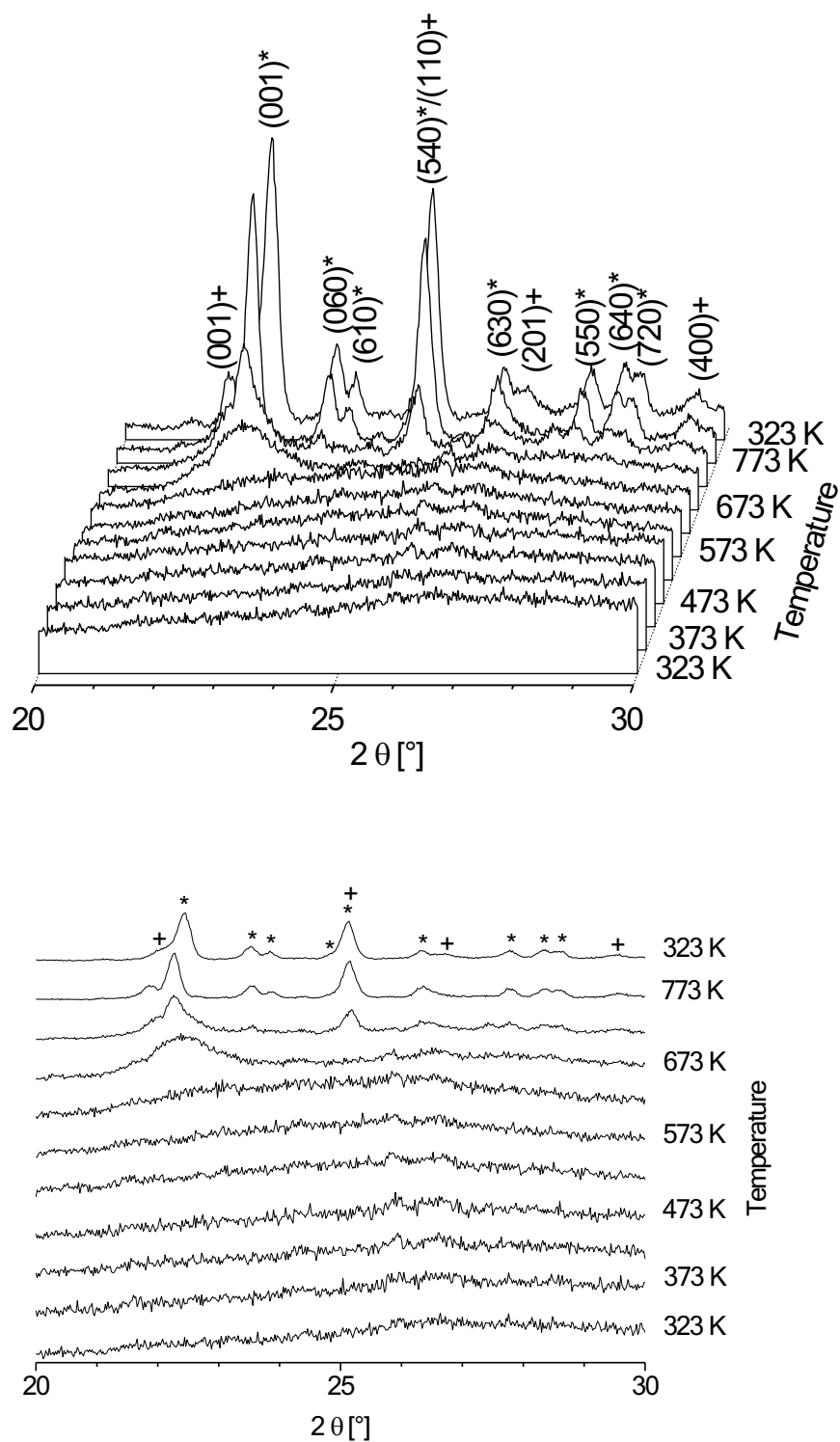


Figure 5.2: Experiment A: evolution of in situ XRD during thermal treatment of *MoVW* oxide precursor in 5% propene and 10% oxygen from 300 K to 773 K. Phase symbols: "*" Mo_5O_{14} -type phase, "+" $Mo_xV_{2-x}O_5$.

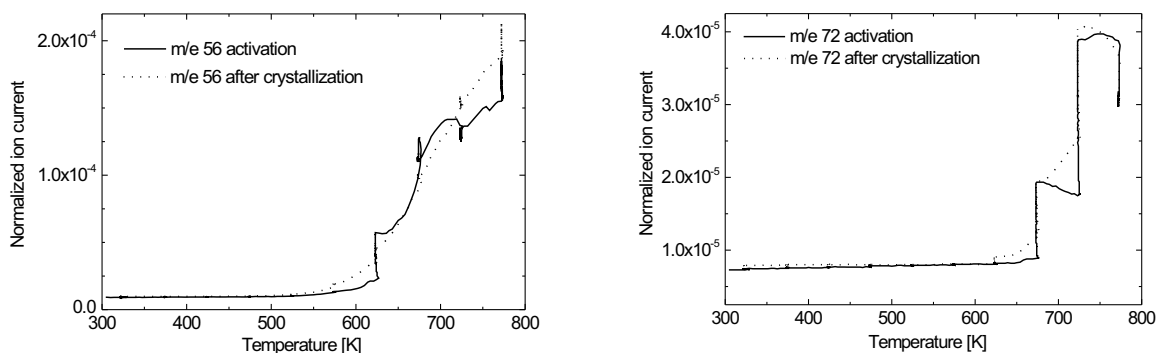


Figure 5.3: Evolution of MS traces acrolein ($m/e = 56$) and acrylic acid ($m/e = 72$) during in situ XRD thermal treatment of *MoVW* oxide precursor and subsequent catalytic test in 5% propene and 10% oxygen from 300 K to 773 K.

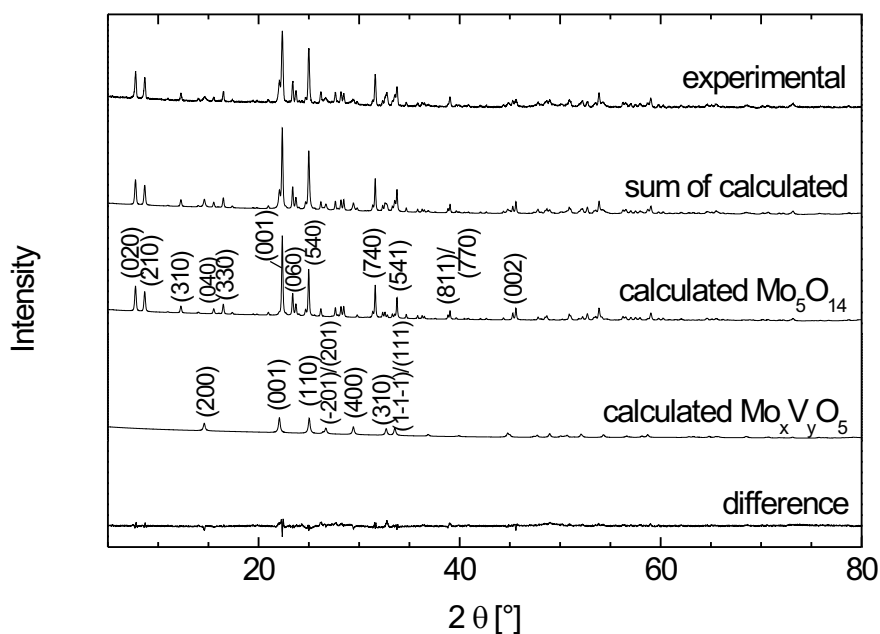


Figure 5.4: Rietveld analysis of XRD pattern after thermal treatment of *MoVW* oxide precursor in 5% propene and 10% oxygen. About 70% Mo_5O_{14} -type structured phase and 30% $Mo_xV_{2-x}O_5$ ICSD [24338] are detected.

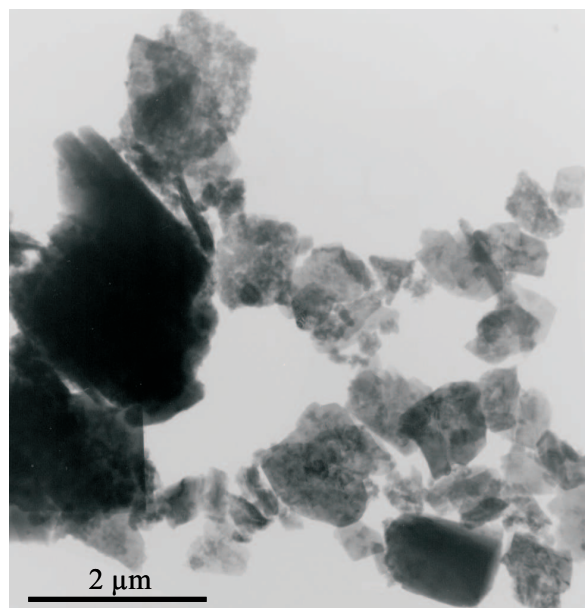


Figure 5.5: Low magnification TEM shows only crystalline material.

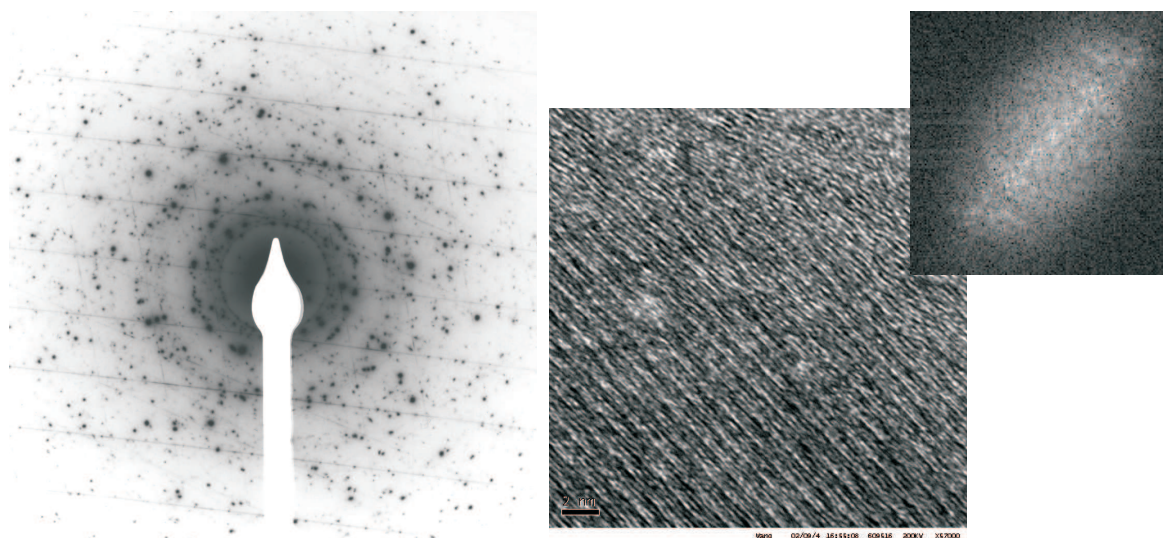


Figure 5.6: Electron diffraction pattern (left) and HRTEM image of Mo_5O_{14} -type structure tilted from $[001]$ zone axis (right).

Experiment B

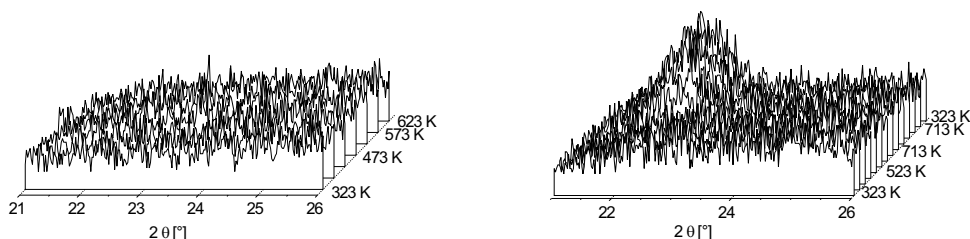


Figure 5.7: Experiment B: in situ XRD during calcination of *MoVW* oxide precursor in 20% oxygen/ nitrogen from 300 K to 623 K, dwell time 10 min at 623 K (left). During thermal treatment for 2 h in 100% helium at 713 K (right).

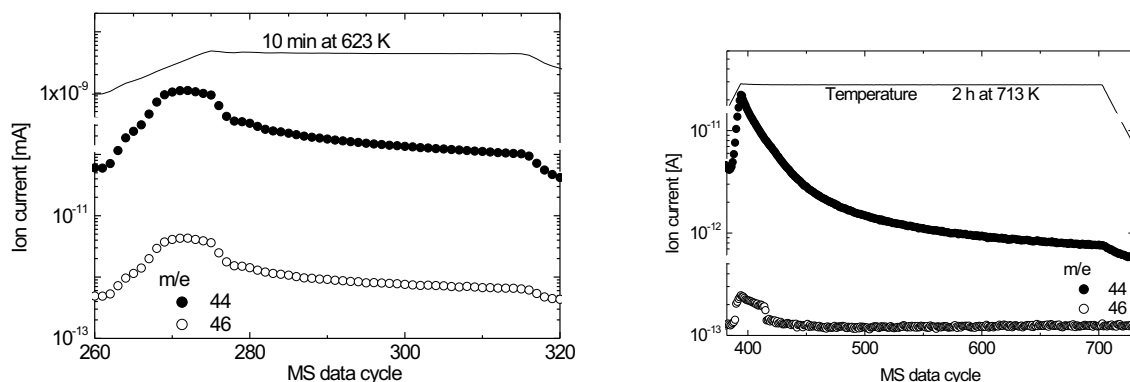


Figure 5.8: Experiment B: evolution of MS traces during in situ XRD experiment of *MoVW* oxide precursor. CO_2 and/ or N_2O ($m/e = 44$) and NO_2 ($m/e = 46$) during 10 min dwell time at 623 K in 20% oxygen/ nitrogen (left), and during 2 h dwell time at 713 K in helium.

In experiment B the dwell time at 623 K in 20% oxygen/ nitrogen was shortened to 10 min compared to the 2 h in the standard procedure. The second treatment step was for 2 h in 100% helium at 713 K. The resulting mixed oxide sample was poorly crystalline and exhibited strongly broadened XRD peaks in the range 21-24° in 2θ , shown in Figure 5.7. In contrast to experiment D, significant amounts of gaseous decomposition products CO_2 or N_2O ($m/e = 44$) and NO_2 ($m/e = 46$) were still detected after the ten minutes dwell time at 623 K. In Figure 5.8 the evolution of the

MS data during calcination and thermal treatment is compared. At the end of the treatment in 20% oxygen/ nitrogen at 623 K and at the end of the subsequent thermal treatment in helium with 2 h dwell time at 713 K both decomposition products of the *MoVW* oxide precursor are still formed.

Experiment C

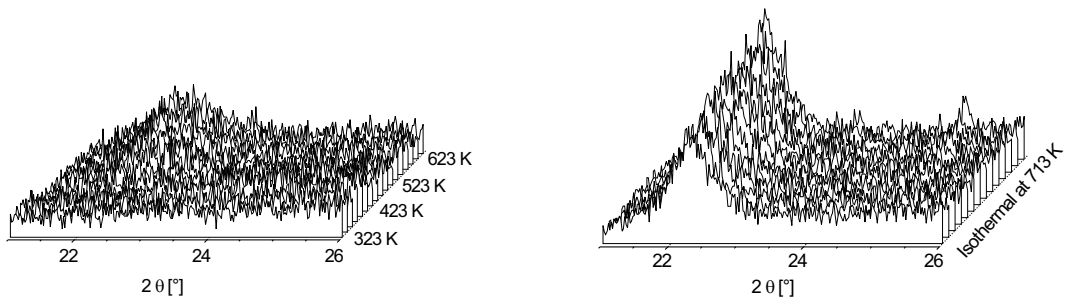


Figure 5.9: Experiment C: in situ XRD at a total gas flow 10 ml/min. During calcination of *MoVW* oxide precursor in 20% oxygen/ nitrogen from 300 K to 623 K (left), and during isothermal treatment in helium at 713 K (right).

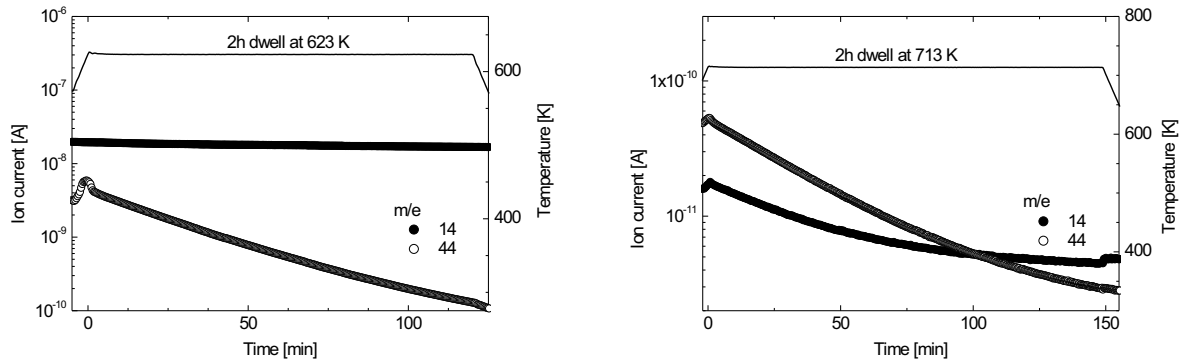


Figure 5.10: Evolution of MS traces during in situ XRD calcination of *MoVW* oxide precursor at a total gas flow of 10 ml/min (Experiment C). CO_2 and/ or N_2O ($m/e = 44$) and NO_2 ($m/e = 46$) during 2 h dwell time at 623 K in 20% oxygen/ nitrogen (left), and during 2 h dwell time at 713 K in helium.

Thermal treatment of the *MoVW* oxide precursor with a dwell time of 2 h in 20% oxygen/ nitrogen at 623 K and in 100% helium at 713 K is denoted as experiment C. The total gas flow was decreased from 100 ml/min (all other experiments) to 10 ml/min. The in situ XRD experiment is shown in Figure 5.9. No significant changes in crystallinity are observed during the isothermal treatment in helium at 713 K. The resulting mixed oxide sample was poorly crystalline and exhibited strongly broadened XRD peaks. As shown below, transmission electron microscopy revealed small crystalline domains that exhibited lattice plane distances similar to those of a Mo_5O_{14} -type structure. In contrast to experiment D or E, significant amounts of gaseous decomposition products (i.e. CO_2 , N_2O , and NO_2 , see Figure 5.10) were still detected after the two-hour dwell time at both temperatures.

The TEM investigations shown in Figure 5.12 proved the presence of $(MoVW)_5O_{14}$ in the thermally treated material. The image presenting the (110) planes shows in a small structure drawing chains octahedra. The dark chains were originally edge-sharing to pentagonal bipyramidal sites, the light gray chains are only corner-linked octahedra. The arrows in Figure 5.11 point at some spherical particles formed during spray-drying of the solution that are still present in the material as well as irregularly shaped particles. EDX data of crystalline and spherical particles confirmed the same cation composition, i.e. *Mo*, *V* and *W* mixed oxides. The electron diffraction pattern shows low crystallinity.

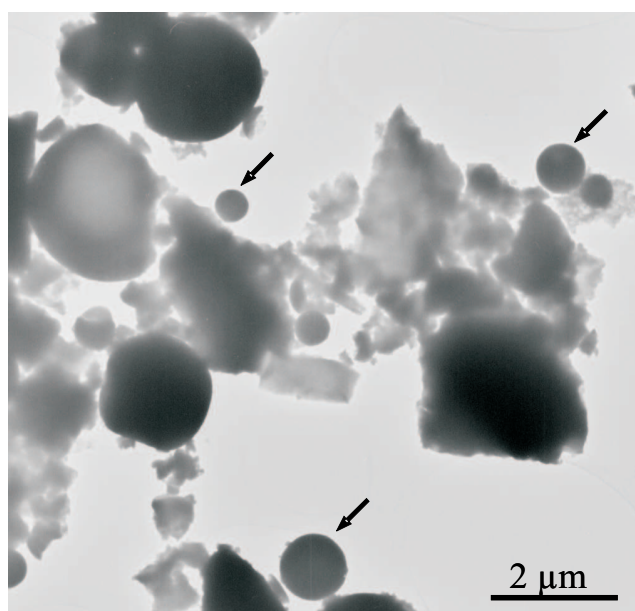


Figure 5.11: Low magnification TEM image shows spherical particles (indicated by arrows) that are amorphous and some crystallites in other parts.

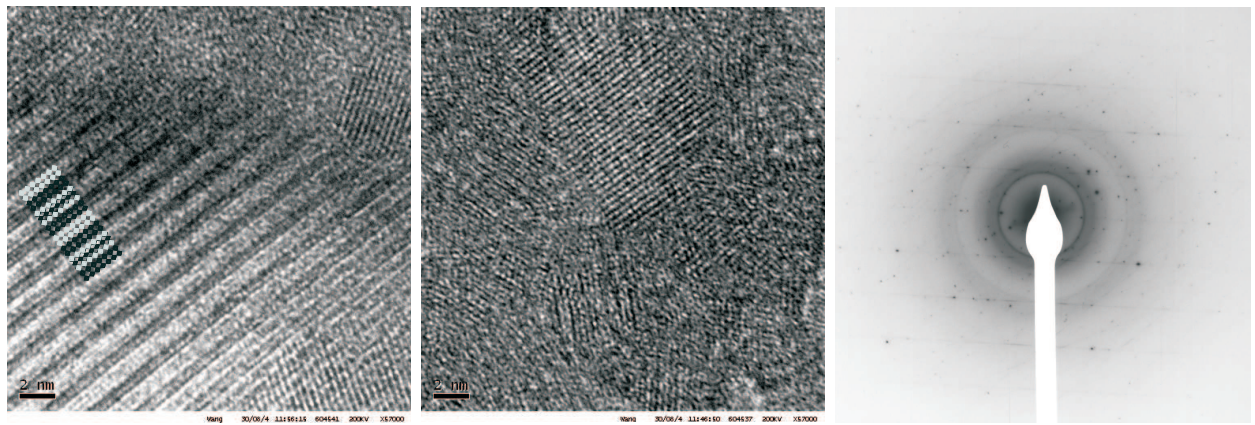


Figure 5.12: HRTEM image with lattice fringes of Mo_5O_{14} -type structure. $d = 16 \text{ \AA}$ corresponds to (110) planes (left), $d = 3.9 \text{ \AA}$ corresponds to (001) planes of the $(MoVW)_5O_{14}$ (center), and corresponding electron diffraction pattern (right).

Experiment D

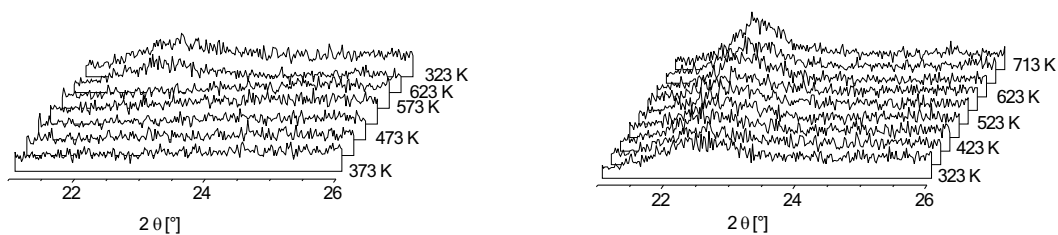


Figure 5.13: Experiment D: in situ XRD during calcination of *MoVW* oxide precursor in 20% oxygen/ nitrogen from 300 K to 623 K (left). Second step is heating in helium from 300 K to 713 K (right).

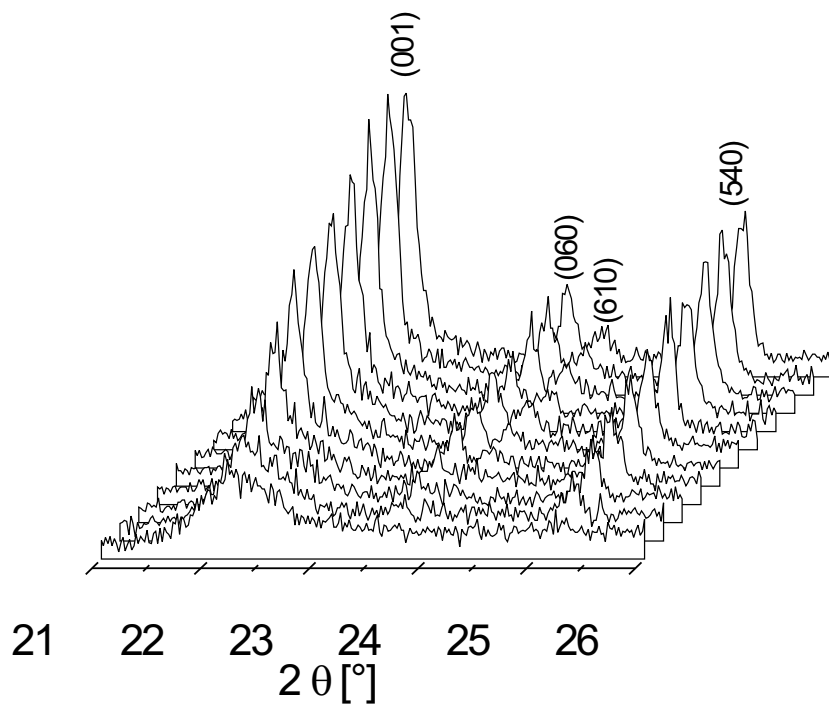


Figure 5.14: Experiment D: in situ XRD during isothermal treatment of *MoVW* oxide precursor in 100% helium at 713 K.

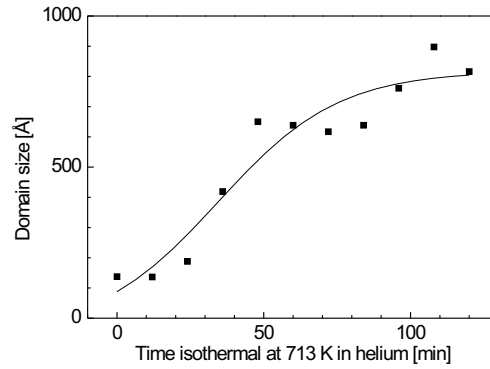


Figure 5.15: Experiment D: domain growth during isothermal treatment of *MoVW* oxide precursor in 100% helium at 713 K.

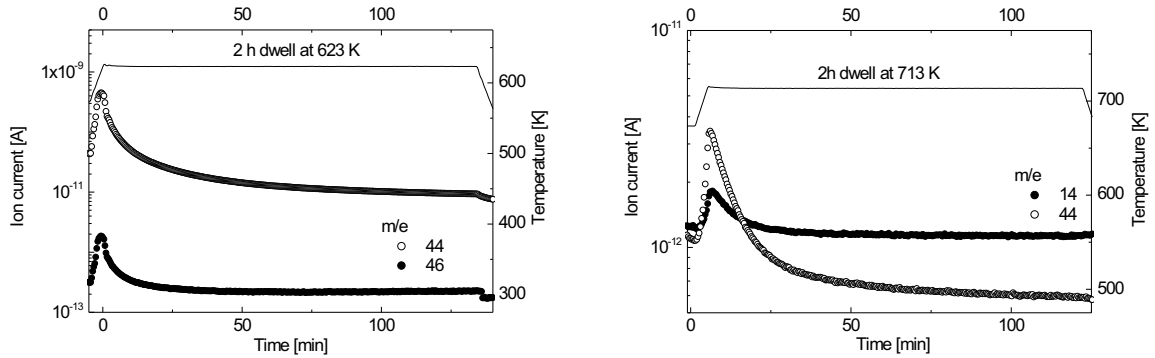


Figure 5.16: Experiment D: evolution of MS traces during in situ XRD calcination of *MoVW* oxide precursor. CO_2 and/ or N_2O ($m/e = 44$) and NO_2 ($m/e = 46$) during 2 h dwell time at 623 K in 20% oxygen/ nitrogen (left), and during 2 h dwell time at 713 K in helium (right).

Experiment D corresponds to the thermal treatment conditions which have been reported in the literature to result in a crystalline single phase $(MoVW)_5O_{14}$ material from the spray dried (*MoVW*) oxide precursor [124]. The two-step procedure employed consisted of heating the precursor in oxygen/nitrogen to 623 K, a dwell time at 623 K of two hours, and subsequently heating the material in helium to 713 K for two hours. As shown in Figure 5.13 and 5.14 the crystallization proceeds during the isothermal treatment in helium at 713 K. The crystallite domain size was calculated from the integral breadth of the (001) reflection. MS traces measured during treatment of the precursor in oxygen/nitrogen and helium are depicted in Figure 5.16. The masses indicating the removal of CO_2 ($m/e = 44$) and NO_2 ($m/e = 46$) were not evolved anymore when the crystallization started during the thermal treatment in helium.

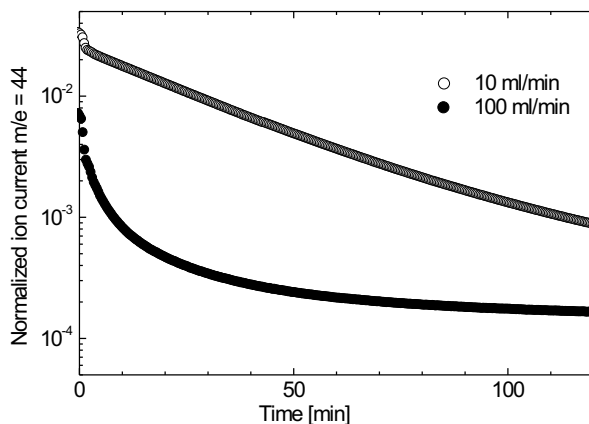


Figure 5.17: Evolution of MS traces of CO_2 ($m/e = 44$) during 2 h isothermal treatment of *MoVW* oxide precursor at 623 K in 20% oxygen/nitrogen (first step) in a total gas flow of 10 ml/min (experiment C) or 100 ml/min (experiment D).

Figure 5.19 shows the stability of the Mo_5O_{14} -type material during subsequent catalytic testing in 5% propene and 10% oxygen. The crystalline Mo_5O_{14} -type oxide exhibited an onset of the formation of acrolein and acrylic acid at 550 K and 630 K, respectively, shown in Figure 5.18. XRD analysis of the oxide after catalysis testing detected traces of $Mo_xV_{2-x}O_5$ phases (< 5 wt-%).

According to TEM investigations of the material obtained after calcination shown in Figure 5.20 is crystalline. No spherical particles as in experiment C were detected. The HRTEM images shown in Figure 5.21 can be assigned to the Mo_5O_{14} -type structure. The image presenting the (120) planes shows in a small structure drawing chains of pentagonal columns. The pentagonal bipyramidal sites (light gray chains) are depleted of one or two edge-sharing surrounding octahedra (white chains). Only corner-linked octahedral sites are dark gray. In the image of the $[3\ 4\ 18]$ zone axis the small structure drawing shows dark shaded the truncated pentagonal columns (pentagonal bipyramids with edge-sharing octahedra). The edge-sharing octahedra are dark gray surrounding gray pentagonal bipyramids. Only corner-linked octahedral sites are light gray. The electron diffraction pattern shows a ring corresponding to $d = 3.9$ Å, and streaks with the same interval can be seen. It can be attributed to the c -axis of $(MoVW)_5O_{14}$.

The TEM investigation of the material obtained after catalytic testing showed crystalline particles with sharp edges Figure 5.22. The lattice fringes obtained in HRTEM (Figure 5.23) correspond to the (200) planes of $(MoVW)_5O_{14}$. The image presenting the (200) planes shows in a small structure drawing chains of pentagonal columns. Some pentagonal bipyramidal sites (light gray chains) are depleted of one edge-sharing octahedron (white) similar to the previous (120) planes shown in Figure 5.21. Other pentagonal bipyramidal sites are completely surrounded by edge-sharing octahedra (three white chains). Only corner-linked octahedral sites are dark gray. In the electron

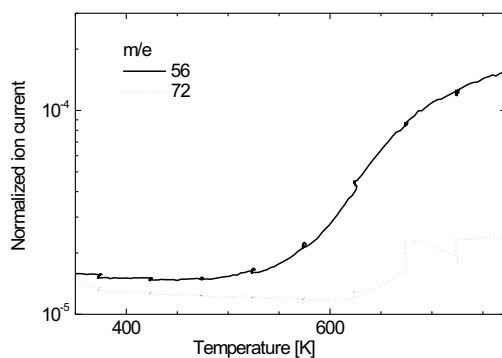


Figure 5.18: Evolution of MS traces acrolein ($m/e = 56$) and acrylic acid ($m/e = 72$) during catalytic test in 5% propene and 10% oxygen from 300 K to 773 K of previously crystallized $(MoVW)_5O_{14}$.

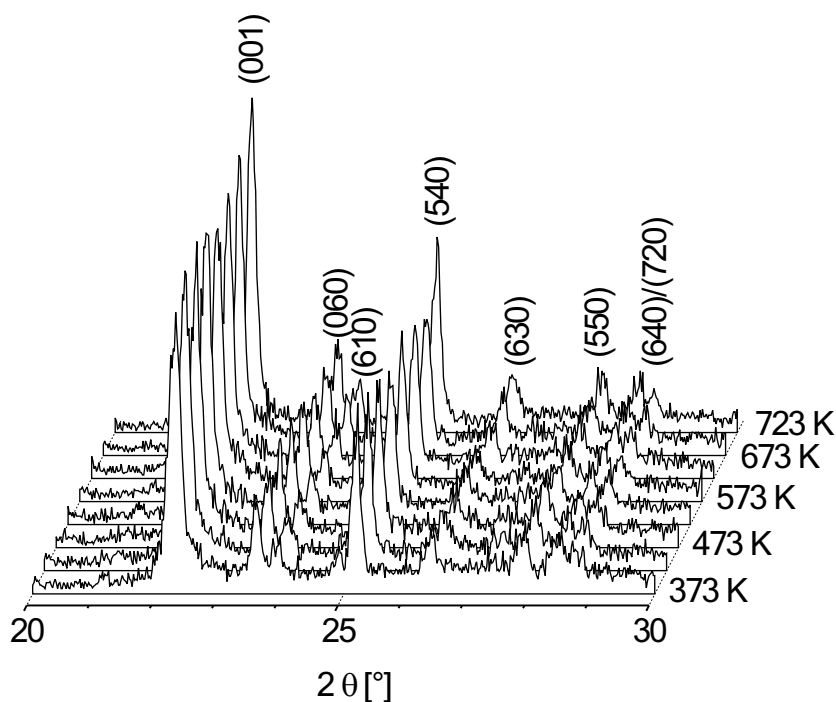


Figure 5.19: In situ XRD during catalytic test in 5% propene and 10% oxygen from 300 K to 773 K of previously crystallized $(MoVW)_5O_{14}$.

diffraction pattern the ring corresponding to $d = 3.9 \text{ \AA}$ and the streaks with the same interval are assigned to the c-axis of $(MoVW)_5O_{14}$.

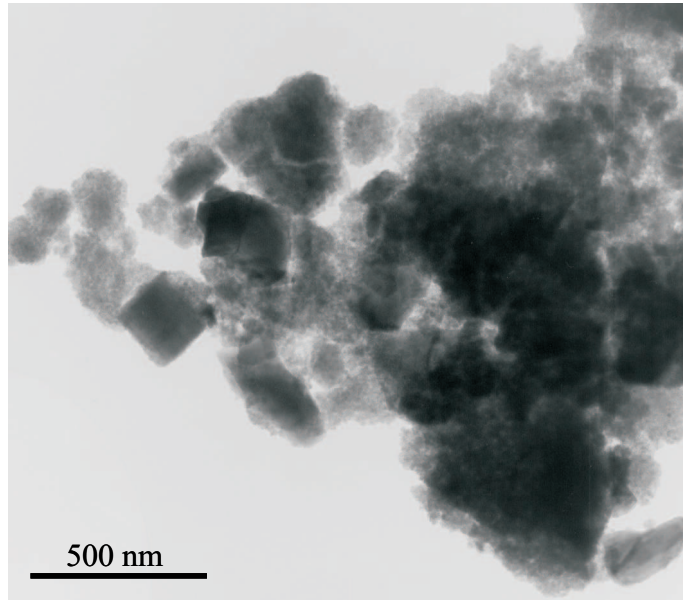


Figure 5.20: Low magnification TEM of material obtained after thermal treatment in experiment D.

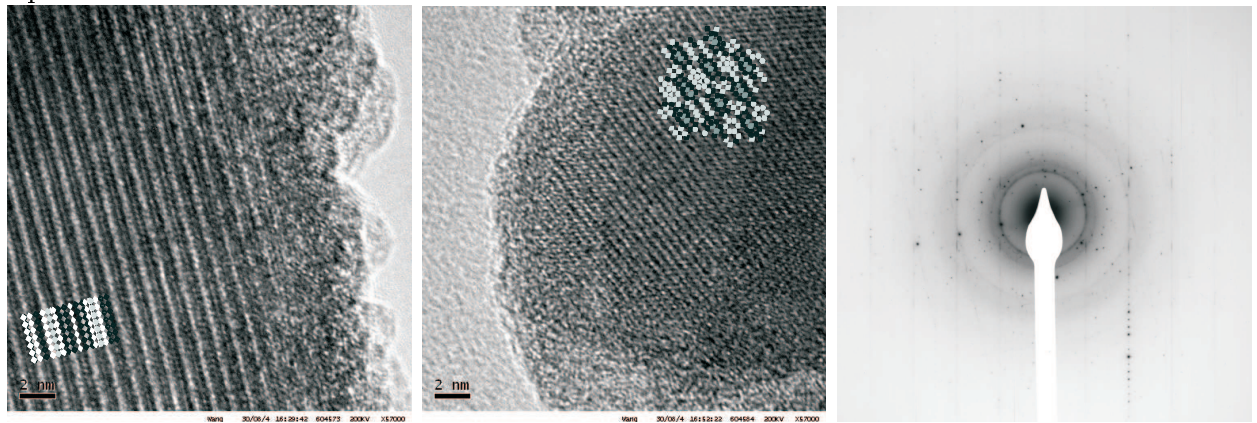


Figure 5.21: HRTEM of Mo_5O_{14} -type structure: image with lattice fringes $d = 10 \text{ \AA}$ corresponds to (120) planes (left), image of $(MoVW)_5O_{14}$ on the $[3418]$ zone axis (center), and electron diffraction pattern (right).

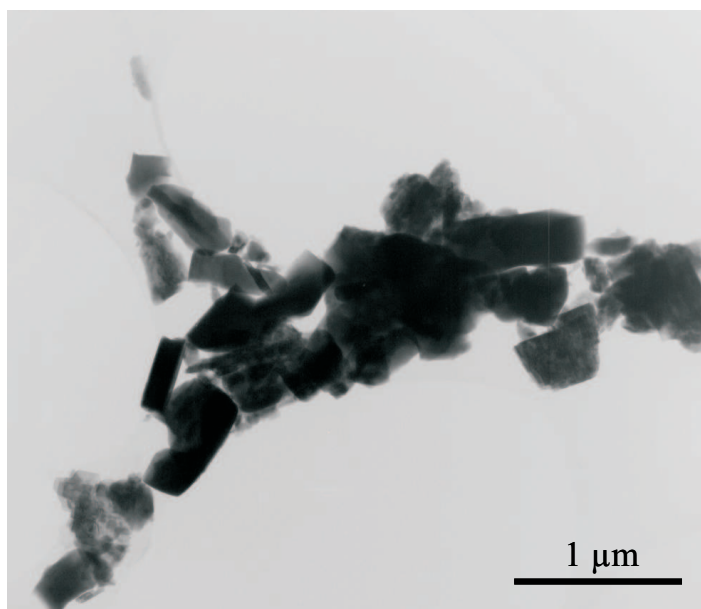


Figure 5.22: Low magnification TEM of material obtained after catalytic testing.

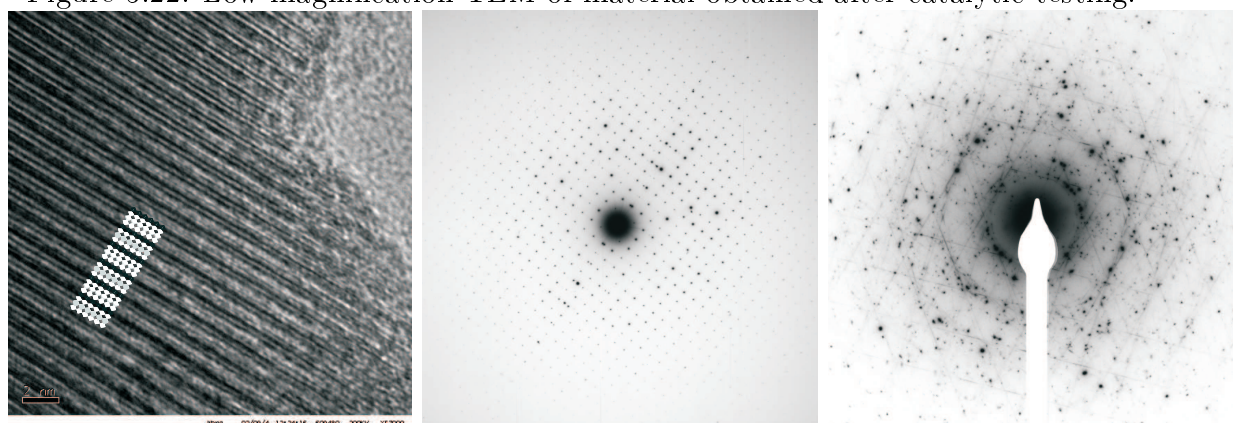


Figure 5.23: HRTEM of $(MoVW)_5O_{14}$ obtained after catalytic test: image with lattice fringes of $d = 11.2 \text{ \AA}$ corresponds to (200) planes (left), image of a single crystal with Mo_5O_{14} -type structure (center), and electron diffraction pattern (right).

Experiment E

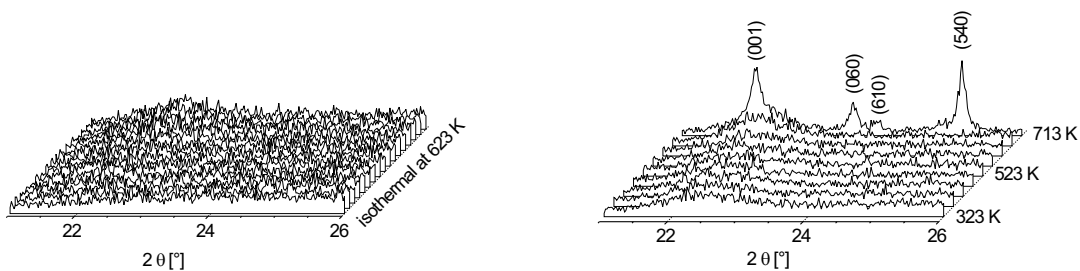


Figure 5.24: Experiment E: in situ XRD during 3 h dwell of *MoVW* oxide precursor in 20% oxygen/ nitrogen at 623 K (left), and during heating in helium 300 K to 713 K (right).

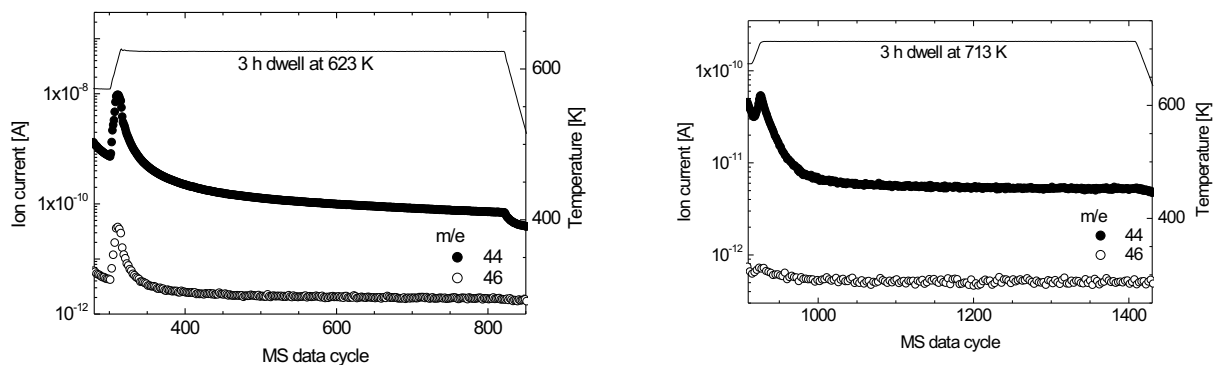


Figure 5.25: Experiment E: evolution of MS traces during in situ XRD calcination of *MoVW* oxide precursor. CO_2 and/ or N_2O ($m/e = 44$) and NO_2 ($m/e = 46$) during 3 h dwell time at 623 K in 20% oxygen/ nitrogen (left), and during 3 h dwell time at 713 K in helium.

A prolonged dwell time of 3 h at 623 K and 713 K in a two-step procedure is denoted as Experiment D. As shown in Figure 5.24 the domain growth started during the isothermal treatment in helium at 713 K. The evolution of MS traces CO_2 and/ or N_2O ($m/e = 44$) and NO_2 ($m/e = 46$) is given in Figure 5.25. Figure 5.26 shows the MS traces monitored during the catalytic test in 5% propene and 10% oxygen from 300 K to 773 K. Onset of catalysis was detected at 540 K for acrolein ($m/e = 56$) and 640 K for acrylic acid ($m/e = 72$). The XRD pattern of the sample after thermal treatment showed besides crystalline single phase $(MoVW)_5O_{14}$ a small amount of X-ray amorphous material which was completely crystallized after catalytic testing.

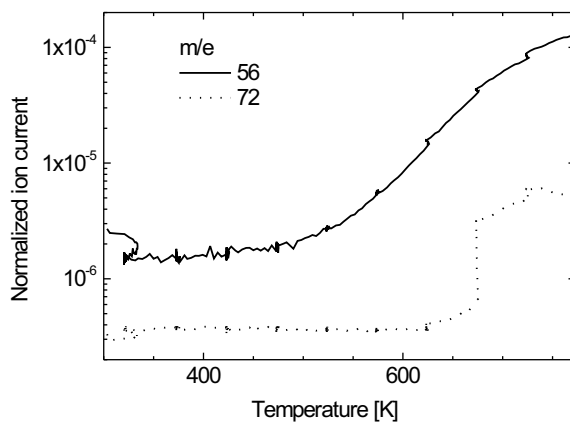


Figure 5.26: Evolution of MS traces acrolein ($m/e = 56$) and acrylic acid ($m/e = 72$) during in situ XRD catalytic test in 5% propene and 10% oxygen from 300 K to 773 K of previously crystallized $(MoVW)_5O_{14}$.

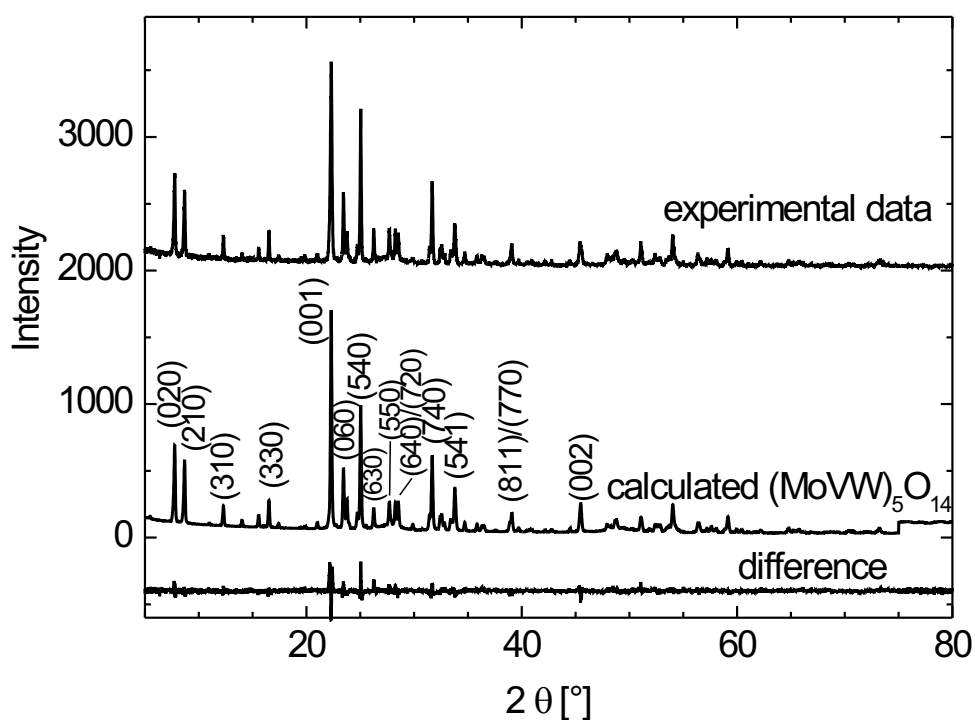


Figure 5.27: Rietveld refinement of $(MoVW)_5O_{14}$ to ex situ XRD pattern obtained after catalytic testing.

Figure 5.27 presents the Rietveld refinement of a $(MoVW)_5O_{14}$ structure model to the experimental XRD pattern obtained after thermal treatment and after subsequent catalysis testing. Only $(MoVW)_5O_{14}$ was detected.

Experiment F

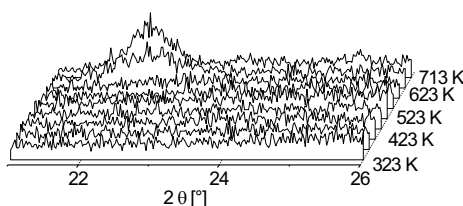


Figure 5.28: Experiment F: in situ XRD during heating of *MoVW* oxide precursor in 20% oxygen/ nitrogen to 713 K.

Thermal treatment of the precursor in synthetic air in a one-step procedure in the temperature range from 300 K to 713 K is denoted as experiment F. From an analysis of the in situ XRD patterns shown in Figure 5.29 the evolution of crystallite size was determined. During the one-step calcination in synthetic air, a crystallite growth at 713 K coincided with the detection of CO_2 , N_2O ($m/e = 44$) and NO_2 ($m/e = 46$) in the gas phase as shown in Figure 5.30. At the time when last $m/e = 44$ is evolved in helium, domains start growing rapidly.

Figure 5.31 shows subsequent catalysis testing in 10% oxygen and 5% propene. The onset of production of acrolein ($m/e = 56$) was detected at 550 K and of acrylic acid ($m/e = 72$) at 670 K. The material obtained after catalytic testing was investigated by XRD structural analysis. After refinement of the $(MoVW)_5O_{14}$ structure model to the experimental XRD pattern some unaccounted intensity remained in the difference curve as shown in Figure 5.32. Besides $(MoVW)_5O_{14}$ as major phase, unidentified peaks at 24.2° , 27.3° , and 49.3° in 2θ were detected in the XRD pattern of the resulting oxide.

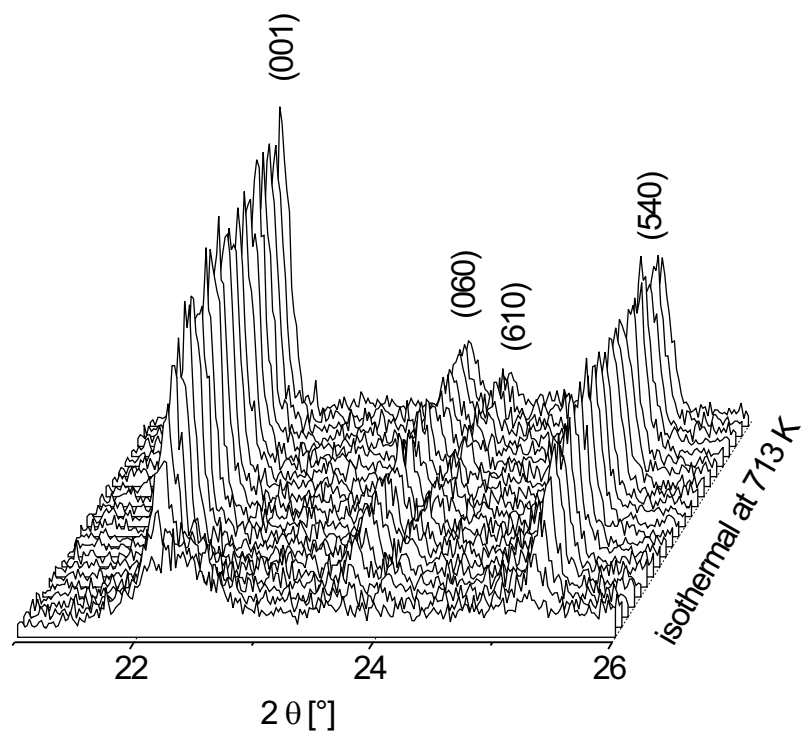


Figure 5.29: Experiment F: in situ XRD during isothermal treatment (4 h) of *MoVW* oxide precursor in 20% oxygen/ nitrogen at 713 K.

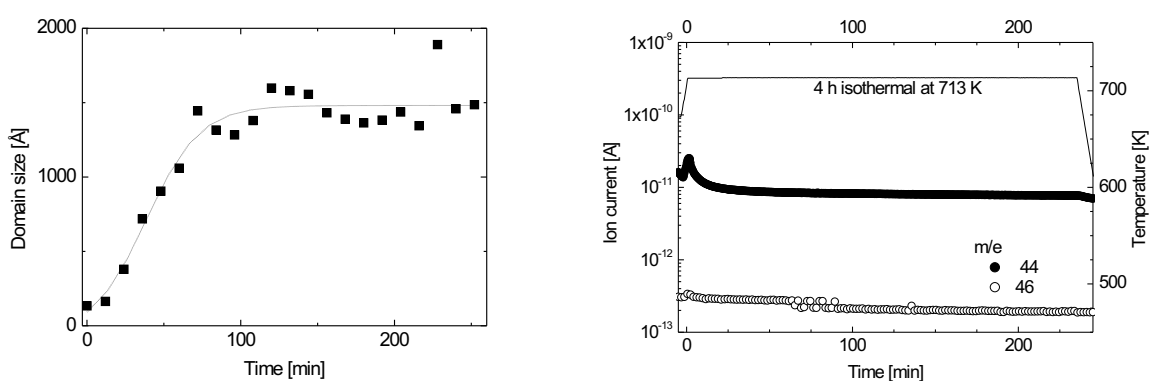


Figure 5.30: Experiment F: crystallite domain growth during in situ XRD calcination of *MoVW* oxide precursor (left), evolution of MS traces at the same time (right). CO_2 and/ or N_2O ($m/e = 44$) and NO_2 ($m/e = 46$) during 4 h dwell time at 713 K in 20% oxygen/ nitrogen.

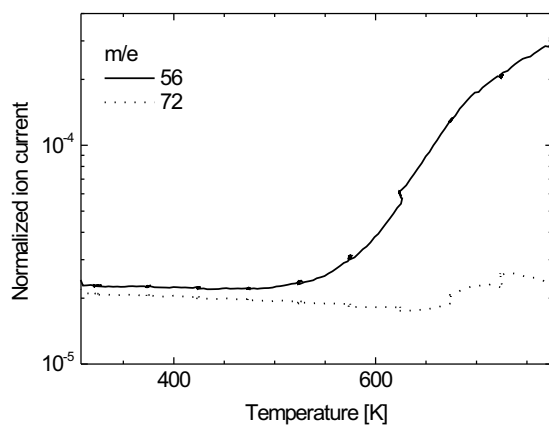


Figure 5.31: MS traces acrolein ($m/e = 56$) and acrylic acid ($m/e = 72$) during in situ XRD catalytic test in 5% propene and 10% oxygen from 300 K to 773 K .

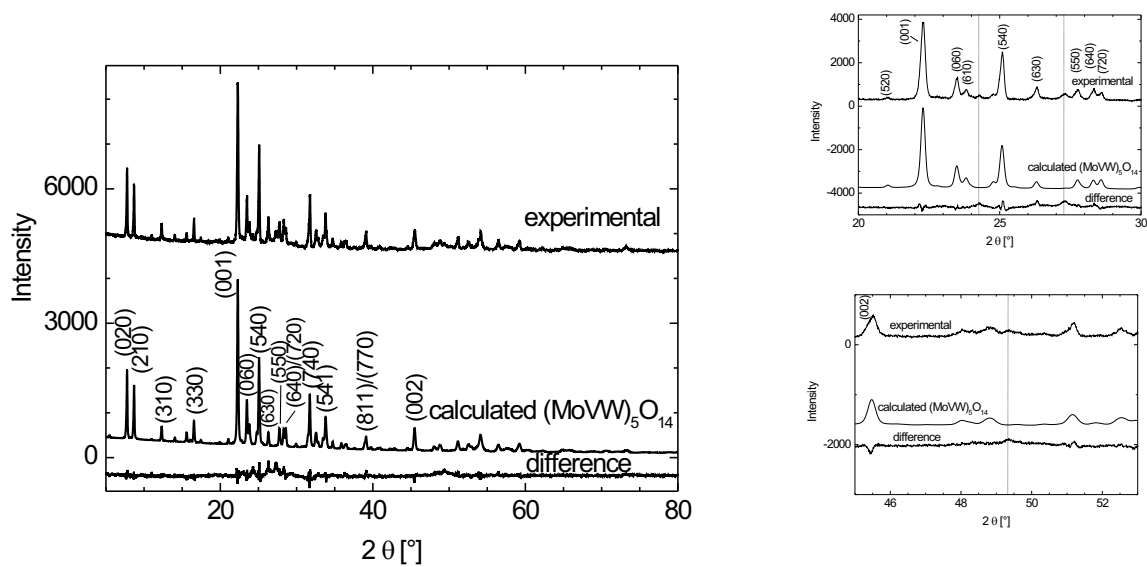


Figure 5.32: Rietveld structure analysis of the sample after catalytic test describes most of the XRD pattern.

Experiment G

Alternatively to the one-step procedure in synthetic air applied in experiment F, experiment G is a one-step thermal treatment in helium in the temperature range from 300 K to 713 K. The evolution of a crystalline phase was observed during the isothermal treatment at 713 K for 2 h (Figure 5.33) by in situ XRD. The evolution of N_2 and/ or CO ($m/e = 28$), CO_2 and/ or N_2O ($m/e = 44$) during the isothermal treatment (Figure 5.34) does not coincide with the domain growth. The material becomes crystalline even though the decomposition products are still released.

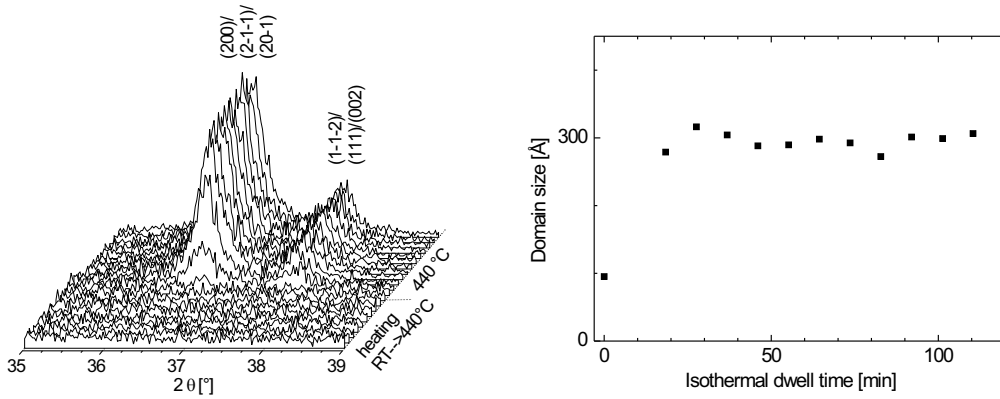


Figure 5.33: Experiment G: in situ XRD during treatment of *MoVW* oxide precursor in 100% helium to 713 K (left), and domain growth during isothermal treatment 2 h at 713 K (right).

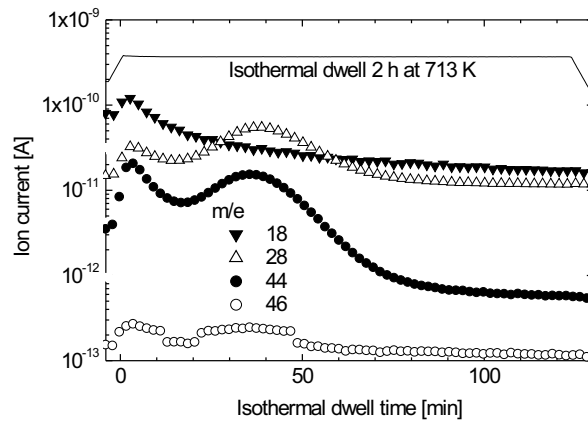


Figure 5.34: Experiment G: evolution of MS traces during in situ XRD calcination of *MoVW* oxide precursor. H_2O ($m/e = 18$), N_2 and/ or CO ($m/e = 28$), CO_2 and/ or N_2O ($m/e = 44$) and NO_2 ($m/e = 46$) during 2 h dwell time at 713 K in 100% helium.

Likewise, the TEM investigation of the material obtained after thermal treatment showed some remaining spherical particles from the spray-drying and irregular shaped particles as shown in Figure 5.35. The electron diffraction pattern shown in Figure 5.36 matches that of MoO_2 and the HRTEM fits on the $[021]$ zone axis of MoO_2 .

An ex situ XRD pattern of the material obtained at 300 K after thermal treatment in helium up to 713 K was analyzed by XRD. Figure 5.37 shows the refinement result of a structure model based on MoO_2 ICSD [27322]. Lattice constants and the metal site occupancy were refined free. Some intensity at 26-27° in 2θ remains unaccounted. This region corresponds to the peaks of hkl -indices $(\bar{1}11)$, (011) , and (110) . Probably an preferred orientation is not accounted for. The peaks overlap strongly and this makes

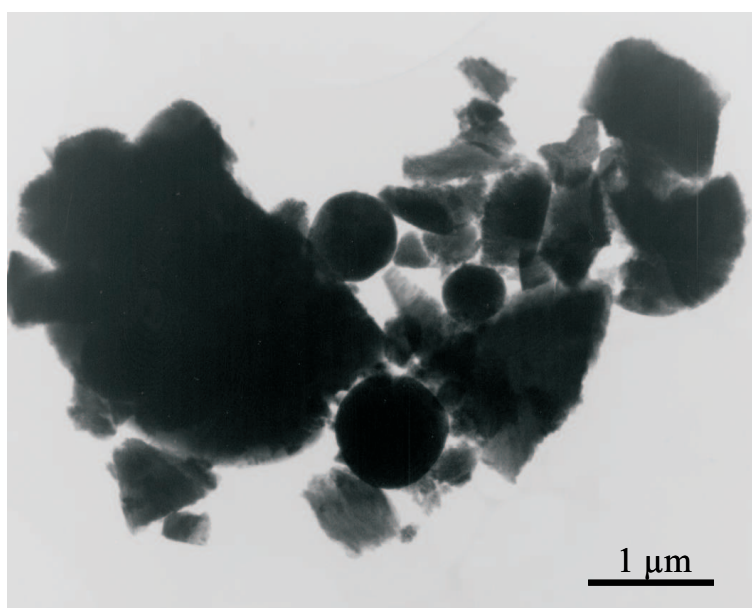


Figure 5.35: Low magnification TEM of material obtained after catalytic testing.

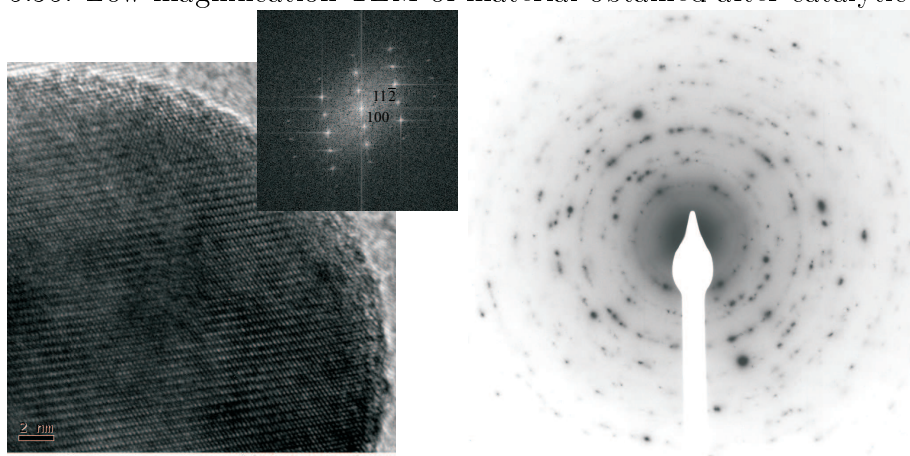


Figure 5.36: HRTEM image on $[021]$ zone axis of MoO_2 -type structure (left), and electron diffraction pattern (right).

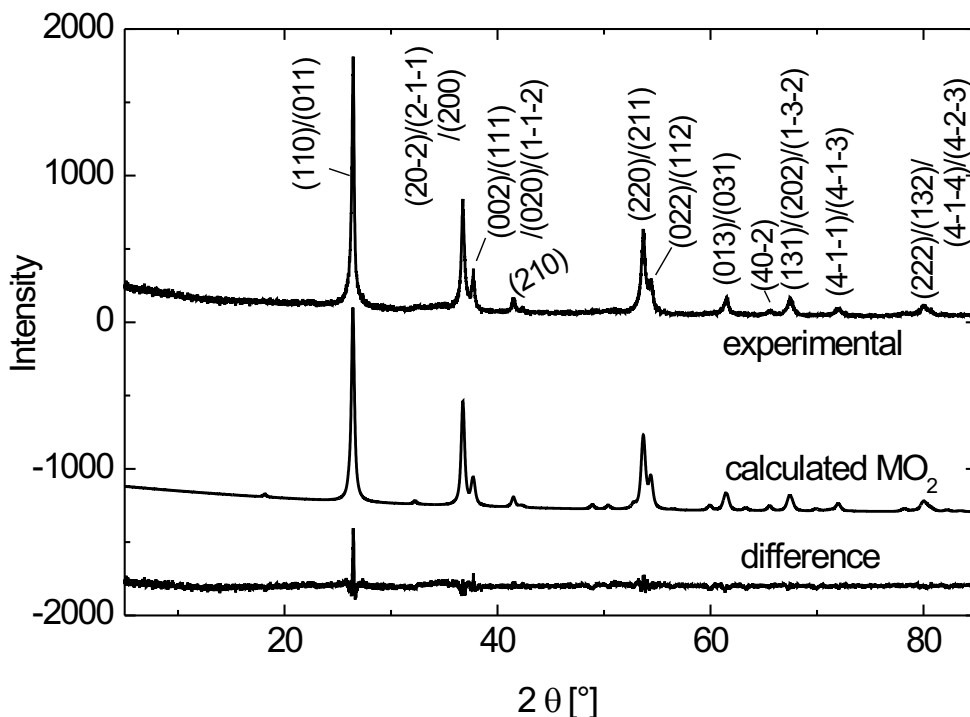


Figure 5.37: Rietveld structure model based on MoO_2 ICSD [27322] refined to the experimental pattern.

analysis uncertain.

The lattice constants of the refined structure model are listed in Table 5.2 and compared to binary MoO_2 . The crystalline material is a monoclinic phase and structurally related to rutile. Similar phases exist for MoO_2 , WO_2 and VO_2 . For description of the monoclinic $MoVW$ oxide the peak positions and peak width were compared to MoO_2 , WO_2 , and VO_2 . The attempt to describe the $(MoVW)O_2$ as a mixture of binary oxides failed. The monoclinic angle of VO_2 shifts peaks to positions completely off the experimental pattern. MoO_2 and WO_2 have lattice constants close to one another, but intensities and shape of several peaks of the experimental pattern cannot be described with a mixture of these two phases.

Under subsequent oxidizing conditions in 20% oxygen or catalytic testing in 5% propene and 10% oxygen several phases besides the Mo_5O_{14} -type structure were formed. The material was analyzed for its composition by refinement of 'hkl'-phases to the experimental XRD pattern. The results are shown in Figure 5.38. In the completely oxidized material 45% MoO_3 ICSD [35076] besides 30% $(MoVW)_5O_{14}$ and 25% $(MoV)_2O_5$ ICSD [24338] were found.

	(<i>MoVW</i>) oxide	<i>MoO</i> ₂ ICSD [23722]
Rwp [%]	11.61	-
GoF	1.24	-
a [Å]	5.69	5.61
b [Å]	4.78	4.82
c [Å]	5.55	5.63
β [°]	120.97	120.95
crystallite size [nm]	31	-

Table 5.2: Lattice parameters refined to material obtained in experiment G compared to binary *MoO*₂ ICSD [27322].

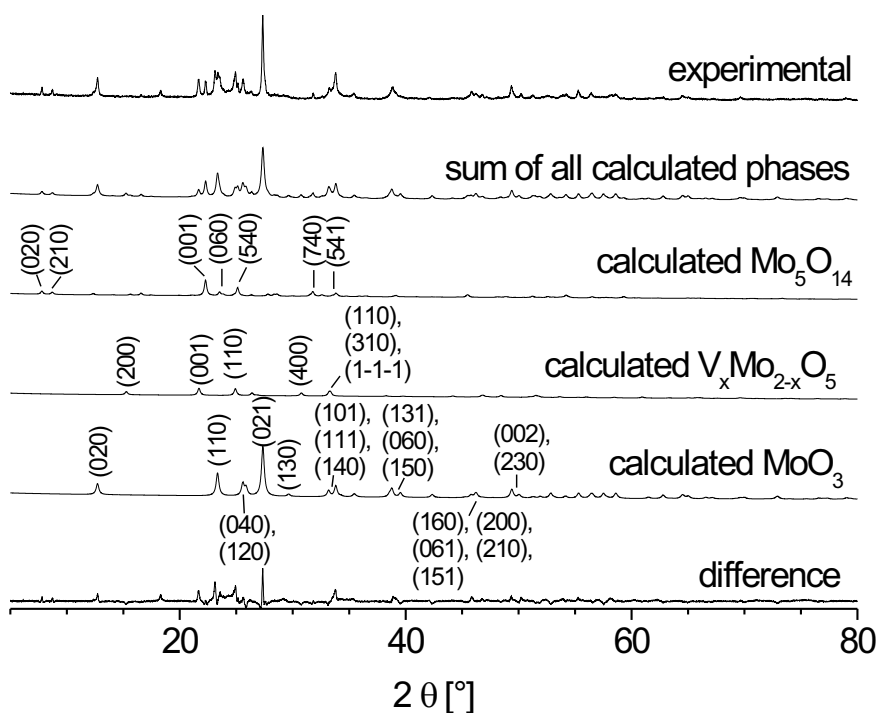


Figure 5.38: Rietveld refinement of ax situ XRD pattern of material obtained from (*MoVW*) *O*₂ after oxidation in 20% oxygen at 773 K.

Experiment H

The carrier gas of the calcination in 20% oxygen was changed to helium instead of nitrogen in experiment H. The standard procedure of 2 h isothermal treatment was applied in 20% oxygen/ helium at 623 K and 100% helium at 713 K. Figure 5.39 shows the second step, treatment in helium. The final material is X-ray amorphous, but has a broad feature in the range 21-23° in 2θ .

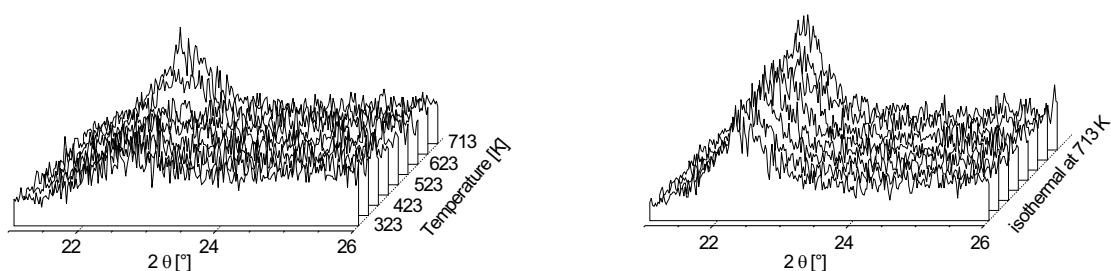


Figure 5.39: Experiment H: in situ XRD during treatment of *MoVW* oxide precursor in 100% helium from 300 K to 713 K (left), and domain growth during isothermal treatment 2 h at 713 K (right). Material previously calcined in 20% oxygen/ helium for 2 h at 623 K.

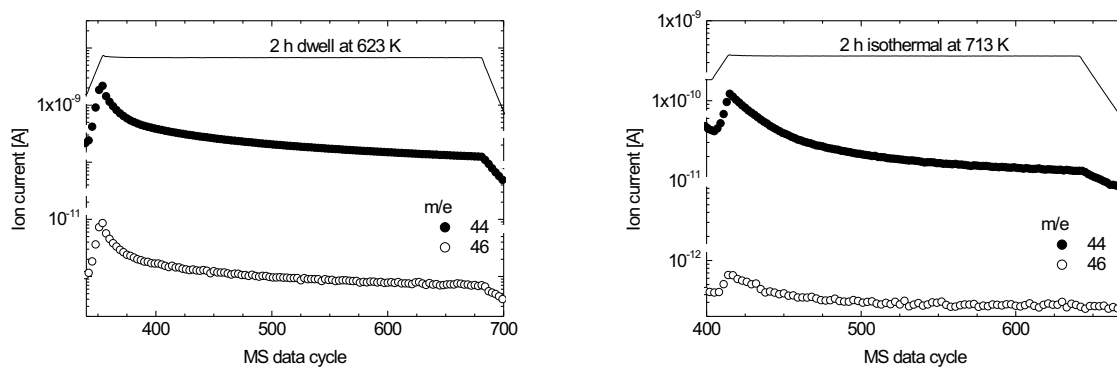


Figure 5.40: Experiment H: evolution of MS traces during in situ XRD calcination of *MoVW* oxide precursor. CO_2 and/ or N_2O ($m/e = 44$) and NO_2 ($m/e = 46$) during 2 h dwell time at 623 K in 20% oxygen/ nitrogen (left) and at 713 K in 100% helium (right).

5.1.2 Thermal analysis of crystallization in TG/ DSC

TG/ DSC studies on the calcination procedure were performed at different heating rates with 2 h dwell time in both atmospheres (Figure 5.41) at a gas flow of 100 ml/min. Experimental setup and fragments used for determination of the gas atmosphere are listed in Paragraph 4.7, Table 4.4. The decomposition temperatures of the *MoVW* oxide precursor depending on heating rate are listed in Table 5.3. At higher heating rates the decomposition steps are shifted to higher temperatures. The distinct steps of mass loss evolve in the same decomposition pattern at all heating rates from 3-10 K/min. The experiment with a heating rate of 1 K/min has a higher mass loss in the 1st and 2nd decomposition step and less in the 3rd decomposition step. The overall mass loss is about 30% at all heating rates. XRD investigation of the samples calcined in the TG/ DSC experiments showed increasing crystallinity at higher heating rates. In the first calcination step in 20% oxygen/ nitrogen three decomposition steps were found. The first endothermic decomposition step started with the heating ramp and

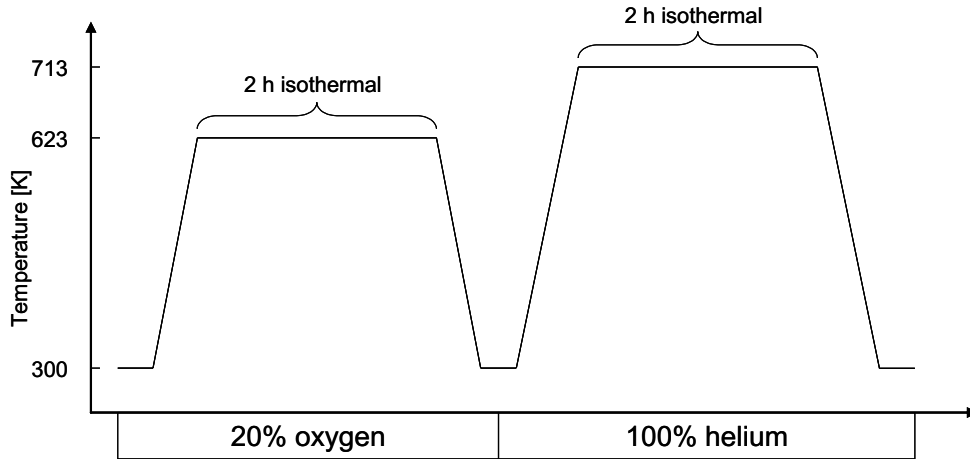


Figure 5.41: Calcination atmosphere of *MoVW* oxide precursor in TG/ DSC experiments. Heating in 20% oxygen to 623 K (1st step) and in 100% helium to 713 K (2nd) at different heating rates.

Decomp. step	Heating rate	10 K/min	5 K/min	3 K/min	1 K/min
1 st	Mass loss [%]	6.86	6.98	6.66	9.08
2 nd	Mass loss [%]	17.95	17.75	17.96	20.15
	Onset T mass loss [K]	450	437	426	408
	Min. endo [K]	523	509	489	-
	Max. exo [K]	558	542	532	518
3 rd	Mass loss [%]	4.18	4.96	4.54	3.37
	Onset T mass loss [K]	574	567	561	560
	Max. exo [K]	613	603	596	-

Table 5.3: Mass loss and onset temperatures obtained in decomposition steps by TG/ DSC during calcination of *MoVW* oxide precursor in 20% oxygen/ nitrogen at different heating rates.

was accompanied by the evolution of water. During the second and third decomposition step water, ammonia, nitrogen oxides and carbon oxides were evolved. The second decomposition step is endothermic, the third exothermic. Interestingly between the second and third decomposition step an exothermic peak was found in the DSC signal, but could not be attributed to a separate step of mass loss. Directly before this intermediate maximum in the DSC curve maxima in the MS signals of $m/e = 44$ (CO_2 or N_2O) and $m/e = 12$ (*carbon*) are present. It cannot be assigned to any decomposition step in AHM [90], APT [145, 146], or vanadium oxalate [147]. Possibly a short exothermic event overlaps with the slower proceeding endothermic second decomposition step and the heat generated in the exothermic process overcomes the heat consumed in the endothermic second decomposition step. In the second step in helium a small mass loss of 1-2% occurred at 600 K accompanied by evolution of NO_2 ($m/e = 46$) and CO_2 or N_2O ($m/e = 44$) and a small exothermic DSC signal, maybe followed by another small signal.

TG/ DSC with heating rate 10 K/min

The calcination of *MoVW* oxide precursor was performed in 20% oxygen/ nitrogen and thermal treatment in 100% helium at a heating rate of 10 K/min. Figures 5.42 and 5.43 show the TG/ DSC signals during the heating ramps correlated to the gas phase. Compared to the lower heating rates, at the high heating rate of 10 K/min the exothermic signal at 558 K is strongest. Additionally, the high heating rate leads to best crystallinity in the product formed.

In Figure 5.42 the endothermic and exothermic signals in the DSC curve correlate with volatile decomposition products detected in the gas phase. In the respective MS traces shoulders occur.

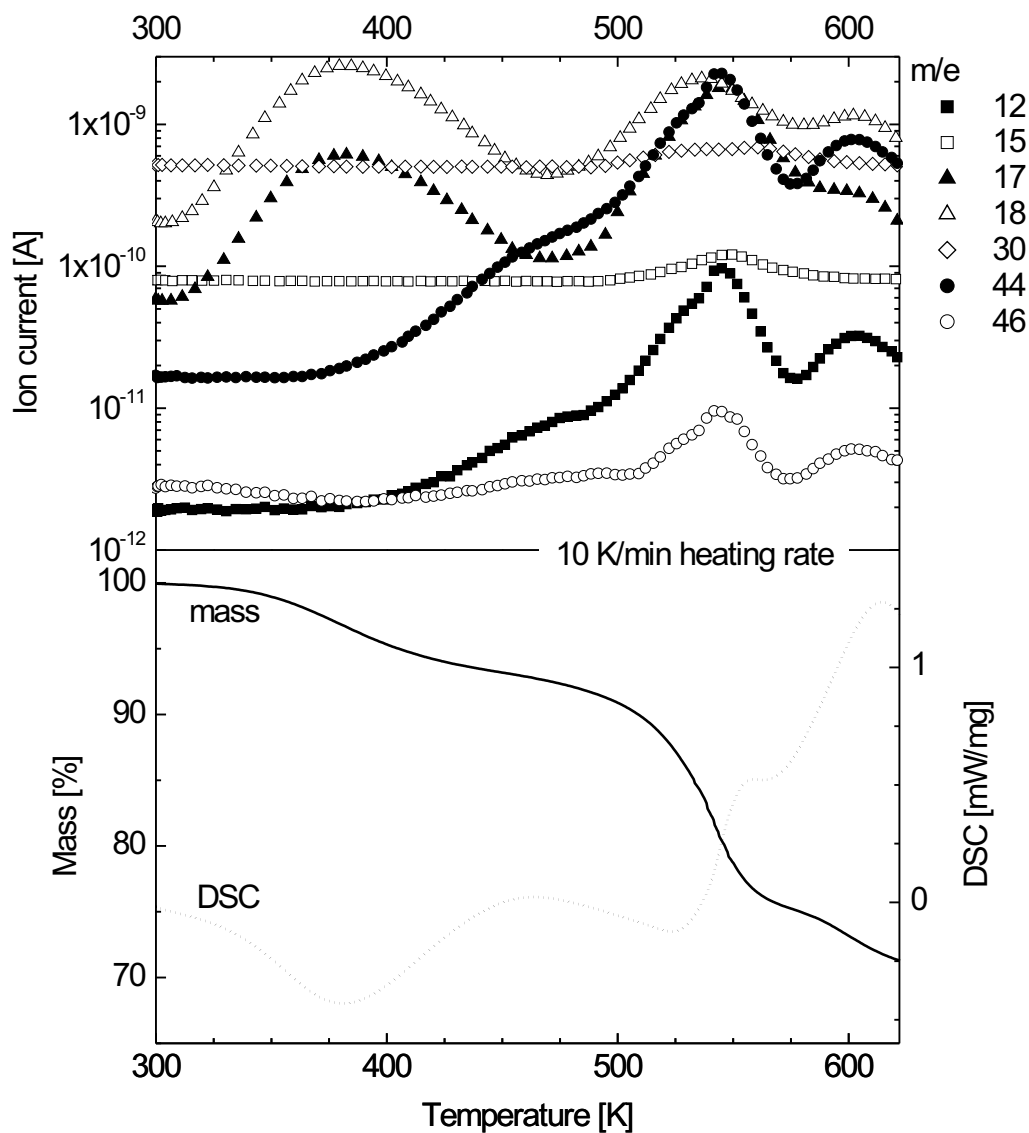


Figure 5.42: TG/ DSC and MS signals of *MoVW* oxide precursor during heating in 20% oxygen/ nitrogen to 623 K at a heating rate of 10 K/min.

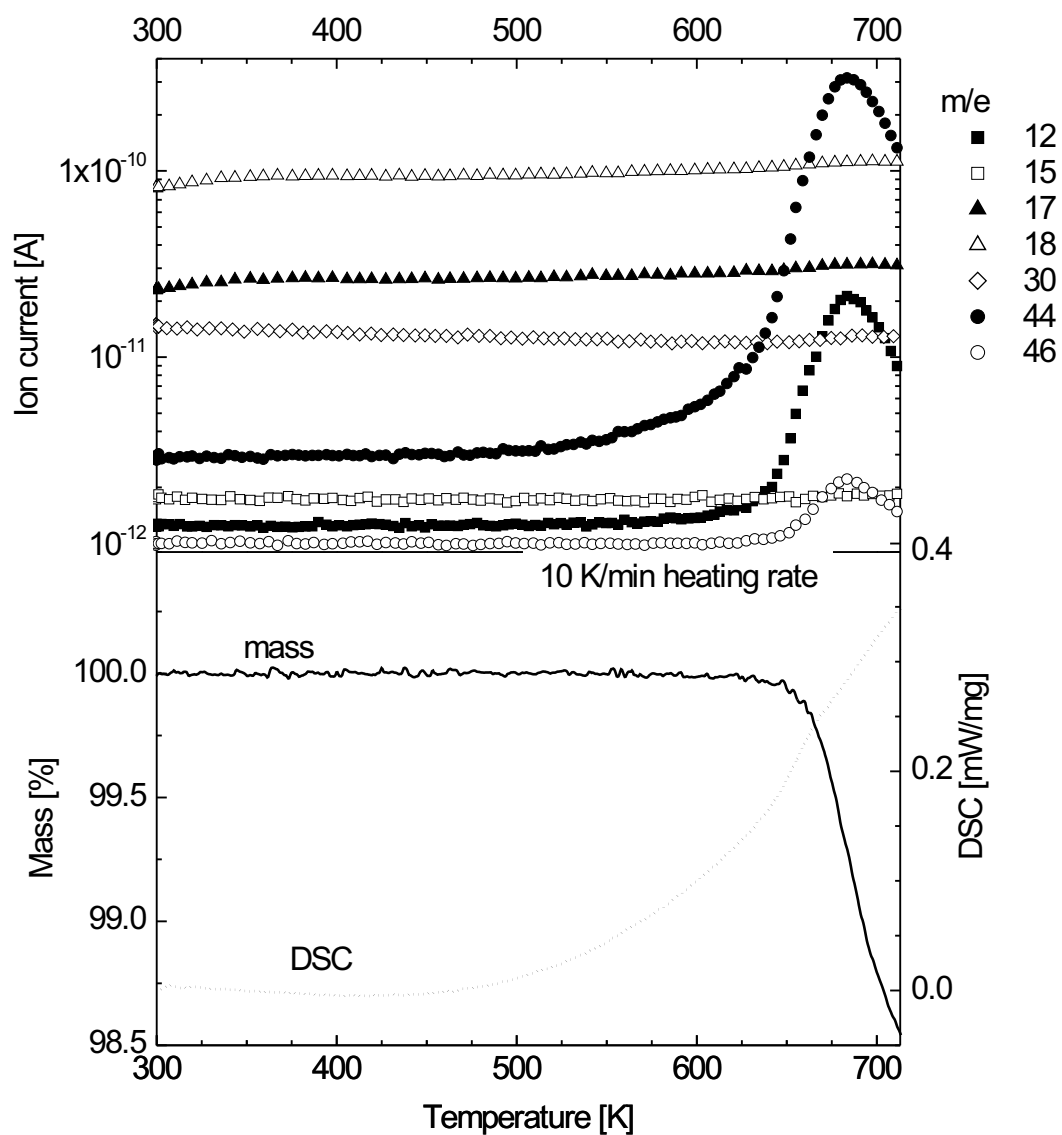


Figure 5.43: TG/ DSC and MS signals of *MoVW* oxide precursor during heating in 100% helium to 713 K at a heating rate of 10 K/min.

TG/ DSC with heating rate 5 K/min

The *MoVW* oxide precursor was calcined in 20% oxygen/ nitrogen and thermally treated in 100% helium at a heating rate of 5 K/min. This experiment corresponds to in situ XRD crystallization experiment D. Figures 5.44 and 5.45 show the data measured during both heating ramps in TG/ DSC and MS gas phase analysis. Alterna-

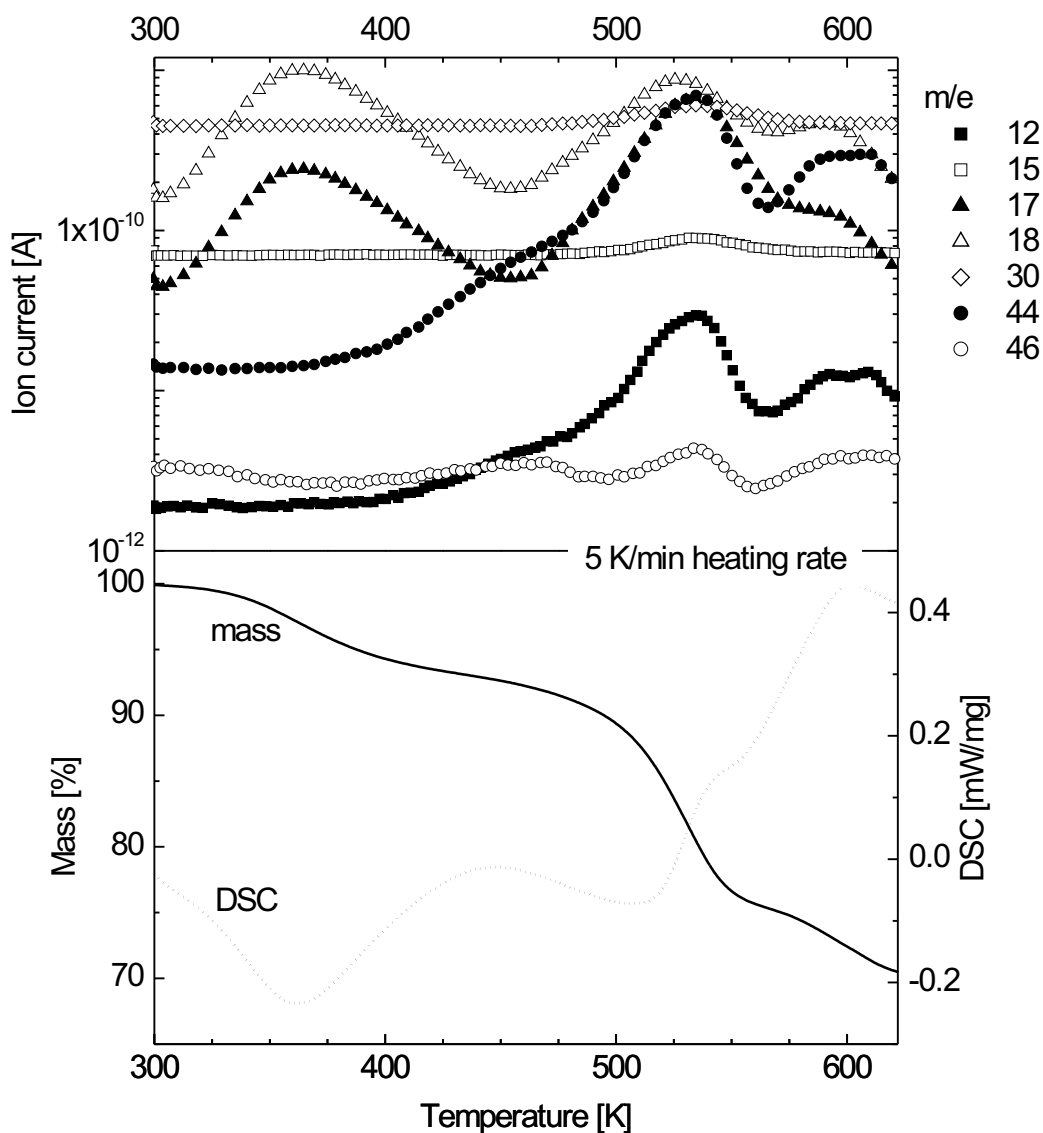


Figure 5.44: TG/ DSC and MS signals of *MoVW* oxide precursor during heating in 20% oxygen/ nitrogen to 623 K at a heating rate of 5 K/min.

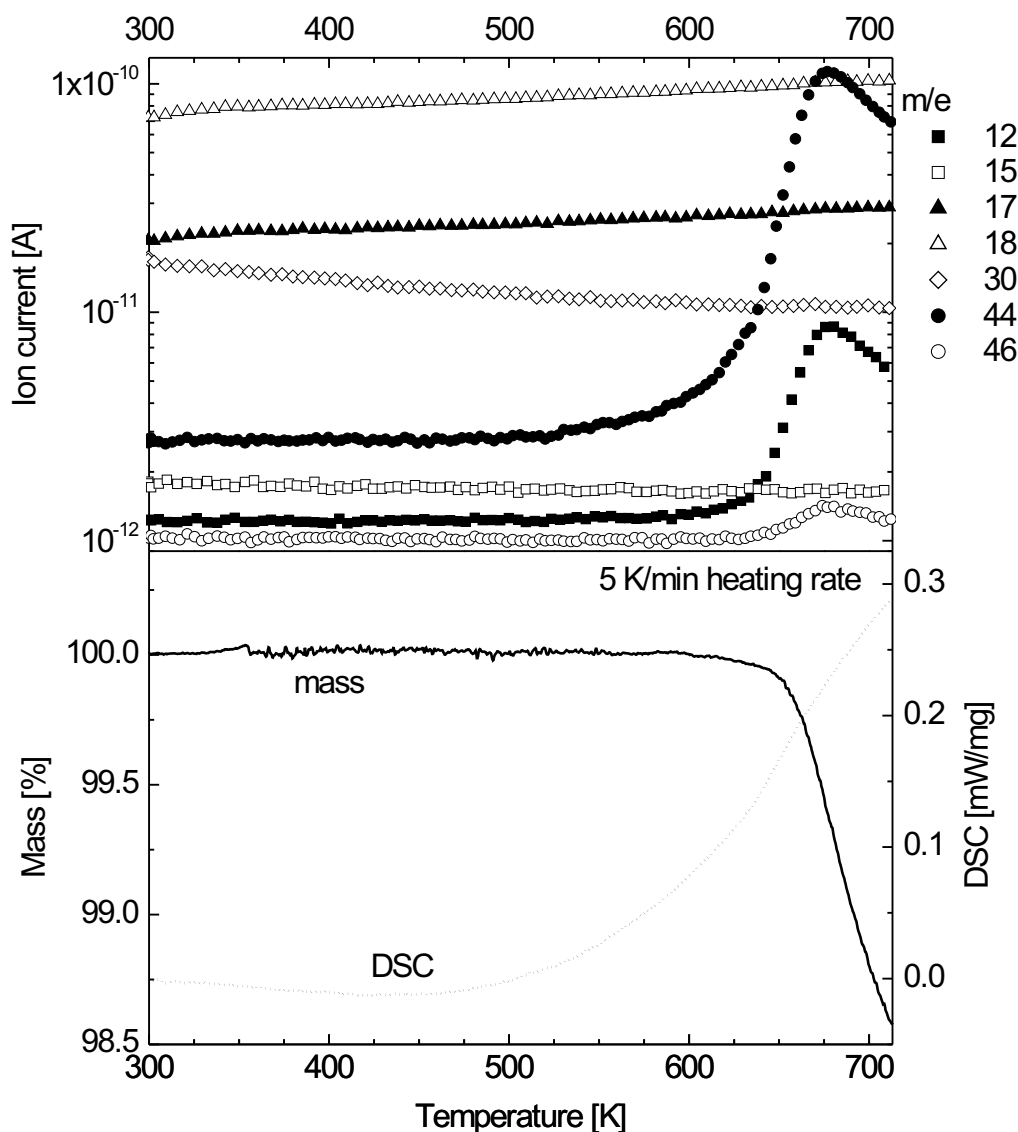


Figure 5.45: TG/ DSC and MS signals of *MoVW* oxide precursor during heating in 100% helium to 713 K at a heating rate of 5 K/min.

tively, the *MoVW* oxide precursor was calcined in 20% oxygen/ helium and thermally treated in 100% helium at a heating rate of 5 K/min. This experiment corresponds to in situ XRD crystallization experiment H. The data obtained in TG/ DSC measurements with gas phase analysis during both heating ramps are shown in Figures 5.46 and 5.47. Changing the carrier gas nitrogen to helium in the first treatment step in 20% oxygen resulted at less crystalline material after the subsequent helium treatment

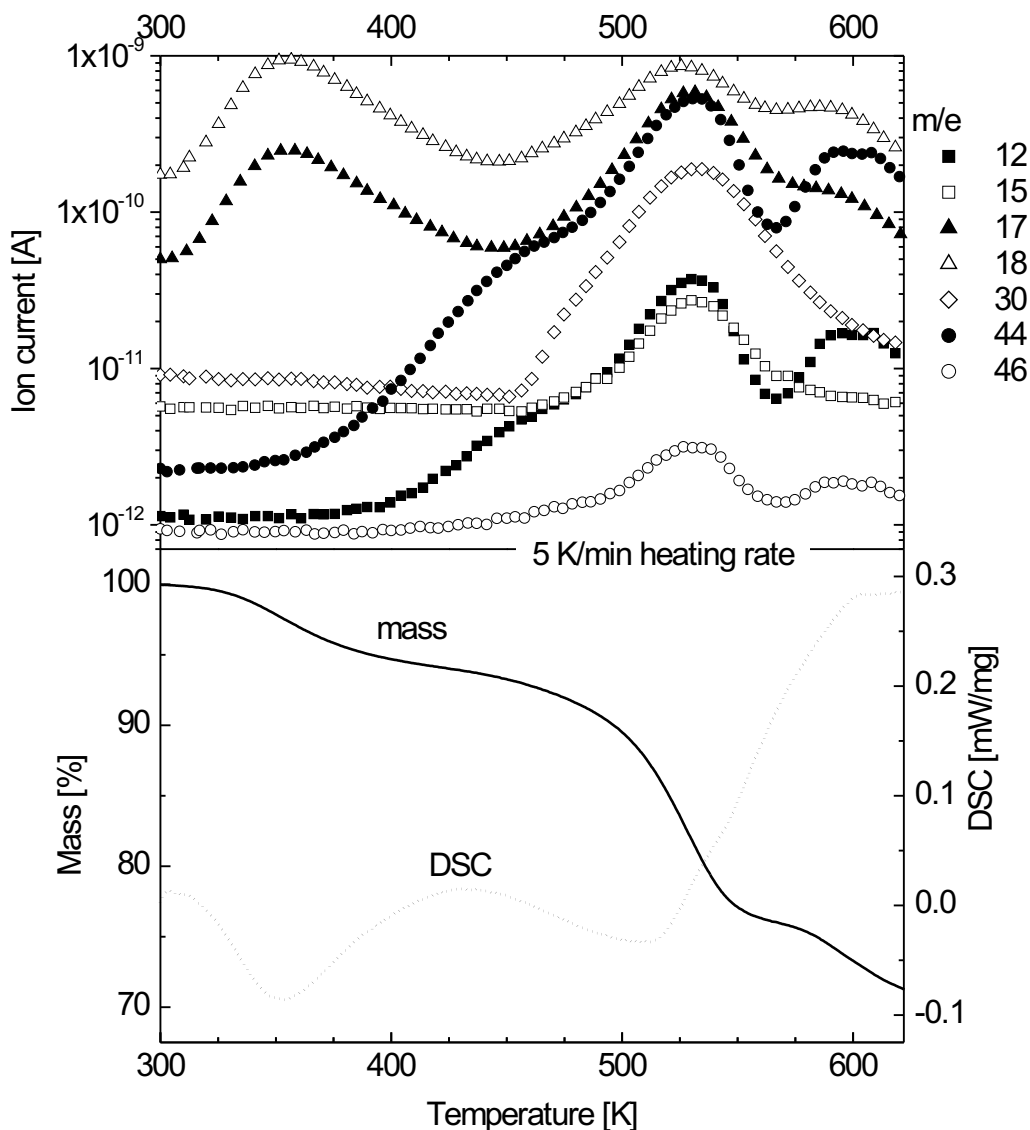


Figure 5.46: TG/ DSC and MS signals of *MoVW* oxide precursor during heating in 20% oxygen/ helium to 623 K at a heating rate of 5 K/min.

than for material treated in nitrogen based atmosphere.

Furthermore, changing the gas atmosphere from 20% oxygen/ nitrogen to 20% oxygen/ helium in the first thermal treatment step resulted in a less crystalline material. Difference in the DSC and MS curves between the calcination in 20% oxygen/ nitrogen and 20% oxygen/ helium was found. In the DSC curve with carrier gas nitrogen less pronounced endothermic and exothermic signals appear. During the first treatment

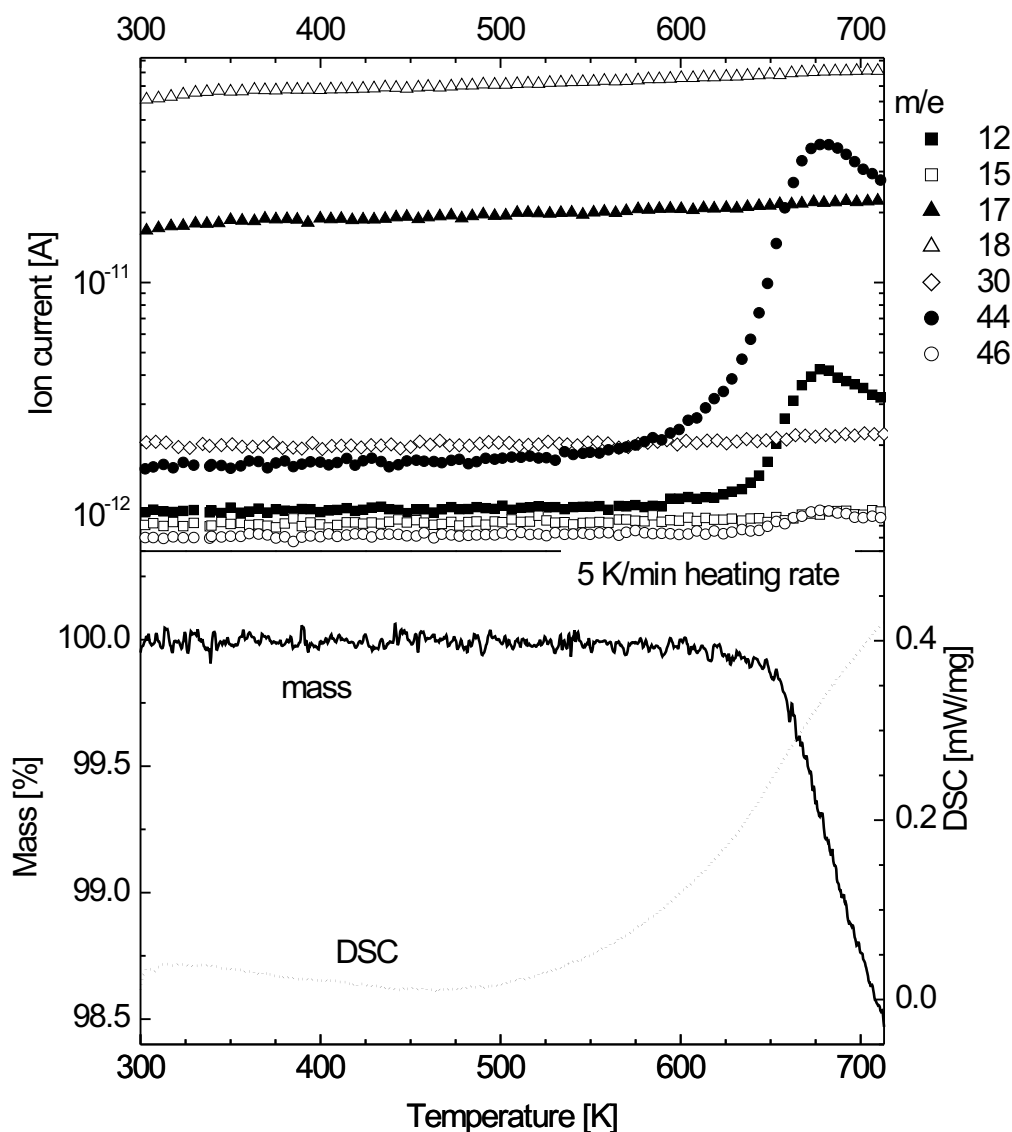


Figure 5.47: TG/ DSC and MS signals of *MoVW* oxide precursor during heating in 100% helium to 713 K at a heating rate of 5 K/min.

step in the helium based atmosphere the exothermic signal at 542 K is nearly absent. Helium has a higher thermal conductivity than nitrogen, this would explain the generally less pronounced thermal heat, but not the absence of one signal. In the MS trace of N_2O ($m/e=46$) the presence of a small peak at about 470 K found in the oxygen/ nitrogen atmosphere was not detected in the oxygen/ helium atmosphere, Figure 5.48. Due to the low temperature an oxidation of released ammonia as described

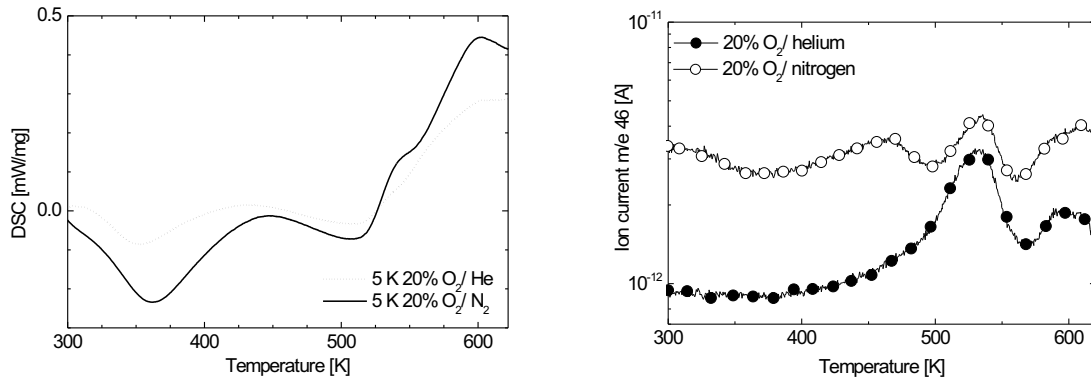


Figure 5.48: Comparison of *MoVW* oxide precursor during heating in 20% oxygen/nitrogen and 20% oxygen/helium from 300 K to 623 K at a heating rate of 5 K/min. DSC curve (left) and MS signal $m/e = 46$ (right).

for APT [148] in the temperature ranges of 530-620 K and 670-720 K is unlikely to explain this gas phase evolution.

Table 5.4 compares onset temperatures, DSC signals, and major gaseous decomposition products of *MoVW* oxide precursor to AHM ($(NH_4)_6 Mo_7O_{24} * 4H_2O$) [90] and APT ($(NH_4)_{10} H_2W_{12}O_{42} * 4H_2O$) [145]. All measurements were conducted in 20% oxygen at a heating rate of 5 K/min and a total gas flow of 100 ml/min. The TG signal measured for the three compounds is compared in Figure 5.49. As the calcination ends at 623 K the TG curve of the *MoVW* oxide precursor ends there. The overall mass loss of the *MoVW* oxide precursor is nearly double that of AHM or APT. Chemically the *MoVW* oxide precursor contains all framework ions present in AHM or APT plus nitrate (from adjusting the pH) and oxalate (introduced as vanadyl oxalate).

$(NH_4)_6 Mo_7O_{24} * 4H_2O$	<i>MoVW</i> oxide precursor	$(NH_4)_{10} H_2W_{12}O_{42} * 4H_2O$
320 K endothermic H_2O	320 K Endothermic H_2O	370 K endothermic H_2O
460 K exothermic H_2O, NH_3	437 K endothermic NO_x, CO_x	450 K endothermic H_2O, NH_3
530 K endothermic H_2O, NH_3	576 K exothermic NO_x, CO_x	500 K endothermic H_2O, NH_3
635 K exothermic H_2O, NH_3	603 K exothermic NO_x, CO_x	650 K exothermic H_2O, NH_3

Table 5.4: Comparison of *MoVW* oxide precursor to AHM and APT. Onset temperatures, thermal characterization, and obtained major gas phase products during decomposition steps measured in TG/ DSC experiments in 20% oxygen at a heating rate of 5 K/min and a total gas flow of 100 ml/min.

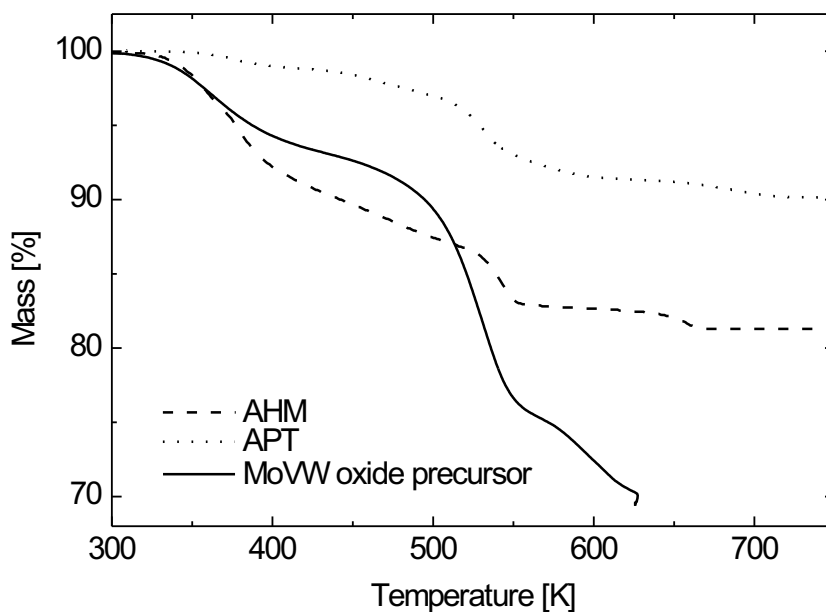


Figure 5.49: TG signals of *MoVW* oxide precursor compared to AHM and APT during heating in 20% oxygen at heating rate of 5 K/min and a total gas flow of 100 ml/min.

TG/ DSC with heating rate 3 K/min

The *MoVW* oxide precursor was calcined at a heating rate of 3 K/min in 20% oxygen/nitrogen and thermally treated in 100% helium. The TG/ DSC signal and MS curves are during heating in both atmospheres are shown in Figures 5.50 and 5.51. In the MS data monitored during the 2nd decomposition step the left shoulder of m/e 18, 44, 46 is not as clear as at heating rate 10 K/min or 5 K/min and becomes even less at heating rate 1 K/min.

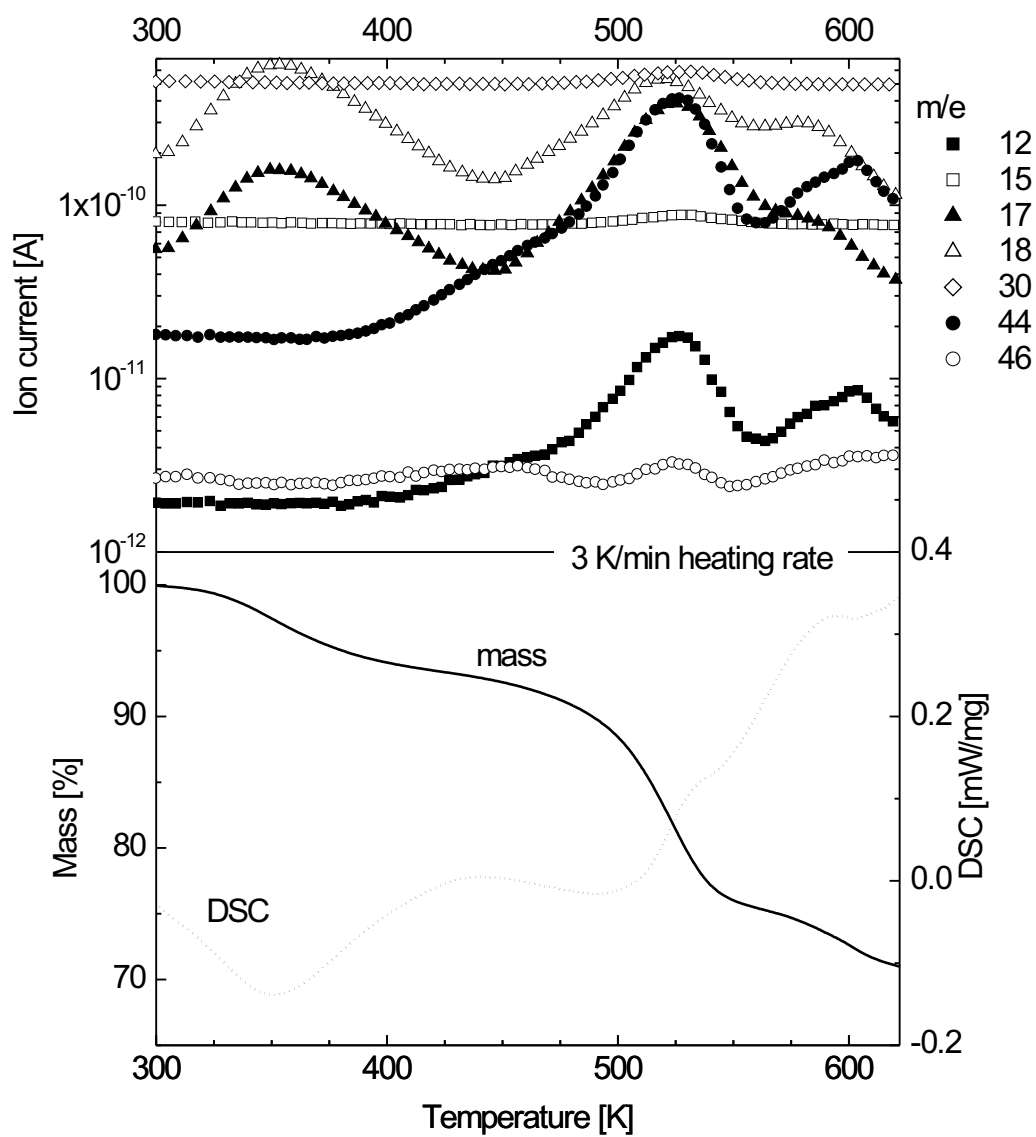


Figure 5.50: TG/ DSC and MS signals of *MoVW* oxide precursor during heating in 20% oxygen/ nitrogen to 623 K at a heating rate of 3 K/min.

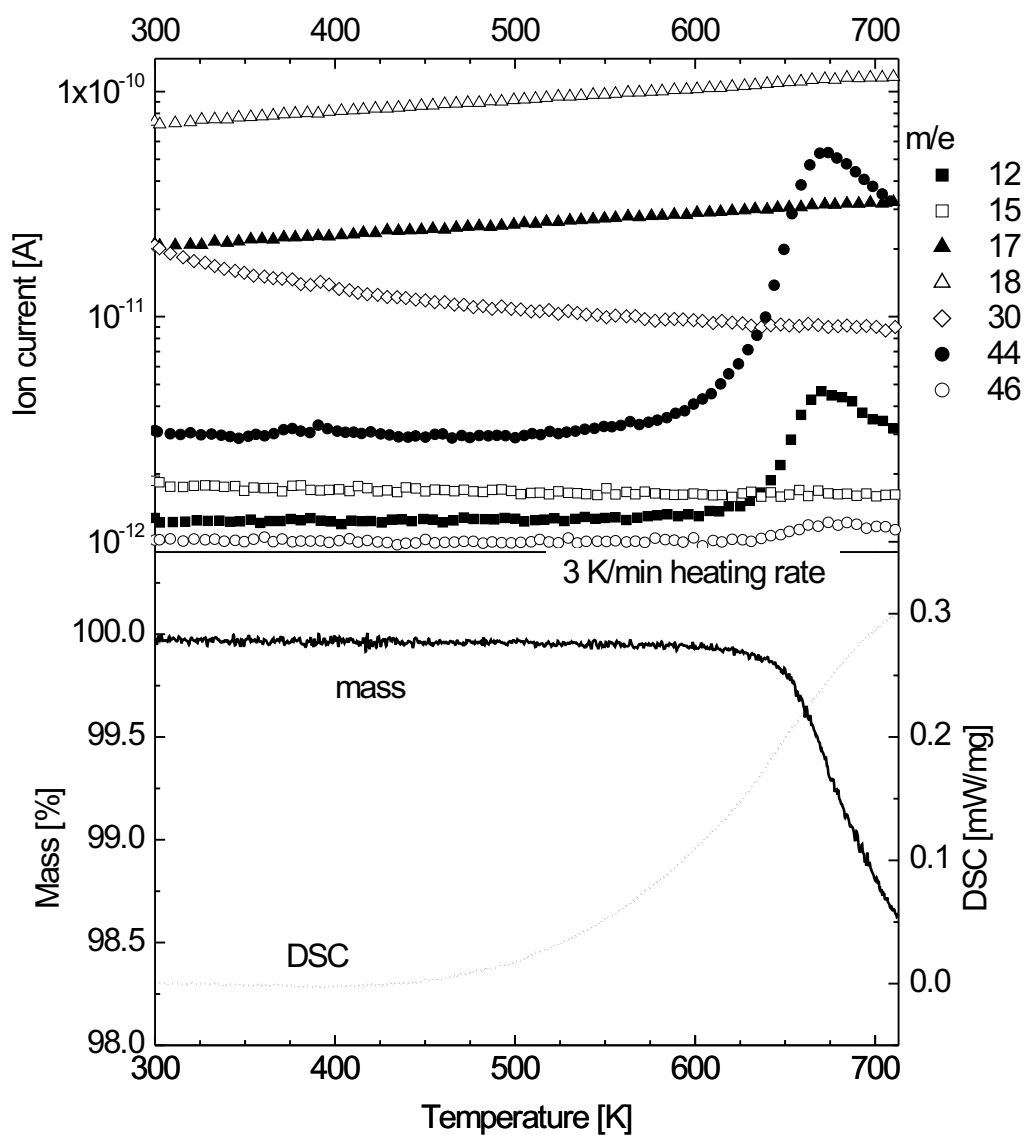


Figure 5.51: TG/ DSC and MS signals of *MoVW* oxide precursor during heating in 100% helium to 713 K at a heating rate of 3 K/min.

TG/ DSC with heating rate 1 K/min

The calcination of (*MoVW*) oxide precursor was performed in 20% oxygen/ nitrogen and thermal treatment in 100% helium at a heating rate of 1 K/min. The signals obtained in TG/ DSC measurements and online gas analysis during heating in both atmospheres are shown in Figures 5.52 and 5.53. These data can be directly com-

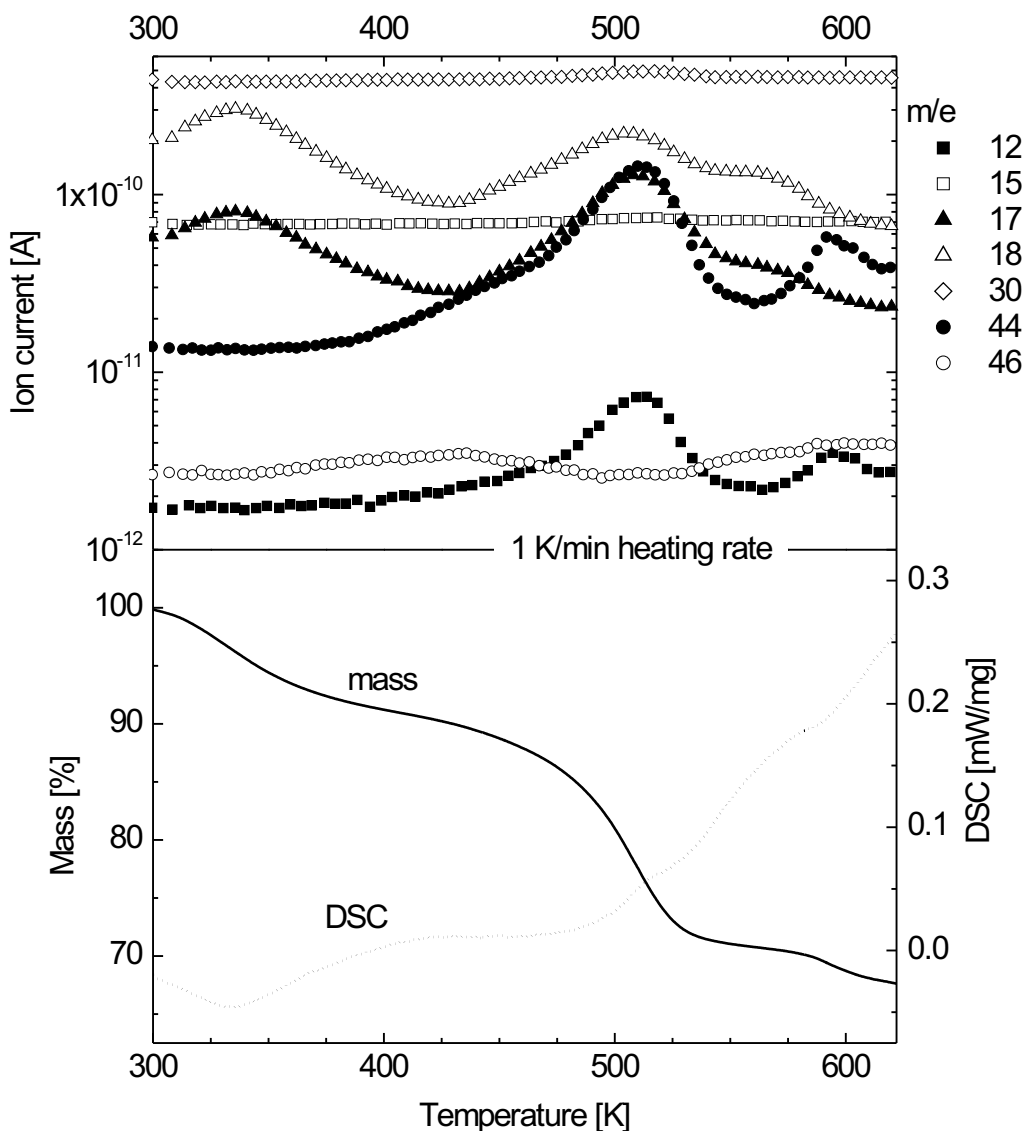


Figure 5.52: TG/ DSC and MS signals of *MoVW* oxide precursor during heating in 20% oxygen/ nitrogen to 623 K at a heating rate of 1 K/min.

pared to the XAFS measurements at the Mo *K*, V *K*, and W *L_{III}* edge described in Paragraph 5.1.3.

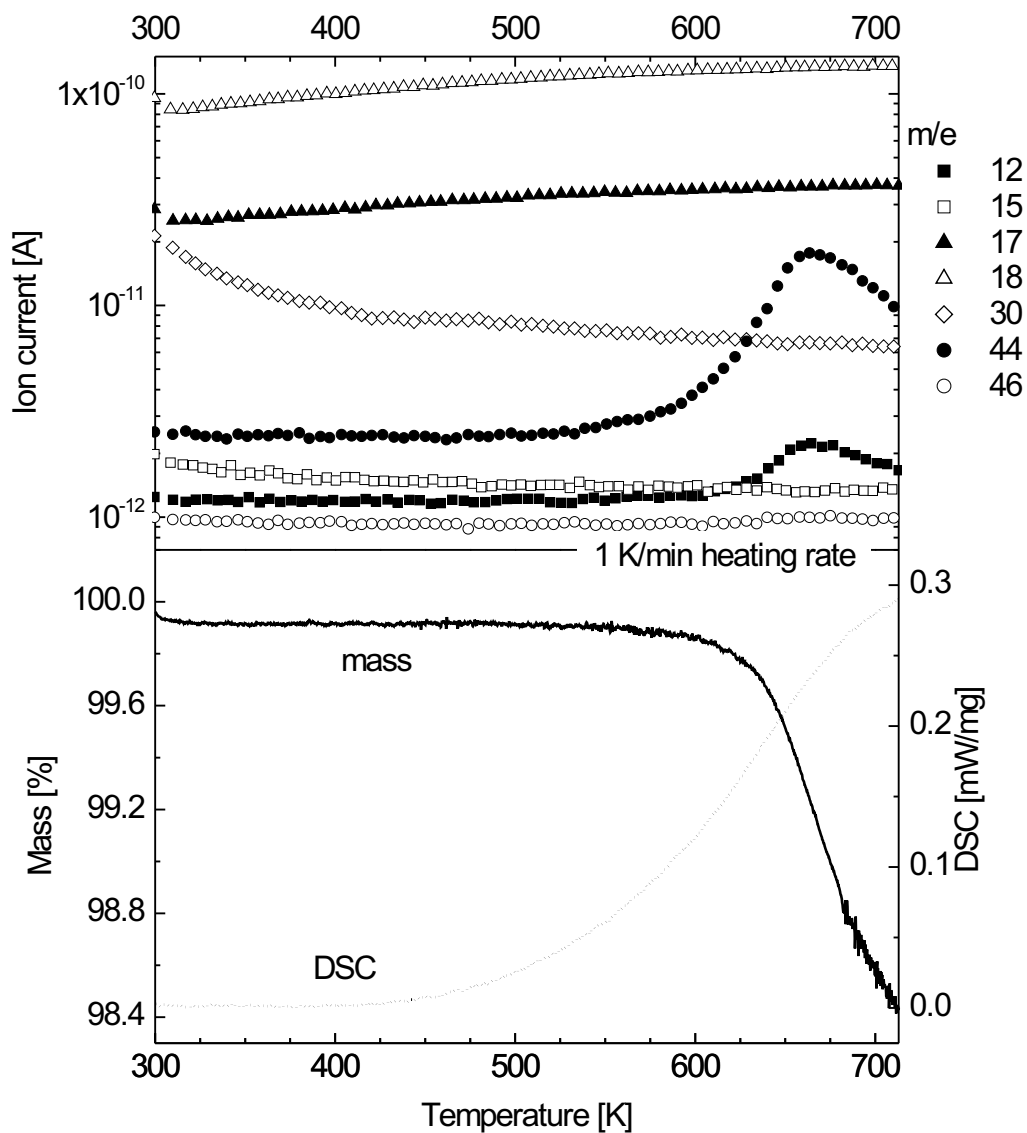


Figure 5.53: TG/ DSC and MS signals of *MoVW* oxide precursor during heating in 100% helium to 713 K at a heating rate of 1 K/min.

TG/ DSC kinetic analysis of calcination

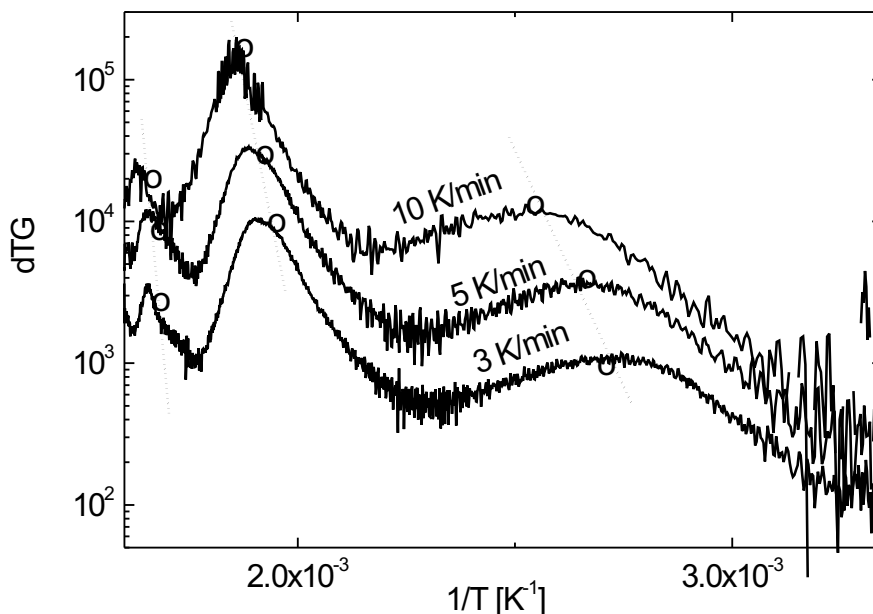


Figure 5.54: Friedman plot: 1st derivative of TG curve over reciprocal temperature during heating of *MoVW* oxide precursor in 20% oxygen/ nitrogen to 623 K. Points of equal partial mass loss are indicated by circles and connected with a line.

Data obtained at heating rates 10 K/min, 5 K/min, and 3 K/min are used for kinetic analysis of the first calcination step of *MoVW* oxide precursor. Three steps of mass loss appear in the TG curves and its derivatives are shown in Figure 5.54. Points of equal partial mass loss are indicated by circles and connected with a line. More information can be extracted using the DSC curve where four signals can be distinguished. Therefore, the Arrhenius plots shown in Figure 5.55 present the maximum change in the DSC curve over the corresponding reciprocal temperature. In a linear fit activation energies of 19 kJ/mol (endothermic 1st step of mass loss), 38 kJ/mol (endothermic event during 2nd step of mass loss), 173 kJ/mol (exothermic event during 2nd step of mass loss), and 121 kJ/mol (exothermic 3rd step of mass loss) are calculated from the slope.

In a model free analysis the activation energies (listed in Table 5.5) were determined by Friedman-analysis on the TG curves. The TG curves exhibit three distinct decomposition steps, but the calculated activation energies exhibit two different activation energies in the range of the second decomposition step. Figure 5.56 shows activation energies determined by Friedman-analysis of TG traces as a function of partial mass loss. A TG trace (10 K/min) is shown for assignment of E_{akt} to certain steps of mass

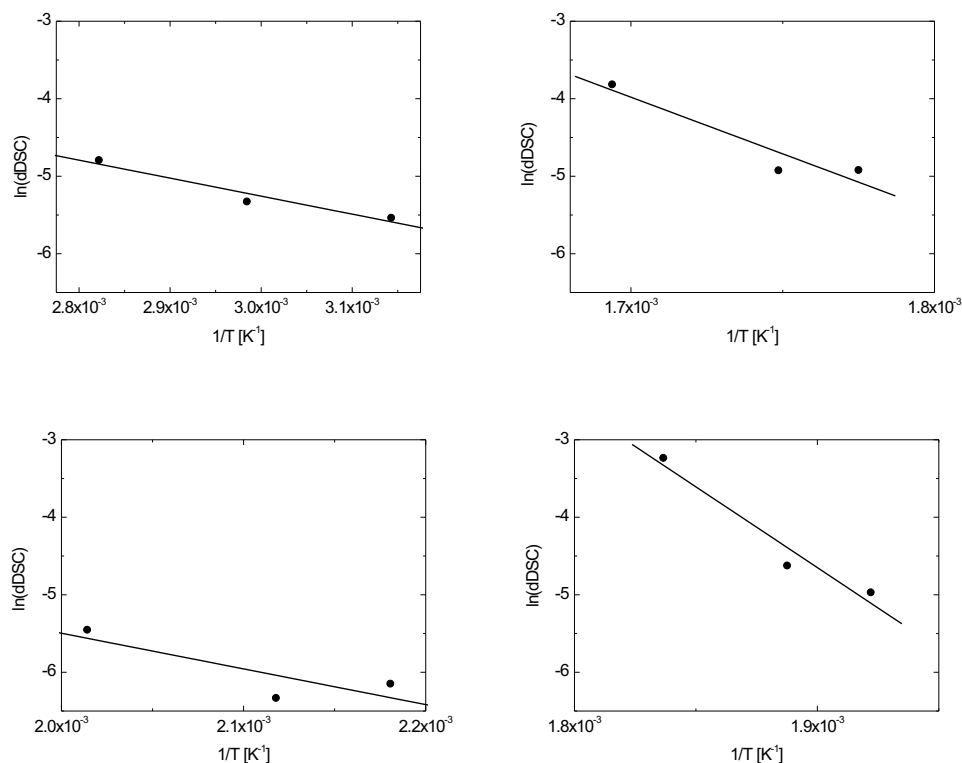


Figure 5.55: Arrhenius relation of maximum change in the DSC curve over the corresponding reciprocal temperature. Upper graphs: endothermic 1st step of mass loss (left) and exothermic 3rd step of mass loss (right), lower graphs: endothermic (left) and exothermic (right) event during 2nd step of mass loss.

loss. In the range of the first and second decomposition step the partial mass loss proceeds with three different regimes of activation energy. At a fractional mass loss of 0.05-0.2 the activation energy is about 130 kJ/mol (first decomposition step). Then at partial mass loss 0.3-0.5 E_{akt} is about 350 kJ/mol and at partial mass loss 0.6-0.7% E_{akt} reaches 460 kJ/mol, both corresponding to the second decomposition step. At higher mass loss in the range of the third decomposition step the values of the activation energy are less reliable due to increasing errors.

Partial mass loss	E_{akt} [kJ/mol]
0.02	144 (+- 28)
0.05	132 (+- 41)
0.10	131 (+- 40)
0.15	132 (+- 42)
0.20	128 (+- 50)
0.25	182 (+- 60)
0.30	286 (+- 23)
0.35	348 (+- 14)
0.40	372 (+- 26)
0.45	345 (+- 26)
0.50	366 (+- 46)
0.55	394 (+- 88)
0.60	455 (+- 78)
0.65	483 (+- 99)
0.70	476 (+- 107)
0.75	417 (+- 175)
0.80	269 (+- 264)
0.85	-84 (+- 248)
0.90	-5 (+- 228)
0.95	521 (+- 321)
0.98	2088 (+- 1455)

Table 5.5: List of activation energies from model-free Friedman-analysis. E_{akt} for each step of partial mass loss. The calculation is based on TG/ DSC experiments in 20% oxygen/ nitrogen at heating rates 3 K/min, 5 K/min, and 10 K/min.

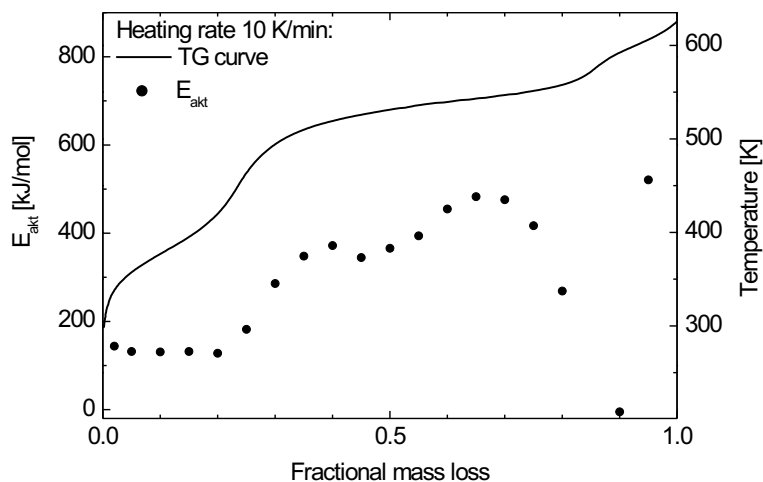


Figure 5.56: Activation energy values determined by Friedman-analysis as a function of partial mass loss during heating of *MoVW* oxide precursor in 20% oxygen/ nitrogen to 623 K. For assignment of E_{akt} to certain steps of mass loss a TG trace (10 K/min) is shown.

5.1.3 In situ XAS crystallization

Characterization of the precursor

For structural insight to the X-ray amorphous precursor material (Figure 5.1) the calcination was investigated by in situ XAS. The initial XANES and $\text{FT}(\chi(k) * k^3)$ of the *MoVW* oxide precursor is different from AHM (Figure 5.57). The narrow range of molybdenum-oxygen distances was refined with two single scattering distances of AHM (ICSD [4153]). For refinement one major *Mo* – *O* distance at ca. 1.70 Å and a minor contribution of a second *Mo* – *O* distance at ca. 2.0 Å (Table 5.6, crystallographic distances, in the FT distances are shifted by ca. 0.3 Å) were used. Not only in the *Mo* – *O* shell the EXAFS spectrum of the precursor shows strong deviations from AHM. In the molybdenum-metal shell of the precursor no remarkable amplitude is detectable (Figure 5.57).

	C.N.	σ [Å ³]	R [Å]
Mo-O	5	0.0078	1.753
Mo-O	1	0.0084	2.016

Table 5.6: Results obtained from refinement of two *Mo* – *O* distances to $\text{FT}(\chi(k) * k^3)$ of *MoVW* oxide precursor measured at the Mo *K* edge. $E_0 = 1$ eV, $\theta_D = 535$ K.

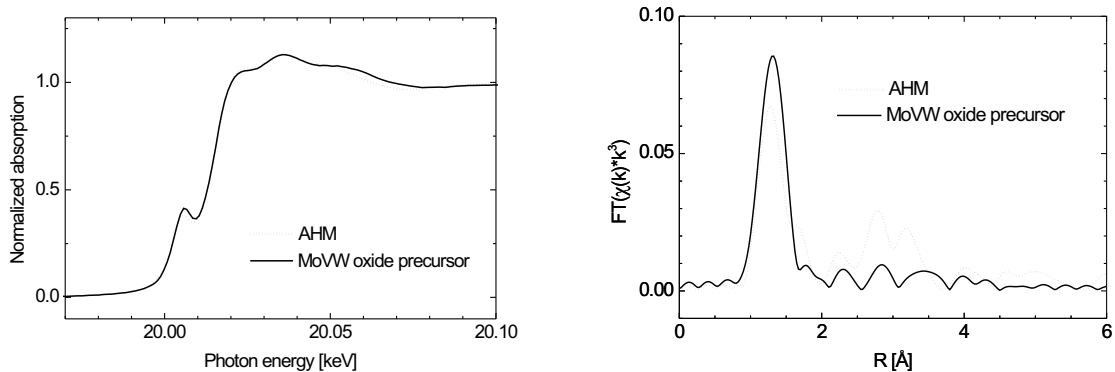


Figure 5.57: Mo *K* edge XANES spectra (left) and $\text{FT}(\chi(k) * k^3)$ (right) of *MoVW* oxide precursor compared to AHM.

At the W *L*_{III} edge shown in Figure 5.58 the $\text{FT}(\chi(k) * k^3)$ of the precursor compared to APT shows different features than the reactant used for preparation. Particularly the distribution of W – O distances differs. To come closer to the structural characteristics of the *MoVW* oxide precursor the W – O shell of the $\text{FT}(\chi(k) * k^3)$ of the precursor was refined with two single scattering paths of APT (ICSD [15237]). The refinement results are listed in Table 5.7. In the precursor the tungsten-oxygen distances show a similar bond length distribution compared to molybdenum-oxygen distances, but different coordination numbers.

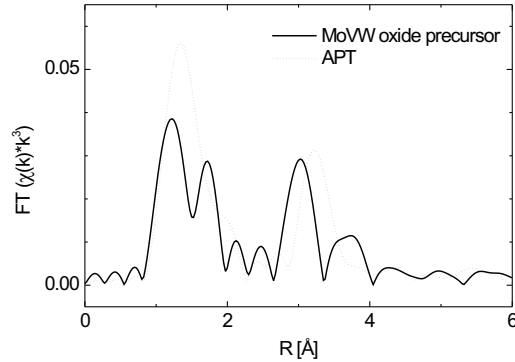


Figure 5.58: $\text{FT}(\chi(k) * k^3)$ of *MoVW* oxide precursor measured at the W L_{III} edge compared to APT.

	C.N.	σ [\AA^3]	R [\AA]
W-O	2.8	0.0062	1.749
W-O	3.2	0.0067	1.949

Table 5.7: Refinement results of two $W - O$ single scattering distances refined to $\text{FT}(\chi(k) * k^3)$ of the *MoVW* oxide precursor measured at the W L_{III} edge. $E_0 = 1$ eV, $\theta_D = 619$ K.

Crystallization at Mo K edge

In the XANES shown in Figure 5.59 changes during calcination in 20% oxygen/ nitrogen are not as obvious as in the $\text{FT}(\chi(k) * k^3)$ shown in Figure 5.61. The XANES spectra taken after the first and second calcination step show a diminishing of the pre-edge peak (Figure 5.60). During calcination in 20% oxygen/ nitrogen the metal-oxygen coordination sphere in the $\text{FT}(\chi(k) * k^3)$ of $(\text{MoVW})_5\text{O}_{14}$ changes compared to the precursor material. The $\text{Mo} - \text{O}$ shell of the entire temperature ramp can be described with two single scattering distances. At increasing temperature an increase in the amplitude is observed for the minor $\text{Mo} - \text{O}$ distance at ca. 2.0 \AA . The divergence in the metal-oxygen distances increases and can be assigned to the structural rearrangement from the precursor material to the Mo_5O_{14} -type structure.

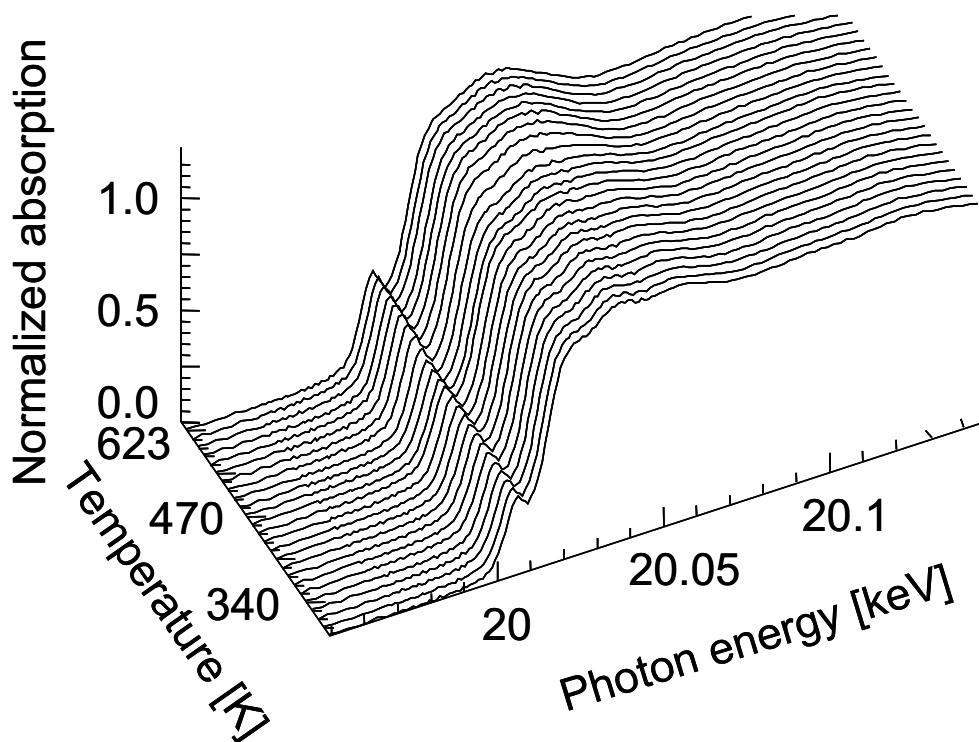


Figure 5.59: In situ XANES at the Mo *K* edge of *MoVW* oxide precursor during heating in 20% oxygen/ nitrogen to 623 K at a heating rate of 1 K/min.

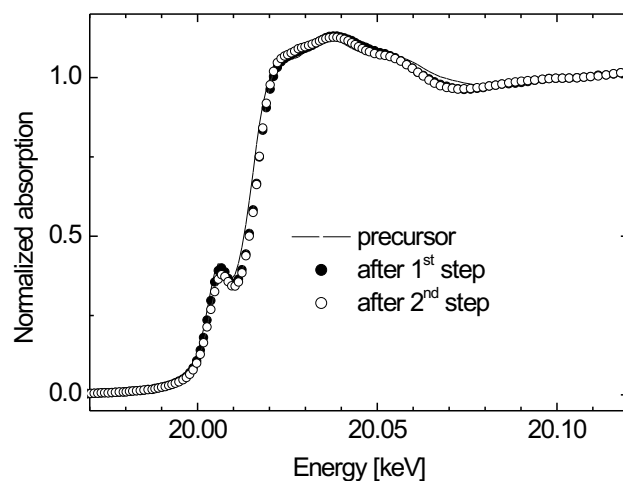


Figure 5.60: XANES comparison of *MoVW* oxide precursor to product after first calcination and second treatment in helium.

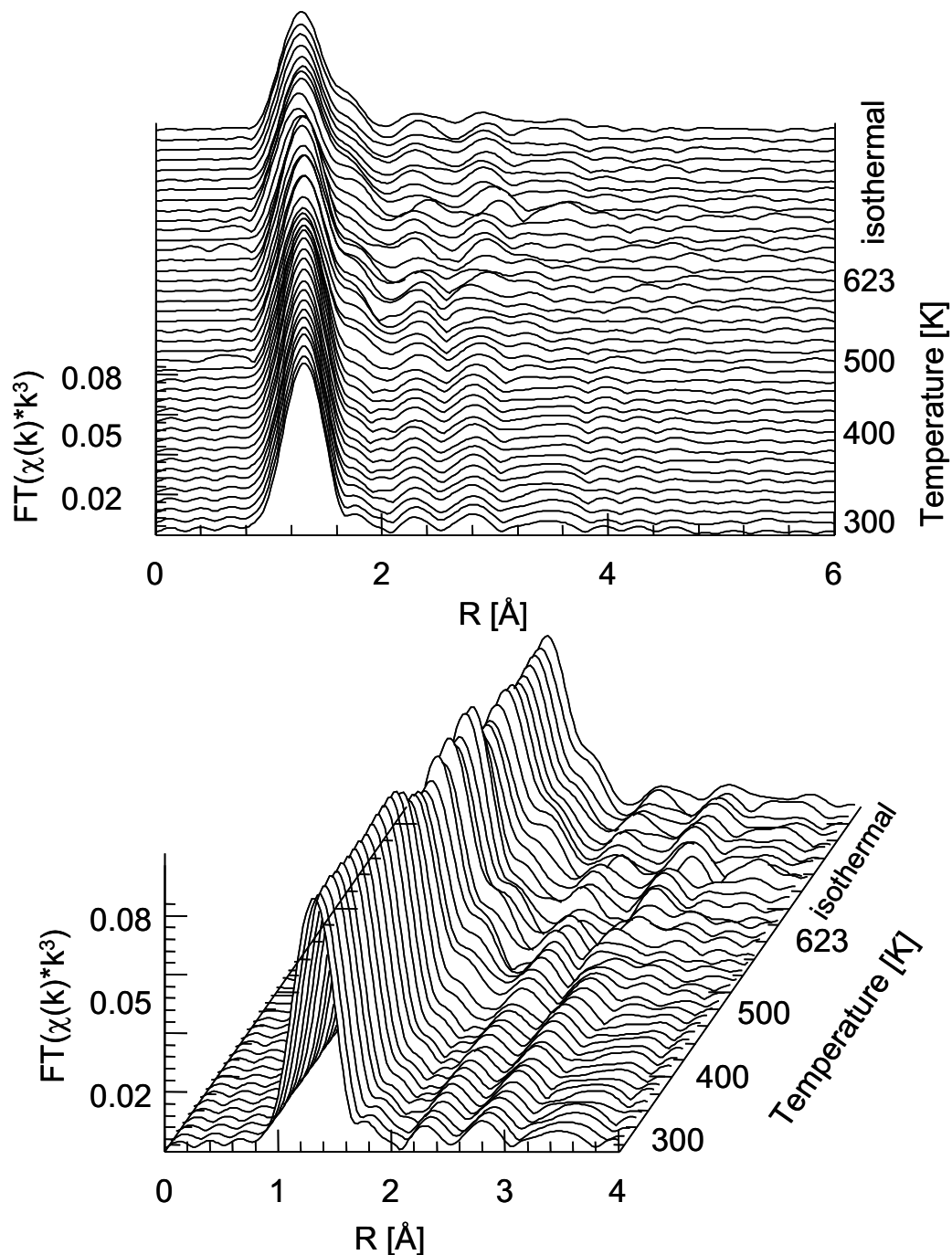


Figure 5.61: Front view and side view on changes in $FT(\chi(k) * k^3)$ of MoVW oxide precursor during treatment in 20% oxygen/ nitrogen at the Mo *K* edge.

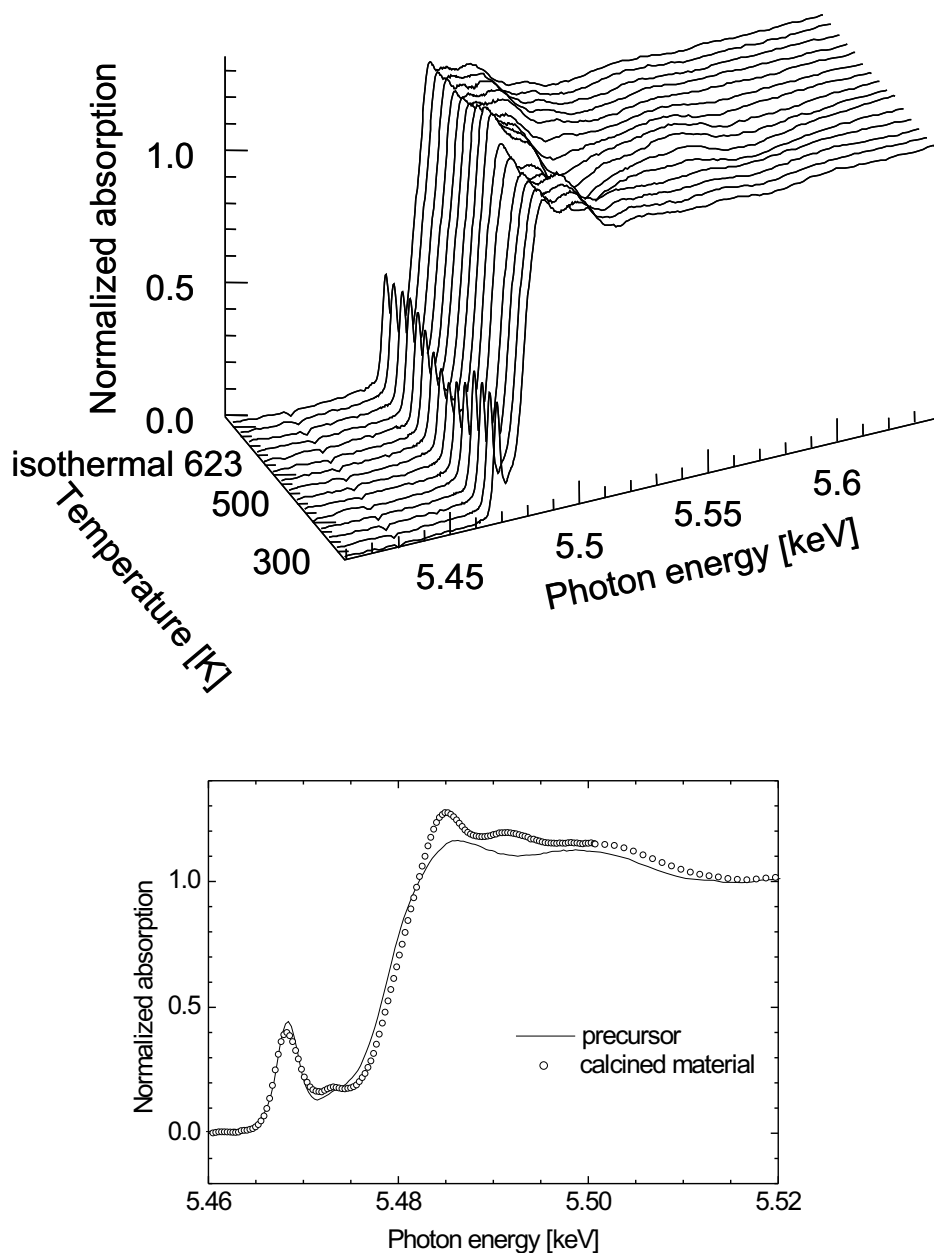
Crystallization at V *K* edge

Figure 5.62: In situ XANES spectra at the V *K* edge during treatment in 20% oxygen/nitrogen of *MoVW* oxide precursor (upper). XANES comparison of *MoVW* oxide precursor to calcined material (lower).

Changes in the XANES spectra taken at the V *K* edge during the first calcination step are shown in Figure 5.62. As a characteristic feature the pre-edge peak goes through a minimum at about 470 K during the first calcination step. At higher heating rate

(10 K/min) the pre-edge peak height minimum is lower but according to the faster heating the time resolution of the XANES becomes worse. Appreciable differences occur in XANES spectra taken before and after the first calcination step. The XANES spectrum of the precursor shows two strong transitions in the edge. The XANES after the first calcination step is composed of three transitions. In the material obtained after the first calcination step the pre-edge peak height is reduced and a transition between pre-edge peak and the edge appears.

Crystallization at W L_{III} edge

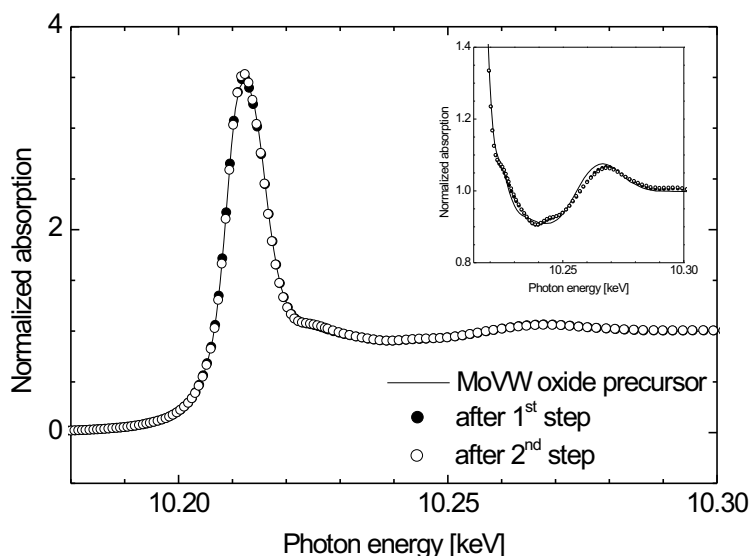


Figure 5.63: XANES comparison of *MoVW* oxide precursor to product after first calcination and second treatment in helium.

As shown in Figure 5.64 the XANES at the W L_{III} edge hardly changes. The evolution of the W L_{III} edge $FT(\chi(k)*k^3)$ during thermal treatment of the precursor in 20% oxygen/nitrogen in the temperature range from 300 K to 623 K are shown in Figure 5.65. While the amplitude of the $FT(\chi(k)*k^3)$ remains nearly constant up to about 450 K, strong changes in amplitude above 450 K indicate several decomposition steps. Analysis of the two oxygen shells in the W L_{III} edge $FT(\chi(k)*k^3)$ resulted in a shortening of nearest-neighbor distances between 400 K and 550 K followed by an increase above 550 K. At ca. 550 K the amplitude has a intermediate maximum. In the tungsten-metal shell the distances shorten in the temperature range from 400 K to 550 K. Then, above 550 K the tungsten-metal distances lengthen up to the initial value.

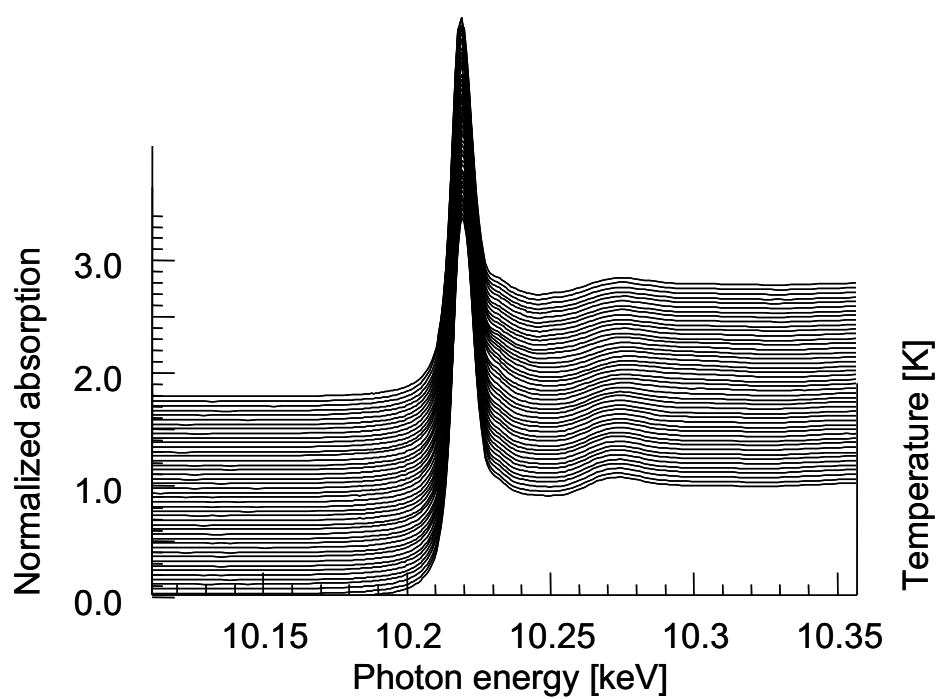


Figure 5.64: In situ XANES spectra at the W L_{III} edge during treatment in 20% oxygen/ nitrogen of *MoVW* oxide precursor.

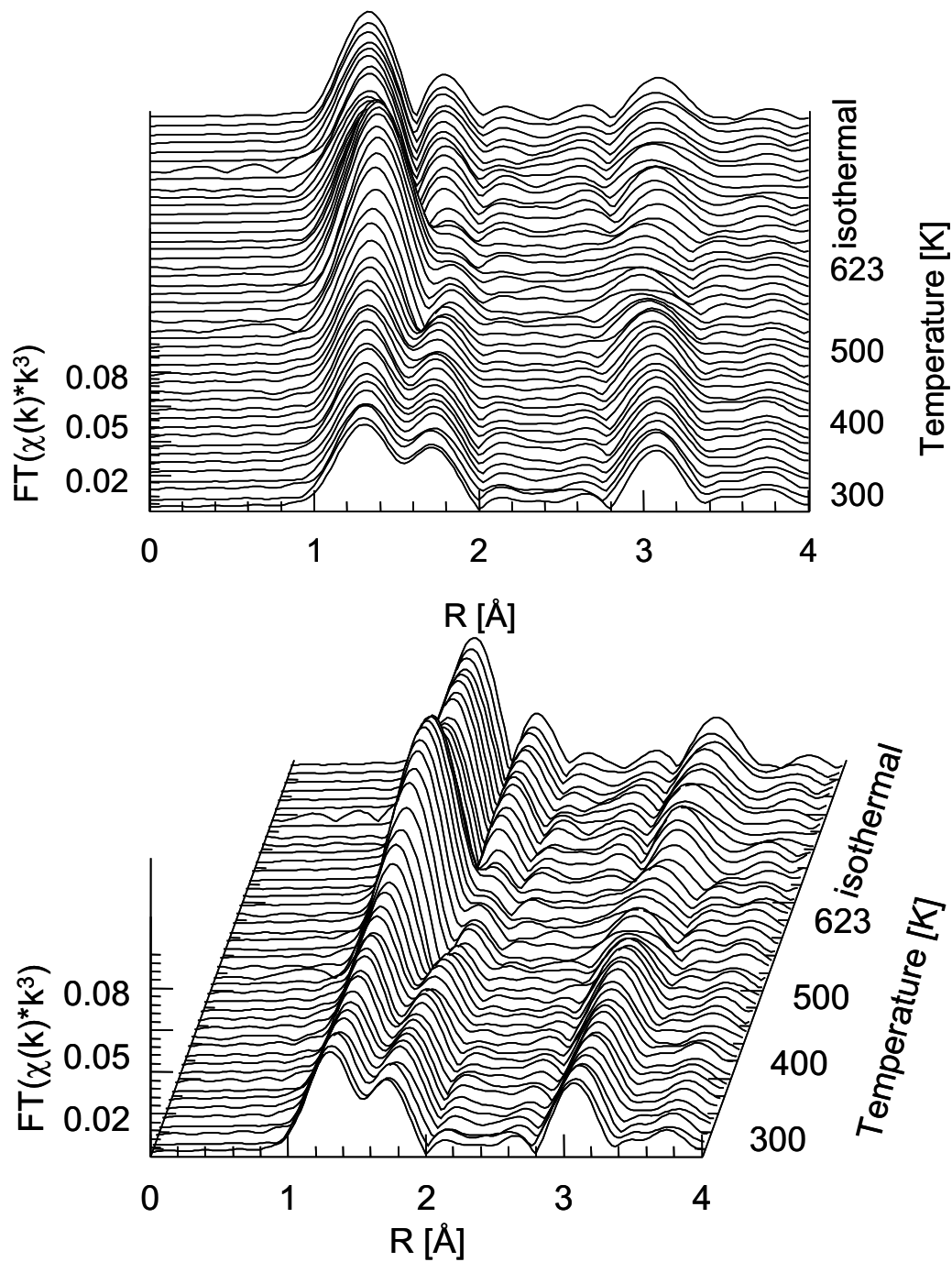


Figure 5.65: Front view and side view on changes in $FT(\chi(k) * k^3)$ of MoVW oxide precursor during treatment in 20% oxygen/ nitrogen at the W L_{III} edge.

Comparison of XAS from all edges

Generally, the XANES and EXAFS spectra of the precursor are different from the spectra of the product after the first thermal treatment step. Figure 5.60 shows that the Mo *K* edge XANES spectrum of the precursor differs from the XANES spectra of

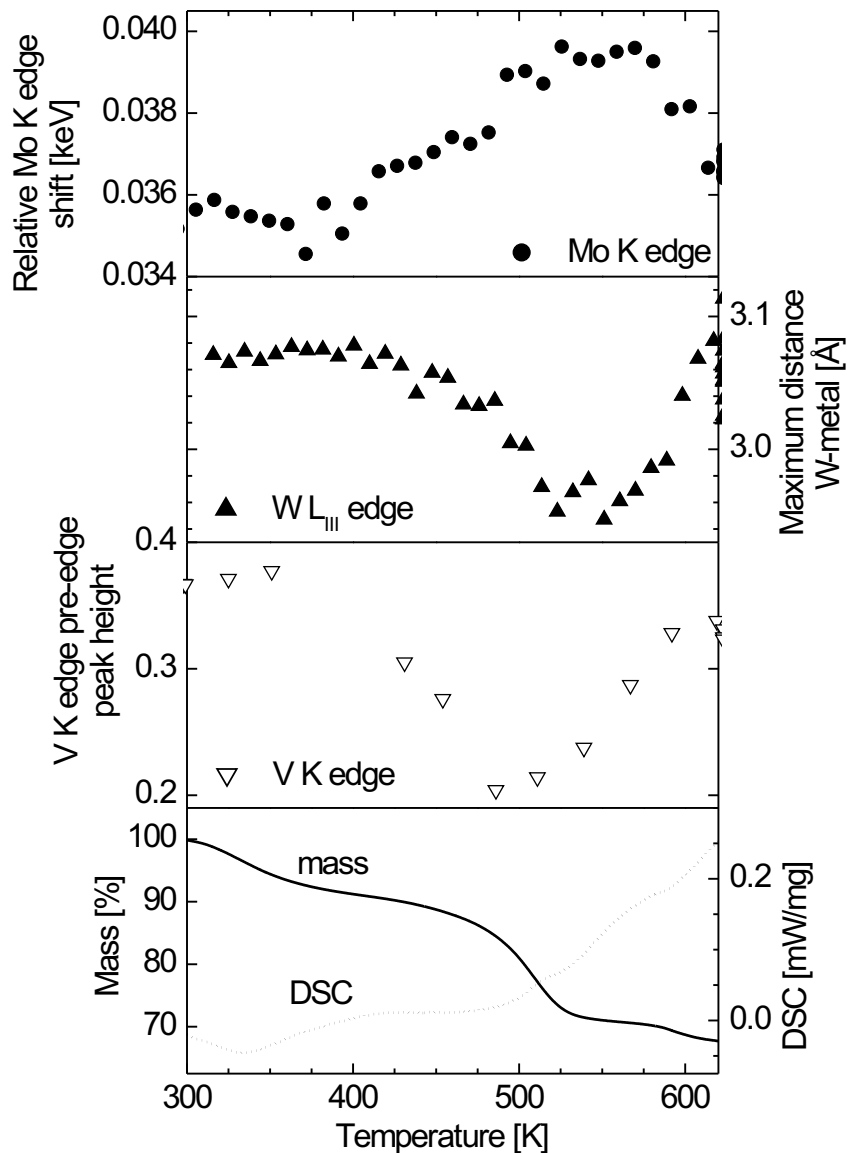


Figure 5.66: Correlation of TG/ DSC signal curves with structural changes of *MoVW* oxide precursor in 20% oxygen/ nitrogen at 1 K/min heating rate at Mo *K* edge, V *K* edge, and W *L_{III}* edge.

the products obtained after thermal treatment of the precursor at 623 K and 713 K. Conversely, the XANES spectrum of the sample obtained after thermal treatment at 623 K that is very similar to that of the sample obtained after treatment at 713 K. This comparison holds not only for the Mo *K* edge, but also for the V *K* edge (Figure 5.62) and the W *L_{III}* edge (Figure 5.64).

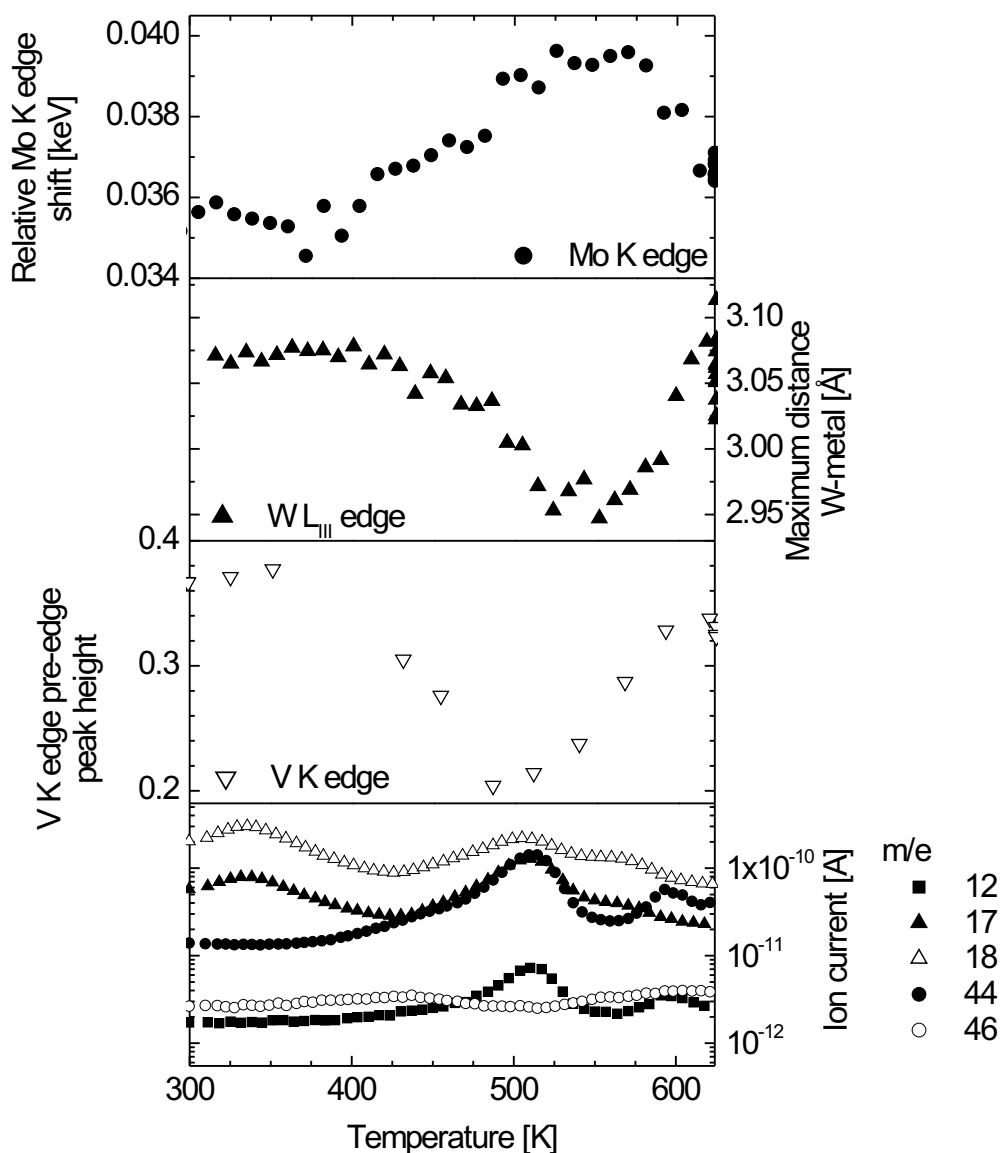


Figure 5.67: Correlation of MS curves measured in TG/ DSC with structural changes of *MoVW* oxide precursor in 20% oxygen/ nitrogen at 1 K/min heating rate at Mo *K* edge, V *K* edge, and W *L_{III}* edge.

Changes during the first calcination step obtained on all three edges are correlated in Figure 5.66 to TG/ DSC data obtained at the same heating rate. The XAS and TG data were measured at a heating rate of 1 K/min. Therefore, temperature differences of 10 or 20 K in Figures 5.66 and 5.67 are real. From this a sequence of events during structural rearrangement can be extracted. The structural changes begin at about 400 K on all edges. This corresponds to the second decomposition step in TG/ DSC which is the decomposition step with highest mass loss. The structural rearrangement starts with the major structural changes around vanadium. First the pre-edge peak height of vanadium reaches its minimum. As the pre-edge peak of vanadium starts increasing again the structural changes at the Mo K and W L_{III} edges reach their turning point.

5.2 XRD structural investigation of $(MoVW)_5 O_{14}$ and $(MoV)_5 O_{14}$

Structure and phase purity of $(MoVW)_5 O_{14}$ and $(MoV)_5 O_{14}$ were verified by XRD. The experimental and theoretical XRD pattern of $(MoVW)_5 O_{14}$ and $(MoV)_5 O_{14}$ shown in Figure 5.68 and 5.69, respectively, and the difference curves are displayed. A schematic representation of the metal sites in the Mo_5O_{14} -type structure is shown in Figure 4.5. The calculated patterns were obtained from a Rietveld refinement of the Mo_5O_{14} -type structure ICSD [27202] to the experimental pattern of the crystalline Mo_5O_{14} -type material. Atomic coordinates were not refined. The good agreement between theory and experiment confirms the absence of additional crystalline phases or superstructures. Moreover, the presence of detectable amounts of amorphous phases was excluded by XRD analysis of a mixture of 50% $(MoVW)_5 O_{14}$ and 50% $\alpha-Al_2O_3$ as internal standard.

The lattice constants and site occupancy factors obtained from the refinement of the Mo_5O_{14} -type structure model are listed in Table 5.8. In case of $(MoV)_5 O_{14}$ the alternative refinement of ' Mo_5O_{14} ' + ' V_5O_{14} ' showed nearly the same difference curve and quality parameters as the refinement of site occupancy factors. In case of $(MoVW)_5 O_{14}$ the alternative refinement of ' Mo_5O_{14} ' + ' V_5O_{14} ' + ' W_5O_{14} ' resulted in a significantly worse description of the experimental XRD pattern than the refinement of site occupancy factors. In the difference curve between the experimental pattern and the calculated pattern of ' Mo_5O_{14} ' + ' V_5O_{14} ' + ' W_5O_{14} ' appeared unaccounted intensity. Especially the intensity of the peaks (020) and (210) are calculated lower than experimentally obtained.

	' Mo_5O_{14} ' + ' V_5O_{14} '	$(MoV)_5 O_{14}$	$(MoVW)_5 O_{14}$	' Mo_5O_{14} ' + ' V_5O_{14} ' + ' W_5O_{14} '
Rwp	11.30	11.14	12.90	14.67
GoF	1.69	1.67	1.19	1.36
a [Å]	22.88	22.88	22.76	22.76
c [Å]	4.00	4.00	3.99	3.99
Mo1	-	0.5122	0.6023	-
Mo2	-	0.5016	0.5056	-
Mo3	-	0.4634	0.4395	-
Mo4	-	0.4852	0.4903	-
Mo5	-	0.4853	0.5159	-
Mo6	-	0.4832	0.5416	-
Crystallite size [nm]	-	196.7	434.6	-
Wt%(Mo)- Rietveld	78	-	-	56
Wt%(V)- Rietveld	22	-	-	33
Wt%(W)- Rietveld	-	-	-	11

Table 5.8: Parameters obtained from structure model (ICSD [27202]) refined to experimental XRD powder pattern of tetragonal $(MoVW)_5 O_{14}$ and $(MoV)_5 O_{14}$.

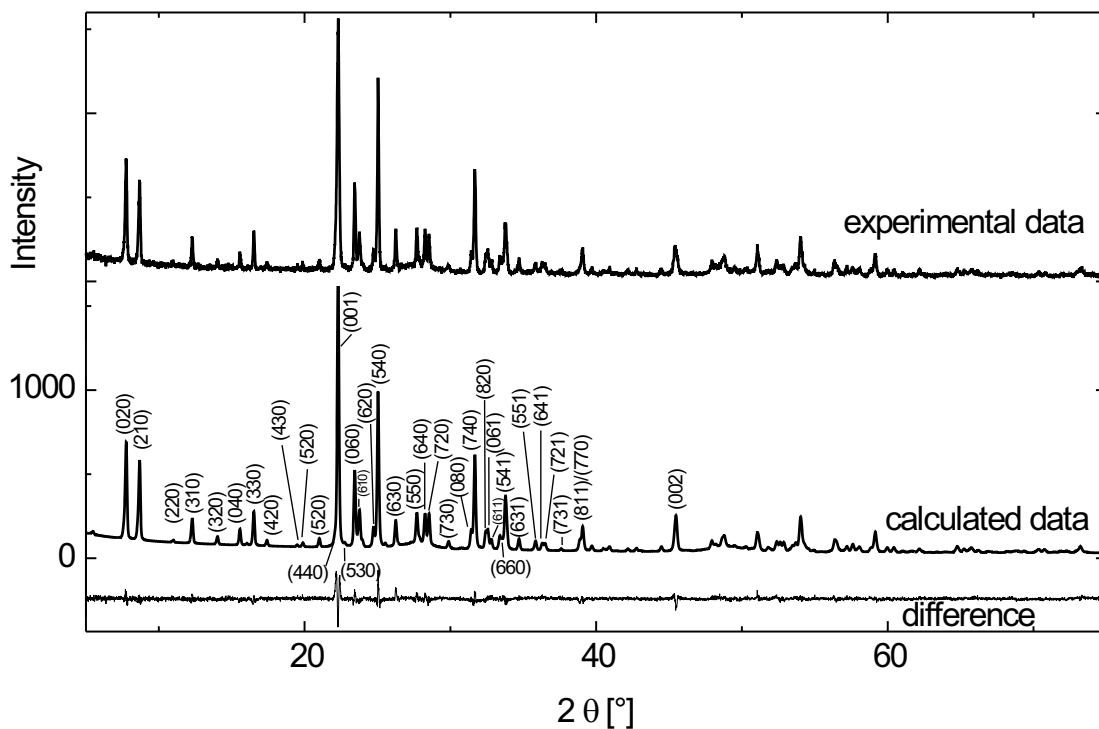


Figure 5.68: Experimental XRD pattern of crystalline $(MoVW)_5O_{14}$ together with a theoretical XRD pattern obtained from a Rietveld refinement of a Mo_5O_{14} -type structure model (ICSD [27202]).

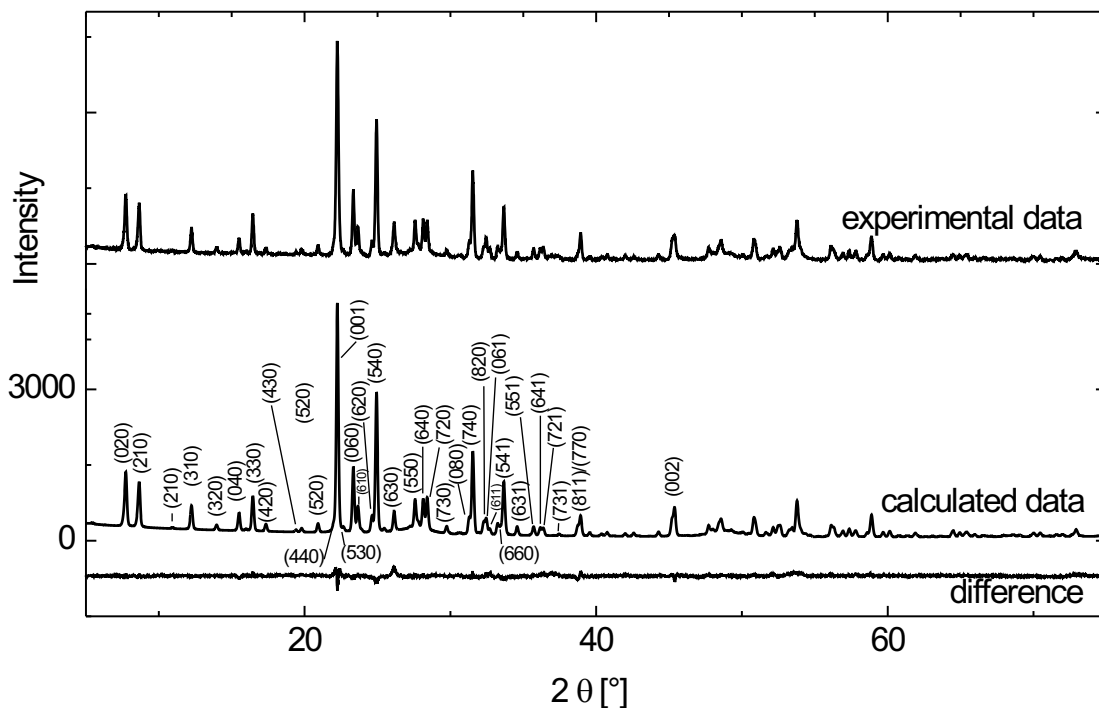


Figure 5.69: Experimental XRD pattern of crystalline $(MoV)_5O_{14}$ together with a theoretical XRD pattern obtained from a Rietveld refinement of a Mo_5O_{14} -type structure model (ICSD [27202]).

5.3 XAS structural investigation of $(MoVW)_5 O_{14}$ and $(MoV)_5 O_{14}$

5.3.1 Refinement strategy

The listing in Table 4.3 covers four constructed $\chi(k)$ with variable contribution from thermal and structural disorder. The following results shown in Figures 5.73 and 5.74 were obtained from refining the model of average distances to the four simulated $\chi(k)$ listed in Tables 5.9-5.12 with variable contribution from thermal and structural (dis)order. The increase or decrease in the coordination numbers obtained from the refined XAFS structure model refers to the average coordination numbers due to the XRD structure. In a structurally disordered but not thermally disordered system (S1, Table 4.3) the effect of averaging the distances in the structure model decreases the Debye temperature and the coordination numbers. In a structurally and thermally disordered system (S3) the effect of thermal disorder increases the coordination numbers in the metal-oxygen and metal-metal shell. In a structurally and not thermally disordered system (S2) the effect of averaging decreases the Debye temperature and increases the coordination numbers of the metal-oxygen and metal-metal shell. In a structurally ordered but thermally disordered system (S4) the effect of thermal disorder increases the coordination numbers in the metal-oxygen shell, and decreases the coordination numbers in the metal-metal shell.

From the results of the structure model refined to the $\chi(k)$'s of the four simulated limiting cases it can be derived that if structural disorder dominates the system, high coordination numbers of metal-metal scattering paths indicate structural order. If thermal disorder dominates the system, high coordination numbers of metal-metal scattering paths indicate a homogeneous distribution of elements on all sites. The extent of thermal (dis)order can be estimated from the Debye temperature and the coordination number of the metal-oxygen shell. In all four simulated systems the Debye

		XRD		XAS			
Mo-O		$R_{average}$ [Å]	C.N. $_{average}$	$R_{average}$ [Å]	C.N. $_{average}$		
short	1.697-1.775 Å	1.7197	1.67	1.7470	2.10		
middle	1.837-2.204 Å	1.9936	3.5	2.0293	2.24		
long	2.300-2.318 Å	2.3067	1	2.3195	1.53		
			\sum 6.17		\sum 5.87		
		XRD		XAS		sum	
Mo-M		$R_{average}$ [Å]	C.N. $_{average}$	$R_{average}$ [Å]	C.N.Mo	C.N.V	C.N.
short	3.235-3.326 Å	3.2701	1.33	3.2744	1.78	0.21	1.99
middle	3.567-3.862 Å	3.6889	3.33	3.6844	1.74	0.07	1.81
long	3.947-3.998 Å	3.9938	2.3	3.9932	2.92	0.14	3.06
			\sum 6.96		\sum 6.44	0.42	6.86

Table 5.9: Model of average distances refined to simulation S1. $\chi(k)$ with structural disorder but thermally not disordered refined with the model of average distances. $E_0=1$ eV, $\theta_D(O)=987$ K, $\theta_D(Mo)=493$ K, $\theta_D(V)=600$ K

Mo-O		XRD	C.N. _{average}	XAS	C.N. _{average}		
		R _{average} [Å]		R _{average} [Å]			
short	1.697-1.775 Å	1.7197	1.67	1.7534	1.86		
middle	1.837-2.204 Å	1.9936	3.5	2.0245	2.53		
long	2.300-2.318 Å	2.3067	1	2.3164	2.05		
			∑ 6.17		∑ 6.44		
Mo-M		XRD	C.N. _{average}	XAS	C.N.Mo	C.N.V	sum C.N.
		R _{average} [Å]		R _{average} [Å]			
short	3.235-3.326 Å	3.2701	1.33	3.2692	0	0.67	0.67
middle	3.567-3.862 Å	3.6889	3.33	3.6610	2.4	0	2.40
long	3.947-3.998 Å	3.9938	2.3	3.9931	3.65	1.03	4.68
			∑ 6.96		∑ 6.05	1.70	7.75

Table 5.10: Model of average distances refined to simulation S2. $\chi(k)$ without thermal and structural disorder refined with the model of average distances. $E_0=-0.26$ eV, $\theta_D(O)=914$ K, $\theta_D(Mo)=541$ K, $\theta_D(V)=600$ K

Mo-O		XRD	C.N. _{average}	XAS	C.N. _{average}		
		R _{average} [Å]		R _{average} [Å]			
short	1.697-1.775 Å	1.7197	1.67	1.7523	2.40		
middle	1.837-2.204 Å	1.9936	3.5	2.0227	2.94		
long	2.300-2.318 Å	2.3067	1	2.2967	1.54		
			∑ 6.17		∑ 6.88		
Mo-M		XRD	C.N. _{average}	XAS	C.N.Mo	C.N.V	sum C.N.
		R _{average} [Å]		R _{average} [Å]			
short	3.235-3.326 Å	3.2701	1.33	3.2686	1.59	0.11	1.70
middle	3.567-3.862 Å	3.6889	3.33	3.6721	2.60	0.35	2.95
long	3.947-3.998 Å	3.9938	2.3	3.9874	2.43	0.17	2.60
			∑ 6.96		∑ 6.62	0.63	7.25

Table 5.11: Model of average distances refined to simulation S3. $\chi(k)$ with thermal and structural disorder refined with the model of average distances. $E_0=1$ eV, $\theta_D(O)=484$ K, $\theta_D(Mo)=264$ K, $\theta_D(V)=600$ K

Mo-O		XRD	C.N. _{average}	XAS	C.N. _{average}		
		R _{average} [Å]		R _{average} [Å]			
short	1.697-1.775 Å	1.7197	1.67	1.7609	2.54		
middle	1.837-2.204 Å	1.9936	3.5	2.0229	4.03		
long	2.300-2.318 Å	2.3067	1	2.2996	2.53		
			∑ 6.17		∑ 9.10		
Mo-M		XRD	C.N. _{average}	XAS	C.N.Mo	C.N.V	sum C.N.
		R _{average} [Å]		R _{average} [Å]			
short	3.235-3.326 Å	3.2701	1.33	3.2861	0.37	0.41	0.78
middle	3.567-3.862 Å	3.6889	3.33	3.6683	2.51	0	2.51
long	3.947-3.998 Å	3.9938	2.3	3.9968	2.47	0.04	2.51
			∑ 6.96		∑ 5.35	0.45	5.80

Table 5.12: Model of average distances refined to simulation S4. $\chi(k)$ with thermal disorder but structural order refined with the average distances. $E_0=1$ eV, $\theta_D(O)=454$ K, $\theta_D(Mo)=265$ K, $\theta_D(V)=445$ K

temperature of the minor metal component vanadium was the upper limit. It seems that due to the refinement strategy the high Debye temperature can be taken as an indicator for the minority component.

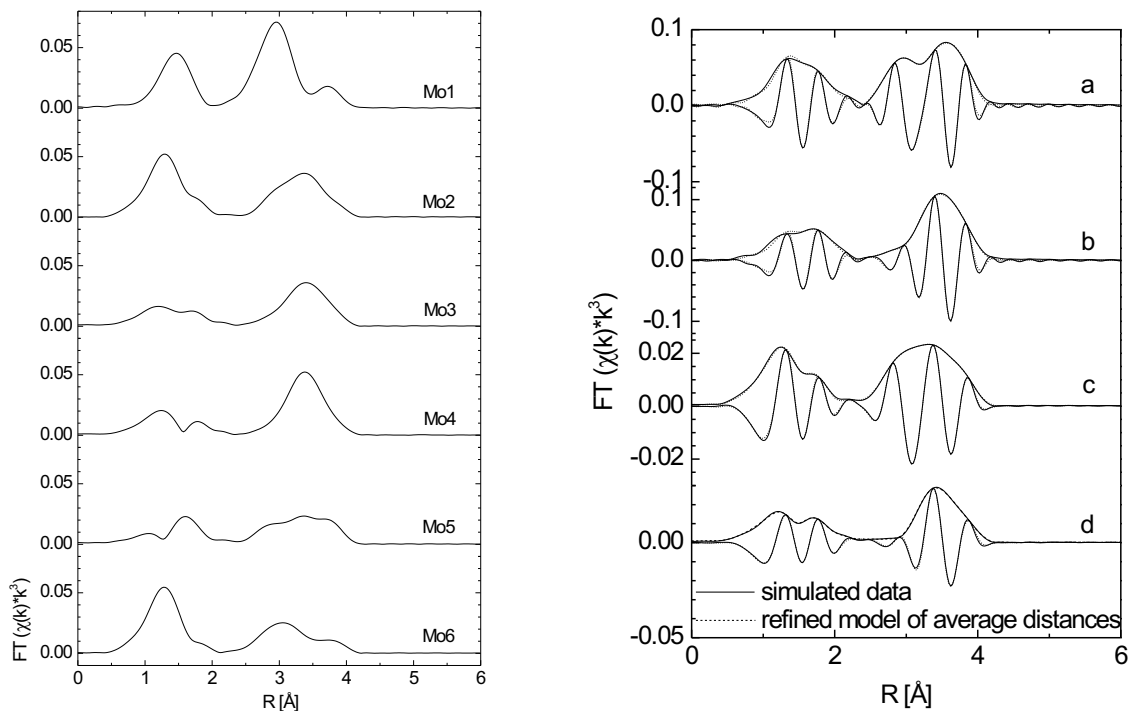


Figure 5.70: Left: simulation of molybdenum on all positions in the Mo_5O_{14} -type structure at a Debye temperature θ_D of 600 K for oxygen and 300 K for molybdenum. The $FT(\chi(k) * k^3)$ for each position is shown. Right: constructed data at the Mo K edge with refined model of average distances. a is simulation S1, b is simulation S2, c is simulation S3, d is simulation S4.

5.3.2 Refinement of $(MoVW)_5 O_{14}$ and $(MoV)_5 O_{14}$

	MoO_3 ICSD[35076] distances	$(MoVW)_5 O_{14}$ distance	$(MoVW)_5 O_{14}$ C.N.	$(MoV)_5 O_{14}$ distance	$(MoV)_5 O_{14}$ C.N.
Mo-O	1.671, 1.734	1.7466	3.12	1.7455	2.09
Mo-O	1.948	2.0161	2.14	2.0233	1.96
Mo-O	2.251, 2.332	2.3682	1.12	2.392	1.58
Mo-Mo	3.438	3.3366	1.34	3.3226	1.14
Mo-Mo	3.696	3.8042	2.44	3.786	1.89
Mo-Mo	3.963	-	-	4.0373	2.29
Mo-V	-	-	-	3.3174	0.42
Mo-V	-	3.7253	0.28	3.7367	1.20
Mo-V	-	-	-	4.0103	3.31
Mo-W	-	3.2937	0.10	-	-

Table 5.13: Parameters from XAFS single edge refinement at Mo K edge. $(MoVW)_5 O_{14}$: $E_0 = -1$ eV; $\theta_D(O) = 735$ K; $\theta_D(Mo) = 334$ K; $\theta_D(W) = 534$ K; $\theta_D(V) = 600$ K; $(MoV)_5 O_{14}$: $E_0 = -1$ eV; $\theta_D(O) = 735$ K; $\theta_D(Mo) = 469$ K; $\theta_D(V) = 520$ K.

	V_2O_5 ICSD[15984] distances	$(MoVW)_5 O_{14}$ distance	$(MoVW)_5 O_{14}$ C.N.	$(MoV)_5 O_{14}$ distance	$(MoV)_5 O_{14}$ C.N.
V-O	1.565, 1.745	1.6135	2.06	1.6138	0.89
V-O	1.763, 1.836	1.8015	1.58	1.9245	2.16
V-O	2.029, 2.835	1.9416	3.55	2.3706	2.11
V-Mo	-	-	-	3.3174	0.13
V-Mo	-	3.7253	2.26	3.7367	1.77
V-Mo	-	-	-	4.0103	0.45
V-V	-	3.7439	1.30	3.7592	1.95

Table 5.14: Parameters from XAFS single edge refinement at V K edge. $(MoVW)_5 O_{14}$: $E_0 = 1$ eV; $\theta_D(O) = 820$ K; $\theta_D(Mo) = 454$ K; $\theta_D(V) = 600$ K; $(MoV)_5 O_{14}$: $E_0 = -0.13$ eV; $\theta_D(O) = 835$ K; $\theta_D(Mo) = 553$ K; $\theta_D(V) = 600$ K.

	WO_3 ICSD[1620] distances		$(MoVW)_5 O_{14}$ distance	$(MoVW)_5 O_{14}$ C.N.
W-O	1.712, 1.735, 1.751, 1.751, 1.753, 1.773, 1.787, 1.796		1.7361	2.98
W-O	1.827, 1.853, 1.856, 1.882, 1.915, 1.935, 1.951, 1.975		1.9648	1.98
W-O	2.048, 2.055, 2.084, 2.115, 2.154, 2.172, 2.196, 2.212		2.2902	0.85
W-W	3.704, 3.715, 3.718, 3.728	W-Mo	3.2937	1.04
W-W	3.784, 3.793, 3.8, 3.804	-	-	-
W-W	3.814, 3.817, 3.863, 3.865	W-W	3.9340	1.09

Table 5.15: Parameters from XAFS single edge refinement at W L_{III} edge. $(MoVW)_5 O_{14}$: $E_0 = -1$ eV; $\theta_D(O) = 764$ K; $\theta_D(Mo) = 360$ K; $\theta_D(W) = 454$ K

The results of the structure model of average distances refined to the experimental $\chi(k)$ of $(MoVW)_5 O_{14}$ and $(MoV)_5 O_{14}$ are listed in Tables 5.13, 5.14 and 5.15. Figures 5.74 and 5.73 show the agreement of experimental $\chi(k)$ with the structure model. In $(MoVW)_5 O_{14}$ the most prominent molybdenum-oxygen distance (1.7466 Å) is

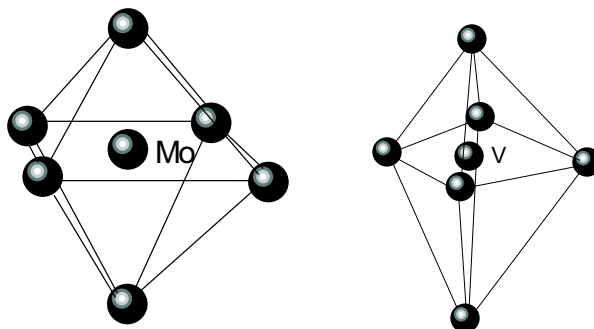


Figure 5.71: Coordination polyhedra around molybdenum centers (left) and vanadium centers (right) constructed from EXAFS structure model of average distances for $(MoV)_5 O_{14}$.

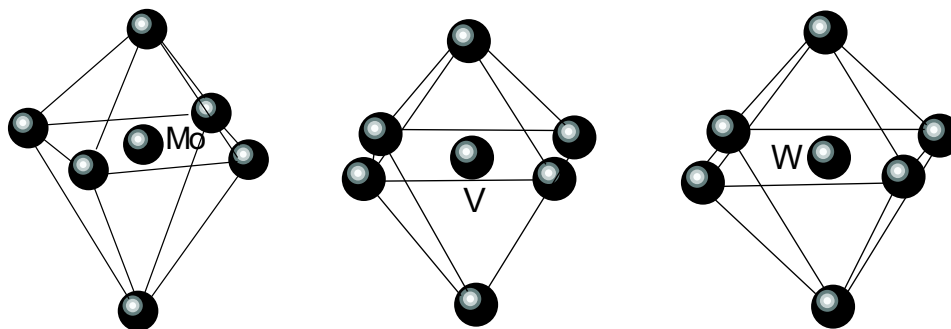


Figure 5.72: Coordination polyhedra around molybdenum centers (left), vanadium centers (center), and tungsten centers (right) constructed from EXAFS structure model of average distances for $(MoVW)_5 O_{14}$.

the shortest. In case of $(MoV)_5 O_{14}$ the two shorter molybdenum-oxygen distances (1.7455 Å and 2.0233 Å) are nearly equally represented. In both $Mo_5 O_{14}$ -type structures the trend to molybdenum-oxygen distances longer than in $\alpha\text{-}MoO_3$ is found (Table 5.13). The bond distance distribution and coordination numbers of tungsten-oxygen bonds is more alike to molybdenum-oxygen in $(MoVW)_5 O_{14}$ than to tungsten-oxygen distances in WO_3 (Table 5.15). The vanadium-oxygen distances in the $Mo_5 O_{14}$ -type structures are more regular than in $V_2 O_5$ (Table 5.14). Still, in $(MoV)_5 O_{14}$ the shortest (1.6138 Å) vanadium-oxygen distance is shorter than that of molybdenum-oxygen (1.7455 Å). In $(MoV)_5 O_{14}$ the middle vanadium-oxygen distance (1.9245 Å) is most prominent. In $(MoVW)_5 O_{14}$ the long vanadium-oxygen distance at about 2.3 Å is not detected.

Generally, the amplitudes of the metal-metal shell are strongly dampened at all edges measured for $(MoVW)_5 O_{14}$ compared to $(MoV)_5 O_{14}$. In $(MoVW)_5 O_{14}$ the short molybdenum-molybdenum distance (3.3366 Å) is shortened compared to $\alpha\text{-}MoO_3$

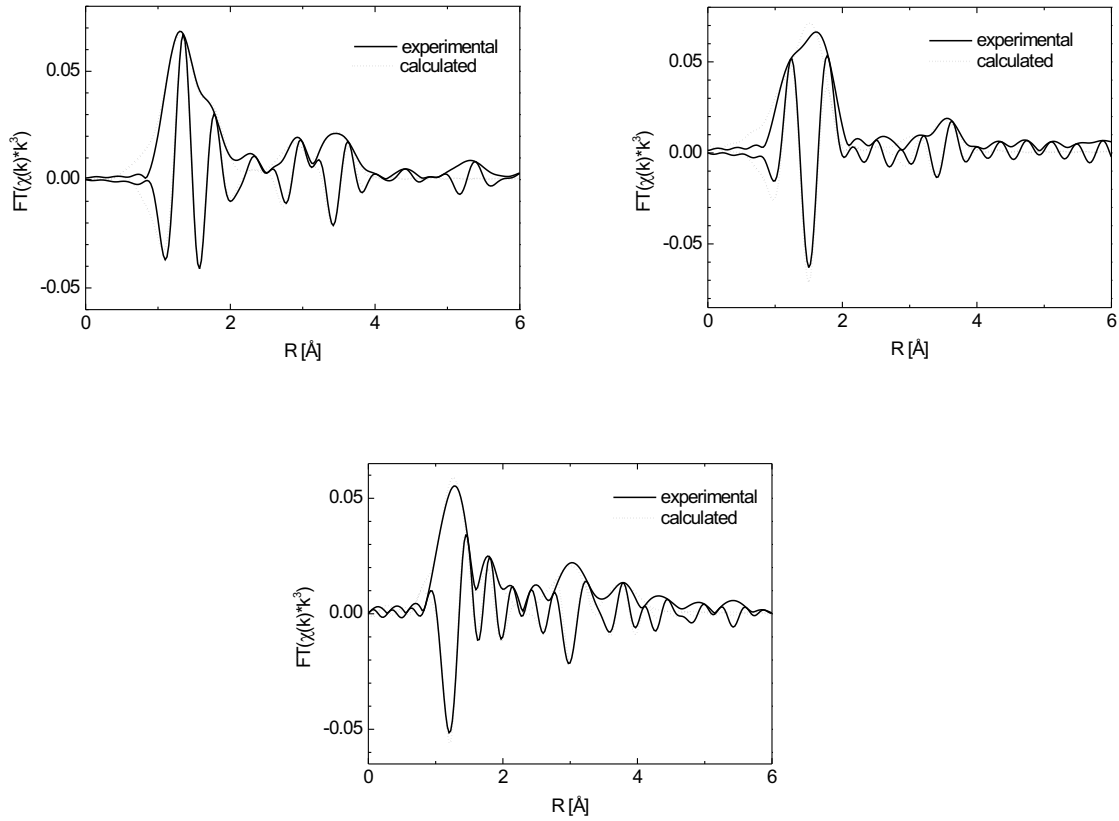


Figure 5.73: Experimental Mo K edge (left), (right), V K edge and W L_{III} edge (center) $\text{FT}(\chi(k) * k^3)$ of $(\text{MoVW})_5 \text{O}_{14}$ together with refined model of average distances.

(3.438 Å). The two longest molybdenum-molybdenum distances found in $\alpha\text{-MoO}_3$ (3.696 Å, 3.963 Å) appear as one distance at an average value of 3.8042 Å. In $(\text{MoVW})_5 \text{O}_{14}$ only the middle molybdenum-vanadium distance at 3.7253 Å is detectable. The 3.7253 Å molybdenum-vanadium distance in $(\text{MoVW})_5 \text{O}_{14}$ is shorter than the middle 3.7367 Å molybdenum-vanadium distance in $(\text{MoV})_5 \text{O}_{14}$. In $(\text{MoV})_5 \text{O}_{14}$ all three molybdenum-vanadium distances were detectable from analyzing both, the V K and Mo K edges. In all cases the molybdenum-vanadium distances are shorter than the corresponding molybdenum-molybdenum distances in $(\text{MoV})_5 \text{O}_{14}$. Still, the shortest molybdenum-vanadium distance in $(\text{MoV})_5 \text{O}_{14}$ (3.3174 Å) is significantly longer than the shortest vanadium-vanadium distance in V_2O_5 (3.058 Å, ICSD [15984]). In $(\text{MoVW})_5 \text{O}_{14}$ the short molybdenum-tungsten distance (3.2937 Å) is shorter than the shortest molybdenum-molybdenum distance (3.3366 Å). Compared to the distances of triclinic WO_3 (ICSD [1620]), the short molybdenum-tungsten distance in $(\text{MoVW})_5 \text{O}_{14}$ indicates a different structure.

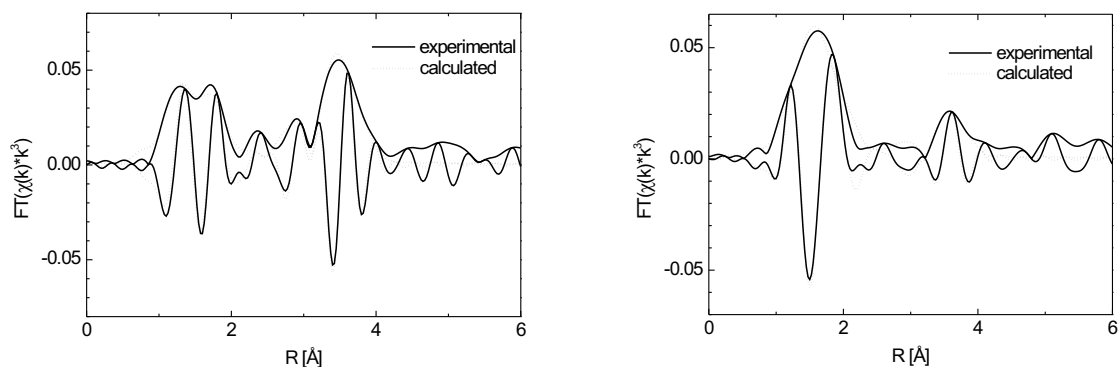


Figure 5.74: Experimental Mo K edge (left) and V K edge (right) $FT(\chi(k) * k^3)$ of $(MoV)_5O_{14}$ together with refined model of average distances.

5.4 Catalytic properties of $(MoVW)_5O_{14}$

	m/e = 56	Norm. activity ($10^{-7} * g^{-1}$)	m/e = 72	Norm. activity ($10^{-8} * g^{-1}$)	BET [m^2/g]
	T_{onset} [K]	@ 707 K	T_{onset} [K]	@ 676 K	
$(MoVW)_5O_{14}$	550	1.886	630	1.66	8.6
$MoVTeNb$ oxide	400	3.445	480	30.36	5.7
$\alpha-MoO_3$	620	2.649	-	-	5.1

Table 5.16: Catalytic properties of $(MoVW)_5O_{14}$ compared to a $MoV_{0.3}Te_{0.23}Nb_{0.125}$ oxide catalyst and $\alpha-MoO_3$ in 2% propene + 4% oxygen.

The catalytic properties of the phase pure crystalline $(MoV)_5O_{14}$ in the selective oxidation of propene were determined using the in situ XRD cell as 'reactor' in the temperature range from 300 K to 773 K (2% propene and 4% oxygen). A non-calibrated mass spectrometer was used for gas phase analysis and the data were normalized to the carrier gas helium. The results obtained were compared to a $MoV_{0.3}Te_{0.23}Nb_{0.125}$ oxide catalyst and $\alpha-MoO_3$.

The MS traces of acrylic acid measured during catalysis testing of the three materials are depicted in Figure 5.75. The onset temperature of catalytic activity to m/e = 56 (acrolein) and m/e = 72 (acrylic acid), and the BET surface area [149] (nitrogen adsorption) of the materials used are given in Table 5.16. $MoV_{0.3}Te_{0.23}Nb_{0.125}$ oxide is a good catalyst for the direct conversion of propane into acrylic acid and therefore easily converts propene into acrylic acid. It is taken as a benchmark catalyst for the formation of acrylic acid. $\alpha-MoO_3$ is the model system for the conversion of propene into acrolein. Regarding the product acrylic acid the activity of the $(MoVW)_5O_{14}$ is one order of magnitude less than the active $MoV_{0.3}Te_{0.23}Nb_{0.125}$ oxide catalyst. Conversely, the formation of acrylic acid was not observed for $\alpha-MoO_3$. The formation of

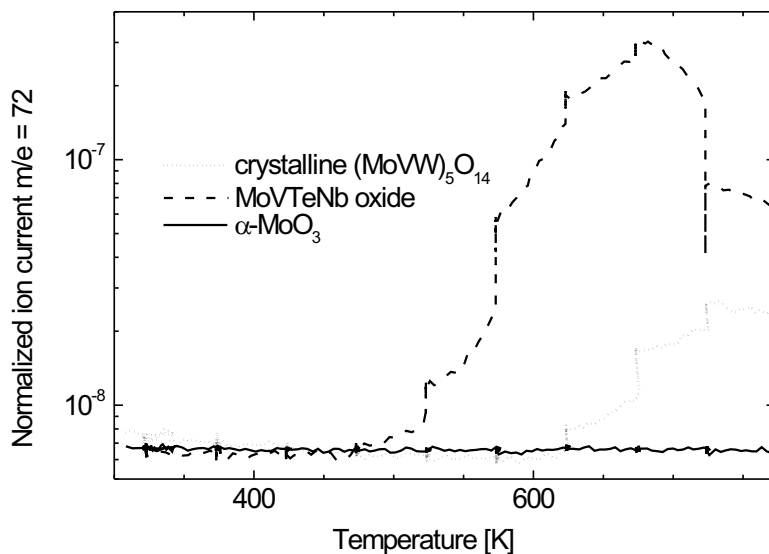


Figure 5.75: Comparison of MS traces of acrylic acid ($m/e = 72$) measured during temperature programmed reaction of 2% propene and 4% oxygen on a $MoVTeNb$ mixed oxide, a $(MoV)_5O_{14}$ (from in situ XRD experiment D), and $\alpha-MoO_3$ catalyst.

acrolein is observed for all three catalysts. The activity of the $(MoVW)_5O_{14}$ is less than that of $MoV_{0.3}Te_{0.23}Nb_{0.125}$ oxide or $\alpha-MoO_3$. But compared to $\alpha-MoO_3$ the $(MoVW)_5O_{14}$ material further oxidizes acrolein into acrylic acid which reduces the amount of detectable acrolein.

5.4.1 In situ XRD

Figure 5.76 shows the long range order of phase-pure crystalline $(MoVW)_5O_{14}$ during catalytic testing in 5% propene and 10% oxygen from 300 K to 773 K. The formation of decomposition products is not observed and the Mo_5O_{14} -type structure is stable up to 773 K under reaction conditions. The selective oxidation products acrolein ($m/e = 56$) and acrylic acid ($m/e = 72$) were detected. As shown in Figure 5.77 no further increase of acrylic acid production above 700 K is observed.

Figure 5.77 shows the dynamics of the lattice constants in $(MoVW)_5O_{14}$ over the investigated temperature range. From 300 K to 773 K the c-axis expands ca. 0.5% linear with increasing temperature. The a- and b-axis ($a=b$, tetragonal lattice) expands ca. 0.1-0.4% over the investigated temperature range. The expansion is not linear with temperature, it essentially occurs at temperatures higher than 720 K.

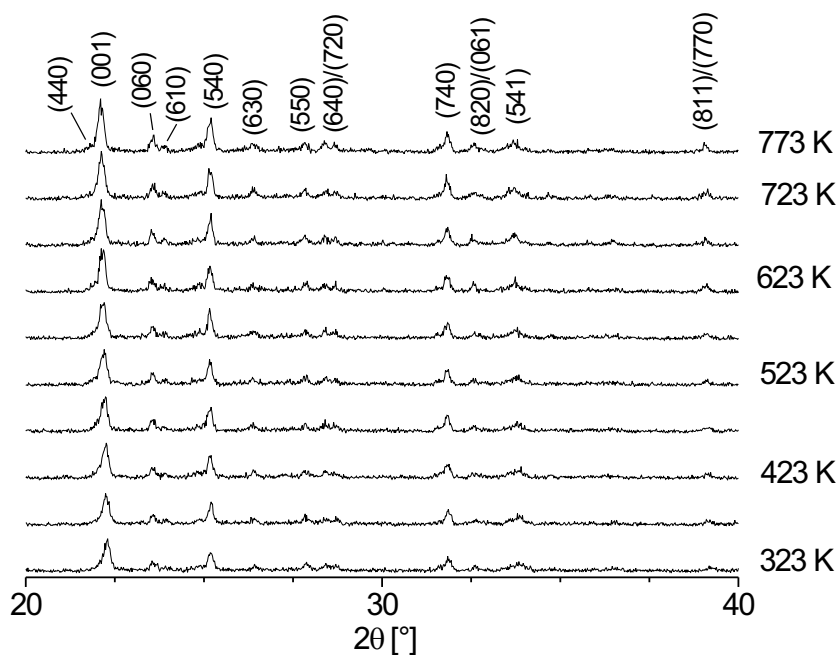


Figure 5.76: Evolution of in situ XRD pattern of $(MoVW)_5O_{14}$ during in situ XRD catalytic test in 5% propene and 10% oxygen from 300 K to 773 K

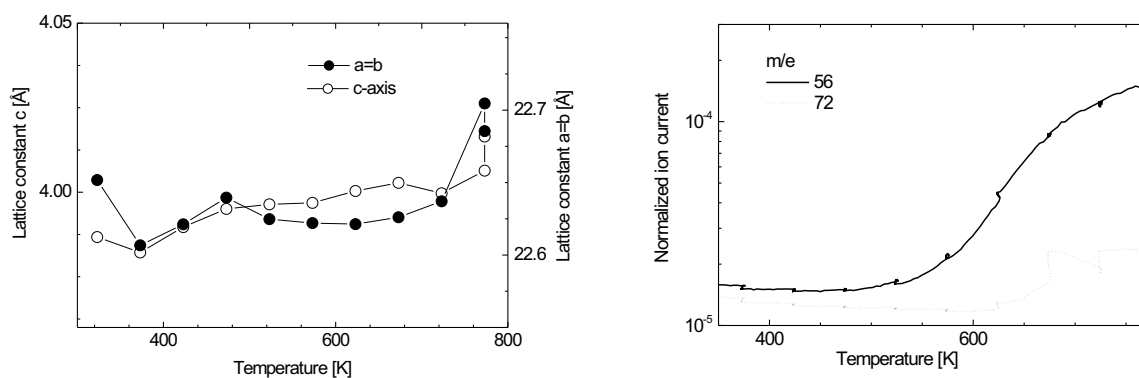


Figure 5.77: Thermal expansion of lattice constants in $(MoVW)_5O_{14}$ (left) and evolution of MS curves of acrolein ($m/e = 56$) and acrylic acid ($m/e = 72$) during in situ XRD catalytic test in 5% propene and 10% oxygen from 300 K to 773 K (right).

5.4.2 In situ XAS

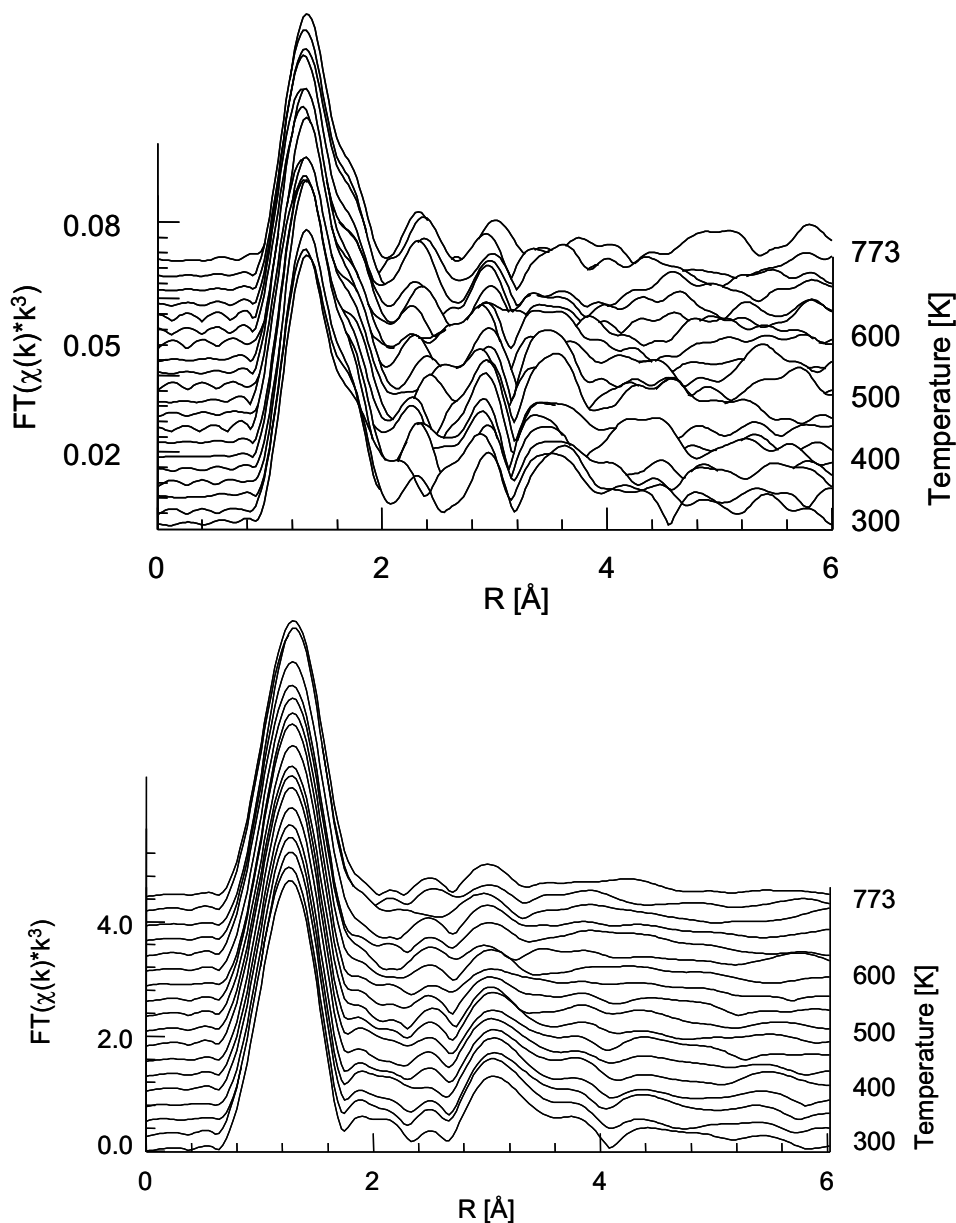


Figure 5.78: Evolution of in situ XAS $FT(\chi(k) * k^3)$ of $(MoVW)_5O_{14}$ at the Mo K edge during heating from 300 K to 773 K in 10% oxygen and 3.3% propene measured (upper) and in 10% oxygen and 10% propene from 300 K to 773 K measured at the W L_{III} edge (lower).

The short range order in the vicinity of all metals in phase-pure crystalline $(MoVW)_5O_{14}$ is stable during catalytic testing in propene and oxygen from 300 K to 773 K (Figures 5.78, 5.79). The amplitudes in the metal-metal shell are decreasing due to thermal disorder. Figure 5.78 shows that in $(MoVW)_5O_{14}$ measured at the W L_{III} edge even

at 773 K the short tungsten-metal distance is present at the initial (300 K) distance. The selective oxidation products acrolein ($m/e = 56$) and acrylic acid ($m/e = 72$) were detected with MS.

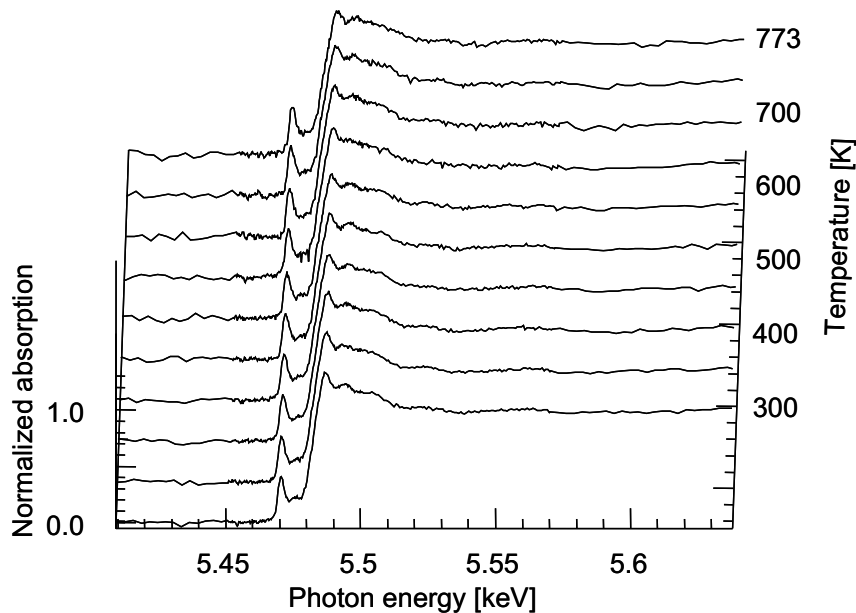


Figure 5.79: In situ XANES spectra of $(MoVW)_5O_{14}$ during heating from 300 K to 773 K in 10% oxygen and 10% propene measured at the V K edge.

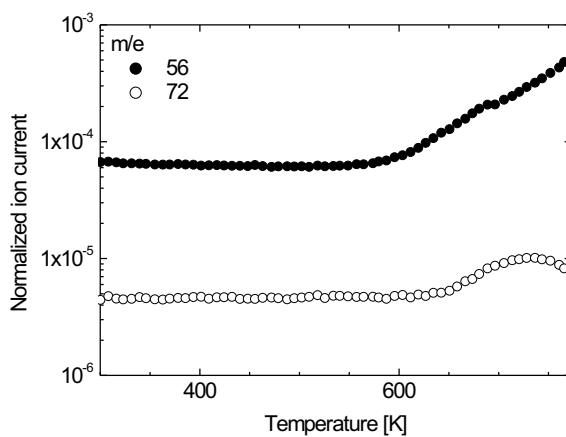


Figure 5.80: MS curves of acrolein ($m/e = 56$) and acrylic acid ($m/e = 72$) during heating of $(MoVW)_5O_{14}$ from 300 K to 773 K in 10% oxygen and 10% propene.

5.5 Catalytic properties of $(MoV)_5O_{14}$

5.5.1 In situ XRD

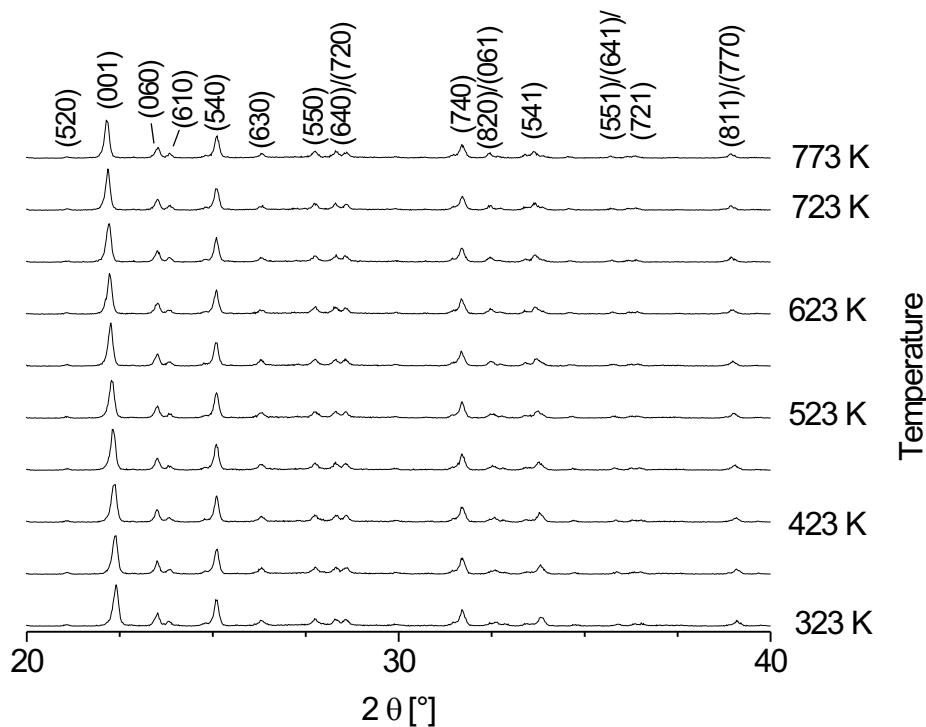


Figure 5.81: Evolution of in situ XRD pattern of $(MoV)_5O_{14}$ during catalytic test in 5% propene and 10% oxygen from 300 K to 773 K.

The long range order of crystalline $(MoV)_5O_{14}$ is stable during catalytic testing in 5% propene and 10% oxygen from 300 K to 773 K (Figure 5.81). The selective oxidation product acrolein ($m/e = 56$) was detected with MS. The lattice expansion observed during heating in the investigated temperature range is shown in Figure 5.82. The c -axis increases linear with temperature. An intermediate expansion is observed for the a - and b -axis ($a=b$, tetragonal lattice) with maximum elongation at 773 K.

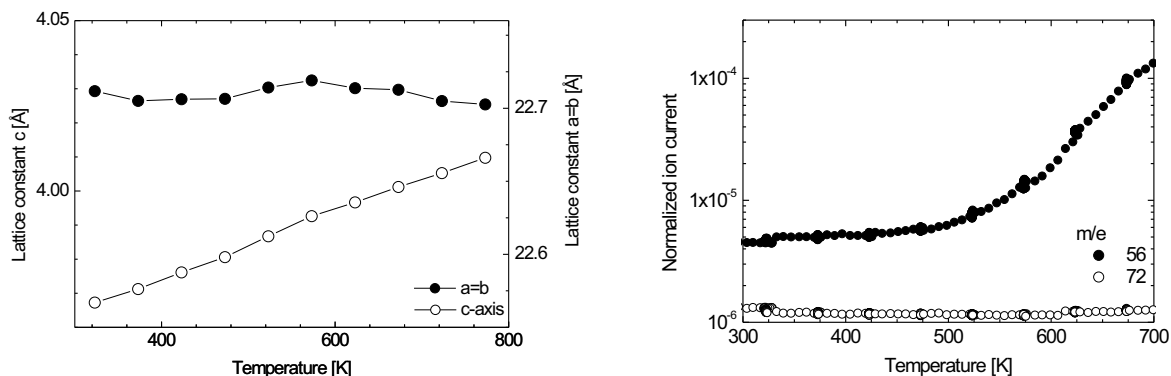


Figure 5.82: Thermal expansion of lattice constants in $(MoV)_5O_{14}$ during catalytic test in 5% propene and 10% oxygen from 300 K to 773 K and evolution of acrolein ($m/e = 56$) and acrylic acid ($m/e = 72$).

5.5.2 In situ XAS

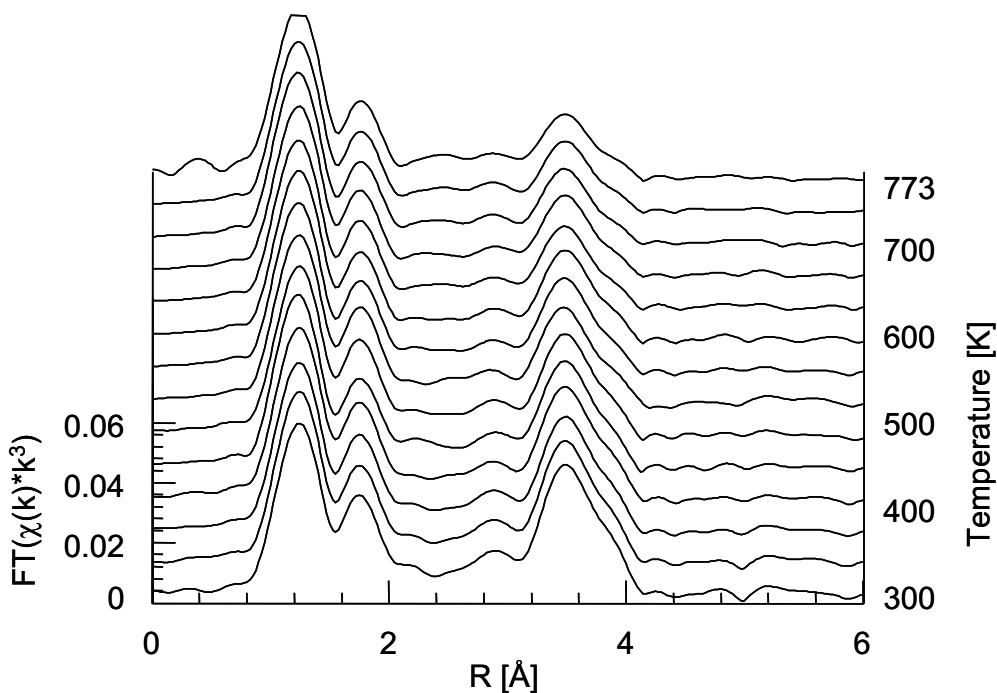


Figure 5.83: Evolution of in situ XAS FT($\chi(k) * k^3$) of $(MoV)_5O_{14}$ during heating from 300 K to 773 K in 10% oxygen and 3.3% propene measured at the Mo K edge.

The short range order in the vicinity of molybdenum and vanadium in calcined crystalline $(MoV)_5O_{14}$ is stable during catalytic testing in propene and oxygen from 300 K

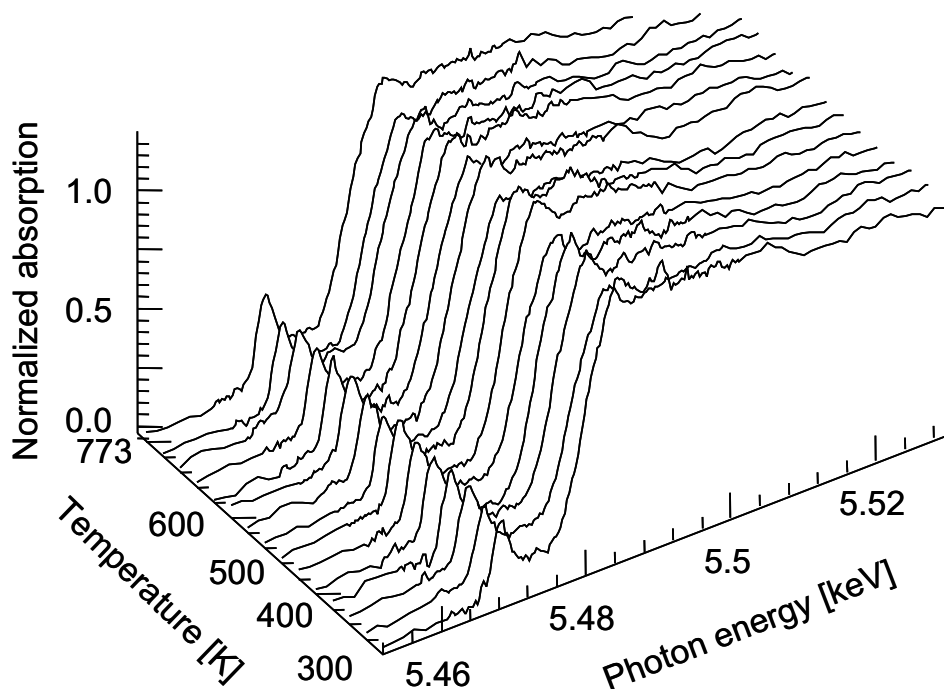


Figure 5.84: Evolution of in situ XANES of $(MoV)_5O_{14}$ during heating from 300 K to 773 K in 20% oxygen and 10% propene measured at the V K edge.

to 773 K (Figures 5.83 and 5.84). In Figure 5.84 the molybdenum-metal shell decreases at increasing temperature. At the V K edge the noisy data is due to the low vanadium content in the sample and the EXAFS extracted from the spectra contains limited information about the vanadium-oxygen shell. The selective oxidation product acrolein ($m/e = 56$) was detected with MS.

5.6 Thermal stability of $(MoVW)_5O_{14}$

5.6.1 In situ XRD

As shown in Figure 5.85 during heating in 20% oxygen the structure of $(MoVW)_5O_{14}$ is maintained up to 773 K, even though the atmosphere is highly oxidizing and not all incorporated metal cations are present in their highest oxidation states. With increasing temperature lattice constants expand. Figure 5.86 shows the structural transformation of $(MoVW)_5O_{14}$ into a MoO_2 -type structure in 10% propene starting from 670 K. At this temperature oxygen mobility in the $(MoVW)_5O_{14}$ is present and sufficiently high.

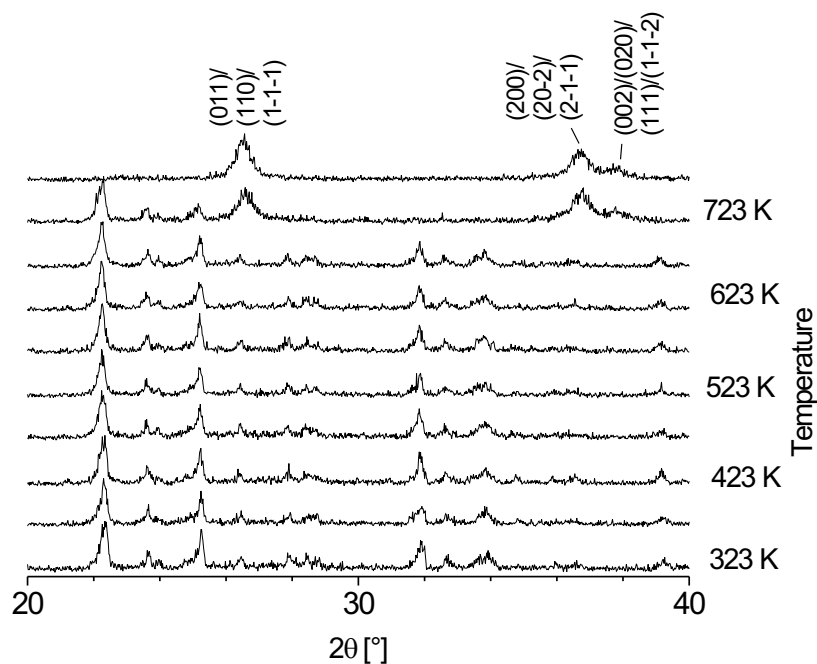


Figure 5.85: Evolution of in situ XRD of $(MoVW)_5O_{14}$ during in situ XRD from 300 K to 773 K in 10% propene.

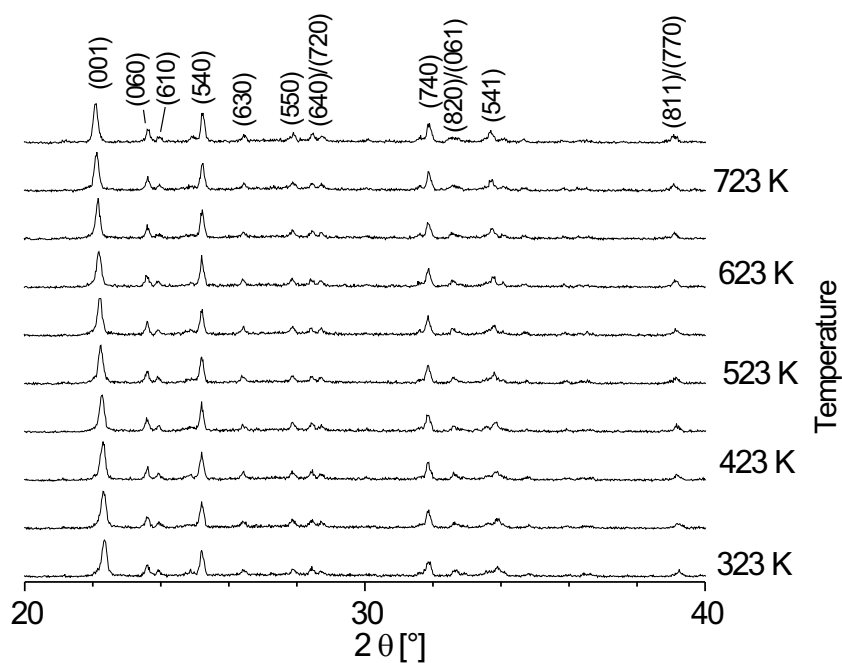


Figure 5.86: Evolution of in situ XRD of $(MoVW)_5O_{14}$ during in situ XRD from 300 K to 773 K in 20% oxygen.

5.6.2 In situ XAS

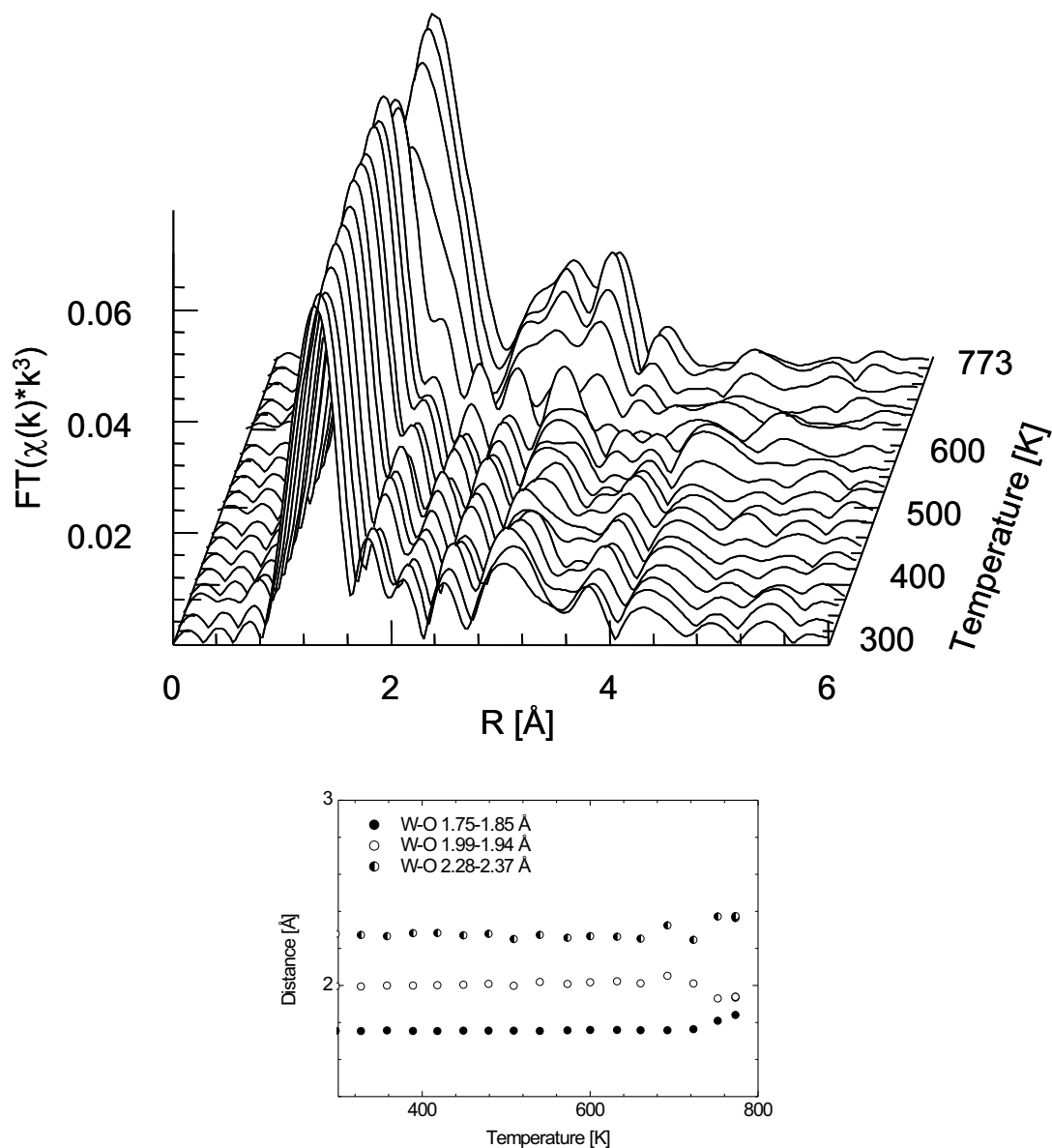


Figure 5.87: Evolution of $FT(\chi(k) * k^3)$ of $(MoVW)_5O_{14}$ during heating from 300 K to 773 K in 10% propene measured at the W L_{III} edge (upper) and tungsten-oxygen distances from EXAFS structure refinement with model of average distances (lower).

Figure 5.89 shows $(MoVW)_5O_{14}$ at the Mo K and W L_{III} edge during heating from 300 K to 773 K in 20% oxygen. The short-range ordered structure remains stable up to 773 K. In the spectra measured at both edges, the Mo K and at the W L_{III} , the amplitude in the metal-metal shell decreases with increasing temperature. The local structure of $(MoVW)_5O_{14}$ during heating from 300 K to 773 K under reducing

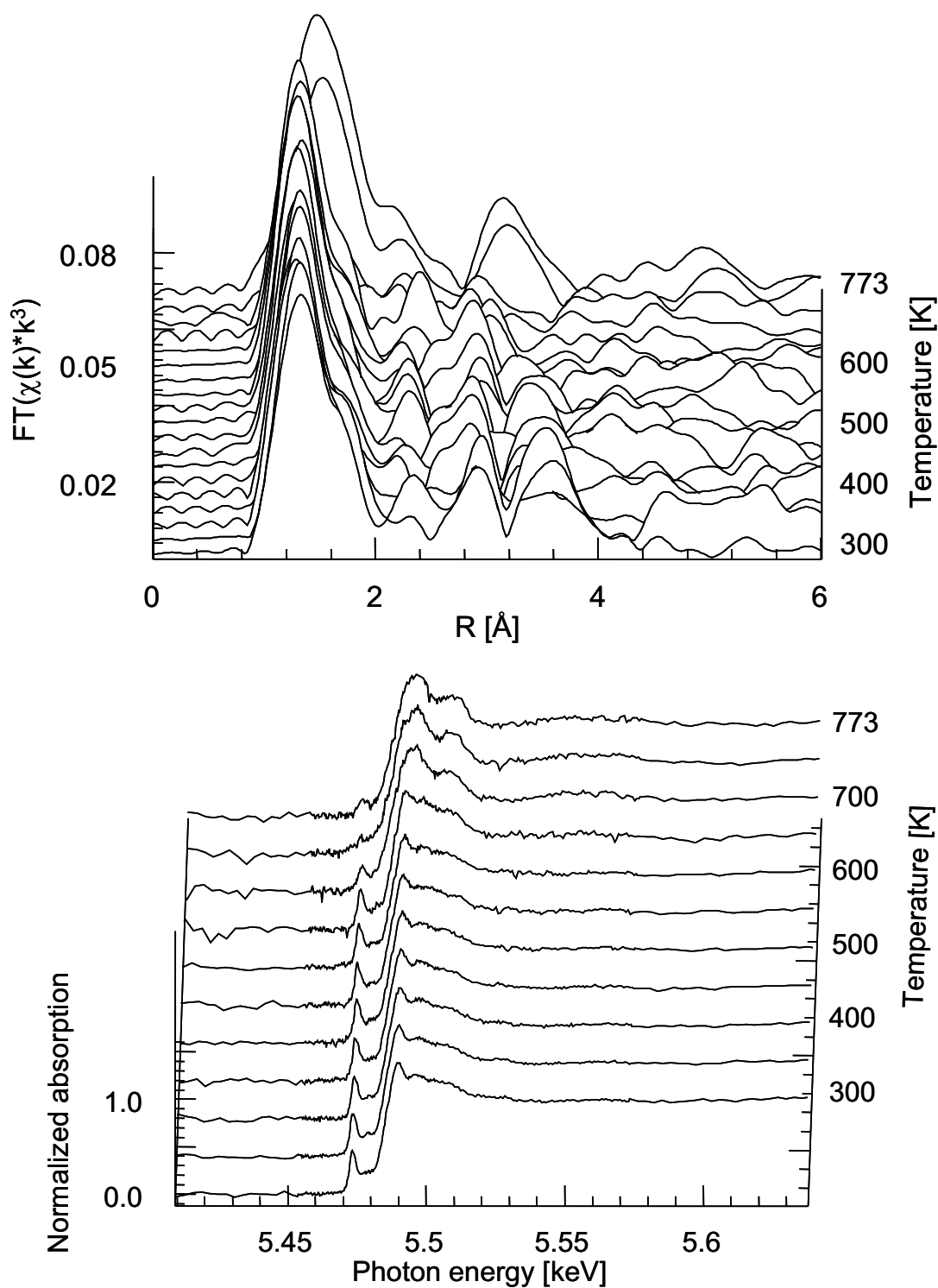


Figure 5.88: Evolution of in situ XAS $FT(\chi(k) * k^3)$ of $(MoVW)_5O_{14}$ measured at the Mo K edge (upper) and XANES spectra measured at the V K edge (lower) during heating from 300 K to 773 K in 10% propene.

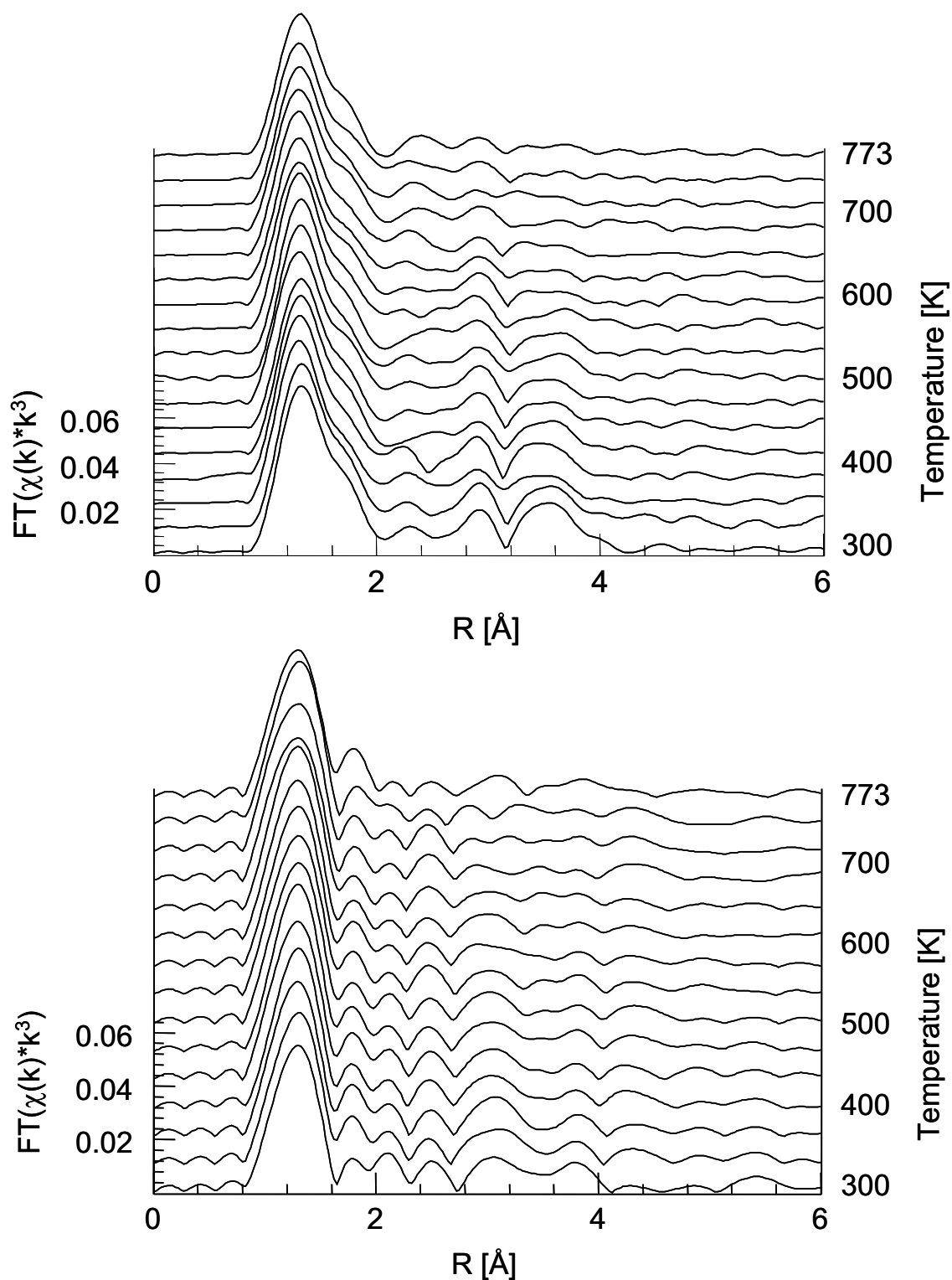


Figure 5.89: Evolution of in situ XAS $FT(\chi(k) * k^3)$ of $(MoVW)_5O_{14}$ in 20% oxygen during heating from 300 K to 773 K measured at the Mo K edge (upper) and W L_{III} edge (lower).

conditions in 10% propene is shown in Figures 5.88 and 5.87. The onset of reduction is observed at about 650 K in the spectra at the V K and W L_{III} edges. At the Mo K edge the onset of reduction was observed at about 685 K. The FT($\chi(k) * k^3$) of $(MoVW)_5O_{14}$ measured at the W L_{III} edge was refined with the model of average distances (Figure 5.87). This model describes the initial experimental spectrum with three $W-O$ single scattering paths, one $W-Mo$ single scattering path, and one $W-W$ single scattering path (Table 5.15). The five distances, one overall E_0 , one Debye temperature for oxygen and another Debye temperature for tungsten were refined. Above 600 K the R-value increased to 20-30%. Therefore the structure model of average distances appropriately describes the spectra up to a temperature of 650 K. At the Mo K edge the model structure refined to the EXAFS spectra of $(MoVW)_5O_{14}$ describes the data adequate up to a temperature of 685 K. In XANES spectra of $(MoVW)_5O_{14}$ measured at the V K edge the pre-edge height decreases from about 650 K.

5.7 Thermal stability of $(MoV)_5O_{14}$

5.7.1 In situ XRD

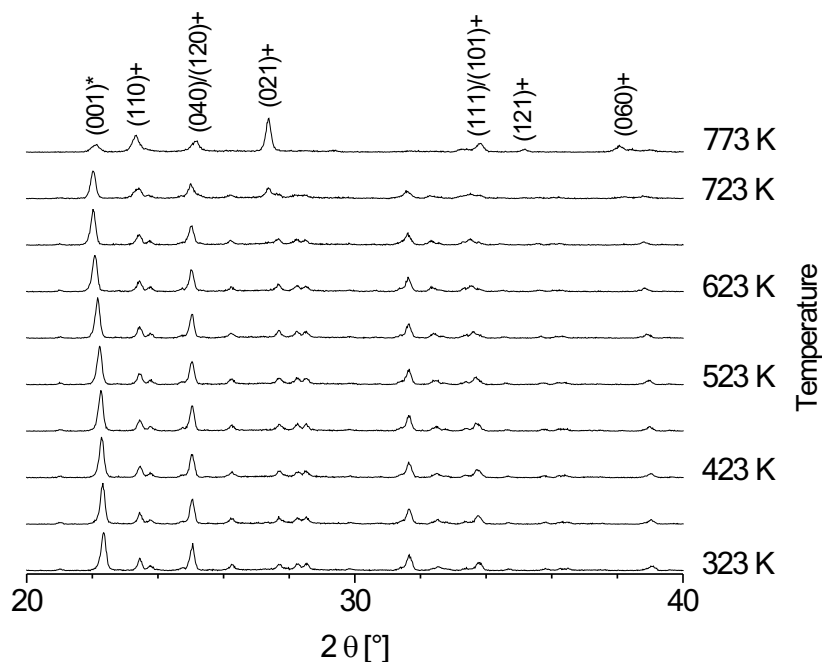


Figure 5.90: Evolution of in situ XRD pattern of $(MoV)_5O_{14}$ during in situ XRD from 300 K to 773 K in 20% oxygen. Phase symbols: "*" Mo_5O_{14} -type phase, "+" $\alpha-MoO_3$ -type phase.

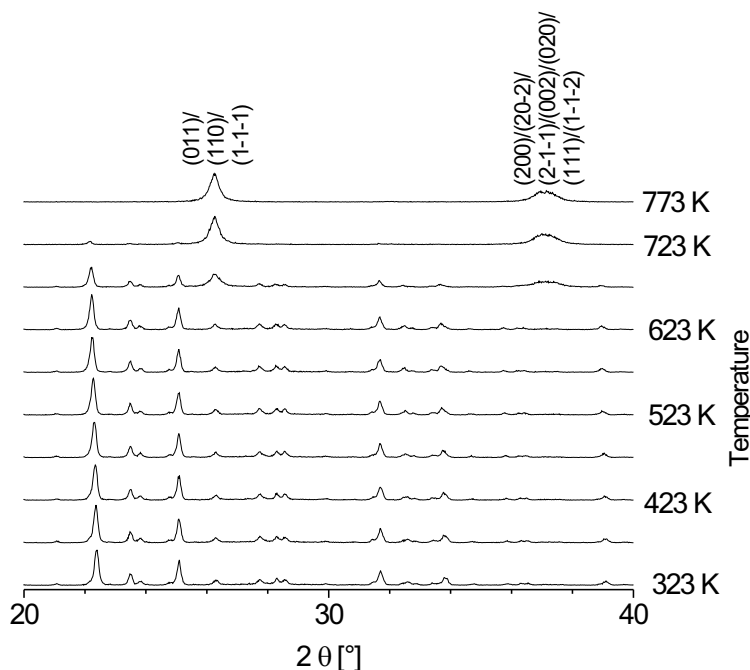


Figure 5.91: Evolution of in situ XRD pattern of $(MoV)_5O_{14}$ during in situ XRD from 300 K to 773 K in 10% propene.

Figures 5.90 and 5.91 show the structural evolution of the long range order in $(MoV)_5O_{14}$ during heating in oxidizing and reducing atmosphere. The heating experiment in 10% propene shows the structural transformation of $(MoV)_5O_{14}$ into a MoO_2 -type structure above 623 K. The reduction of the mixed metal oxide indicates the oxygen mobility at this temperature. During heating in 20% oxygen the Mo_5O_{14} -type structure is stable up to 723 K. Above 723 K the material slowly decomposes into a MoO_3 -type structure. The XRD pattern of the resulting MoO_3 -type compound is described with a 'hkl'-phase based on refined lattice constants from α - MoO_3 (ICSD [35076]).

5.7.2 In situ XAS

Figure 5.92 shows the $FT(\chi(k) * k^3)$ of $(MoV)_5O_{14}$ measured at the Mo K edge during thermal treatment in reducing or oxidizing atmosphere. During heating in 10% propene refinement of the Mo_5O_{14} -type material shows decreasing amplitudes and increasing metal-metal distances with increasing temperature correlating to the lattice expansion observed in XRD. The model structure refined to $(MoV)_5O_{14}$ in 10% propene describes the data of $(MoV)_5O_{14}$ up to 650 K. At this temperature the Mo_5O_{14} -type structure is reduced to a monoclinic MoO_2 -type material. The pre-edge peak height in the XANES spectra of $(MoV)_5O_{14}$ measured at the Mo K and V K edge in 10% propene drop down at 650 K. During heating of $(MoV)_5O_{14}$ in 20% oxygen the model structure

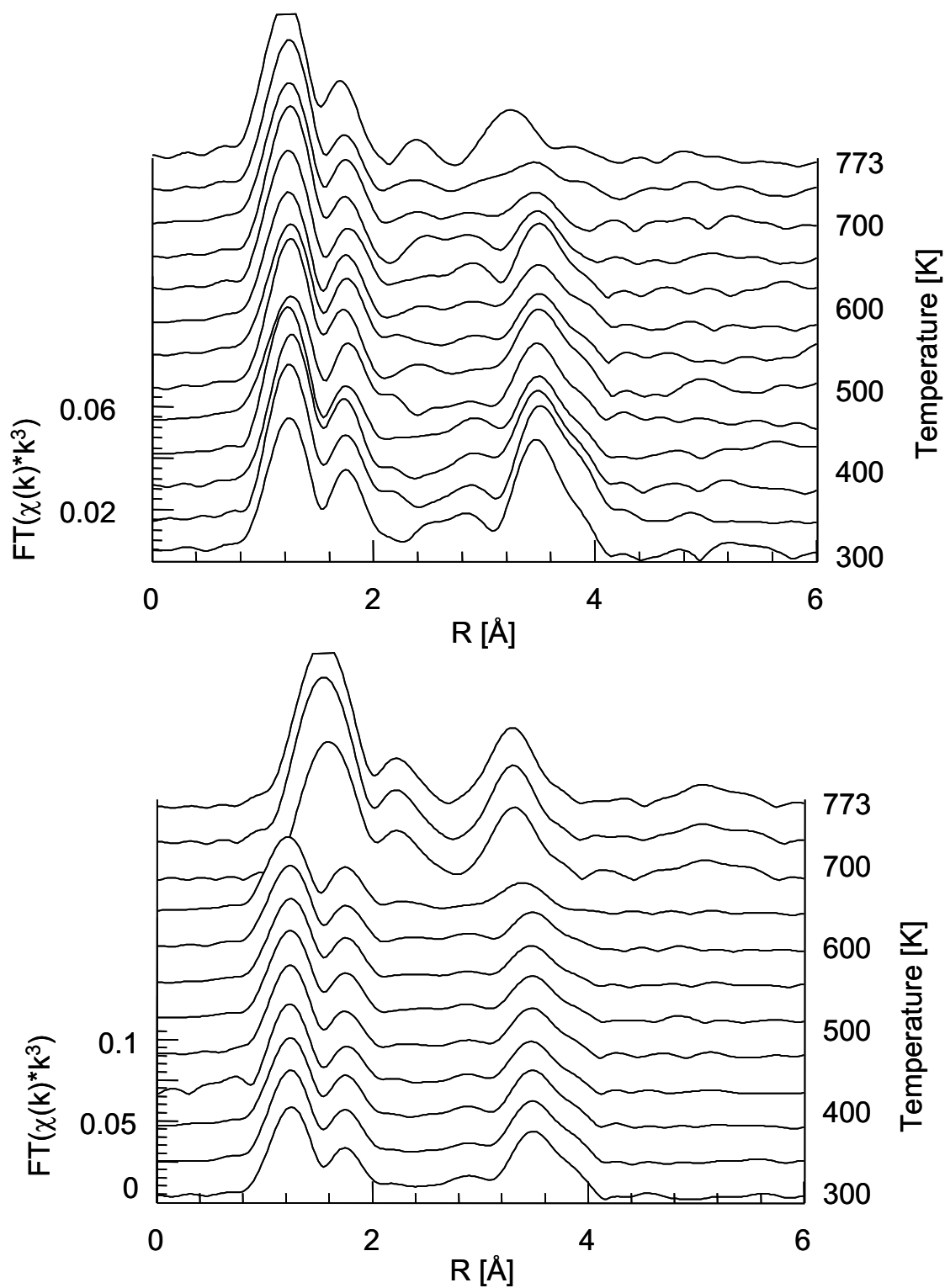


Figure 5.92: Evolution of in situ XAS $FT(\chi(k) * k^3)$ of $(MoV)_5O_{14}$ during heating from 300 K to 773 K in 20% oxygen (upper) and 10% propene (lower) measured at the Mo K edge.

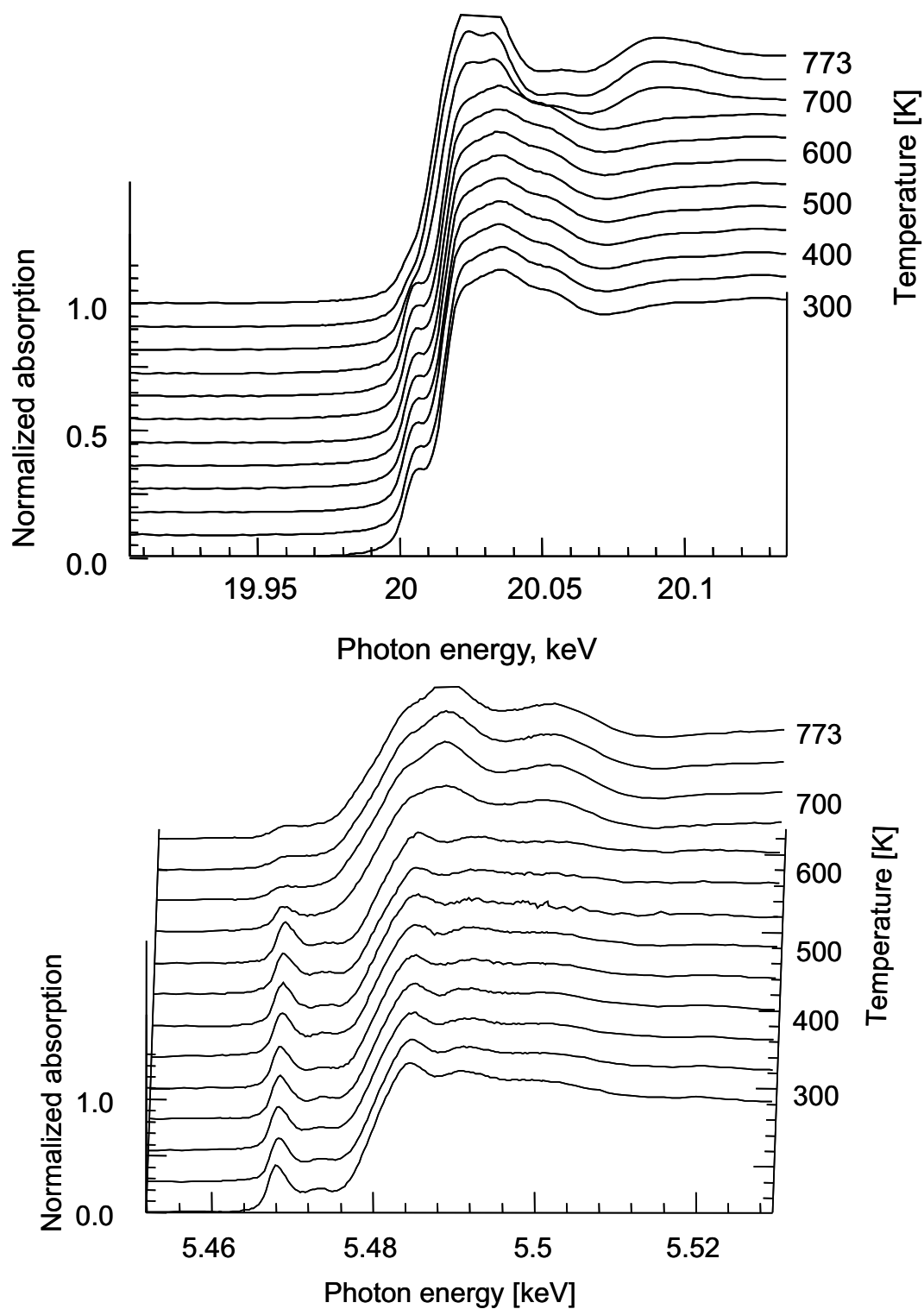


Figure 5.93: In situ XANES spectra of $(MoV)_5O_{14}$ during heating from 300 K to 773 K in 10% propene measured at the Mo *K* edge (upper) and at the V *K* edge (lower).

describes the local environment of molybdenum in $(MoV)_5O_{14}$ up to 700 K. Above 700 K the metal-oxygen shell is not effected, but the maximum of the metal-metal shell is shifted to shorter distances. At 300 K after the experiment the local surrounding of molybdenum can be described with a structure model of five metal-oxygen single scattering distances and four metal-metal single scattering distances similar to the MoO_3 structure (ICSD [35076]). The refinement results are listed in Table 5.17.

		re-ox. MoV	oxide	α - MoO_3
	C.N.	σ [\AA^3]	distance [\AA]	distance [\AA]
Mo-O	1	0.0001	1.6521	1.6708
Mo-O	1	0.0003	1.7174	1.7361
Mo-O	2	0.0031	1.9365	1.9479
Mo-O	1	0.0024	2.2136	2.2519
Mo-O	1	0.0016	2.2938	2.3321
Mo-M	2	0.0091	3.3380	3.438
Mo-M	2	0.0016	3.7075	3.696
Mo-M	2	0.0049	3.9639	3.963
Mo-M	2	0.0043	4.6438	4.699
Mo-M	-	-	-	4.924

Table 5.17: EXAFS refinement of structure model based on MoO_3 to $FT(\chi(k) * k^3)$ of reoxidized (MoV) oxide at Mo K edge.

5.8 Redox properties of $(MoVW)_5O_{14}$ and $(MoV)_5O_{14}$

5.8.1 In situ XRD

The redox properties of $(MoVW)_5O_{14}$ and $(MoV)_5O_{14}$ were tested in isothermal experiments at 773 K (Figure 4.2). The experimental XRD pattern of $(MoVW)_5O_{14}$ and $(MoV)_5O_{14}$ recorded at 773 K in different atmospheres are shown in Figure 5.94. The Mo_5O_{14} -type structure of $(MoVW)_5O_{14}$ and $(MoV)_5O_{14}$ was stable during heating in helium to 773 K. Then the atmosphere was changed and under reducing conditions, either 10% propene or 10% hydrogen, the $(MoVW)_5O_{14}$ and $(MoV)_5O_{14}$ material was completely reduced into a monoclinic MoO_2 -type structure. Refinement of lattice constants starting from MoO_2 (ICSD [23722]) was able to describe the reduced phase. At 773 K in 20% oxygen the $(MoVW)$ dioxide was re-oxidized to the initial $(MoVW)_5O_{14}$ material and retained this structure at room temperature. In case of the (MoV) dioxide the re-oxidation in 20% oxygen leads to an orthorhombic MoO_3 -type structure. The XRD pattern of the product was described with refined lattice constants from α - MoO_3 (ICSD [35076]). Additionally, in the XRD pattern of the spent sample from the in situ XAS redox experiment three peaks assigned to 0.5% $Mo_xV_{2-x}O_5$, e.g. $Mo_{0.56}V_{1.44}O_5$ ICSD [24338], were found. No intermediate phases were detectable in the XRD patterns during reduction and re-oxidation. The simultaneous presence of Mo_5O_{14} -type and MoO_2 -type structure during reduction of both samples and re-oxidation of $(MoVW)$ oxide or simultaneous presence of MoO_2 -type

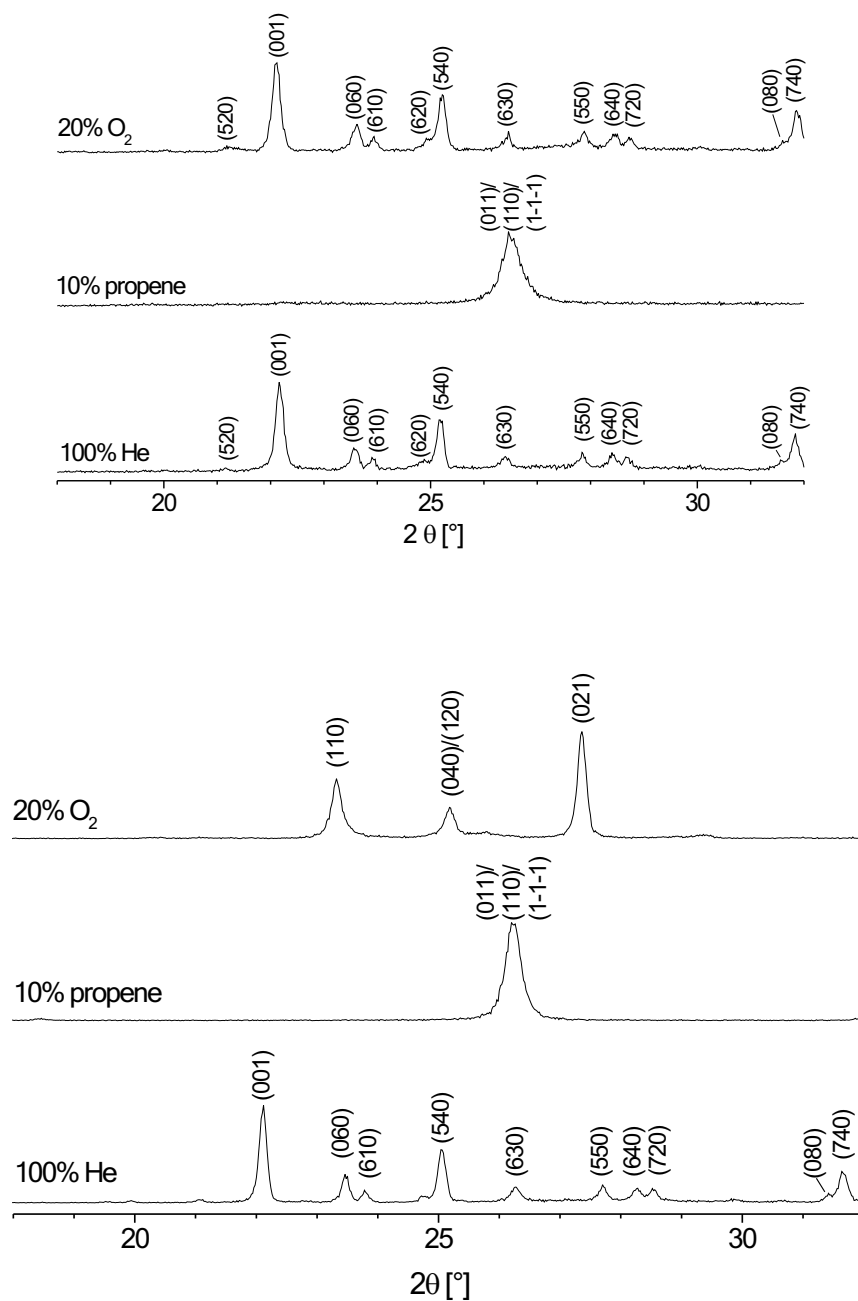


Figure 5.94: In situ XRD of $(MoVW)_5O_{14}$ (upper) and $(MoV)_5O_{14}$ (lower) during isothermal redox experiment at 773 K: in 100% helium, reduction in 10% propene, re-oxidation in 20% oxygen.

	a [Å]	b [Å]	c [Å]	β [°]	V [Å ³]	vanadium content
VO_2	5.74	4.52	5.38	122.61	117.45	1
$(MoVW)_5O_{14}$	5.69	4.79	5.56	121.17	129.66	0.23
$(MoV)_5O_{14}$	5.63	4.84	5.61	120.99	131.22	0.09
MoO_2	5.61	4.86	5.63	120.95	131.53	0
WO_2	5.56	4.90	5.56	120.47	133.09	0

Table 5.18: Lattice constants of structure model (ICSD [23722]) refined to $(MoVW)$ dioxide and (MoV) dioxide compared to VO_2 , MoO_2 and WO_2 .

and MoO_3 -type structure during re-oxidation of (MoV) oxide was observed.

A theoretically calculated mixture of MoO_2 , WO_2 , VO_2 was refined to the reduced material of $(MoVW)_5O_{14}$ and $(MoV)_5O_{14}$. The lattice constants of the binary oxides were fixed during refinement. Certainly no VO_2 is present in the reduced material, because the monoclinic angle of VO_2 shifts the peak positions off the measured peak positions. MoO_2 and WO_2 with their similar lattice constants were refined as a mixture of 96% MoO_2 (crystallite size 14 nm) and 4% WO_2 (crystallite size 85 nm) and resulted in an R-value of 31%. The intensity of some peaks was obviously not accounted.

Compared to this the reduced material of $(MoVW)_5O_{14}$ and reduced $(MoV)_5O_{14}$ were refined as unique phases. The lattice constants refined to the reduced material of $(MoVW)_5O_{14}$ and reduced $(MoV)_5O_{14}$ are compared to VO_2 ICSD [15889], MoO_2 ICSD [23722], and WO_2 ICSD [8217] in Table 5.18. The vanadium content has the strongest effect on lattice constants of the mixed metal dioxides. The more vanadium is incorporated the higher the deviation of a- and c-axis. With increasing vanadium

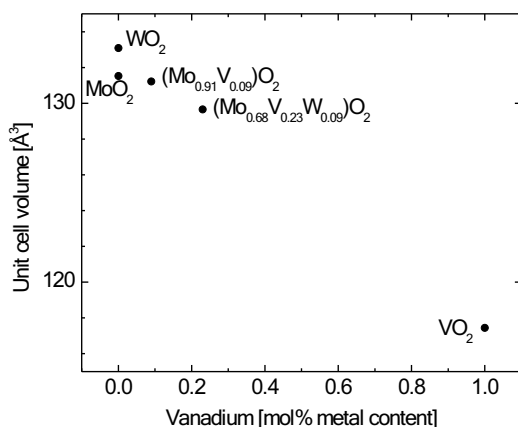


Figure 5.95: Unit cell volume of the monoclinic metal dioxides reduced in propene as a function of vanadium content for $(MoVW)_5O_{14}$ and $(MoV)_5O_{14}$ and binary oxides MoO_2 , VO_2 , and WO_2 as reference compounds.

content the a-axis expands, b-axis and c-axis contract, and the monoclinic angle β becomes larger. As a sum of these effects the volume of the unit cell decreases with increasing vanadium content as shown in Figure 5.95.

5.8.2 In situ XAS

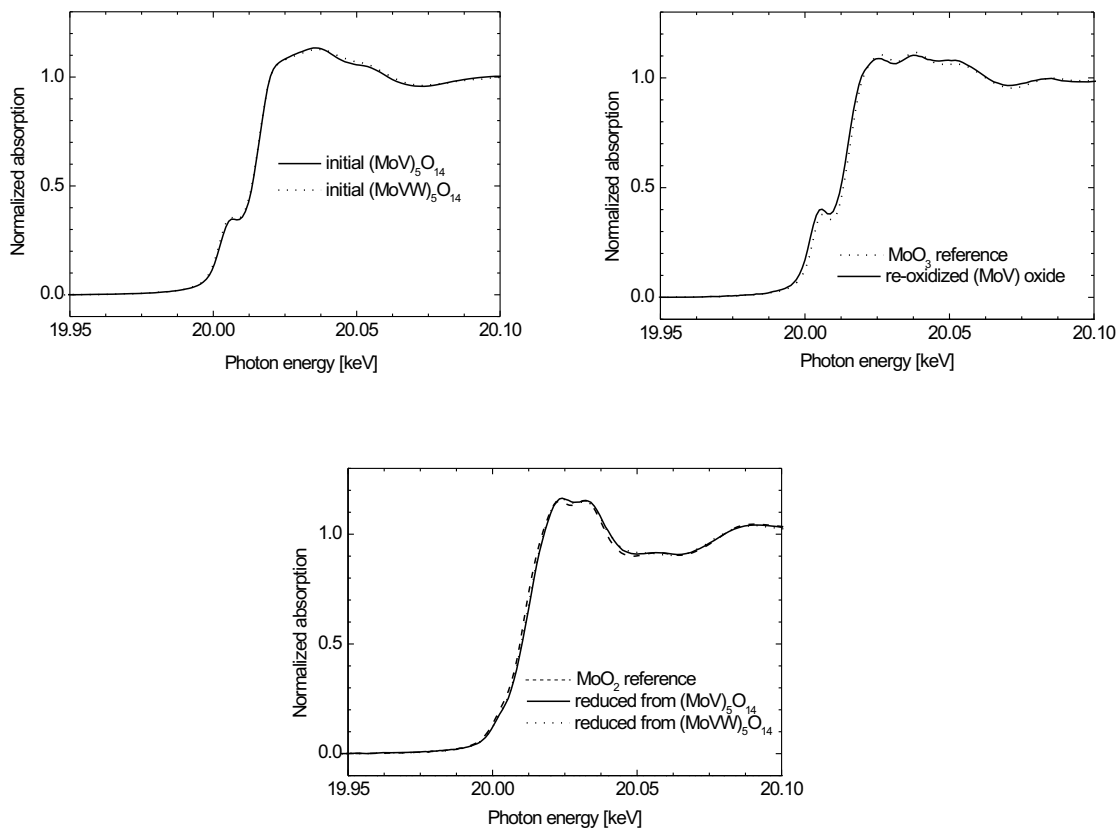


Figure 5.96: In situ XANES spectra at the Mo K edge during redox experiment: XANES of the initial $(MoVW)_5O_{14}$ and $(MoV)_5O_{14}$ (left). XANES spectra of the reduced $(MoVW)$ oxide and (MoV) oxide (center). XANES of re-oxidized (MoV) oxide resembles the MoO_3 reference (right).

The very similar Mo K near-edge spectra of $(MoVW)_5O_{14}$ and $(MoV)_5O_{14}$ shown in Figure 5.96 are indicative of molybdenum centers in a similar local structural coordination in both materials. The same holds for the local structure around the vanadium centers in $(MoVW)_5O_{14}$ and $(MoV)_5O_{14}$ (Figure 5.98). Compared to the V K edge spectra of VO_2 and V_2O_5 references, the average valence of the vanadium centers in $(MoVW)_5O_{14}$ and $(MoV)_5O_{14}$ amounts to about 4.5. XANES spectra at the Mo K , V K , and W L_{III} edges of the initial $(MoVW)_5O_{14}$ are shown in Figure 5.97. Additionally, Figure 5.97 depicts the XANES spectra of the $(MoVW)_5O_{14}$ material obtained

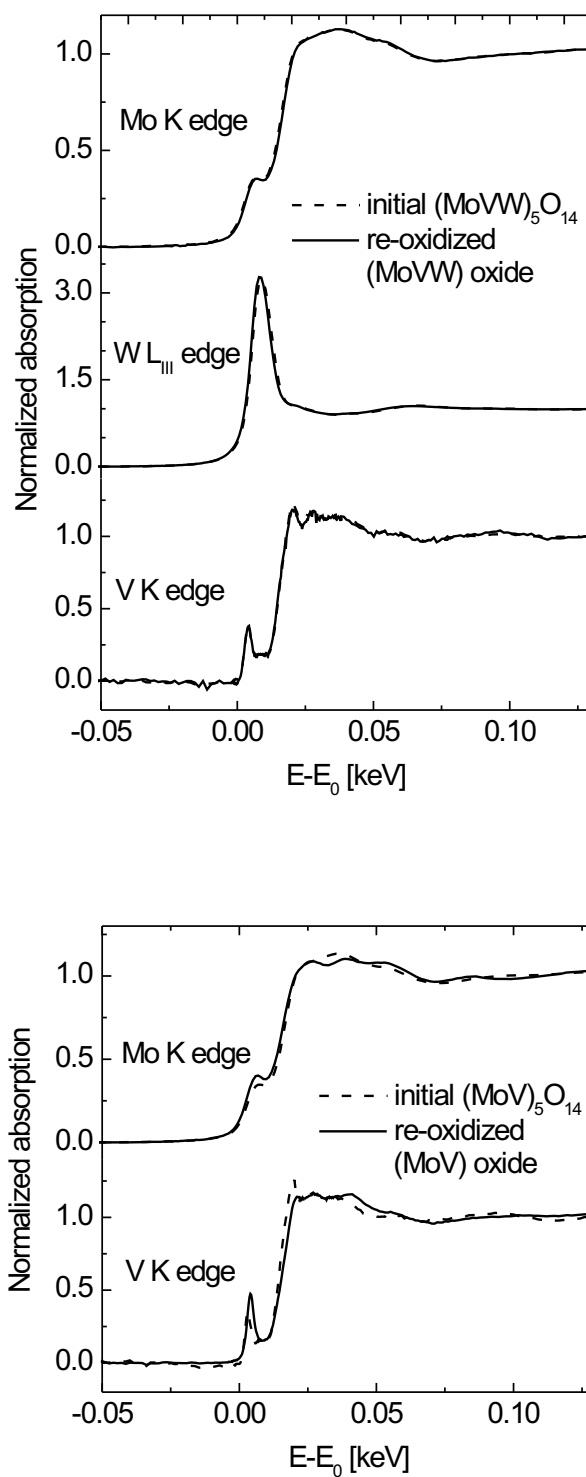


Figure 5.97: XANES of the initial and re-oxidized $(MoVW)_5O_{14}$ at the Mo *K* edge, V *K* edge, and W *L*_{III} edge (upper) and of the initial and re-oxidized $(MoV)_5O_{14}$ at the Mo *K* edge and V *K* edge (lower).

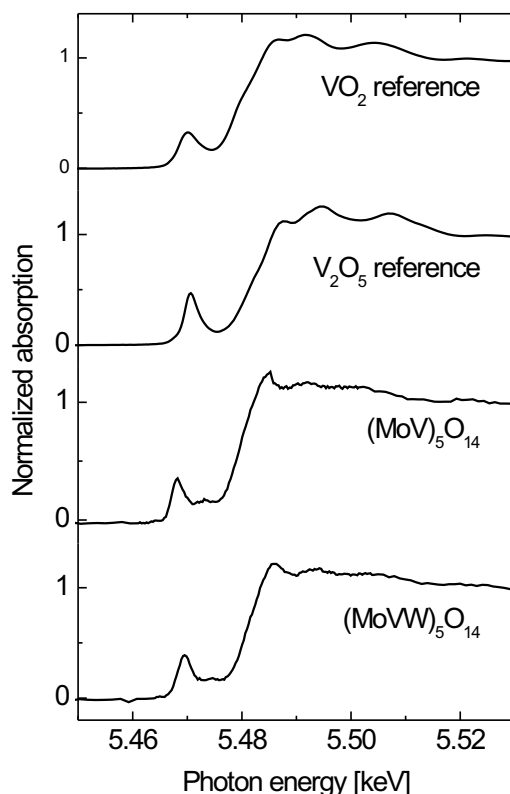


Figure 5.98: XANES spectra taken at V K edge of the initial $(MoVW)_5O_{14}$ and $(MoV)_5O_{14}$ compared to references VO_2 and V_2O_5 .

after a cycle of reduction in propene and re-oxidation at 773 K. Apparently, a similar local and electronic structure of all metal centers is found in the initial and the re-oxidized $(MoVW)_5O_{14}$ material. Conversely, the Mo K (Figure 5.97) and V K near-edge spectra of the initial $(MoV)_5O_{14}$ and the re-oxidized material indicate a different local structure around the molybdenum and vanadium centers. Compared to the spectrum of a MoO_3 reference (Figure 5.96), the molybdenum centers in the MoO_3 -type structure of the re-oxidized (MoV) oxide exhibit a slightly reduced average valence and a different local structure. The latter may be due to the incorporation of vanadium centers in the MoO_3 -type structure.

The position of the second transition maximum in the Mo K edge XANES spectra that is taken as indicator for the average valence [132]. From the edge position the average valence of molybdenum in the as prepared samples is less than Mo^{6+} . XRD analysis of the material obtained from re-oxidizing the (MoV) dioxide yielded a minor amount of a mixed $Mo_xV_{2-x}O_5$ phase (e.g. 0.5% $Mo_{0.56}V_{1.44}O_5$ ICSD [24338]). In the as-prepared $(MoVW)_5O_{14}$ and $(MoV)_5O_{14}$ materials the molybdenum centers exhibited an average valence of less than 6 (about 5.6). A similarly reduced average valence was observed

for the molybdenum centers in the Mo_5O_{14} -type structure obtained from re-oxidizing the (*MoVW*) dioxide. Conversely, the molybdenum centers in the MoO_3 -type structure obtained from re-oxidizing the (*MoV*) dioxide exhibit an average valence of about $Mo^{5.8}$ (Figure 5.96). The local structure and the average valence of the molybdenum centers in the (*MoVW*) dioxide and the (*MoV*) dioxide were similar to those of the molybdenum centers in MoO_2 (Figure 5.96). Slight differences are indicative of the incorporation of vanadium and tungsten in the corresponding MoO_2 -type structures. Thus, in the reduced structures the average valence of molybdenum is assumed in the range of Mo^{4+} . The V *K* near-edge spectra of the dioxides obtained from reducing the corresponding Mo_5O_{14} -type oxides in propene at 773 K are depicted in Figure 5.99. Apparently, the average valance and the local structure of the vanadium centers in the

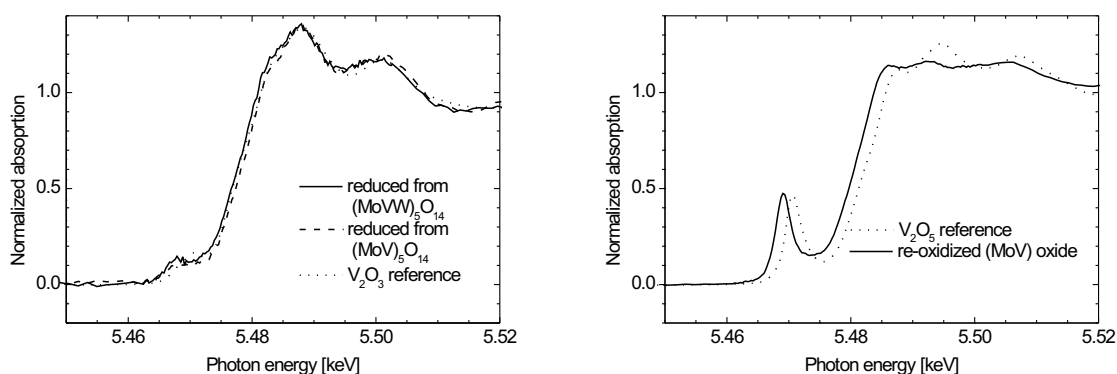


Figure 5.99: In situ XANES spectra at the V *K* edge during redox experiment: XANES spectra of the reduced (*MoVW*) oxide and (*MoV*) oxide (left), the pre-edge peak of re-oxidized (*MoV*) oxide resembles the V_2O_5 reference (right).

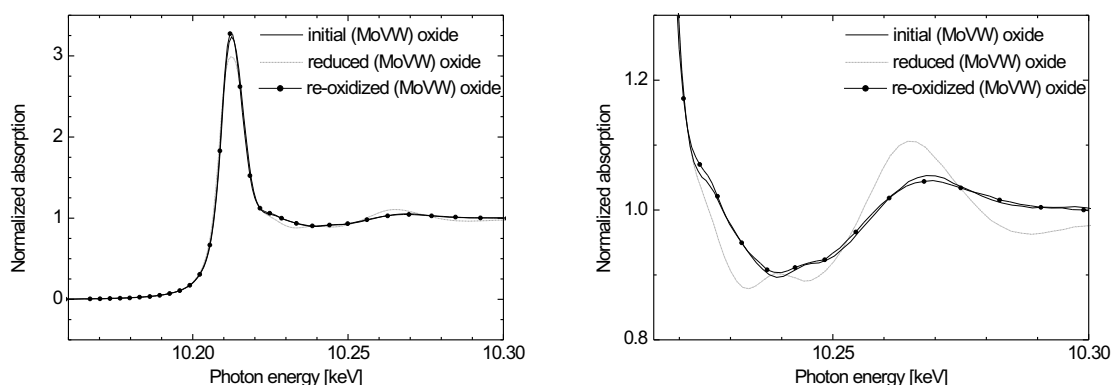


Figure 5.100: Changes in XANES spectra at the W *L*_{III} edge during redox experiment: XANES of initial ($(MoVW)_5O_{14}$) compared to reduced $(MoVW)O_2$ and re-oxidized material (left), magnification behind white line (right).

dioxide materials is similar to those of the vanadium centers in the V_2O_3 reference. Thus, the average valence of vanadium in the reduced structure seems V^{3+} .

Chapter 6

Discussion

6.1 Crystallization and calcination experiments

6.1.1 Comparability of data obtained by different methods

The oxide material obtained in each experiment, either powder from in situ XRD or TG/DSC or powder pressed with *BN* from in situ XAS, were analyzed by XRD. The phase purity was confirmed and crystallinity of the final oxide material was taken as an indicator for the comparability of the data obtained during thermal treatment experiments. For all methods used the crystallinity of the resulting material increased with the heating rate. Generally, the crystallinity of material investigated by XRD and XAS, with gas flow through the sample bed, was better than that obtained by TG/DSC with the sample on the bottom of a small crucible and gas flowing over it. The gas phase evolution was compared and did not differ within the detection limit of the MS.

6.1.2 Structural characterization of the *MoVW* oxide precursor with XAS

The local structure around the various metal centers in the as-prepared amorphous precursor material was determined by XAS. The precursor exhibits reduced amplitude in the molybdenum-metal shell of the precursor compared to those of AHM (Figure 5.57). This is caused by slightly deviating distances to the different neighboring metal centers. The latter results in a destructive interference in the EXAFS function and, thus, a diminished amplitude of the corresponding peaks in the $\text{FT}(\chi(k) * k^3)$. The more symmetric coordination of six oxygen atoms around the molybdenum centers (*Mo*–*O* distances of about 1.75 Å and about 2.0 Å, Table 5.6) in the structure of the precursor material is also characteristically different from that of AHM (*Mo*–*O* distances of about 1.73 Å to about 2.25 Å). The tungsten atoms exhibit a similar coordination by six oxygen atoms (Table 5.7). The XAS W *L*_{III} edge spectrum of the precursor resembles neither that of APT (Figure 5.58) nor that of tungsten in AHM. From the different evolution during the thermal treatment it can be excluded that hydrated binary metal oxides are present in the precursor. The structural evolution of the *MoVW* oxide

precursor is different from that of hydrated MoO_3 [150].

Apparently, the local structure of the precursor material is different from that of the individual starting materials used in the precursor preparation. This is in agreement with the previously reported building blocks present in the precursor solution [151]. These building blocks also deviate from the starting materials used and are strongly dependent on the preparation conditions, an important point in order to arrive at defined material with unique properties [152, 153, 154]. Spray-drying of the precursor solution seems to proceed sufficiently fast in order to maintain the characteristic local structure of the building blocks and to avoid formation of a simple mixture of AHM, APT, and vanadium oxalate. Further results on the characterization of the oxide precursor are described in literature [124]. The deviation of the precursor material from a mechanical mixture of the starting materials (i.e. AHM and APT) is also prominent in the corresponding TG/ DSC experiments (Table 5.4). The TG traces measured at different heating rates continually show the same characteristic decomposition route which indicates that a uniform homogeneity as in solution is maintained in the solid precursor.

6.1.3 Structure-activity correlation of $(MoVW)_5 O_{14}$

The onset of catalytic activity during thermal treatment of the $MoVW$ oxide precursor in propene and oxygen correlated with the simultaneous crystallization of a Mo_5O_{14} -type phase and $Mo_xV_{2-x}O_5$ (Figure 5.2, experiment A). Subsequent heating the mixed oxides in propene and oxygen resulted in a significantly lower onset temperature of catalytic activity (Figure 5.3). Apparently, formation of a long-range ordered crystalline material is a prerequisite for catalytic activity in selective oxidation of propene. However, treatment of the precursor in propene and oxygen yielded a phase mixture containing $(MoVW)_5 O_{14}$ only as a major phase. Figure 5.4 shows the XRD phase analysis of the material by Rietveld refinement containing 70% Mo_5O_{14} -type material and 30% $Mo_xV_{2-x}O_5$. In Figure 5.6 the TEM investigation confirmed the phase mixture determined by XRD.

The single phase crystalline Mo_5O_{14} -type material obtained from a two-step thermal treatment procedure (experiment E) showed the same onset temperature and catalytic behavior as the phase mixture described above. Apparently, Mo_5O_{14} indeed constitutes a potential target structure for highly active selective oxidation catalysts [61]. Therefore, we focused on the formation of crystalline and phase-pure Mo_5O_{14} -type material under varying treatment conditions. The complex relationships between the crystallinity of the resulting Mo_5O_{14} -type material and the varying thermal treatment parameters are described in the following.

6.1.4 Optimized thermal treatment conditions forming single phase $(Mo_{0.68}V_{0.23}W_{0.09})_5 O_{14}$ material

For the formation of crystalline $(Mo_{0.68}V_{0.23}W_{0.09})_5 O_{14}$ from a spray-dried $MoVW$ oxide precursor it is recommended to have gas passing through the precursor and not only flowing over it. Sufficiently high heating rates promote high crystallinity

of the final material. The optimal thermal treatment contains two steps [124]. The first treatment step in 20% oxygen/ nitrogen is performed at elevated temperature (623 K). Isothermal treatment at this temperature is required for removal of volatile decomposition products which can be monitored by MS. Essentially, the duration of the isothermal segment in oxygen/ nitrogen has to be adjusted to the respective gas flow. The second thermal treatment in 100% helium at 713 K is required for removal of last gaseous decomposition products and subsequent crystallization of the material. Again, the duration of the isothermal segment is adjusted to the gas flow and depends on the entire removal of last decomposition products.

Here, ca. 160 mg *MoVW* oxide precursor were heated with 3-4 K/min at a total flow of 100 ml/min (ca. $\frac{1}{3}$ of the gas flowing through the sample). Under these conditions isothermal segments of 3 h at both temperatures turned out to be appropriate.

6.1.5 Influence of redox potential of the gas phase

Assuming metal(V) and metal(VI) centers, the average valence of the metal centers in Mo_5O_{14} -type materials requires 40% of metal(V) centers to be present besides 60% metal(VI) centers. Apparently, 23% vanadium present as vanadium(V) centers in $(MoVW)_5O_{14}$ together with only molybdenum(VI) and tungsten(VI) centers cannot account for the average valence. Therefore, a considerable fraction of the metal centers needs to exhibit a partially reduced average valence. This is in line with findings on propane oxidation catalysts which were catalytically inactive after calcination in air but achieved reasonable performance after calcination in inert [153]. Especially at high temperature calcination the presence of oxygen was reported to be detrimental. Complete oxidation of the metal centers during thermal treatment has to be prevented. Therefore, in agreement with literature [76] the thermal treatment of the precursor in a one-step procedure in oxygen/nitrogen at 713 K resulted in the formation of a mixture of crystalline $(MoVW)_5O_{14}$ material and some unidentified phases.

XAFS [155] investigations on $Mo_8V_2W_yO_x$ stated an average oxidation state of vanadium between +4 and +5 in the thermally treated precursor. In an earlier study [64] it was shown that the thermal treatment of *MoVW* oxide precursor in inert gas may increase defects in the oxide structure that enhance the catalytic activity [156].

Previously the importance of the thermal treatment for the final phase composition and catalytic performance has been observed for partially Mo_5O_{14} -type *MoVNb* oxides [63]. XPS investigations confirmed the influence of the oxygen vacancies on the oxidation states of molybdenum and vanadium [64]. In line with that, molybdenum and vanadium centers in crystalline $(MoVW)_5O_{14}$ material obtained from a two-step procedure (623 K in oxygen/nitrogen, 713 K in helium) maintained a partially reduced average valence. Thermal treatment in oxygen at about 623 K is required for an oxidation of oxalate and ammonia as a prerequisite for the formation of Mo_5O_{14} -type structure and the crystallization process. On the one hand, thermal treatment of the precursor at 713 K is required to initiate crystallization and formation of long-range ordered $(MoVW)_5O_{14}$. On the other hand, treatment of the precursor at 713 K in oxygen results in an undesired further oxidation of the metal centers and formation of additional phases.

Here, a two-step thermal treatment in the preparation procedure appears to be inevitable to obtain phase pure and crystalline Mo_5O_{14} -type materials. Apparently, the sensitivity of the resulting material on the thermal treatment applied is caused by intermediates in the formation of the final bulk and surface structures. Later on the intermediates can form different components depending on treatment conditions and the difficulty is that both, final bulk and surface structures, have to be in appropriate state. In case of $(MoVW)_5 O_{14}$ this includes an oxidizing atmosphere for the formation of the bulk Mo_5O_{14} -type structure (and not the mixed metal dioxide MO_2 with $M = Mo, V, W$). The intermediates formed in oxygen at lower temperatures up to 623 K can be directed to different structures with proper treatment at higher temperature of 713 K. Treatment in inert gas maintained the Mo_5O_{14} -type structure during slight reduction of the surface.

6.1.6 Removal of oxalate, nitrate, and ammonia

A strong dependency of the polycondensation process on the gas phase was observed for AHM [90]. There different products formed during thermal treatment under static conditions or flowing gas. Here, the removal of oxalate, nitrate, and ammonia during treatment of the precursor is affected by the gas flow rate and the dwell time at 623 K (Figure 5.17).

Apparently, a suitable combination of gas flow rate and dwell time has to be selected to sufficiently remove oxalate, nitrate, and ammonia. This is a prerequisite for the crystallization of $(MoVW)_5 O_{14}$ during the subsequent treatment in helium at 713 K. A small flow rate may partially be compensated for by an increased dwell time and vice versa. Amorphous material remaining after the treatment in helium may crystallize under selective oxidation conditions. However, no single phase Mo_5O_{14} -type material will be obtained. A different crystallinity of the Mo_5O_{14} -type oxides obtained from treatment of the precursor in oxygen/nitrogen or oxygen/helium was observed. Treatment of the precursor in 20% oxygen/helium at 623 K resulted in an X-ray amorphous material after the subsequent thermal treatment in helium at 713 K. Conversely, phase pure crystalline $(MoVW)_5 O_{14}$ was obtained when oxygen/nitrogen were used at 623 K. The influence of helium on the thermal treatment is clearly visible in the evolution of the gas phase during the first step at 623 K. NO_2 was formed in three distinct steps during treatment of the precursor in oxygen/ nitrogen. Conversely, evolution of NO_2 in oxygen/ helium occurred in two steps and is shifted to higher temperature. These results indicate the sensitivity of the decomposition route described here on various parameters. Possibly nitrogen with its higher density offers a better sweeping effect than helium. Even the slightly different physical properties of the diluting gas used may considerably alter the properties of the resulting mixed oxide material.

6.1.7 Structural changes during first calcination step

Comparison of in situ XANES spectra (Figures 5.60, 5.62 and 5.63) revealed that the linkage of the structural units present in the precursor during formation of the Mo_5O_{14} -type structure occurs in the first thermal treatment step at 623 K. After the first step

the formation of the local structure is completed and presumably corresponds to the nanocrystalline material mentioned in literature [68, 157]. The resulting structure exhibited a local coordination of the three metal centers that is very similar to that of crystalline $(MoVW)_5O_{14}$. Apparently, the second treatment step in helium is required for complete removal of ammonia, nitrate, and oxalate. Subsequently, crystallization of the long-range ordered Mo_5O_{14} -type structure occurs. Therefore, the discussion of the evolution of the local structure of the precursor during thermal treatment will focus on the first thermal treatment step.

Structural changes during thermal treatment of the precursor exhibited an onset of about 400 K (Figures 5.61, 5.62 and 5.65). The XAS and TG data compared in Figure 5.66 were measured at a heating rate of 1 K/min. Therefore temperature differences of 10 or 20 K discussed in this section are real. The evolution of the V K pre-edge peak height indicates a reversible change in the local structure around the vanadium centers (Figure 5.62). The minimum observed in the average vanadium valence at 470 K coincided with the onset of the second mass loss in TG. This mass loss corresponded mainly to the release of ammonia, nitrate, water, and oxalate. A decrease in the V K pre-edge peak height is indicative of an increase in the symmetry of the local oxygen coordination around the vanadium center. During re-oxidation of vanadium at temperatures above 500 K the symmetry decreased again, possibly due to formation of the Mo_5O_{14} -type structure. The evolution of the local structure around the tungsten centers exhibits a comparable behavior. Significant structural changes around the tungsten centers correlate with the second mass loss at about 470 K. An increasing amplitude of the tungsten-oxygen shell in the $FT(\chi(k) * k^3)$ and a decrease in tungsten-metal distances indicate an intermediate increase in the symmetry of the local structure around the tungsten centers (Figure 5.65 and 5.66).

Loss of ammonia, nitrate, and oxalate from the precursor structure is a prerequisite for the formation of the Mo_5O_{14} -type structure by polycondensation of the precursor subunits. A first maximum in the evolution of CO_2 from decomposition of oxalate occurred at about 450 K. This coincided with the structural changes around the vanadium centers that preceded the changes in the local structure around the molybdenum and tungsten centers. It seems that the oxalate ligands are coordinated to vanadium centers in the precursor structure. Conversely, evolution of ammonia and water coincided with the structural changes around molybdenum and tungsten centers. The minor exothermic DSC signal at 509 K (Figure 5.44) may be correlated with the formation of the Mo_5O_{14} -type structure. This exothermic DSC signal occurs after the evolution of the gaseous decomposition products. The corresponding changes observed in the local structure around the various metal centers corroborate the formation of Mo_5O_{14} -type structure at this temperature. This temperature of bond formation and the crystallization at 713 K in helium is lower than the range of 800-820 K reported in literature [158] for the crystallization of Mo_5O_{14} -type mixed $MoVW$ oxide precursor. Presumably the lower temperature of crystallization can be explained by the different gas phase and heat treatment that causes different kinetic and thermodynamic conditions.

The decomposition route of the precursor encompasses structural rearrangement around the vanadium centers followed by restructuring around the molybdenum and tungsten

centers. This sequence prevents the formation of binary molybdenum oxide, vanadium oxide, and tungsten oxide. Prior to crystallization of the Mo_5O_{14} -type structure a more symmetric but metastable intermediate forms below 500 K. Apparently, the structure of the polyoxometallates in solution constitutes a precursor for the formation of the building blocks of the Mo_5O_{14} -type structure. The increase in symmetry around the various metal centers corresponds to a release of structural constraints and the formation of a more open and reactive polyoxometallate capable of condensing into the Mo_5O_{14} -type structure. The presence of a reactive intermediate phase is indicative of the sensitivity of the decomposition route of the precursor to the Mo_5O_{14} -type structure. Even slight deviations from the optimized treatment conditions will result in the formation of less crystalline or multiple phase materials. Similarly, a strong dependence of the product on the treatment conditions was recently observed for the thermal decomposition of $Nd_2Mo_4O_{15}$ [159]. There the proper treatment conditions gave access to the new non-equilibrium phase $Nd_6Mo_{10}O_{39}$. Likewise the formation of $VNbO_4$ catalyst from precipitate is reported to be strongly dependent on the treatment conditions [160]. Obviously the formation of a certain phase can be directed by control of the preparation conditions.

6.1.8 TG/ DSC investigation of calcination

TG/ DSC data obtained at heating rates 10 K/min, 5 K/min, and 3 K/min were used for kinetic analysis of the first treatment step of $MoVW$ oxide precursor. The first derivative of the TG traces (Figure 5.54) shows a correlation between points of equal partial mass loss and decomposition temperatures over all heating rates. The linear relation indicates the validity of kinetic laws. More information can be extracted using the DSC curve where four signals can be distinguished (the TG curve only gives access to three). The Arrhenius plots shown in Figure 5.55 present the maximum change in the DSC curve over the corresponding reciprocal temperature. In a linear fit through the three data points activation energies of 19 kJ/mol (endothermic first step of mass loss), 38 kJ/mol (endothermic event during second step of mass loss), 173 kJ/mol (exothermic event during second step of mass loss), and 121 kJ/mol (exothermic third step of mass loss) are calculated from the slope. The second step of mass loss in TG (which covers about 50% of the total mass loss) is an overlap of an endothermic and an exothermic process in the DSC curve. The overlapping DSC signals flatten the maximum change of the endothermic DSC signal (slope DSC) and apparently shift it to lower temperatures. In the Arrhenius plot the lower temperature shifts the data point to the right in x-direction and the lower maximum change of the DSC signal (slope DSC) downward in y-direction, both leading to decreased values of activation energy that is calculated from the slope of the linear fit through the data points. Therefore, the activation energies calculated from the Arrhenius plots are apparent values and not absolute numbers. The real value of activation energy is expected to be higher. In order to get more reliable activation energies a model-free analysis (Friedman-Analysis) of the TG curves at heating rates of 10 K/min, 5 K/min, and 3 K/min (Table 5.5) was applied. Even though in the TG traces and its derivatives only three distinct steps of mass loss are observed four regimes of apparent activation energies

were calculated from the data series. The values of activation energies determined by Friedman-Analysis are higher than those calculated from the Arrhenius plot as it is expected for the overlapping of an endothermic and an exothermic process. In the range of the third decomposition step the values of the activation energy are less reliable due to the increasing errors. This could be due to the end of the heating ramp or indicate that another reaction mechanism occurs (e.g. parallel reactions).

The spread of data points is less for the first decomposition step and the exothermic event during the second decomposition step. In the first decomposition step the loss of physisorbed water is a nearly separated decomposition step that does not overlap with another one. The Arrhenius approach and Friedman plot are valid here. The fact that the first two processes observed by DSC are endothermic leads to the assumption of decomposition steps, which is supported by the evolution gaseous products. The last two processes are exothermic, which can be interpreted as a phase transformation, in this case a bond formation of the Mo_5O_{14} -type structure. Phase transitions usually occur at well-defined temperatures and the relatively small spread of data points in the Arrhenius plot of the exothermic event during the second decomposition step corroborates the structure formation. In this process the precursor units, most likely polyoxometallates, are linked three-dimensional and form the Mo_5O_{14} building blocks. These building blocks could be a disordered predecessor of the Mo_5O_{14} -type structure. The relatively high absolute values of apparent activation energies obtained from the kinetic analysis indicate that the underlying process is structural rearrangement in a solid.

6.1.9 Anisotropic crystallization of the Mo_5O_{14} -type structure

Studies on $MoVNb$ oxide catalysts for the selective oxidation of ethane reported a strong but diffuse X-ray reflection near 4.00 \AA [161], that corresponds to the distance of two corner-sharing octahedra and which is the lattice constant in (001) direction of e.g. Mo_5O_{14} -type structures, M1- and M2 phase.

Previous studies on amorphous colloids have found an anisotropic crystallization along the (001) axis in orthorhombic, trigonal, and hexagonal structures [162]. Similarly, on the route to the tetragonal Mo_5O_{14} -type structure an anisotropic crystallization process is observed. During the crystallization of the Mo_5O_{14} -type structure from the precursor as shown in Figures 5.2 and 5.14 the first peak that occurs in the diffraction pattern is the (001) reflection. Actually, in the first step of the two-step calcination procedure (Figure 5.13) this reflection is extremely broadened. The anisotropic crystallization seems characteristic for the Mo_5O_{14} -type structure as it is observed under calcination conditions (experiment D) as well as under thermal treatment in propene and oxygen (experiment A). Apparently, the structure formation starts with chains of corner-sharing MO_6 -octahedra ($M = Mo, V, W$). Prior to crystallization the chains orientate towards direction of the c-axis, seen as diffuse broad reflection in XRD. This happens in the first step of the two-step thermal treatment procedure. Later in the second step after removal of oxalate, nitrate, and ammonia the periodicity of the structural motifs of the Mo_5O_{14} -type structure is established. At the beginning of the crystallization the condensation of the building blocks into a compact three-dimensional

aggregate is favored and perpendicular to that direction the structure remains disordered in the ab-plane, seen as growth of the (001) reflection. The similarity of the XANES spectra of molybdenum, vanadium and tungsten after the first and second treatment step (Figures 5.60, 5.62 and 5.63) approve the assumption that the characteristic structural motifs of the Mo_5O_{14} -type structure and the proper arrangement of elements are already present after the first treatment step, but are not periodically linked in the ab-plane. Possibly the pentagonal columns (pentagonal bipyramids with edge-sharing octahedra) are formed in the first calcination step. In the second thermal treatment the arrangement of the regular arrangement of the pentagonal columns to one another is established.

TEM images detected spherical particles from spray-drying, crystalline domains, and irregularly shaped aggregates (Figure 5.11). A different extent of long range order in the crystallographic directions was detected by XRD during formation of the Mo_5O_{14} -type structure. Principally anisotropic crystallization is not expected to form spherical particles and aspherical particles do not provide optimum diffusion conditions. Accordingly, the dwell times for the treatment and removal of ammonia, nitrate, and oxalate from the precursor material are elongated.

6.1.10 Structure formation of $(MoVW)_5O_{14}$

A previous study on the deactivation characteristics of an acrolein oxidation catalyst [163, 164] ($Mo_{12}V_3W_{1.2}Mn_3O_{53}$) elucidated the kinetics of crystallization in air and nitrogen. The authors concluded that the activity of the material is related to the presence of an amorphous phase. Crystallization and formation of long-range ordered phases coincided with the deactivation of the catalyst. Conversely, the $(MoVW)_5O_{14}$ catalyst described here exhibited a correlation between the formation of a crystalline Mo_5O_{14} -type structure and the onset of catalytic activity (Figures 5.2 and 5.57).

The two-step thermal treatment procedure [124] referred to in the literature has been developed empirically. Nevertheless, no detailed insight to the underlying mechanism was provided. In analogy to AHM [90] the process can be seen as an abstraction of excess oxygen from the terminal positions and the removal of ammonium ions leading to sequential condensation. This is achieved by polycondensation during thermal decomposition of the polyoxometallates.

From the results described here, a good understanding emerges of the necessity to use a two-step procedure to obtain phase pure and crystalline Mo_5O_{14} -type structured material because the polycondensation proceeds depending on the kinetic and thermodynamic conditions defined by the gas phase. An oxidizing atmosphere at moderate temperatures (about 600 K) is required for the re-oxidation of the metal centers after release of gaseous decomposition products, polycondensation, and formation the local arrangement of the Mo_5O_{14} -type structure. However, formation of a long-range ordered crystalline Mo_5O_{14} -type structure requires complete removal of ammonia, nitrate, water, and oxalate at an increased temperature. This treatment has to be performed in helium to avoid further oxidation of the metal centers, decomposition of Mo_5O_{14} -type material, and formation of phase mixtures.

6.1.11 Direct morphology imaging by TEM

The crystallinity and phase composition of the calcined material were directly investigated by TEM. Three different morphologies were found in the samples: spherical particles as formed during spray-drying [124], crystalline material, and irregularly shaped particles.

The occurrence of these three morphologies in the samples correlates to the degree of crystallinity as observed by XRD. In X-ray amorphous material that still contained oxalate, nitrate, and ammonia (either treated at low gas flow rate or at shortened dwell time in the first treatment step), spherical particles besides crystalline material and irregularly shaped particles were detected (Figure 5.11). At higher gas flow rate or dwell time in the first treatment step oxalate, nitrate, and ammonia are efficiently removed and consequently in the TEM images only crystalline material was detected (Figure 5.20). Apparently, the irregularly shaped particles are present after the collapse of the spherical particles and before formation of crystalline domains.

The question if the irregularly shaped particles are the intermediate state during the structural rearrangement from *MoVW* oxide precursor into $(MoVW)_5O_{14}$ or amorphous $(MoVW)_5O_{14}$ cannot be solved. The irregularly shaped particles were always accompanied by crystalline material and spherical particles, so eventually they are a mixture of Mo_5O_{14} building blocks separated by precursor material. Due to the XAS results it could be that in the irregularly shaped particles the coordination of vanadium by oxalate etc. is removed and rearranges with molybdenum and tungsten centers to Mo_5O_{14} building blocks. The coordinatively unsaturated metal centers in an irregularly shaped particle are sensitive to the oxygen partial pressure in the gas phase. Therefore, before removal of last precursor material between the Mo_5O_{14} building blocks at 773 K the atmosphere is changed to inert. Crystallization, even in nanocrystalline domains, occurs only after removal of last precursor material between the Mo_5O_{14} building blocks.

The assignment of the observed lattice fringes to the Mo_5O_{14} -type structure suggests that the surface topology of the particles differs not significantly from the bulk structure. The surface termination as observed by TEM (Figures 5.12, 5.21, and 5.23) is not representing the slightly preferred bulk orientation in (001) direction of the crystalline particles observed in the XRD refinement. The [3418] zone axis is a diagonal view on pentagonal columns truncated so that the pentagonal block units (pentagonal bipyramids with edge-sharing octahedra) have different amount of edge-sharing octahedra. The (110) plane, (200) plane and (120) plane are different views on the pentagonal columns and chains of edge-sharing octahedra along the c-axis. The planes have a 'furrow'-structure made of corner-sharing octahedra which are separated by pentagonal block units. Some pentagonal block units are partly depleted of their edge-sharing octahedra.

6.1.12 Perspectives from reduced mixed metal dioxide

Interestingly, the *MoVW* oxide precursor directly heated in helium to 773 K for 2 h forms an X-ray crystalline MoO_2 -type phase, even though the MS traces still show evo-

lution of ammonia, nitrate, water, and oxalate. In line with the incomplete removal of ammonia, nitrate, water, and oxalate the TEM images reveal spherical particles. Eventually, if the spherical particles were less after the oxidation of the thermally treated material a higher amount of $(MoVW)_5 O_{14}$ can be expected. It has to be pointed out, that the formation of the MoO_2 -type phase from the $MoVW$ oxide precursor proceeds completely different from the formation of $(MoVW)_5 O_{14}$.

In isothermal redox experiments described in Paragraph 5.8 the re-oxidation of reduced $(MoVW)_5 O_{14}$ shows that it is possible to obtain the Mo_5O_{14} -type structure via oxidation of a mixed metal oxide in MoO_2 -type structure. This offers an alternative preparation route to $(MoVW)_5 O_{14}$, maybe avoiding the described preparation from solution and calcination. It indicates that the way to the Mo_5O_{14} -type structure is not blocked when the mixed metal oxide precursor has linked in a long range ordered three-dimensional structure as MoO_2 -type. From the mixed metal dioxide the Mo_5O_{14} -type structure can be formed if the structure contains the proper metal center ordering. This metal center ordering is maintained at 773 K in propene atmosphere and does not rapidly transform into the binary metal dioxides MoO_2 , VO_2 , and WO_2 .

6.2 Structural characterization of $(MoVW)_5O_{14}$ and $(MoV)_5O_{14}$

6.2.1 XRD investigation of $(MoVW)_5O_{14}$ and $(MoV)_5O_{14}$

The structure model based on the Mo_5O_{14} -type structure (ICSD [27202]) adequately describes the experimental XRD patterns (Figures 5.69). From that sufficient phase purity for extended structure analysis was assumed. The results of the two alternative refinement strategies that were tested on each experimental XRD pattern (Table 5.8) suggest a homogeneous site occupancy in $(MoV)_5O_{14}$. This result is based on the good agreement of the structure model with refined site occupancy factors and the alternative refinement of ' Mo_5O_{14} ' + ' V_5O_{14} '. In a statistical distribution of elements on all sites, the refinement of site occupancy factors should work as well as refinement of one structure per metal. Conversely, a preferred site occupancy was obtained for $(MoVW)_5O_{14}$. The alternative refinement of ' Mo_5O_{14} ' + ' V_5O_{14} ' + ' W_5O_{14} ' does not describe the experimental XRD pattern of $(MoVW)_5O_{14}$ as good as the refinement of site occupancy factors. In $(MoVW)_5O_{14}$ the higher site occupancy factors on positions Mo1 and Mo6 indicate the site preference of tungsten for the pentagonal bipyramidal site in and octahedra edge sharing to the pentagonal bipyramidal site. Position Mo3 in $(MoVW)_5O_{14}$ has the lowest site occupancy factor indicating a preferred occupation by vanadium.

6.2.2 Investigation of XAFS refinement strategy on simulated data

In literature several cases of averaging distances in a complex or unknown material were applied successfully [136, 137, 138]. The model of average distances for the XAFS refinement was derived from the structure model obtained in refinement to the experimental XRD pattern (Table 4.2). Then the model of average distances and the XAFS refinement strategy were applied to XAFS simulations of the complete structure (Table 4.3). The evaluation aims at differences that indicate an (in)homogeneous distribution of elements on the six crystallographic sites.

The general result of averaging regardless of structural (dis)order is a decrease in the Debye temperature of the major elements in the compound (Table 5.9-5.12). The applied refinement strategy was able to exclude metal-metal distances in the structure model that were the absent ones in the simulated $\chi(k)$ (S2 and S4 Tables 5.10 and 5.12, coordination number of zero). A decrease in the coordination numbers of the metal-metal shell can be either because of averaging the distances in the XAFS structure model in a structurally disordered system (S1) or because of thermal disorder in a structurally ordered system (S4). An increase in the coordination numbers of the metal-metal shell can be either the effect of averaging in a structurally ordered system (S2) or effect of thermal disorder in a structurally disordered system (S3).

For interpretation of a high coordination number in the metal-metal shell it needs to be known whether thermal or structural disorder dominates the system. The prevailing

sort of disorder can be estimated from analysis of the metal-oxygen shell. In the simulated data the metal-oxygen shell seems little effected from the structural (dis)order contained in the metal-metal shell, and independently provides information on the extent of thermal disorder. A decrease in the coordination numbers of the metal-oxygen shell is an effect of averaging the distances in the XAFS structure model describing a structurally disordered system (S1). An increase in the coordination numbers of the metal-oxygen shell is an effect of averaging in a structurally ordered system (S2). Thermal disorder additionally increases the coordination numbers of the metal-oxygen shell (S3 and S4).

6.2.3 XAFS refinement of $(MoVW)_5 O_{14}$ and $(MoV)_5 O_{14}$

The low coordination numbers of molybdenum-oxygen and vanadium-oxygen scattering paths of $(MoV)_5 O_{14}$ indicate low thermal disorder and therefore structural information may be extracted from the experimental data. The refinement results of the experimental $(MoVW)_5 O_{14}$ and $(MoV)_5 O_{14}$ are compared to the simulation at 5000 K Debye temperature (not thermally disordered system).

Decreased amplitudes were obtained for the metal-metal shell of the XAFS spectra at all edges measured for $(MoVW)_5 O_{14}$ compared to $(MoV)_5 O_{14}$. The maximum in the amplitude in the metal-metal shell is highest in $(MoV)_5 O_{14}$ at the Mo K edge (Figure 5.74). High amplitudes occur in case of positive interference of scattering paths, which is most likely in well-ordered structures and at low thermal disorder. The high amplitude of $(MoV)_5 O_{14}$ indicates small deviations from the single crystal structure. This may be because of the higher content of foreign ($V+W$) atoms in the molybdenum matrix of $(MoVW)_5 O_{14}$ (23% V and 9% W) than in $(MoV)_5 O_{14}$ (9% V). The shape of the amplitudes in the metal-metal shell of the experimental XAFS spectra at all edges measured for $(MoV)_5 O_{14}$ and $(MoVW)_5 O_{14}$ are significantly different. The shape of the amplitude that is determined by the different amount of neighbors at short or long distances is characteristic for each element. The short metal-metal distance in the experimental XAFS spectra of $(MoVW)_5 O_{14}$ showed significantly different amplitudes at all three edges (Figure 5.73). At the W L_{III} edge the short distances in the tungsten-metal shell of the XAFS spectrum are stronger pronounced than in the experimental XAFS spectra measured at the Mo K and V K edge of $(MoVW)_5 O_{14}$. Apparently, tungsten occupies the coordination geometry with the highest amount of short metal-metal distances, the pentagonal block unit (pentagonal bipyramids with edge-sharing octahedra). Conversely, the experimental XAFS spectrum measured at the V K edge shows the most prominent scattering paths in the range of the long vanadium-metal distance which indicates corner-sharing linkage to all neighboring metal centers and the short metal-metal distance is less pronounced than in the experimental XAFS spectra from Mo K and W L_{III} edges. The XANES investigations in Paragraph 5.8.2 revealed the average valence of vanadium between +4 and +5. The reduced valence compared to V_2O_5 increases the ionic radius and stabilizes vanadium when substituting the larger molybdenum. The binary vanadium oxide V_4O_9 (ICSD [15041]) contains vanadium in both valence states as $(MoVW)_5 O_{14}$. This structure has squared pyramidal coordination with two groups of vanadium-oxygen distances: 1.58-1.65 Å and

1.86-2.0 Å. The two groups of vanadium-oxygen distances agree with the refinement results obtained from the experimental XAFS spectrum of $(MoVW)_5 O_{14}$, where the long vanadium-oxygen distance at about 2.3 Å was not detected (Table 5.14).

6.2.4 Characterization of $(MoVW)_5 O_{14}$ and $(MoV)_5 O_{14}$

The data obtained from XRD refinement agree with the results of the XAFS structure investigation for both measured samples. In the experimental XAFS spectra of $(MoV)_5 O_{14}$ all three molybdenum-vanadium distances are detected from Mo *K* and V *K* edge. This is in agreement with the homogeneous distribution of molybdenum and vanadium on all sites as found in the XRD investigation. Only one vanadium-vanadium distance is found in the XAFS refinement besides the three molybdenum-vanadium distances. This finding supports a homogeneous distribution of vanadium in a molybdenum matrix. The low vanadium content (9%) in the sample makes further significant vanadium-vanadium distances unlikely.

The refined site occupancy factors in the structure model refined to the experimental XRD pattern of $(MoVW)_5 O_{14}$ indicate a preferred site occupancy of vanadium and tungsten in the Mo_5O_{14} -type structure. If tungsten was mostly located on the pentagonal bipyramidal site and the neighboring octahedra (position Mo1 and Mo6) this confirms the strongly pronounced short molybdenum-tungsten distance found in the XAFS refinement. By XRD vanadium is preferably located in octahedra that are only corner sharing with their neighbors (position Mo4). On this site the most frequent distance corresponds to the middle molybdenum-vanadium distance as found in the XAFS structure model of $(MoVW)_5 O_{14}$.

Regarding the question if vanadium exclusively occupies the pentagonal bipyramidal sites like its heavy analogue tantalum, this seems not to be the case. In $(MoV)_5 O_{14}$ vanadium is rather homogeneously distributed on all sites, presumably because the small vanadium does not sufficiently stabilize the pentagonal bipyramidal coordination geometry. In $(MoVW)_5 O_{14}$ it was up to now unclear which metal site is occupied by vanadium and tungsten. The preferred site occupancy of tungsten in and directly neighbored to the pentagonal bipyramidal sites in $(MoVW)_5 O_{14}$ may be the reason for its structure stabilizing and structure directing effect. Vanadium in $(MoVW)_5 O_{14}$ prefers octahedrally coordinated sites Mo3 and Mo4 (Figure 4.5) which are only corner-sharing with their neighbors. On these sites vanadium is stabilized by the more flexible coordination geometry than in the more rigid pentagonal bipyramidal block units. Apparently, $(MoV)_5 O_{14}$ has a distribution of both metals on all sites, whereas in $(MoVW)_5 O_{14}$ a preferred site occupancy of vanadium and tungsten in a molybdenum matrix occurs. Since the metals contained in the compounds under investigation have different characteristic coordination geometry, atomic radii, and redox potentials they are assumed to prefer one or the other coordination environment of oxygen anions and stabilize or destabilize the short metal-metal distances at the pentagonal bipyramidal block units. The observed ordering helps explaining the structural stability, catalytic activity and selectivity obtained for $(MoVW)_5 O_{14}$.

6.3 Bulk structural properties of $(MoVW)_5 O_{14}$ and $(MoV)_5 O_{14}$

6.3.1 Average valence of molybdenum

For the determination of the average valence of molybdenum with XAS different approaches exist in literature. For binary molybdenum oxides the shift in the Mo K edge position of the second maximum in the XANES is determined [132]. In the mixed molybdenum oxides $MoVW$ oxide and MoV oxide this procedure can be carefully adapted and works reasonably for most spectra shown. In the XANES spectra of $(MoVW)_5 O_{14}$ and $(MoV)_5 O_{14}$ the average valence of molybdenum is less than Mo^{6+} . This is in agreement with ESR and UV/vis investigations on structure and properties of $Mo_3Nb_2O_{14}$ oxide [165]. In Figure 5.96 the molybdenum centers in the re-oxidized MoV oxide in the MoO_3 -type structure have a higher edge energy according to the second maximum in the XANES compared to a α - MoO_3 reference. Conversely, the edge of the re-oxidized MoV oxide is located at lower energy than that of the MoO_3 reference. It is chemically not reasonable to assume molybdenum with an average valence higher than Mo^{6+} as in MoO_3 . From this special situation it is reasonable to assume a slightly reduced average valence of $Mo^{5.8+}$ in the re-oxidized MoV oxide. The different local structure may be due to the incorporation of vanadium in the MoO_3 -type structure. Another possible explanation may be the presence of a minor amount of $Mo_xV_{2-x}O_5$ (e.g. ICSD [24338]) detected by XRD analysis of the re-oxidized MoV oxide material.

6.3.2 Average valence of vanadium

The average valence of vanadium in several vanadium compounds has been previously investigated by XAS [131] at the V K edge. There the XANES features that are characteristic for the respective coordination geometry (octahedral, tetrahedral etc.) are analyzed for their distortion from the ideal symmetry of the coordination polyhedron that indicates the average valence of vanadium. In case of (distorted) octahedral oxygen coordination around the vanadium centers the pre-edge peak height is analyzed. For molybdenum doped vanadium oxides in the V_2O_5 structure the shift in the V K edge position has been used [40]. This procedure is refused because it is based on binary vanadium oxides and tested on $V_{major}Mo_{minor}$ oxides. The pre-edge peak height was developed and tested on various vanadium-oxygen based compounds and seems to have a wider validity.

6.3.3 Change in unit cell volume owing to metal substitution

The long-range structural data presented indicate an influence of the vanadium centers on the geometric structure of the Mo_5O_{14} -type materials studied. $(MoVW)_5 O_{14}$ and $(MoV)_5 O_{14}$ were prepared with different amounts of vanadium (23 % and 9 %, respectively). Previously, variations of the unit cell volume were found to be consistent with changes in the ionic radii of the elements incorporated [45, 71]. Vanadium

is smaller than molybdenum and tungsten, which are nearly equal in size. The more vanadium in the structure, the smaller the unit cell volume. Accordingly, a decrease in the lattice constants (Table 5.8) and the volume of the unit cell was found with an increasing vanadium content. Likewise, the distortion of the dioxide phases obtained from reduction of the Mo_5O_{14} -type materials from the nearly rutile-type MoO_2 also increases with increasing vanadium content (Table 5.18). Hence, $(MoVW)$ dioxide possesses a smaller unit cell volume than (MoV) dioxide.

6.3.4 Effect of vanadium on electronic and geometric structure

Partially reduced vanadium centers in selective oxidation catalysts are assumed to enhance the hydrogen abstraction from hydrocarbon reactants. Accordingly, in the Mo_5O_{14} -type metal oxides investigated, the vanadium centers exhibit an average valence of less than 5 (Figure 5.98). During thermal treatment under reducing conditions, the vanadium centers are reduced prior to the molybdenum centers. Mo K XANES spectra measured during temperature programmed treatment of $(MoVW)_5O_{14}$ and $(MoV)_5O_{14}$ in 10% propene showed an onset of transformation into a MoO_2 -type structure at a temperature of about 685 K (Figure 5.88). Conversely, V K and W L_{III} XANES spectra measured during treatment of $(MoVW)_5O_{14}$ and $(MoV)_5O_{14}$ in 10% propene exhibited an onset of structural changes at about 650 K (Figure 5.88 and 5.87). In particular, a decrease in the characteristic V K pre-edge peak height at about 650 K was observed. The decreasing pre-edge peak height is indicative of an onset of reduction of the vanadium centers in the Mo_5O_{14} -type structures prior to a detectable reduction of the molybdenum centers. This may be in agreement with a participation of the vanadium centers in the active site of Mo_5O_{14} -type catalysts for selective oxidation. Conversely, the tungsten centers in the mixed oxide catalysts may rather play a structural role than being involved in the catalytic cycle. The $(MoVW)$ dioxide and (MoV) dioxide obtained from reduction of the Mo_5O_{14} -type materials exhibit a reduced average valence of the vanadium centers (Figure 5.99) compared to the molybdenum centers (Figure 5.96). This is in agreement with previous reports on the average valence of vanadium centers in vanadium oxides doped with up to 10 % molybdenum [40]. There, the authors did not detect changes in the molybdenum average valence but reduction of vanadium to preserve electro neutrality of the materials. Likewise in our material the vanadium is easier reduced than molybdenum.

6.3.5 Stabilizing effect of tungsten in Mo_5O_{14} -type structures

The two samples $(MoVW)_5O_{14}$ and $(MoV)_5O_{14}$ were transformed into a monoclinic MoO_2 -type phase (Figure 5.94) during thermal treatment under reducing conditions (10 % propene) at about 670 K and 720 K, respectively. During treatment under oxidizing conditions (20 % oxygen), the Mo_5O_{14} -type structure of $(MoVW)_5O_{14}$ was stable at 773 K (Figure 5.85). Conversely, the $(MoV)_5O_{14}$ material slowly undergoes a phase transformation into MoO_3 -type material starting at 723 K (Figure 5.90). Apparently, the $(MoVW)_5O_{14}$ material exhibited a higher stability under reducing and oxidizing conditions compared to the tungsten-free $(MoV)_5O_{14}$ material. The onset tempera-

ture of the transformation of $(MoV)_5O_{14}$ in oxygen into the MoO_3 -type structure is close to the onset temperature of the reduction of $(MoV)_5O_{14}$ in propene. On the one hand, the oxygen mobility in the oxide materials is a prerequisite for both, reduction to the MoO_2 -type phase and oxidation to the MoO_3 -type phase. On the other hand, tungsten in the $(MoVW)_5O_{14}$ material stabilizes the Mo_5O_{14} -type structure and prevents complete oxidation, even under conditions of sufficient oxygen mobility and a high oxidation potential of the gas phase. It could be that tungsten somehow inhibits, delays or hinders a structural reorganization and segregation of the metal centers in the MoO_2 -type phase. Thus, during re-oxidation the initial Mo_5O_{14} -type structure is formed.

The redox-stability of the $(MoVW)_5O_{14}$ catalyst indicates a 'folding' from corner-sharing octahedra to edge-sharing linkage accompanied by release of one lattice oxygen [157, 166]. This mechanism occurring to numerous neighbored metal centers forms a shear plane. Additionally, a mechanism that forms a pentagonal cavity by rotation of a square of four corner-sharing octahedra [167] is likely to explain the re-formation of the Mo_5O_{14} -type structure. A cation can migrate into the pentagonal cavity and thus form the pentagonal bipyramidal coordinated site with edge-sharing octahedra. The redox-stability is meaningful for the catalytic activity because after oxygen insertion into the allyl radical the respective metal site is reduced and the local structure collapses. Then re-oxidation occurs and forms back the active site.

The stabilizing and structure directing effect of tungsten in the $(MoVW)$ oxide is particularly apparent in the re-oxidation behavior of the corresponding $(MoVW)$ dioxide. The tungsten centers in the MoO_2 -type material obtained from reducing $(MoVW)_5O_{14}$ exert a strong structure-directing effect under oxidizing conditions. Eventually, re-oxidation of the $(MoVW)$ dioxide leads to the re-formation of the Mo_5O_{14} -type structure. It has been reported, that the Mo_5O_{14} -type structure can be obtained from thermal treatment of suitable molecular mixed metal precursors [124]. The corresponding reaction proceeds through a series of polycondensation steps resulting in the three-dimensional Mo_5O_{14} -type structure. It seems that it is possible to transform the tetragonal $(MoVW)_5O_{14}$ material into a monoclinic MoO_2 -type structure, and to then re-oxidize the $(MoVW)$ dioxide into the Mo_5O_{14} -type structure. This ability is most likely due to the defined cation assembly in the monoclinic structure which does not provide a driving force for further cation rearrangement.

Similar to our $(MoVW)_5O_{14}$ material, the reduction and re-oxidation properties of a $(MoVNb)_5O_{14}$ system as a suitable model catalyst have been recently discussed [168]. Most likely in the $(MoVNb)_5O_{14}$ a specific metal center ordering facilitates the reversible reduction of the Mo_5O_{14} -type structure. The $(MoVNb)_5O_{14}$ as well as the $(MoVW)_5O_{14}$ material studied here combine redox properties with a sufficient catalytic performance as it was recently reported for $MoVNbTe$ oxides [169]. Therefore, $(MoVW)_5O_{14}$ can be used as a model system for the redox behavior of the more complex $MoVTenb$ oxides applied in the selective oxidation of propane.

6.4 Catalysis of Mo_5O_{14} -type material

6.4.1 The model catalyst system $(MoVW)_5O_{14}$

Under reaction conditions no changes in the long range order of $(MoVW)_5O_{14}$ and $(MoV)_5O_{14}$ were detected (Figures 5.76, 5.81). Short range investigation did not exhibit structural changes or changes in oxidation state of the incorporated metals (Figures 5.78, 5.79 $(MoVW)_5O_{14}$, Figure 5.84 $(MoV)_5O_{14}$).

Previously, the increased activity and selectivity of a $MoVW$ oxide precursor during thermal treatment in a mixture of acrolein and oxygen was assigned to the presence of $(MoVW)_5O_{14}$ phase [65]. Similarly, a nanocrystalline Mo_5O_{14} -type structure was found for the catalysts of high activity and selectivity [68]. The crystalline, single phase $(MoVW)_5O_{14}$ obtained here under optimized treatment conditions was active in the selective oxidation of propene to acrolein and acrylic acid. Together with the findings in literature this is a strong evidence for the validity of $(MoVW)_5O_{14}$ as a model system for the selective oxidation of propene/ acrolein into acrylic acid. Therefore, it was compared to a highly active mixed oxide catalyst ($MoV_{0.3}Te_{0.23}Nb_{0.125}$ oxide [170]) and α - MoO_3 for comparison (Figure 5.75). The $(MoVW)_5O_{14}$ catalyst exhibited a smaller yield of acrylic acid than the mixed oxide catalyst, whereas the yield of acrylic acid significantly exceeded that of MoO_3 . Moreover, the $MoV_{0.3}Te_{0.23}Nb_{0.125}$ oxide catalyst exhibited an onset temperature of catalytic activity of about 500 K compared to about 620 K of the $(MoVW)_5O_{14}$ catalyst. Additionally, the $MoV_{0.3}Te_{0.23}Nb_{0.125}$ oxide catalyst significantly deactivated at about 700 K. At temperatures above 700 K, the activity of the $MoV_{0.3}Te_{0.23}Nb_{0.125}$ oxide material approaches that of the $(MoVW)_5O_{14}$ catalyst. The different behavior of the two active catalysts indicates an additional functionality of the $MoV_{0.3}Te_{0.23}Nb_{0.125}$ oxide that is not present in the $(MoVW)_5O_{14}$ catalyst. This functionality may account for the low temperature activation of propene and it appears to deteriorate at elevated temperatures.

The crystalline $(MoVW)_5O_{14}$ model catalyst is active and selective in the oxidation of propene to acrylic acid. This distinguishes it from α - MoO_3 . Apparently, understanding the catalytic properties of crystalline $(MoVW)_5O_{14}$ constitutes only one step towards an understanding of highly active mixed oxide catalysts like $MoV_{0.3}Te_{0.23}Nb_{0.125}$ oxide that are active for the direct conversion of propane to acrylic acid.

6.4.2 Structure-functionality correlation of $(MoVW)_5O_{14}$ and $(MoV)_5O_{14}$ for different products in catalysis

In the selective oxidation of propene on the $(MoVW)_5O_{14}$ catalyst the formation of both, acrolein and acrylic acid was observed. But on a $(MoV)_5O_{14}$ only the formation of acrolein was detected (Figures 5.76 and 5.81, respectively), even though studies in literature [46, 56, 171, 172, 173, 174] prove the formation of acrylic acid on MoV oxides (not single phase Mo_5O_{14} -type structure). It can not be excluded that the absence of acrylic acid on the $(MoV)_5O_{14}$ catalyst in Figure 5.81 was due to the reaction conditions (e.g. reactor geometry, space velocity) or detection limit of the MS. Certainly the formation of acrylic acid is much higher on a $(MoVW)_5O_{14}$ catalyst than

on a $(MoV)_5O_{14}$ material and this finding is elucidated with respect to structural and chemical differences.

Both model catalyst materials exhibited the Mo_5O_{14} -type structure which was stable under reaction conditions (Figures 5.76 and 5.81), hence the different product distribution can not be attributed to another target structure. Despite of that $(MoVW)_5O_{14}$ and $(MoV)_5O_{14}$ differ in their chemical composition; the amount of vanadium (23% and 9%, respectively), and the presence, respectively absence of tungsten. Considering the concept of an active site it requires a specific ensemble of metals at the surface that is more likely to occur if the bulk structure forms a similar structural motif. Even though the structure of $(MoV)_5O_{14}$ may be promising the chemical composition and/or metal center ordering is inappropriate being detrimental to the catalytic performance. The different product distribution observed on $(MoV)_5O_{14}$ and $(MoVW)_5O_{14}$ could be an effect of the homogeneous and heterogeneous metal site occupancy that is directly resulting from the different metal composition. The different chemical composition of $(MoVW)_5O_{14}$ and $(MoV)_5O_{14}$ may favour another chemical and structural surface termination in the same manner or as a result of the preferred metal site occupancy in $(MoVW)_5O_{14}$ and homogeneous site distribution of metals in the bulk structure of $(MoV)_5O_{14}$. This is even more likely as the TEM images obviously show a surface topology that resembles termination of the bulk.

Changing selectivity as a result of another metal site occupancy could also be explained by the concept of site isolation. Similarly, the distribution of elements in the M1 phase of the $MoVNbTe$ oxide catalyst system was elucidated on the corresponding $MoVTaTe$ oxide [175]. A characteristic site occupancy for the different elements incorporated was found. Additionally, the substitution of Nb by Ta changed the crystal morphology and catalytic performance, even though $MoVNbTe$ oxide and $MoVTaTe$ oxide were both M1 phase materials. Therefore, the heterogeneous site occupancy like that determined in the $(MoVW)_5O_{14}$ material is assumed to be a necessary condition for its catalytic activity and selectivity.

6.4.3 Reaction mechanism for the selective oxidation of propene

Previous studies on binary Mo oxides have shown formation of acrolein from propene [80]. The different product distribution obtained for $(MoVW)_5O_{14}$ and $(MoV)_5O_{14}$ suggests different activation mechanisms (or activating functionalities) for the formation of acrolein and acrylic acid as it was reported for $MoVCu$ oxides [176].

The data presented in this work show the formation of acrolein on $\alpha-MoO_3$, $(MoV)_5O_{14}$, $(MoVW)_5O_{14}$ and $MoVTeNb$ oxide. Additionally, on $(MoVW)_5O_{14}$ and $MoVTeNb$ oxide the structural and chemical circumstances allow the formation of acrylic acid.

On $(MoVW)_5O_{14}$ different onset temperatures and curve shape over the investigated temperature range were detected for the formation of acrolein and acrylic acid. Eventually, two different types of functionalities are assumed necessary for the formation of acrolein and acrylic acid. Tungsten in the $(MoVW)_5O_{14}$ could be more than just a structure-stabilizing agent. Its inhomogeneous distribution and structure-directing properties could enable site-isolation and redox-stability of the active surface species. Another more general statement can be drawn from comparison of the catalytic per-

formance of $(MoV)_5O_{14}$ and $(MoVW)_5O_{14}$. For the catalytic activity of a material it matters which reaction is investigated, even though all are selective oxidation reactions based on C_3 hydrocarbons. The often used approach that homologous hydrocarbons or to a different extent oxidized derivatives of the same hydrocarbon are treated the same in selective oxidation, or making no differentiation between oxidation and ammoxidation, needs to be taken with care. The active sites required for activation of different homologous hydrocarbons or to a different extent oxidized derivatives of the same hydrocarbon may deviate as in case of $(MoV)_5O_{14}$ and $(MoVW)_5O_{14}$. Even though the bulk structure may not be effected, the presence of active sites and the underlying reaction mechanism on the catalyst can be totally different due to its metal composition.

For the $(MoVW)_5O_{14}$ catalyst a 'core-shell model' was suggested [64, 177]. According to that the core consists mostly of Mo_5O_{14} -type oxide, and the 'shell' has a higher degree of reduction and an unknown structure. The 'core' and the 'shell' may act differently in the catalytic process. While the 'shell' provides a high number of active sites and allows fast surface oxygen diffusion, the 'core' may act as the electron-accepting reservoir. The bulk structure of the core could act as imprinting matrix for the metal arrangement in the outermost layer.

TEM investigations of $(MoVW)_5O_{14}$ have shown a surface termination that is conform with the bulk structure. Still, the unknown surface termination, e.g. Figure 5.21, may serve as the 'shell' around the Mo_5O_{14} -type core. This 'shell' could be some nanocrystalline $(MoVW)_5O_{14}$ material like described [68].

The selective oxidation of propene on *BiMo* oxides is theoretically explained with an experimentally [178, 179] and theoretically [7, 180] convenient mechanism. The proposed mechanism requires three neighbored metal sites, one of them molybdenum, two others bismuth. The bismuth site activates the $C - H$ bond and then the allyl radical is adsorbed on the molybdenum for oxygen insertion. Like this metal ensemble, on $(MoVW)_5O_{14}$ the proximity of certain metal centers that sufficiently activate the $C - H$ bond but do not directly oxidize propene to CO_2 may be important for the reaction. Due to the electronic peculiarity of bismuth an electron lonepair is assumed to participate in the O_2 chemisorption, reduction and dissociation. On $(MoVW)_5O_{14}$ the partial reduced metal centers provide lonepairs for the O_2 chemisorption. Because of the partial reduction a strongly structure stabilizing agent (tungsten) that re-directs and preserves the linkage of polyhedra is necessary in $(MoVW)_5O_{14}$.

6.4.4 Consideration of active site models proposed in literature

Detailed models on the catalytically active site for the selective oxidation of propene to acrylic acid were suggested previously. In the reaction on *MoVSb* oxides it was suggested that the hexagonal sites in the M1 phase promote the formation of acrylic acid from propene [181] on *Sb* sites. These findings do not explain the catalytic activity on the deviating structure of $(MoVW)_5O_{14}$ with empty hexagonal channels and without antimony.

For selective ammoxidation of propene to acrylonitrile on *MoVTe* oxides an active site for the propene (amm)oxidation was located on the M2 phase [112]. The catalytic

centers determined on the M2 phase of $MoVTe$ oxide resemble that assumed for the propene oxidation on $BiMo$ oxides [179]. In detail a catalytically active site in the M2 phase was proposed: Te^{4+} located in a hexagonal channel of the M2 structure, an edge-sharing Mo^{6+} -octahedron and a neighbored spectator Mo^{6+} -octahedron are arranged on the basal (001) plane [169]. According to the TEM results (Figures 5.12, 5.21, and 5.23) the (001) plane is not a preferred surface termination on $(MoVW)_5O_{14}$. Moreover, the surface termination shows mostly chains of octahedra and not the ab-plane. This and the absence of tellurium in the hexagonal channels makes this scenario unlikely.

Recent studies on M2 phase $MoVTe$ oxides for selective ammoxidation of propene have shown that an ensemble of tellurium and molybdenum is necessary for the activation of propene [182]. Partial replacement of molybdenum by tungsten improved the selectivity at the expense of acrolein. Vanadium was found to be merely a structure adjusting agent. These results confirm the positive effect of tungsten for the formation of acrylic acid on $(MoVW)_5O_{14}$.

Tungsten in M2 phase $MoVTe$ oxides and $(MoVW)_5O_{14}$ could improve via the bulk structural stability the site isolation at the surface thus leading to the observed increase in acrylic acid formation. In $(MoVW)_5O_{14}$ the expansion of lattice constants during heating in propene and oxygen from 300 K to 773 K (Figure 5.77) is anisotropic. The c-axis increases linear with temperature, but the expansion of the a- and b-axis essentially occurs at temperatures above 720 K. This temperature correlates to a stagnation or decrease of the acrylic acid formation in the catalysis data of $(MoVW)_5O_{14}$ (Figure 5.75 no further increase of acrylic acid formation above 720 K, Figure 5.76 no further increase of acrylic acid formation above 700 K, Figure 5.80 decreasing acrylic acid formation above 720-730 K). Thus, the elongation in a/b-direction, possibly the cumulative effect of both, elongation in a/b- and in c-direction, coincides with the deactivation of the catalyst material. The unit cell of the Mo_5O_{14} -type structure is shown in Figure 4.5. The c-axis of ca. 4 Å is oriented parallel to the pentagonal columns, and the ab-plane presents the regular arrangement of the pentagonal columns to one another. Slight lengthening of pentagonal columns along the c-axis does not affect the catalytic performance. But pentagonal columns detaching from one another (elongation in a/b- direction) reduces the formation of selective oxidation products. It cannot be excluded that expansion in c-direction is harmful, too, if a certain limit is exceeded. In EXAFS data probing the short range order around tungsten (Figure 5.78) at 773 K the short tungsten-metal distance is still present at its initial distance. Apparently, the pentagonal bipyramids and their edge-sharing octahedra are a rigid unit and not affected by the elongation of a- and b-axis. Therefore, the expansion in a/b- direction can be attributed to the corner sharing octahedra between pentagonal columns (position M3 and M4 in Figure 4.5).

As a consequence, the less defined location of metals on position M3 and M4 (which is principally effected by both, expansion in a/b- and c-direction) correlates to decreasing acrylic acid formation. This finding on the bulk structure properties has implication for the reaction mechanism: the surface termination on the bulk structure as seen in the TEM images (Figures 5.12, 5.21, 5.23) exposes metals of position M3 and M4 at the surface. Apparently, the however 'ordered' metal ensemble at the surface accom-

plishing selective oxidation to acrylic acid is sensitive to metals on position M3 and M4 being out of place. The still ordered rigid pentagonal columns are thus not sufficient for the formation of acrylic acid. Eventually, in the selective oxidation reaction the pentagonal columns adjust the vicinity of metals on position M3 and M4. The pentagonal columns then represent a site isolating unit.

When the preferred location of vanadium in exclusively corner-sharing octahedra like M3 or M4 is considered and assigned to the catalytically relevant structure dynamics, Mo_5O_{14} -type materials could be representative for $MoVTaNb$ oxide materials, too. The V K edge XANES spectra of both, $(MoVW)_5O_{14}$ and $(MoV)_5O_{14}$ material, exhibit the same features despite of their differing catalytic performance. The distinct local and electronic structure of vanadium in both Mo_5O_{14} -type materials coincide with those of vanadium centers in $MoVTaNb$ oxide materials as presented in literature [183]. The catalytic dynamics of vanadium can selectively oxidize propene into acrylic acid together with a redox-stabilizing agent (e.g. tungsten) which stabilizes the structure and enables re-formation of characteristic metal ensembles at the surface. If the preferred location of W in pentagonal block units leading to structure stabilization, redox stability and site isolation correlates to acrylic acid formation, this could be the basic principle how $(MoVW)_5O_{14}$ gets higher acrylic acid formation than $(MoV)_5O_{14}$.

Summary

Crystallization

The thermal treatment of a $Mo_{0.68}V_{0.23}W_{0.09}$ oxide precursor was investigated with respect to the influence of treatment parameters on crystallinity and phase purity of the resulting $(MoVW)_5O_{14}$ oxide. The studies have shown that the mixed oxides obtained from varying treatment procedures contained different phases of variable crystallinity. The proper metal ratio does not necessarily form the desired material. An optimized two-step procedure was found that resulted in formation of crystalline $(MoVW)_5O_{14}$ material. This procedure encompasses thermal treatment at 623 K in 20% oxygen/nitrogen for 3 h and treatment at 713 K in helium for 3 h. The most important preparation parameter for the formation of a crystalline Mo_5O_{14} -type phase appeared to be the redox potential of the gas atmosphere at a given temperature. Furthermore, treatment parameters that influence the removal of gaseous products from the precursor (i.e. gas flow and dwell time) strongly affected the properties of the resulting oxide. Evolution of the short-range order structure around the various metal centers during thermal treatment was elucidated by in situ XAS. Formation of an intermediate phase shortly before crystallization of $(MoVW)_5O_{14}$ was observed.

Structure

Two mixed metal oxides, $(Mo_{0.91}V_{0.09})_5O_{14}$ and $(Mo_{0.68}V_{0.23}W_{0.09})_5O_{14}$ phases were structurally characterized. The structural analysis of $(MoV)_5O_{14}$ indicated a homogeneous distribution of molybdenum and vanadium on all sites. Conversely, for $(MoVW)_5O_{14}$ a preferred site occupancy of different elements on the different sites was found. From XRD and XAS investigations tungsten is mostly located in the pentagonal bipyramids and its neighboring octahedral sites. The stabilizing effect of tungsten in $(MoVW)_5O_{14}$ can be assigned to its site preference in the Mo_5O_{14} -type structure. Vanadium prefers corner linked octahedra not edge-sharing to the pentagonal block unit.

Properties

Bulk structural properties and stabilities of crystalline single phase $(Mo_{0.91}V_{0.09})_5O_{14}$ and $(Mo_{0.68}V_{0.23}W_{0.09})_5O_{14}$ phases were investigated under reducing and oxidizing reaction conditions. A stabilizing effect of tungsten in the $(MoVW)_5O_{14}$ sample under oxidizing conditions was found. Additionally, tungsten centers in a $MoVW$ dioxide

material obtained from reducing $(MoVW)_5 O_{14}$ exert a pronounced structure-directing effect under re-oxidation conditions. The effect of tungsten centers on the particular bulk structural properties of $(MoVW)_5 O_{14}$ may account for the structural promoting effect of tungsten in selective oxidation.

Moreover, the crystalline $(MoVW)_5 O_{14}$ but not $(MoV)_5 O_{14}$ material exhibited catalytic activity in the selective oxidation of propene to acrylic acid. Obviously catalytically active material is obtained with the combination of the appropriate metal composition and the proper preparation conditions. As single phase crystalline $(MoVW)_5 O_{14}$ the material is a suitable model system for more complex metal oxides utilized in the selective oxidation of propene.

Acknowledgement

Research presented in this thesis was performed from August 2003 till December 2006 in the department of Inorganic Chemistry at the Fritz-Haber-Institute of the Max-Planck Society guided by Prof. Dr. Robert Schlögl and Prof. Dr. Thorsten Ressler.

Thanks a lot to all who contributed to the success of this work!

Special thank is to:

Prof. Dr. Robert Schlögl for the possibility to work on that subject in his department, for continous support and discussion

Prof. Dr. Thorsten Ressler for sharing his broad knowledge and supervision all the years

Dr. Annette Trunschke for discussion and support

Dr. Rolf Jentoft for many methodological instructions, extensive discussion and other good counsel

Dr. Olaf Timpe and Dr. Andreas Blume for good cooperation and excellent sample preparation

Dr. Frank Girgsdies for a lot of XRD support and other good conversation

Edith Kitzelmann for a lot of amusement besides many XRD's

Giesela Lorenz taking care of all that may happen to a PhD and her great sense of humor

Dr. Jürgen Osswald, Dr. Alexandra Szizybalski and Dr. Benjamin Kniep for discussions on all kinds of science, the rest of life and funny beamtimes

Patrick Kurr for amusement in the office, Anne Dennstedt for sharing night shifts with pleasure, Bernd Steinhauer for mutual support, Peter Schnörch and Almudena

Celaya for cooperation and company

Dr. Konstantin Klementiev for consultation and immediate support whenever the viper code needed extension

Dr. Julia Wienold, an expert in this field who was always available for questioning

Dr. Di Wang for TEM measurements and discussion

Ute Röper for help in the last state of writing up

Manuel for critical reading and the Rödel Family in general :)

References

- [1] L. T. Weng and B. Delmon, *Applied Catalysis A*, **1992**, *81*, 141–213.
- [2] R. K. Grasselli, *Topics in Catalysis*, **2002**, *21*(1-3), 79–88.
- [3] R. K. Grasselli, *Topics in Catalysis*, **2001**, *15*(2-4), 93–101.
- [4] P. Mars and D. W. van Krevelen, *Chemical Engineering Science*, **1954**, *3*, 41–59.
- [5] A. Nilsson, L. G. M. Pettersson, B. Hammer, T. Bligaard, C. H. Christensen, and J. K. Nørskov, *Catalysis Letters*, **2005**, *100*(3-4), 111–114.
- [6] M. Dieterle and G. Mestl, *Physical Chemistry Chemical Physics*, **2002**, *4*, 822–826.
- [7] A. B. Anderson, D. W. Ewing, Y. Kim, R. K. Grasselli, J. D. Burrington, and J. F. Brazdil, *Journal of Catalysis*, **1985**, *96*(1), 222–233.
- [8] M. Niwa, M. Mizutani, M. Takahashi, and Y. Murakami, *Journal of Catalysis*, **1981**, *70*(1), 14–23.
- [9] J. B. Goodenough, *Physical Review*, **1972**, *B5*(8), 2764–2774.
- [10] T. Narbeshuber, E. Gehrler, and U. Balfanz; DE 10150944 A1; BASF.
- [11] T. G. Alkhozov, K. Yu. Adzhamov, and F. M. Poladov, *Reaction Kinetics and Catalysis Letters*, **1977**, *7*(1), 65–68.
- [12] D.-H. He, W. Ueda, and Y. Moro-Oka, *Catalysis Letters*, **1992**, *12*, 35–44.
- [13] P. Botella, J. M. Lopez Nieto, and B. Solsona, *Journal of Molecular Catalysis*, **2002**, *184*(1-2), 335–347.
- [14] DE 1173887; Stamicarbon.
- [15] M. Dugal, M. Weisbeck, and G. Wegener; DE 10247784 A1; Bayer.
- [16] M. M. Lin, *Applied Catalysis A - General*, **2001**, *207*(1-2), 1–16.
- [17] JP 57010094 B4; Japan Synthetic Rubber.
- [18] S. Unverricht and H. Hibst; DE 19815281 A1; BASF.

- [19] V. H. Rane, A. M. Rajput, A. J. Karkamkar, and V. R. Choudhary, *Applied Energy*, **2004**, *77*(4), 375–382.
- [20] M. M. Bhasin, J. H. McCain, B. V. Vora, T. Imai, and P. R. Pujado, *Applied Catalysis A*, **2001**, *221*(1-2), 397–419.
- [21] M. Tanimoto, H. Himeji-shi, I. Mihara, H. Aboshi-ku, T. Kawajiri, and H. Himeji-shi; EP 0711745 B1; Nippon Shokubai.
- [22] A. Tenten, H. Hibst, F.-G. Martin, L. Marosi, and V. Kohl; DE 4405514 A1; BASF.
- [23] E. Balcells, F. Borgmeier, I. Griřtede, and H.-G. Lintz, *Catalysis Letters*, **2003**, *87*, 195–199.
- [24] R. K. Grasselli, J. D. Burrington, D. J. Buttrey, P. DeSanto, C. G. Lugmair, A. F. Volpe Jr., and T. Weingand, *Topics in Catalysis*, **2003**, *23*(1-4), 5–22.
- [25] L. Kihlborg, *Arkiv För Kemi*, **1963**, *21*(44), 471–495.
- [26] K. Kosuge, *Journal of Physical Chemistry Solids*, **1967**, *28*, 1613–1621.
- [27] H. Oppermann, G. Stöver, and E. Wolf, *Crystal Research and Technology*, **1985**, *20*, 883–887.
- [28] Inorganic Crystal Structure Database, Fachinformationszentrum (FIZ) Karlsruhe, Germany.
- [29] B. G. Brandt, *Chemical Communications, University of Stockholm*, **1971**, pages 1–41.
- [30] L. Kihlborg, *Arkiv För Kemi*, **1963**, *21*, 357–364.
- [31] L. Kihlborg, *Arkiv För Kemi*, **1963**, *21*(42), 443–459.
- [32] H. Fujishita, M. Sato, S. Sato, and S. Hoshino, *Journal of Solid State Chemistry*, **1987**, *66*, 40–46.
- [33] V. L. Volkov, G. Sh. Tynkacheva, A. A. Fotiev, and E. V. Tkachenko, *Russian Journal of Inorganic Chemistry*, **1972**, *17*(10), 1469–1470.
- [34] P. Mahe-Pailleret, *Revue de Chimie Minerale*, **1970**, *7*, 807–846.
- [35] H. A. Eick and L. Kihlborg, *Acta Chemica Scandinavica*, **1966**, *20*, 1658–1666.
- [36] P. Pailleret, J. Borensztajn, W. Freundlich, and A. Rimsky, *Comptes Rendus Hebdomadaires des Seances de l'Academie des Sciences - Serie C, Sciences Chimiques*, **1966**, *263*, 1131–1133.
- [37] L. Kihlborg, *Acta Chemica Scandinavica*, **1967**, *21*, 2495–2502.

- [38] H. A. Eick and L. Kihlberg, *Acta Chemica Scandinavica*, **1966**, 20(3), 722–729.
- [39] L. M. Plyasova, L. P. Soloveva, G. N. Kryukova, V. A. Zabolotnyi, and I. P. Olenkova, *Zhurnal Strukturnoi Khimii*, **1981**, 32, 110–115.
- [40] F. Haaß, A. H. Adams, T. Buhrmester, G. Schimanke, M. Martin, and H. Fuess, *Physical Chemistry Chemical Physics*, **2003**, 5, 4317–4324.
- [41] C. Tenailleau, E. Suard, J. Rodriguez-Carvajal, M. P. Crosnier-Lopez, and P. Lacorre, *Chemistry of Materials*, **2002**, 14, 3569–3575.
- [42] C. Tenailleau, E. Suard, J. Rodriguez-Carvajal, J. Gibaud, and P. Lacorre, *Journal of Solid State Chemistry*, **2003**, 174, 431–440.
- [43] N. Yamazoe, T. Ekström, and L. Kihlberg, *Acta Chemica Scandinavica A*, **1975**, 29, 404–408.
- [44] R. C. T. Slade, A. Ramanan, B. C. West, and E. Prince, *Journal of Solid State Chemistry*, **1989**, 82, 65–69.
- [45] T. Ekström and M. Nygren, *Acta Chemica Scandinavica*, **1972**, 26(5), 1827–1835.
- [46] A. H. Adams, F. Haaß, T. Buhrmester, J. Kunert, J. Ott, H. Vogel, and H. Fuess, *Journal of Molecular Catalysis A*, **2004**, 216(1), 67–74.
- [47] M. Dieterle; *In situ Resonance Raman Studies of Molybdenum Oxide based Selective Oxidation Catalysts*; PhD thesis, Technische Universität Berlin, **2001**.
- [48] A. Magneli, *Acta Crystallographica*, **1953**, 6, 495–500.
- [49] Hollemann-Wiberg, *Lehrbuch der Anorganischen Chemie*; deGruyter, 101. auflage ed., 1995; Anhang IV, p. 1839.
- [50] R. Hayn and R. J. Fischbeck, *Zeitschrift für Physik B-Condensed Matter*, **1989**, 76(1), 33–41.
- [51] I. E. Maxwell, P. van den Brink, R. S. Downing, A. H. Sijpkens, S. Gomez, and T. Maschmeyer, *Topics in Catalysis*, **2003**, 24(1-4), 125–135.
- [52] J. Greeley, J. K. Nørskov, and Manos Mavrikakis, *Annual Review of Physical Chemistry*, **2002**, 53, 319–348.
- [53] B. L. Kniep, T. Ressler, A. Rabis, F. Girgsdies, M. Baenitz, F. Steglich, and R. Schlögl, *Angewandte Chemie - International Edition*, **2004**, 43(1), 112–115.
- [54] J. Osswald; *Active-Site Isolation for the Selective Hydrogenation of Acetylene: the Pd – Ga and Pd – Sn Intermetallic Compounds*; PhD thesis, Technische Universität Berlin, **2005**.

- [55] S. B. Abd Hamid, D. Othman, N. Abdullah, O. Timpe, S. Knobl, D. Niemeyer, J. Wagner, D. Su, and R. Schlögl, *Topics in Catalysis*, **2003**, *24*(1-4), 87–95.
- [56] J. Kunert, A. Drochner, J. Ott, H. Vogel, and H. Fuess, *Applied Catalysis A*, **2004**, *269*, 53–61.
- [57] M. S. Spencer and M. V. Twigg, *Annual Review of Materials Research*, **2005**, *35*, 427–464.
- [58] H. Topsoe, *Journal of Catalysis*, **2003**, *216*(1-2), 155–164.
- [59] Y. Iwasawa, *Journal de Physique IV*, **1997**, *7*(C2), 67–81.
- [60] S. Breiter, M. Estenfelder, H.-G. Lintz, and H. Hibst A. Tenten, *Applied Catalysis A*, **1996**, *134*, 81–89.
- [61] V. M. Bondareva, T. V. Andrushkevich, G. I. Aleshina, L. M. Plyasova, L. S. Dovlitova, O. B. Lapina, D. F. Khabibulin, and A. A. Vlasov, *Reaction Kinetics and Catalysis Letters*, **2006**, *87*(2), 377–386.
- [62] V. M. Bondareva, T. V. Andrushkevich, G. I. Aleshina, R. I. Maksimovskaya, L. M. Plyasova, L. S. Dovlitova, and E. B. Burgina, *Reaction Kinetics and Catalysis Letters*, **2006**, *88*(1), 183–191.
- [63] J. C. Vedrine, E. K. Novakova, and E. G. Derouane, *Catalysis Today*, **2003**, *81*(2), 247–262.
- [64] G. Mestl, Ch. Linsmeier, R. Gottschall, M. Dieterle, J. Find, D. Herein, J. Jäger, Y. Uchida, and R. Schlögl, *Journal of Molecular Catalysis A*, **2000**, *162*, 463–492.
- [65] O. Ovsitser, Y. Uchida, G. Mestl, G. Weinberg, A. Blume, J. Jäger, M. Dieterle, H. Hibst, and R. Schlögl, *Journal of Molecular Catalysis A*, **2002**, *185*, 291–303.
- [66] G. Mestl, *Journal of Raman Spectroscopy*, **2002**, *33*, 333–347.
- [67] T.V. Andrushkevich, *Kinetics and Catalysis*, **1997**, *38*(2), 266–276.
- [68] J. B. Wagner, D. S. Su, S. A. Schunk, H. Hibst, J. Petzold, and R. Schlögl, *Journal of Catalysis*, **2004**, *224*, 28–35.
- [69] L. Kihlberg, *Acta Chemica Scandinavica*, **1969**, *23*(5), 1834–1835.
- [70] T. Ekström, *Acta Chemica Scandinavica*, **1972**, *26*(5), 1843–1846.
- [71] T. Ekström and M. Nygren, *Acta Chemica Scandinavica*, **1972**, *26*(5), 1836–1842.
- [72] T. Ekström, *Materials Research Bulletin*, **1972**, *7*, 19–26.
- [73] T. Ekström and R. J. D. Tilley, *Journal of Solid State Chemistry*, **1976**, *19*, 125–133.

- [74] L. Kihlberg, *Arkiv För Kemi*, **1963**, 21(40), 427–437.
- [75] N. Yamazoe and L. Kihlberg, *Acta Crystallographica*, **1975**, B31, 1666–1672.
- [76] P. DeSanto, D. J. Buttrey, R. K. Grasselli, C. G. Lugmair, A. F. Volpe, B. H. Toby, and T. Vogt, *Topics in Catalysis*, **2003**, 23(1-4), 23–38.
- [77] R. K. Grasselli, D. J. Buttrey, P. DeSanto, J. D. Burrington, C. G. Lugmair, A. F. Volpe, and T. Weingand, *Catalysis Today*, **2004**, 91-92, 251–258.
- [78] M. Baca, A. Pigamo, J. L. Dubois, and J. M. M. Millet, *Topics in Catalysis*, **2003**, 23(1-4), 39–42.
- [79] N. Watanabe and W. Ueda, *Industrial and Engineering Chemistry Research*, **2006**, 45, 607–614.
- [80] T. Ressler, J. Wienold, R. E. Jentoft, and F. Girgsdies, *European Journal of Inorganic Chemistry*, **2003**, pages 301–312.
- [81] H. T. Evans jun., B. M. Gatehouse, and P. Leverett, *Journal of the Chemical Society, Dalton Transactions*, **1975**, 6, 505–514.
- [82] M. T. Averbuch-Pouchot, I. Tordjman, A. Durif, and J. C. Guitel, *Acta Crystallographica*, **1979**, B35, 1675–1677.
- [83] H. d'Amour and R. Allmann, *Zeitschrift fuer Kristallographie, Kristallgeometrie, Kristallphysik, Kristallchemie*, **1972**, 136, 23–47.
- [84] J. B. Parise, III E. M. McCarron, and A. W. Sleight, *Materials Research Bulletin*, **1987**, 22(6), 803–811.
- [85] G. Svensson and L. Kihlberg, *Reactivity of Solids*, **1987**, 3, 33–43.
- [86] F. Harb, B. Gerand, G. Nowogrocki, and M. Figlarz, *Solid State Ionics*, **1989**, 32/33, 84–90.
- [87] E. M. McCarroni and J. C. Calabrese, *Journal of Solid State Chemistry*, **1991**, 91, 121–125.
- [88] J. Guo, P. Zavalij, and M. S. Whittingham, *Journal of Solid State Chemistry*, **1995**, 117, 323–332.
- [89] Y. T. Hu and P. K. Davies, *Journal of Solid State Chemistry*, **1993**, 105, 489–503.
- [90] J. Wienold, R. E. Jentoft, and T. Ressler, *European Journal of Inorganic Chemistry*, **2003**, pages 1058–1071.
- [91] J. A. A. Ketelaar, *Zeitschrift fuer Kristallographie, Kristallgeometrie, Kristallphysik, Kristallchemie*, **1936**, 95, 9–27.
- [92] P. D. Dernier and M. Marezio, *Physical Review*, **1970**, B2, 3771–3776.

- [93] E. Salje, *Acta Crystallographica*, **1977**, *B33*, 574–577.
- [94] A. Magneli and G. Andersson, *Acta Chemica Scandinavica*, **1955**, *9*(8), 1378–1381.
- [95] G. Andersson, *Acta Chemica Scandinavica*, **1956**, *10*, 623–628.
- [96] D. J. Palmer and P. G. Dickens, *Acta Crystallographica*, **1979**, *B35*, 2199–2201.
- [97] B. O. Marinder, *Materials Research Bulletin*, **1975**, *10*, 909–914.
- [98] H. A. Eick and L. Kihlberg, *Acta Chemica Scandinavica*, **1966**, *20*, 722–729.
- [99] M. M. Dobson and R. J. D. Tilley, *Acta Crystallographica*, **1988**, *B44*(5), 474–480.
- [100] K. Viswanathan, K. Brandt, and E. Salje, *Journal of Solid State Chemistry*, **1981**, *36*, 45–51.
- [101] M. R. Sundberg, N. D. Zakharov, I. P. Zibrov, Yu. A. Barabanenkov, V. P. Filonenko, and P. Werner, *Acta Crystallographica*, **1993**, *B49*, 951–958.
- [102] Yu. A. Barabanenkov, M. D. Valkovskii, N. D. Zakharov, I. P. Zibrov, A. I. Popov, and V. P. Filonenko, *Zhurnal Neorganicheskoi Khimii*, **1992**, *37*, 19–24.
- [103] L. Kihlberg, *Acta Chemica Scandinavica*, **1960**, *14*, 1612–1622.
- [104] A. Müller and S. Roy, *Russian Chemical Reviews*, **2002**, *71*(12), 981–991.
- [105] A. Müller and S. Roy, *Coordination Chemistry Reviews*, **2003**, *245*, 153–166.
- [106] J. B. Goodenough, *Materials Research Bulletin*, **1967**, *2*, 165–184.
- [107] J. B. Goodenough, *Materials Research Bulletin*, **1971**, *6*(10), 967–976.
- [108] A. Müller, P. Kögerler, and A. W. M. Dress, *Coordination Chemistry Reviews*, **2001**, *222*, 193–218.
- [109] L. Kihlberg, *Arkiv För Kemi*, **1963**, *21*(44), 471–495.
- [110] T. Ressler, R. E. Jentoft, J. Wienold, M. M. Günter, and O. Timpe, *Journal of Physical Chemistry B*, **2000**, *104*, 6360–6370.
- [111] T. Ressler, O. Timpe, T. Neisius, G. Mestl, M. Dieterle, and R. Schlögl, *Journal of Catalysis*, **2000**, *191*, 75–85.
- [112] P. DeSanto, D. J. Buttrey, R. K. Grasselli, C. G. Lugmair, A. F. Volpe, B. H. Toby, and T. Vogt, *Zeitschrift für Kristallographie*, **2004**, *219*(3), 152–165.
- [113] J. Holmberg, R. K. Grasselli, and A. Andersson, *Applied Catalysis A: General*, **2004**, *270*, 121–134.

- [114] R. K. Grasselli, D. J. Buttrey, P. DeSanto Jr., J. D. Burrington, C. G. Lugmair, A. F. Volpe Jr., and T. Weingand, *Catalysis Today*, **2004**, 91-92, 251–258.
- [115] R. A. Young, *The Rietveld Method*; Oxford university press, 1993.
- [116] P. Luger, Eds., *Modern X-Ray Analysis on Single Crystals*; deGruyter, 1980.
- [117] W. Massa, Eds., *Kristallstrukturbestimmung*; Teubner, 1996.
- [118] F. Girgsdies, W. S. Dong, J. K. Bartley, G. J. Hutchings, R. Schlögl, and T. Ressler, *Solid State Sciences*, **2006**, 8(7), 807–812.
- [119] J. J. Rehr and A. L. Ankudinov, *Radiation Physics and Chemistry*, **2004**, 70, 453–463.
- [120] A. L. Ankudinov and J. J. Rehr, *Journal of Synchrotron Radiation*, **2003**, 10, 366–368.
- [121] D. C. Koningsberger and R. Prins, Ed., *X-Ray Absorption*; John Wiley and Sons, 1987.
- [122] D.C. Koningsberger, B. L. Mojet, G. E. van Dorssen, and D. E. Ramaker, *Topics in Catalysis*, **2000**, 10, 143–155.
- [123] B. M. Weckhuysen, Eds., *In-situ spectroscopy of catalysts*; American Scientific Publication, 2004.
- [124] S. Knobl, G. A. Zenkovets, G. N. Kryukova, O. Ovsitser, D. Niemeyer, R. Schlögl, and G. Mestl, *Journal of Catalysis*, **2003**, 215, 177–187.
- [125] Y. Uchida, G. Mestl, O. Ovsitser, J. Jäger, A. Blume, and R. Schlögl, *Journal of Molecular Catalysis A*, **2002**, 187, 247–257.
- [126] DIFFRAC plus Evaluation Package release 2003.
- [127] H. Rietveld, *Acta Crystallographica*, **1967**, 22, 151–152.
- [128] TOPAS Version 2.1 Bruker AXS.
- [129] P. Thompson, D. E. Cox, and J. B. Hastings, *Journal of Applied Crystallography*, **1987**, 20, 79–83.
- [130] T. Ressler, R. E. Jentoft, J. Wienold, M. M. Günter, and O. Timpe, *Journal of Physical Chemistry B*, **2000**, 104(27), 6360–6370.
- [131] J. Wong, F. W. Lytle, R. P. Messmer, and D. H. Maylotte, *Physical Review B*, **1984**, 30(10), 5596–5610.
- [132] T. Ressler, J. Wienold, R. E. Jentoft, and T. Neisius, *Journal of Catalysis*, **2002**, 210, 67–83.

- [133] T. Ressler, *Journal of Synchrotron radiation*, **1998**, *5*, 118–122.
- [134] K. V. Klementev, *Journal Physics D: Applied Physics*, **2001**, *34*, 209–217.
- [135] J. J. Rehr, C. H. Booth, F. Bridges, and S. I. Zabinsky, *Physical Review B*, **1994**, *49*, 12347–12350.
- [136] C. Degueldre and S. Conradson, *Applied Physics A-Materials Science and Processing*, **2001**, *73*(4), 489–494.
- [137] A. Mizuno, T. Itami, A. San-Miguel, G. Ferlat, J.F. Jal, and M. Borwoski, *Journal of Non-Crystalline Solids*, **2002**, *312*, 74–79.
- [138] J.X. Gao, B.W. Wang, T. Liu, J.C. Wang, C.L. Song, Z.D. Chen, T.D. Hu, Y.N. Xie, J. Zhang, and H.A. Yang, *Journal of Synchrotron Radiation*, **2005**, *12*(3), 374–379.
- [139] P. Debye, *Annalen der Physik*, **1910**, *33*(16), 1427–1437.
- [140] G. G. Li, F. Bridges, and C. H. Booth, *Physical Review B*, **1995**, *52*(9), 6332–6348.
- [141] G. Dalba and P. Fornasini, *Journal of Synchrotron Radiation*, **1997**, *4*, 243–255.
- [142] NETZSCH Proteus - Thermal Analysis, Version 4.0+, 2000.
- [143] NETZSCH Thermokinetics, Version 2000.9b.
- [144] L. Reich, *Journal of Polymer Science Part B: Polymer Letters*, **1965**, *3*(3), 231–234.
- [145] O. Kirilenko, F. Girgsdies, R. E. Jentoft, and T. Ressler, *European Journal of Inorganic Chemistry*, **2005**, *11*, 2124–2133.
- [146] I. M. Szilagyi, J. Madarasz, F. Hange, and G. Pokol, *Solid State Ionics*, **2004**, *172*(1-4), 583–586.
- [147] A. K. Davies, J. V. Gilligan, and S. A. Jones, *Journal of Thermal Analysis*, **1996**, *44*, 1567–1576.
- [148] J. Madarasz, I. M. Szilagyi, F. Hange, and G. Pokol, *Journal of Analytical and Applied Pyrolysis*, **2004**, *72*(2), 197–201.
- [149] S. Brunauer, P. H. Emmett, and E. Teller, *Journal of the American Chemical Society*, **1938**, *60*, 309–319.
- [150] A. Kuzmin and J. Purans, *Journal of Physics: Condensed Matter*, **2000**, *12*, 1959–1970.

- [151] S. Knobl, G. A. Zenkovets, G. N. Kryukova, R. I. Maksimovskaya, T. V. Larina, N. T. Vasenin, V. F. Anufrienko, D. Niemeyer, and R. Schlögl, *Physical Chemistry Chemical Physics*, **2003**, *5*, 5343–5348.
- [152] M. M. Lin, *Applied Catalysis A - General*, **2003**, *250*(2), 305–318.
- [153] M. M. Lin, *Applied Catalysis A - General*, **2003**, *250*(2), 287–303.
- [154] H. Watanabe and Y. Koyasu, *Applied Catalysis A - General*, **2000**, *194-195*, 479–485.
- [155] G. Schimanke, M. Martin, J. Kunert, and H. Vogel, *Zeitschrift für Anorganische und Allgemeine Chemie*, **2005**, *631*, 1289–1296.
- [156] K. Brückman, R. Grabowski, J. Haber, A. Mazurkiewicz, J. Sloczynski, and T. Wiltowski, *Journal of Catalysis*, **1987**, *104*(1), 71–79.
- [157] H. Werner, O. Timpe, D. Herein, Y. Uchida, N. Pfänder, U. Wild, R. Schlögl, and H. Hibst, *Catalysis Letters*, **1997**, *44*, 153–163.
- [158] M. Dieterle, G. Mestl, J. Jäger, Y. Uchida, H. Hibst, and R. Schlögl, *Journal of Molecular Catalysis A*, **2001**, *174*, 169–185.
- [159] R. S. Barker and I. R. Evans, *Journal of Solid State Chemistry*, **2006**, *179*(6), 1918–1923.
- [160] F. Cavani, N. Ballarini, M. Cimini, F. Trifiro, M. Banares, and M. O. Guerrero-Perez, *Catalysis Today*, **2006**, *112*, 12–16.
- [161] E. M. Thorsteinson, T. P. Wilson, F. G. Young, and P. H. Kasai, *Journal of Catalysis*, **1978**, *52*, 116–132.
- [162] X. Cao, L. Li, and Y. Xie, *Journal of Colloidal and Interface Science*, **2004**, *273*, 175–180.
- [163] L. B. Levy and P. B. DeGroot, *Journal of Catalysis*, **1982**, *76*, 385–392.
- [164] P. B. DeGroot and L. B. Levy, *Journal of Catalysis*, **1982**, *76*, 393–404.
- [165] P. Afanasiev, *Journal of Physical Chemistry B*, **2005**, *109*(39), 18293–18300.
- [166] J. F. Bradzil, D. D. Suresh, and R. K. Grasselli, *Journal of Catalysis*, **1980**, *66*, 347–367.
- [167] B. G. Hyde and M. O’Keefe, *Acta Crystallographica A*, **1973**, *29*, 243–248.
- [168] M. Roussel, M. Bouchard, E. Bordes-Richard, K. Karim, and S. Al-Sayari, *Catalysis Today*, **2005**, *99*(1-2), 77–87.

- [169] R. K. Grasselli, D. J. Buttrey, J. D. Burrington, A. Andersson, J. Holmberg, W. Ueda, J. Kubo, C. G. Lugmair, and A. F. Volpe, *Topics in Catalysis*, **2006**, *38*(1-3), 7–16.
- [170] P. Beato, A. Blume, F. Girgsdies, R. E. Jentoft, R. Schlögl, O. Timpe, A. Trunschke, G. Weinberg, Q. Basher, F. A. Hamid, S. B. A. Hamid, E. Omar, and L. Mohd Salim, *Applied Catalysis A General*, **2006**, *307*(1), 137–147.
- [171] K. Krauß, A. Drochner, M. Fehlings, J. Kunert, and H. Vogel, *Journal of Molecular Catalysis A*, **2000**, *162*, 413–422.
- [172] K. Krauß, A. Drochner, M. Fehlings, J. Kunert, and H. Vogel, *Journal of Molecular Catalysis A*, **2002**, *177*, 237–245.
- [173] T. V. Andrushkevich, *Catalysis Reviews - Science and Engineering*, **1993**, *35*(2), 213–259.
- [174] H. Vogel, R. Böhling, and H. Hibst, *Catalysis Letters*, **1999**, *62*, 71–78.
- [175] P. DeSanto, D. J. Buttrey, R. K. Grasselli, W. D. Pyrz, C. G. Lugmair, A. F. Volpe, T. Vogt, and B. H. Toby, *Topics in Catalysis*, **2006**, *38*(1-3), 31–40.
- [176] B. Stein, C. Weimer, and J. Gaube, *3rd World Congress on Oxidation Catalysis*, **1997**, pages 393–402.
- [177] G. Mestl, *Topics in Catalysis*, **2006**, *38*(1-3), 69–82.
- [178] L. C. Glaeser, J. F. Bradzil, M. A. Hazle, M. Mehicic, and R. K. Grasselli, *Journal of the Chemical Society - Faraday Transactions I*, **1985**, *81*(11), 2903–2912.
- [179] R. K. Grasselli, J. D. Burrington, D. J. Buttrey, P. DeSanto, C. G. Lugmair, A. F. Volpe, and T. Weingand, *Topics in Catalysis*, **2003**, *23*(1-4), 5–22.
- [180] Y. H. Jang and W. A. Goddard, *Topics in Catalysis*, **2001**, *15*(2-4), 273–289.
- [181] W. Ueda, Y. Endo, and N. Watanabe, *Topics in Catalysis*, **2006**, *38*(4), 261–268.
- [182] J. Holmberg, S. Hansen, R. K. Grasselli, and A. Anderson, *Topics in Catalysis*, **2006**, *38*(1-3), 17–29.
- [183] M. Baca and J. M. M. Millet, *Applied Catalysis A General*, **2005**, *288*(1-2), 243–243.

Curriculum vitae

Personal data

Eva Rödel
Marschnerstr. 14
12203 Berlin
Germany

Born 20.04. 1979 in Berlin, Germany

Education

- 1985-1989 Sachsenwald elementary school, Berlin
- 1989-1991 Gymnasium Steglitz (secondary school), Berlin
- 1991-1998 Hermann-Ehlers high school, Berlin (extension courses in chemistry and biology)
- 10.06.1998 Abitur school certificate

Studies

- 1.10.1998-30.06.2003 chemistry studies at Freie University Berlin, elective subject crystallography
- 13.06.2003 diploma thesis in chemistry on '*Experimental charge density distribution of the tripeptide L-Alanyl-L-alanyl-L-alanin by means of high-resolution X-ray diffraction at 20 Kelvin*'
at Freie University Berlin with Prof. Dr. Luger
- 1.08.2003-31.12.2006 PhD thesis in chemistry on '*In situ bulk structural investigation of Mo₅O₁₄-type mixed metal oxide catalysts for partial oxidation reactions*'
at Fritz-Haber Institute, Berlin, with Prof. Dr. Schlögl and Technical University, Berlin, with Prof. Dr. Ressler

Posters and conferences

- 29.-30. January 2004 Hamburg, Germany
HASYLAB Usermeeting and XAS Satellite meeting
- 17.-19. March 2004 Weimar, Germany
XXXVII. Jahrestreffen Deutscher Katalytiker in Verbindung mit dem Fachtreffen Reaktionstechnik
Poster *'In situ bulk structural investigations of molybdenum oxide catalysts under partial oxidation reaction conditions'* E. Rödel, R.E. Jentoft, R. Schlögl, T. Ressler
- 13.-15. September 2004 Marburg, Germany
12. Vortragstagung FG Festkörperchemie und Materialforschung (GdCh)
Poster *'In situ investigations of structure-activity correlations of mixed molybdenum oxide catalysts'* E. Rödel, R.E. Jentoft, R. Schlögl, T. Ressler
28. September-1. October 2004 Saarbrücken, Germany
NDCat-2004 French-German Summer School of Research
Poster *'In situ bulk structural investigations of mixed molybdenum oxide catalysts'* E. Rödel, R.E. Jentoft, R. Schlögl, T. Ressler
- 27.-28. January 2005 Hamburg, Germany
HASYLAB Usermeeting and XAS Satellite meeting
Poster *'Structural in situ XAS investigations of mixed molybdenum oxide catalysts'* E. Rödel, B. Kniep, S. Knobl, R. Schlögl, T. Ressler
- 16.-18. March 2005 Weimar, Germany
XXXVIII. Jahrestreffen Deutscher Katalytiker
Poster *'In situ investigations of structure-activity correlations of mixed molybdenum oxide catalysts'* E. Rödel, S. Knobl, R. Schögl, T. Ressler
- 26.-29. May 2005 Hirschegg, Austria
Seminar zur Festkörperchemie (Seminar of Solid state chemistry)
28. August-1. September 2005 Sofia, Bulgarien
EuropaCat VII
Flash presentation and poster *'In situ structural investigations of the (MoVW)₅O₁₄ type mixed molybdenum oxide catalysts'* E. Rödel,

S. Knobl, R. Schlögl, T. Ressler

- 26.-27. January 2006 Hamburg, Germany
HASYLAB Usermeeting and XAS Satellite meeting
Poster '*In situ XAS investigation of tungsten as structure directing agent during formation of Mo_5O_{14} type partial oxidation catalysts*'
E. Rödel, R. Schlögl, T. Ressler
- 15.-17. March 2006 Weimar, Germany
XXXIX. Jahrestreffen Deutscher Katalytiker in Verbindung mit dem Fachtreffen Reaktionstechnik
Poster '*In situ investigation of tungsten as structure-directing agent during formation of Mo_5O_{14} type partial oxidation catalysts*' E. Rödel, S. Knobl, R. Schögl, T. Ressler
- 23.-27. April 2006 Toledo, Spain
Operando II Second International Congress on operando spectroscopy
Poster '*In situ investigations of the formation of a $(MoVW)_5O_{14}$ type mixed molybdenum oxide catalyst*' E. Rödel, R. Schlögl, T. Ressler

Publications

- E. Rodel, M. Messerschmidt, B. Dittrich, P. Luger; Atomic and bond topological properties of the tripeptide L-alanyl-L-alanyl-L-alanine based on its experimental charge density obtained at 20 K; Organic & Biomolecular Chemistry 4 (3) 475-481, 2006
- E. Rödel, O. Timpe, A. Trunschke, G.A. Zenkovets, G.N. Kryukova, R. Schlögl, T. Ressler; Structure stabilizing effect of tungsten in mixed molybdenum oxides with Mo_5O_{14} -type structure; submitted to Catalysis Today
- E. Rödel, S. Knobl, R. Schlögl, T. Ressler; In situ investigations of the structure formation of a Mo_5O_{14} -type mixed oxide catalyst; in preparation

Others

E. Rödel, R. E. Jentoft, T. Ressler; In Situ Investigations of Structure-activity correlations of Mixed Molybdenum Oxide Catalysts; *Zeitschrift für anorganische und allgemeine Chemie* 630/11, 1756, 2004

E. Rödel, S. Knobl, R.E. Jenoft, T. Ressler; In situ investigations of structure-activity correlations of mixed molybdenum oxide catalysts; *HASYLAB Annual Report 2004*, 847-848, 2004

E. Rödel, R. Schlögl, T. Ressler; In situ XAS investigation of tungsten as structure directing agent during formation of Mo_5O_{14} type partial oxidation catalysts; *HASYLAB Annual Report 2005*, 1105-1106, 2005